Development of a Microchannel Reactor Model

Muhammad Parak
Department of Chemical Engineering
University of Cape Town

Dissertation in partial requirement of Master of Science in Chemical Engineering

September 2, 2011

Abstract

The development and future wide-spread use of hydrogen fuel cells is inhibited by the problems associated with hydrogen storage. A possible alternative is to store and then reform hydrocarbons to yield hydrogen in an on-board fuel processing system. Microchannel reactors have reduced mass and heat transfer limitations compard to fixed bed reactors and are thus able to exploit fast intrinsic kinetics. Furthermore, their high surface area to volume ratio reduces their size for a constant throughput, increasing their potential for miniaturised deployment.

Current microchannel reactor models are either over simplified and neglect important subtleties, or too complex and are not usable for optimisation or sensitivity studies. Previous studies use low order finite element methods to solve model PDEs. These can be replaced by the more efficient collocation method which has been used to model chemical systems up to 2-dimensions while a suitable 3-dimensional solver is unavailable. The objective of this project is therefore to develop a comprehensive model that obeys the phenomenological laws and is fast enough to be used for optimisation.

A 3-dimensional single phase model was developed for rectangular microchannel reactors and applied to a single channel. This accounted for laminar flow in the channel bulk with reaction at all walls and perpendicular diffusion described by the Maxwell-Stefan formulation. An energy balance accounted for heat transfer by conduction and convection with options for adiabatic and isothermal operation. The laminar flow profile was given by an analytical expression while pressure was assumed constant and axial velocity was increased proportionately to temperature. Internal transport limitations were neglected.

The model resulted in a system of DAEs which was converted to a set of transient ODEs and steady state NLEs by applying orthogonal collocation to spatial derivatives. Numerical efficiency was ensured by the implementation of a three step algorithm. The transient equations were solved on a coarse mesh using concentration ramp up of reactive species and a ramp down of inert species from the initial state of a reactor filled with inert. This solution was repeatedly interpolated onto a fine mesh as the initial guess for the steady state solution. The algorithm provided stability as the transient algorithm did not solve above 275 mesh points while the algorithm was tested to 1701 points. The algorithm was also significantly more numerically efficient than the purely transient solver.

The model performance was evaluated using the water-gas shift reaction. Where mass and heat transport limitations were induced, convergence to a mesh-free solution was obtained with an $[11, 9, 9]$ mesh which was solved within ∼686 s. The overall mass and energy balances were met to within $10^{-2}\%$. Mesh-free solution times were dependent on the reactor conditions. For practical operating conditions they ranged from $\sim 13\,s$ for an isothermal approximate plug flow case to $\sim 40\,s$ for an isothermal transport limited regime for similar overall mass balance tolerances. These tests confirmed the model's computational efficiency compared to low order FEM-based models.

The model was able to predict expected outcomes for mass and energy transport in the steady state. These included correct mass flux directions and species profiles, thermal expansion of the gas and speedup of fluid flow and equalisation of perpendicular composition and temperature profiles after reaction equilibrium was reached.

The model was validated against experimental data reported by Germani et. al, 2005. This consisted of isothermal CO conversion curves as a function of inlet temperature for different Pt/CeO_2 catalysts. Regression was carried out on the activation energy and kinetic rate. The model predicted the reported conversions with a goodness of fit of 0.9984. The model performed with satisfactory stability and computational efficiency.

A critical examination was conducted of the test of mass transport limitations by increasing the hydraulic diameter of a channel of arbitrary cross-section. Simulations were conducted using a 1-dimensional radial model, based on the second Damköhler number and the full 3-dimensional model. Increasing hydraulic diameter at constant space velocity and residence time required that the catalyst layer thickness be increased. This increased the total flux off the reaction surface which led to a higher conversion. An increase in channel hydraulic diameter did not independently increase diffusional distance without increasing overall conversion. The test could therefore not be applied to wall coated reactors.

The dependence of conversion on channel diameter varied between the 1-dimensional and 3-dimensional models. After an initial increase in both the conversion then plateaued off in the former and decreased in the latter due to mass transport limitations induced by the laminar flow profile. The extent of mass transport limitations was quantified by the concentration effectiveness factor. This was found to be lower in the case of the 3-dimensional model compared to the 1-dimensional model because of laminar flow. This result is consistant with original Damköhler studies. The extent to which laminar flow dominated mass transport was documented for different reactor conditions. While a unified criterion was not developed, this study indicated the limitations of applying axial 1-dimensional models and both the Damköhler- and Mears criteria to respectively evaluate reactor conversion and mass transport effects.

Acknowledgments

In the name of Allah, Most Beneficent, Most Merciful.

> *"Read! In the name of your Rabb (Cherisher and Sustainer), Who has created (all that exists). (He) has created man, out of a leech-like clot. Read! And your Rabb is the Most Generous, Who has taught (the writing) by the pen. He has taught man that which he knew not. Nay! Verily, man does transgress all bounds. Because he considers himself self-sufficient."* (The Holy Qur'an, 96:1-5)

All praise be to Allah the Creator and Sustainer of the heavens and the earth, the seen and the unseen, that which is apparent and that which is not. Praise be to Allah for giving this student the opportunity to increase in knowledge. May it be a source of benefit in this world and the next.

The Prophet (peace be upon him) said ""Whoever does not give thanks to the people does not give thanks to Allah" (Ahmad, 2:258). So acknowledgments cannot end here.

The first to thank is my supervisor **Prof. Klaus Möller**. Thank you for giving me the opportunity to apply myself to this project and for the direction, advice and encouragement along the way. I appreciated your open-door policy and hope you will keep this practice. Thank you for the years of hard work in obtaining the knowledge which you very willingly shared with me.

I appreciate the financial assistance from my bursar, **Sasol** and from the **SA College Croll Scholarship** and **Council Postgraduate Scholarship**.

Thanks to my fellow modelers **Ashton**, **Hari** and **Matt** for your company and help and **Alistair Hughes** for the patience to listen to and willingness to help with any modelling issues. I am grateful for the assistance of **Mr Graham Inggs** for the general help with Linux, and compilation problems.

Nabeel, **Rinesh**, **Maryam**; thanks for putting up with my mood swings as my model converged and then (for no good reason) did not.

I extend my warmest gratitude to my family without whose unconditional support I would not be typing this today.

Contents

List of Figures

List of Tables

Nomenclature

Roman Symbols

$[B_{eff}]$	inverse of the effective diffusivity matrix	$[s/m^2]$
$[D_{eff}]$	effective diffusion matrix	$[m^2/s]$
ΔH_{rxn}	heat of reaction	[kJ/mol]
$\dot{m}$	mass flow rate	[kg/s]
[**J**]	Jacobian matrix	[n/a]
$\mathbf{d}_i$	molecular diffusion driving force	[1/m]
e	total energy flux vector	$[J/m^2.s]$
F	external force per unit mass	[N/kg]
F	matrix function	[n/a]
f	general function value	[n/a]
g	external body force vector	$[m/s^2]$
J	molar diffusional flux	$[mol/s.m^2]$
q	heat flux vector	$[J/m^2.s]$
u	general solution variable	[n/a]
v	fluid velocity	[m/s]
$\mathbf{v}_i$	velocity of species i relative to stationary co-ordinates	[m/s]
A	first order derivative collocation matrix in each dimension (x,y,z)	[-]
a, b	limits of domain	[m]
A_{surf}	surface area catalyst exposed to channel bulk	$[m^2]$

Ac	ratio of catalyst volume to surface area	$[m^3_{cat}/m^2]$
AR	aspect ratio = W_I/H_I	[-]
B	second order derivative collocation matrix in each dimension (x,y,z)	[-]
c_p	constant pressure heat capacity	[J/mol.K]
c_t	total concentration	$[mol/m^3]$
c_v	constant volume heat capacity	[J/mol.K]
D^T	thermal diffusion coefficient	[kg/m.s]
D_{disp}	Talor-Aris dispersion coefficient	$[m^2/s]$
D_h	hydraulic diameter	$[m]$
$D_{i,j}$	binary diffusivity of species i in j	$[m^2/s]$
$D_{i,m}$	diffusivity of species i in mixture	$[m^2/s]$
e	efficiency of CPU usage	[-]
$E(t)$	residance time distribution	[-]
E_a	activation energy	[J/mol]
E_{sys}	system energy	[J/kg]
F_0	inlet molar flowrate	[mol/s]
f_{par}	fraction of parallelised code	[-]
H	channel height	[m]
ia	Jacobi polynomial parameter	[n/a]
$J^{(\alpha+1,\beta+1)}$	Jacobi polynomial	[n/a]
k_0	first order rate constant	$[m^3/s.kg_{cat}]$
k_B	Boltzmann constant	$[m^2kg/s^2K]$
K_{eq}	equilibrium constant	[-]
k_g	gas phase mass transport coefficient	$[m/s]$
L	channel length	[m]

L_e	laminar flow entrance length	[m]
L_p	pulse length	[m]
m, n	reaction rate orders	[-]
M_i	molar mass of species i	[kg/mol]
n	number of collocation points in each direction x,y of z	[-]
n_{bal}	number of balances, includes 5 species, 1 overall mass and 1 energy balance	[-]
n_{pts}	number of points in solution mesh, equals $n_x \times n_y \times n_z$	
n_x, n_y, n_z	number of collocation points in x,y,z dimensions	[-]
$N_{y,i}$	y-component molar flux	$[mol/m^2.s]$
$N_{z,i}$	z-component molar flux	$[mol/m^2.s]$
$NRMSE$	Normalised Root Mean Square Error	[%]
Nt	total flux	$[mol/m^2s]$
P	pressure	[Pa]
p	number of computer processors	[-]
R	ideal gas constant	[J/K.mol]
R	residual	[n/a]
r	radial position	[m]
$R_{1,3}$	fraction of mass transport limitations due to laminar flow	[-]
R_c	channel radius	[m]
R_i	rate of consumption of species i	$[mol/s.m^3_{cat}]$
r_{obs}	observed reaction rate	$[mol/s.m^3]$
R_p	particle radius	[m]
S	speedup ratio in multicore processing	[-]
SV	Heterogeneous space velocity	$[mol/s.kg_{cat}]$
T	temperature	[K]

t	time	[s]
t'	time for radial variation disappearance in Taylor-Aris analysis	[s]
T_0	inlet temperature	[K]
V_{cat}	catalyst volume	$[m^3]$
V_{reac}	reactor fluid volume	$[m^3]$
v_s	speed of sound	[m/s]
v_x	x-component fluid velocity	$[m/s]$
W	channel width	[m]
w_k	test function	[n/a]
X	reactor conversion	[% CO]
X, Y, Z	normalised domain of (x,y,z)	[-]
x, y, z	space variables	[m]
XSA	cross-sectional Area	$[m^2]$

Abbreviations

BFDM Backwards Finite Difference Method

CFD Computational Fluid Dynamics

CFDM Central Finite Difference Method

DAE Differential-Algebraic Equation

DE Differential Equation

DST Department of Science and Technology

FEM Finite Element Method

HTS High Temperature Shift

HySA Hydrogen South Africa

LFR Laminar Flow Reactor

LTS Low Temperature Shift

NLE Non-Linear Equation

OC Orthogonal Collocation

OCFEM Orthogonal Collocation on Finite Elements Method

ODE Ordinary Differential Equation

PDE Partial Differential Equation

PGM Platinum Group Metals

RTD Residance Time Distribution

VLE Vapour-Liquid Equilibrium

WGS Water-Gas Shift

Dimensionless numbers

γ	Dirac-delta tensor	[-]
Da_{II}	second Damköhler Number	[-]
Kn	Knudsen number	[-]
M_T	Thele modulus	[-]
M_W	Weitz-Prater modulus	[-]
Ma	Mach number	[-]
Pe	Peclet number	[-]
Re	Reynolds number	[-]
Sh	Sherwood number	[-]

Greek Symbols

α, γ	sigmoid function parameters	[n/a]
$\alpha_{i,j}$	thermal diffusion factor matrix	[-]
β	equilibrium rate limitation	[-]
χ_i	mole fraction of species i	[-]
η_c	external concentration effectiveness factor	[-]

η_{int}	internal effectiveness factor	[-]
κ	check in BSL	[Pa.s]
λ	thermal conductivity	[W/m.K]
λ_{gas}	mean free path in gas phase	[m]
λ_m	mixture thermal conductivity	[W/m.K]
μ	viscosity	[Pa.s]
μ_p	chemical potential	[]
ν_i	reaction coefficient species i	[-]
ϕ	general solution variable	[n/a]
ϕ	trial function	[n/a]
ϕ_{dis}	viscous dissipation function	[]
π	molecular momentum flux tensor	[]
Ψ	matrix of all solution variables at all points	[n/a]
ρ	fluid density	$[kg/m^3]$
ρ_{cat}	catalyst density	$[kg/m^3]$
σ	molecular diameter	$[m]$
τ	residance time	[s]
τ	viscous momentum flux tensor	[]
τ_D	diffusive time	[s]
υ	flux physical constraint parameter	[-]
ζ_i	volume fraction	[-]

Chapter 1

Background

1.1 Context

The Department of Science and Technology (DST) has recently launched Hydrogen South Africa (HySA) as part of its plan to develop competence in the field of hydrogen technology. Hydrogen fuel cells are expected to be the next major energy converter after the internal combustion engine. Importantly, these fuel cells and hydrogen generation devices require platinum group metal (PGM) catalysts. As South Africa has 75% of the world's proven platinum reserves, the development of local expertise in adding value to these reserves is of importance to the countries economic growth.

As part of its strategy, it has looked to South Africa's strength in catalysis, largely as a result of SASOL's reliance on catalytic processes as a competitive advantage over international companies. It has chosen the University of Cape Town's Chemical Engineering Department and MINTEK to host the Centre for Competence for Catalysis. This center will develop and test catalysts necessary for both hydrogen production and use in fuel cells (Campbell 2009). This study represents the one of the first steps in developing mobile fuel processing technology at the centre.

1.1.1 Process intensification

Process intensification is one of the most important trends in chemical engineering today. It is driven by the development of devices that drastically improve processes by decreasing equipment size, energy usage and waste generation thereby leading to more economical and sustainable industries. It is achieved by either reducing the size of existing equipment or incorporating multiple unit operations into single devices. The degree of size reduction was initially proposed to be 100-fold yet a decrease by a factor 2 can also be considered

process intensification (Stankiewicz & Moulijn 2000). These devices are either derived from new equipment or methods and a variety of these are shown in Figure 1.1.

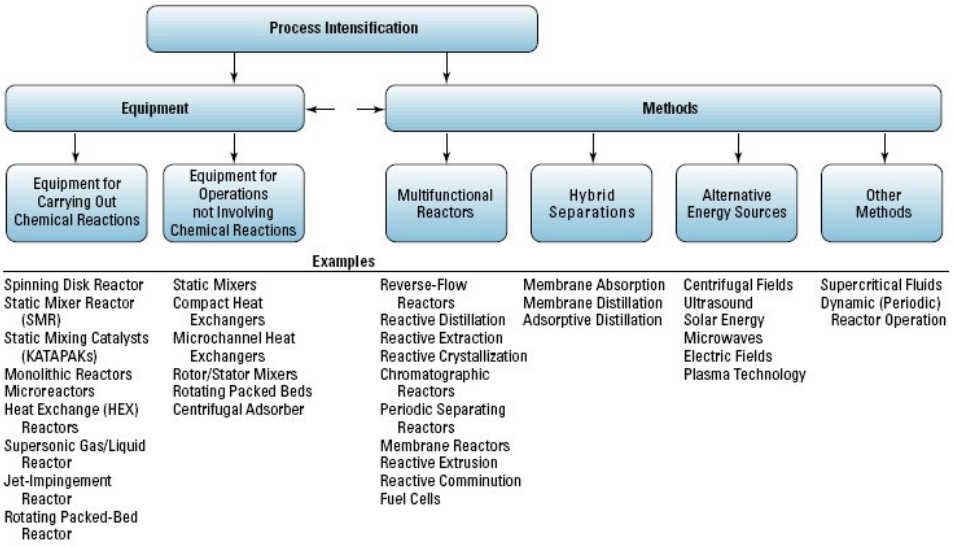

Figure 1.1: Schematic diagram of different methods of process intensification with microchannel reactors on the left (Stankiewicz & Moulijn 2000).

One of the process intensifying devices is the microchannel reactor (also sometimes called a microreactor) which falls under the equipment for chemical reactions. These devices consist of catalyst coated channels of micrometer diameter arranged as regular grids on metal or silica supports. Microchannels are also used in micro heat exchangers, or in a reactor/heat exchanger combination. One of the most important consequences of the use of microchannel reactor devices is the minaturisation of process equipment. This occurs because when the size of the reaction channel decreases, the phase surface area to volume ratio increases. In the case of a solid-fluid system, it means a decrease in the transport distance to a wall or catalyst surface, while in a gas-liquid system it means the transport distance to the phase boundary. The particular effects of a decrease in length scale are:

- decrease in diffusion distances
- increase in concentration and temperature gradients
- increase in specific surface area in catalytic reactions
- increase in specific interface area in multiphase flow

In all cases, the reduction in transport distance leads to the dominance of surface effects over bulk limitations. This, in turn leads to a decrease in equipment size needed for either mass or heat transfer limited reactions. (Hessel et al. 2004).

A second important feature of microchannel reactors is that they can be in dual purpose functions. An example is its application as a reactor-heat exchanger that can be used

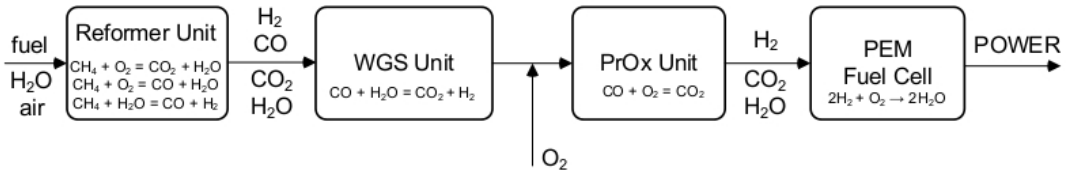

Figure 1.2: Schematic of fuel processing system adapted from (Spatenka et al. 2005).

to both integrate two unit operations and reduce reactor size by reducing heat transfer limitations and allowing the reaction to follow an optimal rate pathway (Baier & Kolb 2007).

1.1.2 General applications

The current energy shortage has led to a search for new sources of energy. This includes the use of Gas-to-Liquid (GTL) processes to convert stranded sources natural gas to useful liquid fuels. These sources include remote sources of natural gas far from pipelines or conversion offshore gas as an alternative to flaring or re-injection. Other sources of carbon include biomass or methane from waste sources (Fitzgerald et al. 2008). This technology is still in development in the USA by Velocys Inc. and in the UK by CompactGTL in partnership with the Brazilian oil company Petrobras.

A second application is in the manufacture of high value specialty chemicals (Brand et al. 2006). This is especially applicable to chemicals that are not subject to the economy of scale such as pharmaceuticals or fine chemicals. Here, microchannel technology allows for flexible production with small capital and running costs. Work in this field is research-based and industrial applications are limited.

1.1.3 Mobile fuel processors

Systems for proposed future mobile energy generation use fuel cell technology for energy conversion. The solid polymer electrolyte membrane (PEM) fuel cell is currently the focus of attention and requires high quality hydrogen for efficient operation. However, the development and future wide-spread use of hydrogen fuel cells is inhibited by the problems associated with hydrogen storage, namely its explosive nature and low energy storage density. An alternative is to store hydrocarbons or alcohols which can be reformed to yield hydrogen in a multi-step fuel processing system (Tonkovich et al. 1999). A schematic example is shown in Figure 1.2.

The reformer unit is used for primary hydrogen generation. The water-gas shift (WGS) unit provides primary carbon monoxide cleanup and secondary hydrogen production,

while the partial oxidation unit provides secondary carbon monoxide cleanup. Removal of carbon monoxide to levels below $50\,ppm$ is necessary to prevent poisoning of the downstream PEM catalysts (Germani et al. 2005).

Conventional fuel processing technology is typically based on fixed bed reactors. These show slow observed kinetics and as a result do not scale well with the small modular nature of fuel cells. On the other hand, microchannel reactors are able to exploit fast intrinsic kinetics as a result of their reduced mass and heat transfer limitations. This, together with their high surface area to volume ratio reduces the size of fuel processing equipment without lowering throughput which makes them ideal for miniaturised deployment (Tonkovich et al. 1999).

1.1.4 Reactor Modelling

Reactor modelling has been applied to conventional stirred, fixed bed and tubular reactors to predict flow patterns, transfer limitations and reactor conversion. These models have successfully enabled process design and optimisation, accurate control systems and failure modelling. The applications of microchannel reactors are expected to cover all these reactor types which includes gas and liquid flow as well as gas/liquid or liquid/liquid multiphase flow. This flow is further affected by reaction often on a solid catalyst surface. There are, however two important aspects that make modelling microchannel reactors simpler than conventional reactors.

Their laminar flow patterns (Tonkovich et al. 1999) are well defined compared to the turbulent flow in conventional reactors. In contrast, turbulent models need to account for velocity fluctuations often well below the resolution of the dimensional grid. These fluctuations are often taken into account in an empirical manner often with limited application. As mass and heat transfer are strong functions of fluid velocity accurate accurate flow models are required. Currently there is, however no turbulent model that is both computationally inexpensive and universally applicable. As microchannel reactors do not need turbulent models, there is the potential for a general model that is both accurate and computationally inexpensive. (Hessel et al. 2004)

A second advantage of microchannel reactors over conventional reactors is that instead of scaling up for increased production, they 'number up'. Production is increased by increasing the number of channels, while maintaining the critical channel dimensions and so hydrodynamics. This means that a model for a lab scale reactor can be just as accurately applied to a commercial reactor. This is contrasted to a conventional reactor where hydrodynamics vary from bench to pilot plant, to full commercial scale. This leads to inaccurate model representations and consequently extended design and testing periods (Fitzgerald et al. 2008). Modelling therefore provides a powerful tool to design

and commercialise microchannel reactors as a result of their well-defined flow and uniform structure.

Chapter 2

Literature Review

This section outlines important factors which need to be considered in the development of an accurate model for the microchannel reactor. A description of previous modelling studies and their limitations is also presented. An analysis of the system must consider the reactor geometry, flow regime, mass and heat transfer processes and the reaction kinetics and thermodynamics. The WGS reaction is selected as a case study of a heat transfer-limited reaction.

2.1 Industrial Microstructuring

The methods used in industrial preparation of microchannel reactor components are reviewed to describe the physical environment to be modelled.

2.1.1 Materials of construction

A material of construction is necessary to obtain a thermal conductivity. The material has to take into account two main factors: heat transfer and chemical species. Microchannel heat exchangers are made from a variety of metals to take advantage of high heat transfer rates, including aluminium alloys, copper, silver, titanium and stainless steel (Brand et al. 2006). The fuel processor reactions convert to high hydrogen concentrations which can cause embrittlement in conventional metals. Typical supports used in experimental work are therefore limited to stainless steel (Goerke et al. 2004) and alumina ceramics (Wheeler et al. 2004). As stainless steel has the higher heat transfer rate it would be most suitable for any reactor-heat exchanger. The thermal conductivity of stainless steel is 18 W/m.K (Welty et al. 2001).

2.1.2 Channel shape

Techniques for microstructuring are considered to determine the geometric limits of applying the model. The first stage in preparing a microchannel reactor is creating channels on a foil. There are two main methods of doing this: mechanical micromachining and wet chemical etching. Micromachining is a 'simple' process that can be used to create rectangular or square grooves on either metals or ceramics. This is shown in Figure 2.1a. Typical dimensions of tools are $< 1000\,\mu m$, preferably below $500\,\mu m$, to a minimum of $50\,\mu m$ for commercial application. The aspect ratio (AR) determines the channel height. The technical limits for 50, 100 and $200\,\mu m$ diameters are $1:1$, $1:4$ and $1:10$ respectively.

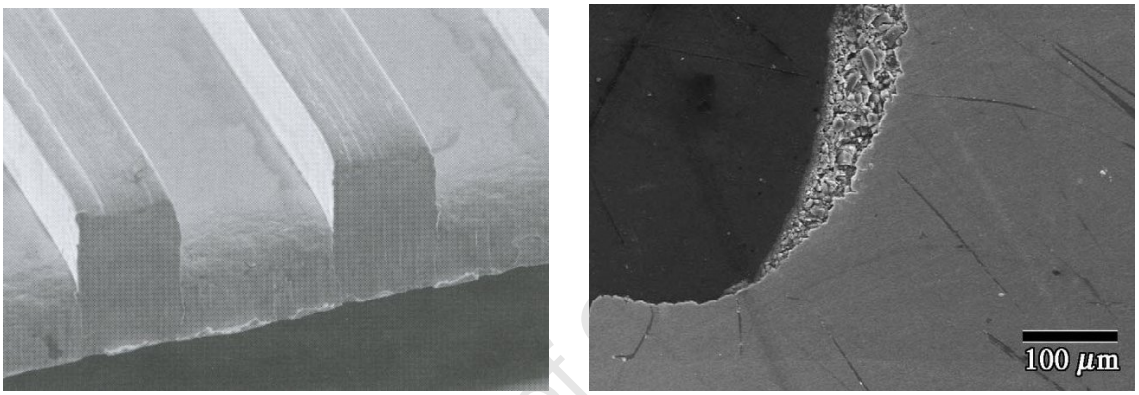

(a) Rectangular microchannels prepared by micromachining (Brandner et al. 2006)

(b) Catalyst deposited on spherical microchannel (Germani et al. 2005).

Figure 2.1: Scanning electron microscopy images of the cross sections of microchannels.

Wet chemical etching is a more flexible method than micromachining as it is cheap and allows for the formation of hemispherical channels (Brandner et al. 2006). However, reactor/heat exchangers use rectangular channels, to increase compactness. Typical dimensions are shown in Figure 2.2. This configuration yields an aspect ratio of $2.9:1$, however studies on a microchannel fuel vapouriser were conducted with aspect ratios between 4 and $17:1$ (Tonkovich et al. 1999). The reactor length is a function of the conversion desired and this is a parameter to be determined in the model. For indicative purposes reactor lengths for WGS shift kinetic experiments and modelling range between 2.5–16 cm (Kolb et al. 2005; Baier & Kolb 2007).

Micromachining can lead to the formation of burrs, or raised edges on the top surface of the micromachined edge. This will reduce the accuracy of bonding, leading to irregularly shaped channels. If burr formation occurs regularly, electropolishing needs to be applied for removal.

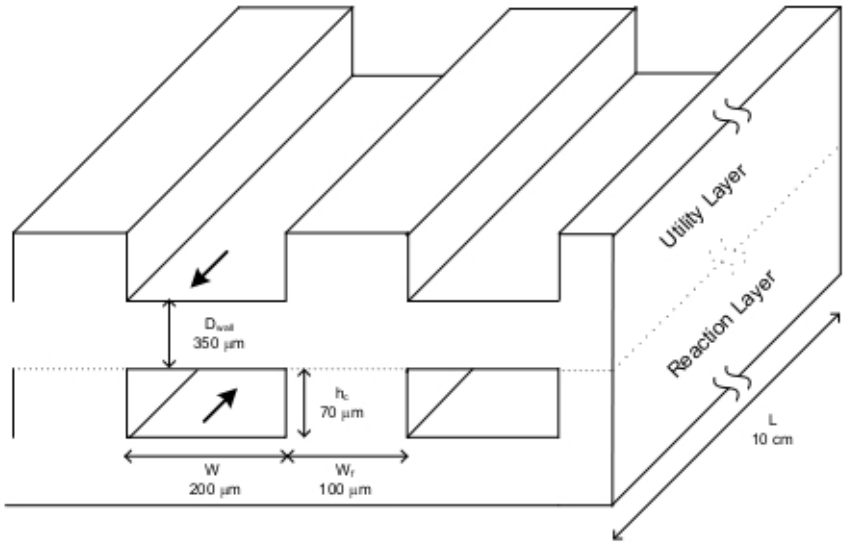

Figure 2.2: Schematic drawing of typical microchannel dimensions adapted from (Goerke et al. 2004).

2.1.3 Catalyst loading

The technique used for catalyst coating determines which of the four available channel surfaces is catalyst coated. Two main methods used are wash coating and sol-gel coating. Wash coating is used to coat one side of the foil by immersion in a catalyst slurry prior to stacking (Hessel et al. 2004). This yields asymmetric reaction channels (Goerke et al. 2004) with catalyst only on the bottom face and two side faces. The sol-gel method pumps a sol through microchannels after the foils are stacked resulting in a catalyst coat on all faces. This method has been applied to WGS catalysts with a range of catalyst layer thicknesses of 1–10 μm (Germani et al. 2005). This is the most likely method for future automated coatings (Hessel et al. 2004).

2.1.4 Reactor Construction

The formation of the channels and the final configuration of the reactor is completed by first bonding the etched sheets together followed by packaging and sealing the compilation of sheets.

Bonding Metal or silica foils are stacked together and bonded to form the reaction or utility channels. Some of the techniques used are diffusion bonding, welding or gluing in the case of silica foils. Of importance to modelling is the accuracy of the bonding to produce regularly shaped channels throughout the reactor. In particular, there may

be misalignment due to surface quality from etching or bonding techniques or by burr formation when micromachining. As noted in Section 2.1.2, burr formation can be treated by electropolishing. Techniques to avoid alignment errors include mechanical alignment by pins, assembly under a microscope, or in automated processes by use of laser diodes or photosensors (Brandner et al. 2006).

In some experimental applications the platelets may also not be bonded but rather just pressed together in a housing. This could lead to fluid bypass channels and blank platelets need to be alternately inserted to avoid this (Germani & Schuurman 2006)

Packaging and mixing The microstructured arrangement has to be packaged to be connectible to other pieces of process equipment. This is done by inserting it into a casing and welding it closed. This procedure yields devices that are leak-free and can withstand high pressures up to 100 MPa. (Brandner et al. 2006). Micromixers can be employed at the reactor inlet and exits to mix reactant and product streams. This results in a well-mixed inlet flow that ensures even distribution to all microchannels (Goerke et al. 2004).

2.1.5 Channel configuration

Typical heat exchangers use a cross-current exchange configuration where foils are stacked crosswise and connected by diffusion bonding (Ehrfeld et al. 2000). The justification for this is that the hot and cold streams enter the reactor on different faces. However, with suitable arrangement a counter- or co-current heat exchanger can be assembled (Gokhale et al. 2005).

A combined reactor-heat exchanger for the WGS reaction has been proposed (TeGrotenhuis et al. 2002) and modelled (Baier & Kolb 2007). Both co- and counter current exchangers yield exponentially decreasing reaction temperature profiles comparable to the optimal temperature profile along the rector. This makes it possible to take advantage of maximum reaction rates along the entire length of the reactor with either configuration. Counter-current arrangements are however favoured as they show more efficient heat transfer (Baier & Kolb 2007). Cross flow exchangers are not suitable for this purpose as they regulate temperature across the reaction channels, thereby creating a temperature profile across the reactor, rather than along it as required.

2.1.6 Production Scaleup

Microchannel reactors for laboratory scale experiments usually consist of single foil stacks. These are have limited throughput ranging in the order of $^{mg}/_{hr}$ to $^{kg}/_{hr}$. However when a

few thousand $^{kg}/_{hr}$ production is required scaling has to occur to reach the desired total mass flow. An understanding of throughput scaleup procedures is important to determine the macro-shape of the reactor as this determines the inlet linear flow rate and velocity. Of secondary importance is the macro-behaviour of heat dissipation in the entire device. Production scaleup can be achieved in three ways: scaling, numbering up or equaling (Brandner et al. 2006).

Scaling Scaling involves increasing the characteristic length of the channel to accommodate higher throughput. However as the advantages of microchannel reactors lie with the small characteristic lengths, this almost always leads to a drop in performance. For example the characteristic length of a microchannel reactor is its hydraulic diameter. If this were to increase then longer diffusion paths would lead to an increase in mass transfer limitations and a drop in conversion.

Numbering up The 'numbering up' of the number of channels per platelet and the number of stacked platelets does keep the characteristic length of the reactor constant. Whereas laboratory scale devices have ∼100 channels over two platelets (Germani et al. 2005) proposed reactors are expected to contain hundreds of plates with thousands of channels for Fischer-Tropsch synthesis (Fitzgerald et al. 2008). The major difficulty anticipated with numbering up is the even flow distribution across all microchannels. This is necessary to maintain even pressure drop and the same residence time in each channel so that reactor conversion remains constant throughout operation. Even flow is not easily achieved but is possible with the use of well designed distributors (Brandner et al. 2006).

Equalling A third method of scaleup that potentially avoids uneven distributions is that of equalling or external numbering-up. This requires the devices to be kept as small as possible while production scaleup is achieved by adding additional devices in parallel to the first. This splits the flow between identical microchannel blocks (Tonkovich et al. 2005).

2.1.7 Process equipment

A combination of the production scaleup methods is the most likely for scaleup to current commercial capacity. A system of reactors can contain multiple numbered-up reactor blocks all housed in the same macro-assembly. Furthermore, multiple assemblies can be operated in parallel to form the complete reactor. This has been proposed for use in for a steam methane reforming reactor which combines five reactor blocks in each of four

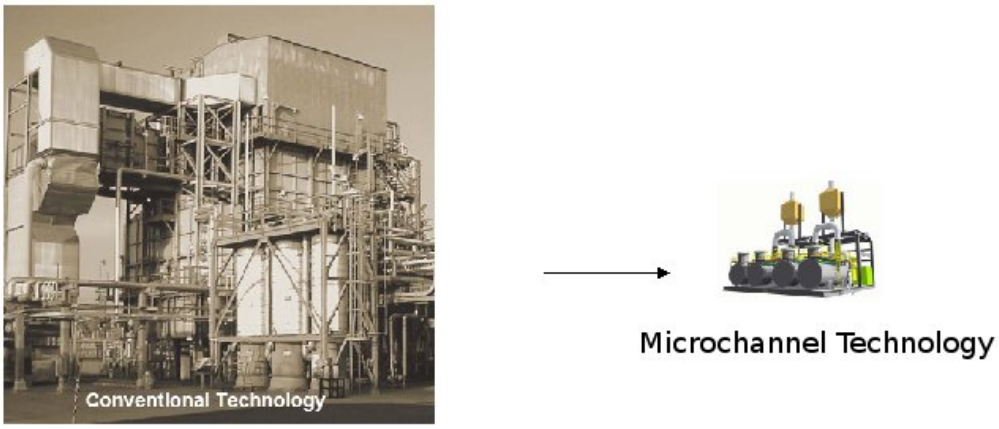

Figure 2.3: Macro-reactor consisting of four assemblies each containing 5 microchannel reactor blocks (Tonkovich et al. 2005) compared to a conventional steam methane reformer (Tonkovitch 2008).

Table 2.1: Fully specified flow problem adapted from Bird et al. (2002)

Balance	Balance	Variable
Continuity Equation	Overall Mass Balance	ρ
Equation of Motion	Momentum Balance	$\mathbf{v}$
Heat Equation	Enthalpy Balance	T
The Equation of State		$p = f(\rho,\mathrm{T})$
The Equations for the Viscosities		$\mu = g(\rho, T)$

assemblies. A capacity of $0.4^{\mathrm{m}^3}/_{\mathrm{s}}$ in each assembly will yield about $2\,m^3_{H_2}/s$ (Tonkovich et al. 2005).

The size of this reactor is compared to a current industrial reformer that produces $\sim 6.5^{\mathrm{m}^3_{\mathrm{H}_2}}/_{\mathrm{s}}$ (Tonkovitch 2008) in Figure 2.3. The microchannel based reactor is about 10% of the original reactor size for a similar production rate.

2.2 The Equations of Change

To fully describe the flow and transport limitations in a microchannel the equations of change need to be solved. These, together with their boundary conditions provide a fully specified set of equations to solve the pressure, velocity, density and temperature distributions in the fluid. The equations are: given in Table 2.1.

2.3 Flow Phenomena

A flow model is necessary to determine the bulk flow patterns through microchannels. This is necessary to determine the concentration of reacting species at the catalyst surface, which affects conversion through the concentration dependence of the reaction kinetics. The flow regime is governed by momentum balances which yield expressions for radial flow velocity profiles and axial pressure drop.

2.3.1 Continuum Model

Flow fields can be modelled in two basic ways: either fundamentally as a collection of molecules or as it is observed as a continuum. These are called *molecular models* and *continuum models* respectively. Molecular models are further subdivided into *deterministic methods* in which the future state of the system is determined by its present state and is independent of any randomness and *statistical methods* in which a fluid with a distribution of microscopic configurations, or microstates, can lead to an understanding of its observed macrostate properties. Continuum models have the fluid properties (concentration, temperature, pressure etc.) defined at each point in space and time. These models are mathematically simpler to treat and are more familiar to fluid dynamicists than the molecular models and their use is advised where possible (el Hak, 1999).

2.3.1.1 The criterion for Continuum Models

The continuum model is valid under two conditions. The first is that volume elements be large enough compared to microscopic structures so that fluid properties can be averaged over them but also small enough so that differential calculus can be used over them. The second is that each volume element must not be far from thermodynamic equilibrium, i.e. that all physical properties be uniform over each volume element. The first criterion is almost always satisfied, but the second requires validation.

This is done for gasses by considering the situation where the volume element contains just a single molecule because of the level of rarifaction of the gas it contains. A highly rarified gas causes the system to move out of thermodynamic equilibrium as the as the properties within that system are constrained to discreet particles and cannot be said to be uniform. The level of rarifaction is determined by the average distance a particle travels between collisions, or the mean free path, λ_{gas}. For an ideal gas this is given as a function of temperature and pressure by

$$\lambda_{gas} = \frac{k_B T}{\sqrt{2}\pi P \sigma^2} \tag{2.1}$$

Table 2.2: Knudsen number regimes

Knudsen number	Flow Regime	Equation
$Kn \to 0$	Neglect molecular diffusion	Euler
$Kn \leq 10^{-3}$	No-slip BC	Navier-Stokes
$10^{-3} \leq Kn \leq 10^{-1}$	Slip-flow BC	Navier-Stokes
$10^{-1} \leq Kn \leq 10$	Transition regime	
$Kn > 10$	Free-molecule flow	

where k_B is the Boltzmann constant and σ is the particle diameter. A rarefied gas will be present where λ_{gas} is much higher than a characteristic flow dimension, D_h therefore the continuum model will be defined where λ_{gas} is much smaller than D_h. The Knudsen number, Kn expresses ratio of these dimensions as

$$Kn = \frac{\lambda_{gas}}{D_h} \tag{2.2}$$

The Knudsen number regimes are well reported (el Hak, 1999) and are reproduced in Table 2.2. The continuum model is generally valid for Knudsen numbers less than 0.1. Knudsen numbers greater than this are encountered for rarefied gasses in micro-flow devices and high altitude or low pressure applications. This makes it necessary to check this condition for microchannel applications (Arzamendi et al., 2009a).

2.3.1.2 Types of Continuum Models

Application of the conservation laws to mass, momentum and energy leads to a set of partial differential equations that are defined at every point in space, $\mathbf{x}_i = \{x, y, z\}$ and time, t. These are reproduced from literature (el Hak, 1999) in Equations 2.3 - 2.5, but their derivations are provided in A.1 for purposes of understanding and as a basis for further derivations.

$$\frac{\partial \rho}{\partial t} + (\nabla \cdot \rho \mathbf{v}) = 0 \tag{2.3}$$

$$\rho \left[\frac{\partial \mathbf{v}}{\partial t} + (\mathbf{v} \cdot \nabla \mathbf{v}) \right] = - (\nabla \cdot \pi) + \rho \mathbf{g} \tag{2.4}$$

$$\rho \left[\frac{\partial E_{sys}}{\partial t} + (\mathbf{v} \cdot \nabla E_{sys}) \right] = - (\nabla \cdot \mathbf{q}) + (\pi \cdot \nabla \mathbf{v}) \tag{2.5}$$

where ρ is the fluid density, $\mathbf{v}$ is the velocity vector, π is the (second-order) molecular momentum flux tensor, $\mathbf{g}$ the external body force per unit mass on the fluid, E_{sys} is the internal energy and $\mathbf{q}$ is the heat flux vector and includes conduction and radiation.

The set consisting of Equations 2.14, 2.4 and 2.5 consist of 5 equations[1] for 17 unknowns, p, $\mathbf{v}$, π, E_{sys}, and $\mathbf{q}$. These are underspecified and further assumptions about the fluid are required.

Navier-Stokes Equations The required relationships are as follows. For an isotropic Newtonian fluid[2] the molecular stress tensor is defined as

$$\begin{aligned}\pi_{ij} &= -p\delta_{ij} + \tau_{ij} \\ &= -p\delta_{ij} + \mu\left(\frac{\partial v_j}{\partial x_i} + \frac{\partial v_i}{\partial x_j}\right) + \left(\frac{2}{3}\mu - \kappa\right)\left(\frac{\partial v_x}{\partial x} + \frac{\partial v_y}{\partial y} + \frac{\partial v_z}{\partial z}\right)\delta_{ij}\end{aligned} \tag{2.6}$$

For a Fourier fluid with negligible radiative conduction the heat flux vector is defined as

$$\mathbf{q} = -\lambda\nabla T \tag{2.7}$$

And for an ideal gas the internal energy and pressure relations are

$$dE_{sys} = c_v dT \tag{2.8}$$

and

$$p = \frac{\rho RT}{M} \tag{2.9}$$

The application of these assumptions to Equations 2.5, 2.4 and 2.5 lead to the following fully specified set of equations

$$\frac{\partial \rho}{\partial t} + (\nabla \cdot \rho\mathbf{v}) = 0 \tag{2.10}$$

$$\rho\left[\frac{\partial v_j}{\partial t} + v_i\frac{\partial v_j}{\partial x_i}\right] = -\frac{\partial p}{\partial x_j} + \rho g_j + \frac{\partial}{\partial x_i}\left[\mu\left(\frac{\partial u_j}{\partial x_i} + \frac{\partial u_i}{\partial x_j}\right) + \left(\frac{2}{3}\mu - \kappa\right)\left(\frac{\partial v_x}{\partial x} + \frac{\partial v_y}{\partial y} + \frac{\partial v_z}{\partial z}\right)\delta_{ij}\right] \tag{2.11}$$

[1] Note that there are three momentum balances, one for each component of $\mathbf{v}$

[2] An isotropic fluid is one that has no preferred direction of motion.

$$\rho c_v \left(\frac{\partial T}{\partial t} + v_i \frac{\partial T}{\partial x_i} \right) = \frac{\partial}{\partial x_i} \left(\lambda \frac{\partial T}{\partial x_k} \right) - P \frac{\partial v_i}{\partial x_i} + \phi_{dis} \tag{2.12}$$

The 6 balances in Equations 2.10, 2.11 and 2.12 combined with the thermodynamic gas law (in this case the ideal gas law, Equation 2.9) form a fully specified set to describe the 6 dependent variables ρ, $\mathbf{v}$, T and p. The momentum balances with the Newtonian assumptions in Equation 2.11 are referred to as the Navier-Stokes equations.

The energy balance, Equation 2.12 contains the *viscous dissipation function,* ϕ_{dis} which accounts for the irreversible conversion of mechanical energy into thermal energy and a heating of the fluid. As this process is irreversible, the Second Law of Thermodynamics states that the function must be positive. It is given by the expression

$$\phi_{dis} = \frac{1}{2}\mu \left(\frac{\partial u_j}{\partial x_i} + \frac{\partial u_i}{\partial x_j} \right)^2 + \left(\frac{2}{3}\mu - \kappa \right) \left(\frac{\partial v_x}{\partial x} + \frac{\partial v_y}{\partial y} + \frac{\partial v_z}{\partial z} \right)^2 \tag{2.13}$$

The second term from the right accounts for the change in volume of the fluid element induced by the pressure on its sides. This term is normally neglected in microchannel applications (Hessel et al., 2004). The viscous heating term is however proportional to $\frac{1}{D_h^2}$ with constant velocity so as channel diameter decreases this effect increases substantially and can no longer be neglected. The regions of applicability have been studied by (Sekulic et al., 1997) and (Richardson et al., 2000).

Euler Equations In the limit as $Kn \to 0$ transport terms are neglected. These include the heat conduction, viscous dissipation and viscous diffusion terms. The fluid is now referred to as non-conducting and inviscid. The equations that describe this system are as follows (el Hak, 1999)

$$\frac{\partial \rho}{\partial t} + (\nabla \cdot \rho \mathbf{v}) = 0 \tag{2.14}$$

$$\rho \left[\frac{\partial v_j}{\partial t} + v_i \frac{\partial v_j}{\partial x_i} \right] = -\frac{\partial P}{\partial x_j} + \rho g_j \tag{2.15}$$

$$\rho c_v \left(\frac{\partial T}{\partial t} + v_i \frac{\partial T}{\partial x_i} \right) = -p \frac{\partial v_i}{\partial x_i} \tag{2.16}$$

The momentum balances in Equation 2.15 are referred to as the Euler equations. If this is integrated along a streamline, the Bernoulli equation results which directly relates pressure and velocity. This is given in Equation 2.17.

$$^1/_2 v^2 + gx + \int_{P_0}^{P_1} \frac{dP}{\rho(P)} = const \tag{2.17}$$

2.3.2 Compressibility

Continuum flow can be considered either compressible or incompressible. The change of a fluid's density upon impact with another body (i.e. viscous and inertial effects) may lead the flow to compress and the flow has to be treated as compressible. In this case, the mass balance in Equation 2.3 applies. Many fluids are difficult to compress, which means that their density can be assumed constant. For such an incompressible fluid the mass balance in Equation 2.3 simplifies to

$$\nabla \cdot \mathbf{v} = \mathbf{0} \tag{2.18}$$

Incompressible flows are easier to treat than compressible flows, so this is a very useful simplifying assumption. The applicability of this assumption to gasses is valid in certain circumstances. If a fluid flow velocity v is sufficiently less than the speed of sound in that fluid[3], v_s then the fluid can be considered incompressible. The ratio of these scalars is formalised in the Mach number, Ma

$$Ma = \frac{v}{v_s} \tag{2.19}$$

The necessary condition for incompressible flow is $Ma < 0.3$. This condition is however not a sufficient one and effects other than inertial and viscous ones need to be considered. If pressure or temperature changes are strong then the fluid is to be considered compressible. In the case of temperature, this could occur upon wall heating or cooling either due to an external heat source/sink or a chemical reaction. This can cause significant density changes regardless of the value of the Mach number and compressability must be accounted for.

A second situation arises from the compression/expansion of a fluid in a closed vessel. This results in a change in pressure and/or temperature and the density of the fluid changes. A subtle difference here is that the fluid has compressibility and not the flow.

2.3.2.1 Boundary conditions

The Knudsen flow regime analysis in Table 2.2 provides the boundary condition for the solid-fluid interface. Here the choice is between no-slip and slip conditions.

No-slip BC At a solid-fluid interface the fluid velocity equals the velocity of the solid wall. This generally applies both in the tangential and normal directions. In the case of the tangential velocity component this means that $v_x = 0$ and is called the no-slip boundary

[3]The speed of sound in air is $\sim$300 m.s^{-1}

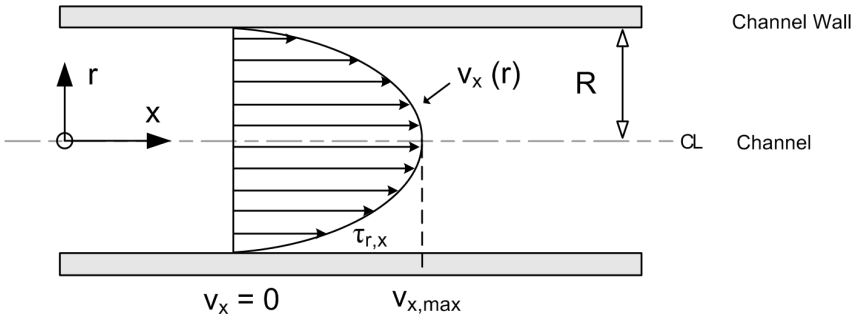

Figure 2.4: Characteristics of laminar flow adapted from (Bird et al. 2002).

condition. This occurs in the regime $Kn \leq 10^{-3}$. However in the case of chemical reaction, adsorption, absorption, dissolution or melting the normal velocity components do not equal zero. Here the velocities are given by the fluxes of fluid components with the driving force being the phenomena listed (Bird et al., 2002).

Slip BC Slip flow occurs when a tangential velocity is present at a solid-liquid interface. Here the continuum assumption starts to break down as intermolecular forces become less important than forces between the molecule and the solid. The region of $10^{-3} \leq Kn \leq 0.1$ has been studied for slip flow effects in microchannels (Hettiarachchi et al., 2008).

2.3.3 Laminar flow

The flow regime expected is given by the Reynolds number, Re. The requirement for laminar flow is $Re < 2,100$ for flow in a circular tube and $0 < Re_L < 50,000$ for flow over a flat plate of length L (Bird et al., 2002). Flow in microchannel reactors is typically laminar as the expected Re lies below 500 (Hoebink & Marin 1998). Laminar flow consists of axial stream lines where fluid flows in parallel layers with no bulk flow between the layers. This provides a radial resistance to mass flow (Bird et al. 2002). A further characteristic of laminar flow is the development of a radial velocity profile, shown in Figure 2.4.

Development of the Flow Profile A radial velocity profile shown in Figure 2.4 above, develops along the channel length as a result of shear forces exerted on the fluid by the wall. This force, $\tau_{r,x}$ acts in the axial direction (x) and is exerted on a streamline parallel to it i.e. in the r-direction. The magnitude of this force can be given for Newtonian fluids, by Newton's Law of Viscosity.

$$\tau_{r,x} = \mu \frac{dv_x}{dy} \tag{2.20}$$

Each successive streamline exerts a shear force on the adjacent streamline, which leads to a gradual decrease in the fluid velocity from the center of the channel to the wall. This means that the velocity is maximum at the channel center ($v_{x,max}$) and minimum at the channel wall ($v_x = 0$). The velocity at the channel wall is given by the boundary condition at a solid-fluid interface. This is taken as the 'no-slip condition' where the fluid velocity at the wall equals the wall velocity. So if flow is measured with respect to a stationary channel wall, then the fluid velocity at the wall surface is zero. This means that there is no bulk flow at the channel wall.

The laminar flow profile develops over an entrance length. The order of this length for laminar flow in a circular tube is given by the following expression (Bird et al. 2002).

$$L_e = 0.035 D_h Re \tag{2.21}$$

This is generally neglected as it forms less than 10% of the total reactor length and experimental work has shown that profile development does not affect reactor performance (Hoebink & Marin 1998). As a result the shape of the fully developed profile can be used for microchannel flow. The velocity profile is parabolic for isothermal, incompressible flow in a cylindrical pipe and is easily defined by the following equation (Bird et al. 2002).

$$v_x(r) = 2v_{x,avg}\left[1 - \left(\frac{r}{R}\right)^2\right] \tag{2.22}$$

where the average velocity is $v_{x,avg} = \frac{l}{\tau}$ or equivalently where (Bird et al., 2002)

$$2v_{x,avg} \equiv v_{x,max} = \frac{(P_0 - P_L)\,R^2}{4\mu L} \tag{2.23}$$

and the channel radius, R is approximated by half the hydraulic diameter $D_h$in the case of rectangular co-ordinates

$$D_h = \frac{2WH}{W + H} \tag{2.24}$$

However, in the case of non-isothermal, compressible flow, a set of Navier-Stokes momentum balances have to be solved simultaneously with the materials and energy balances for a rigorous solution (Raja et al. 2000).

Other flow profiles Analytical flow profiles have been derived for fully developed flow through non-circular ducts. The study of (Spurk, 1997) considers the laminar flow though an infinitely long duct with the Hagen-Poiseuille assumptions of constant temperature and linear pressure drop. The differential equation to be solved is

$$\frac{\partial^2 v_x}{\partial y^2} + \frac{\partial^2 v_x}{\partial z^2} = \Delta v_x \tag{2.25}$$

where Δv_x is given by Poisson's equation

$$\Delta v_x = \frac{1}{\mu}\frac{\partial P}{\partial x} \tag{2.26}$$

with constant $\frac{\partial p}{\partial x}$. No-slip boundary conditions apply. This is integrated using Fourier series to give the velocity v_x as a function of position (y, z)

$$v_x(y,z) = \frac{\partial p}{\partial x}\frac{1}{2\mu}\left(\frac{H^2}{4} - z^2 + \frac{8}{H}\sum_{n=1}^{\infty}\frac{(-1)^n}{m^3}\frac{\cosh(mx)}{\cosh(mW/2)}\cos(my)\right) \tag{2.27}$$

where $m = \frac{\pi}{H}(2n-1)$. A further study (Spiga & Morini 1994) used a Fourier sine transform to give the velocity v_x as a function of position (y, z)

$$v_x(y,z) = \frac{16H^2}{\pi^4}\sum_{n\,odd}^{\infty}\sum_{m\,odd}^{\infty}\frac{\sin\left(n\pi\frac{y}{W}\right)\sin\left(m\pi\frac{z}{H}\right)}{nm\left(\left(\frac{H}{W}\right)^2 n^2 + m^2\right)} \tag{2.28}$$

The disadvantage of these analytical solutions is that they rely on infinite series which can be computationally expensive.

Pressure Drop Pressure drop for non-isothermal flow involves the coupling of momentum and energy equations and is a complex procedure for non-Eulerian systems. As a result of the orderly flow patterns shown in laminar flow systems, a low pressure drop is expected (Tonkovitch 2008). Pressure drop in a microchannel reactor has been shown to be of the order of $10\,mbar$ over a $2.5\,cm$ long reactor and is not expected to play a role in reactor performance (Kolb et al. 2005).

2.3.4 Residence time distribution

The laminar velocity profile results in a residence time distribution within the reactor. Equation 2.22 shows that the minimum time a fluid element spends in the reactor is $\frac{\tau}{2}$ given that the maximum velocity is $2v_{avg}$. The distribution of fractions of fluid spending time $t + dt$ is given by the function $E(t)$. This is derived in for a laminar flow reactor (Fogler 2006) starting with the velocity profile in Equation 2.22. The distribution function is given by Equation 2.29 and is illustrated in Figure 2.5.

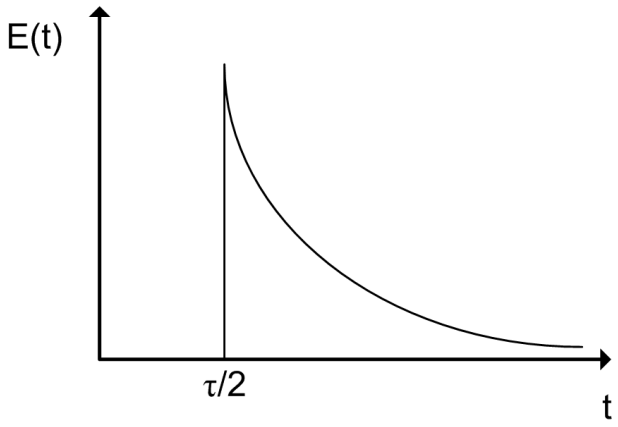

Figure 2.5: Residence time distribution of an LFR.

$$E(t) = \begin{cases} 0 & t < \frac{\tau}{2} \\ \frac{\tau^2}{2t^3} & t \geq \frac{\tau}{2} \end{cases} \tag{2.29}$$

The given $E(t)$ states that below the minimum residence time, none of the fluid elements that entered the reactor at $t = 0$ exit the reactor, while at the maximum residence time, the maximum fraction of fluid elements exit. This point corresponds to the fluid elements in the maximum velocity stream at the channel center. The fraction of fluid elements exiting the reactor then decreases with time to asymptote to zero in the limit $\lim_{t\to\infty} E(t) \to 0$. The function never reaches zero as there will always be fluid elements at the wall with zero velocity and hence residence times that tend to infinity.

The form of the RTD in Equation 2.29 also contains the mean residence time, τ which is a function of fluid velocity. This indicates that even in a heterogeneous reactor, a change in the fluid velocity will change the RTD curve and so the reactor behaviour.

2.4 Transport Limitations

Microchannel reactors demonstrate superior performances in comparison to conventional packed bed reactors for mass transfer limited reactions (Brandner et al. 2006; Karakaya et al. 2009). However, the transport of reacting species from the bulk fluid to the catalyst surface and the presence of a porous catalyst layer on the channel wall indicate that the influence of internal and external mass transfer limitations on the overall kinetics still has to be accounted for (Spatenka et al. 2005). It is therefore necessary to review possible transport limitations along with the criterion for their presence. The criterion for mass transport limitations are well known for fixed bed reactors, but new methods for testing these limitations have recently been developed specifically for microchannel reactors (Walter et al. 2005).

2.4.1 Comparison to transport in fixed bed reactors

The difference in flow patterns between fixed bed reactors and microchannel reactors is described to obtain an understanding of the different approach that needs to be taken when evaluating for transport limitations in microchannel reactors.

Fixed bed reactors Fixed bed reactors have catalyst particles surrounded by reactant flow. The flow around this particle can be described by film theory. The external mass transport resistance takes place in a stagnant film around the catalyst particle and the remainder of the reactant is considered as a well-mixed bulk flow. The mass transport in the film is by molecular diffusion. The thickness of the film is a model parameter and can be obtained for different geometries and film conditions by appropriate correlations for the Sherwood number, Sh. Transport limitations are decreased by increasing the flow velocity. This decreases the film thickness and enhances mass (and heat) transport. Internal transport limitations depends on the relative rates of reaction and diffusion of reactants in the pores of the catalyst particle. For an internal transport limitation to exist, the rate of reaction has to be greater then the rate of diffusion.

Microchannel reactors Microchannel reactors have two conditions that differentiate them from fixed bed reactors; their laminar flow pattern and catalyst-coated walls. This means that a particle in the center of the channel will have to travel by molecular diffusion perpendicular to the direction of bulk flow to reach the catalyst surface. The driving force for this motion is the concentration gradient generated by the wall reaction. Furthermore, the laminar flow profile means that this particle will have a lower residence time than one closer to the wall. This means that the assumption of a perfectly mixed bulk and stagnant film is not applicable to microchannel reactors. The thickness of the stagnant layer and the radius of the microchannel are also not comparable hence traditional film theory breaks down.

Internal transport limitations are similar to fixed bed reactors. This means that as concentration is expected to be lowest at the center of pellets so too is it lowest at the catalyst wall (Walter et al. 2005). Internal mass transfer limitations are however expected to be small compared to external limitations. This is because the catalyst layer is thinner than the channel diameter which leads to shorter diffusion lengths.

The analogy between heat and mass transfer limitations means that the same factors affect heat transfer as those that affect mass transfer. In particular, short thermal diffusion paths lead to rapid heat transfer and allows for accurate control of temperature distributions in microchannel reactors (Hessel et al. 2004). Furthermore, the tests for heat transfer limitations are the same as those for mass transfer limitations.

2.4.2 Criterion for external transport limitations

Laminar flow in microchannels means that reactant molecules have to be transported normal to the flow direction in order to reach the catalyst-coated wall. External mass transfer therefore relies on radial molecular diffusion and thus becomes more significant at higher channel diameters. This is because of the longer radial diffusion paths to the catalyst surface (Baier & Kolb 2007). This external mass transfer is driven by radial concentration gradients developed by the reaction. In contrast to fixed bed reactors, flow in microchannels does not give any physical significance to a well mixed bulk phase nor a stagnant film on the wall (Walter et al. 2005). This means that film models that provide criterion for the presence of external mass transfer should be used with caution in a microchannel model. These have, however been used by (Kolb & Hessel 2004; Goerke et al. 2009) to justify the absence of external transport limitations.

Damköhler number The regions of mass transfer and kinetic control in an isothermal system are delimited by the second Damköhler number, Da_{II}. The boundaries for a circular channel with plug flow and first order reaction the regions are defined as (Walter et al., 2005):

$$\begin{aligned} \frac{k_s R}{D_{AB}} &< 0.1 && kinetic\,regime \\ 0.1 \leq \frac{k_s R}{D_{AB}} &\leq 100 && transient\,regime \\ \frac{k_s R}{D_{AB}} &> 100 && mass\,transfer\,controlled\,regime \end{aligned} \tag{2.30}$$

Where R is the channel radius, k_s is the surface reaction rate constant ($^{m}/_{s}$). As noted by Damköhler, these limits can be lower for laminar flow as the molecules in the center of the channel travel faster than those at the edges. This means that they have a smaller residence time and a higher chance of leaving the reactor without being converted.

Mears criterion The Mears criterion is based on the Damköhler number (Mears, 1971). This has been used to justify the absence of external mass transport limitations in different microchannel modelling studies Kolb & Hessel 2004; Goerke et al. 2009. This criterion has been derived for fixed bed reactors (Mears, 1971) and is reported as

$$\frac{r_{obs} R_p}{k_g c_i} < \frac{0.15}{n} \tag{2.31}$$

where r_{obs} is the observed reaction rate per unit particle volume ($^{gmol}/_{s.m^3}$), R_p is the

catalyst particle radius (m), k_g is the mass transfer coefficient between the gas and the particle ($^{m}/_{s}$), c_i is the inlet concentration of the species in question ($^{gmol}/_{m^3}$) and n is the reaction order. The particle diameter R_p is analogous to the hydraulic diameter D_h of the microchannel and is reported as such by (Kolb & Hessel, 2004). In another modification of this law, the particle diameter R_p has been substituted by the ratio of catalyst volume and surface area, $^{V_{cat}}/_{A_{surf}}$ and the 0.15 criterion substituted with 0.05 for use in microchannels without any stated justification.

The Mears criterion should be used with caution given the previous discussion on the differences between the treatment of mass transport in fixed bed and microchannel reactors.

Sherwood number The Sherwood number is given by

$$Sh = \frac{k_g D_h}{D_{AB}} \tag{2.32}$$

The Sherwood number tends to a constant value of 3.66 in most microchannel applications and can therefore be used as a general criterion of the effect of channel diameter on mass transport (Kolb & Hessel, 2004). As D_h decreases, the mass transport coefficient increases. This leads to higher transport rates at lower channel diameters and so lower mass transport limitations.

Radial diffusive time The radial diffusive time τ_D is used as a criterion to verify the presence of radial concentration profiles. This is calculated as (Arzamendi et al., 2009a)

$$\tau_D = \frac{D_h^2}{4D_{AB}} \tag{2.33}$$

This is to compare the time-scale of diffusion to the time-scale of flow, or residence time τ in the relation $\frac{\tau}{\tau_D}$. If τ/τ_D is low then the diffusion time is slow compared to the the residence time and suggests that radial concentration profiles can develop. This is calculated as 44 - 375 in the same study and is taken as justification of the development of radial profiles and hence the use of a 3-dimensional CFD model.

2.4.3 Criterion for internal transport limitations

The similarity between the mechanisms of internal transport in fixed bed and microchannel reactors mean that the criterion for the presence of transport limitations in fixed bed reactors can be applied to microchannel reactors.

Thiele modulus The Thiele modulus can be used to determine whether pore diffusion effects significantly decrease the reaction rate if the form of the rate law is known. This is defined for a first order reaction by (Levenspiel 1999)

$$M_T = L_c\sqrt{\frac{k_{obs}}{D_{eff}}} \tag{2.34}$$

where L_c is a characteristic length (m), D_{eff} is the effective diffusion coefficient $(\mathrm{m^3_{gas}/m_{solid}.s})$ and k_{obs} is the observed rate constant $(\mathrm{m^3_{gas}/m^3_{solid}.s})$ as a function of temperature. This can be used to calculate the internal effectiveness factor η_{int} by the expression for a flat plate

$$\eta_{int} = \frac{\tanh M_T}{M_T} \tag{2.35}$$

Weitz-Prater modulus The Weitz-Prater modulus is used for the estimation of internal mass transport limitations when the form if the rate law is not known but only its observed rate law. This modulus is given by (Levenspiel 1999)

$$M_W = M_T^2\eta_{int} = \frac{L_c^2 r_{eff}}{c_t\chi_i D_e}\frac{n+1}{2} \tag{2.36}$$

where r_{eff} is the observed reaction rate per unit particle volume, $c_t\chi_i$ is the reactant concentration at the surface, D_{eff} is the effective diffusivity and n is the reaction order. For criterion for $\eta_{int} \leq 0.95$ is $M_W < 1$ (Mears, 1971) and for insignificant internal mass transfer resistance, $\eta_{int} \to 1$ is $M_W < 0.15$ (Levenspiel, 1999).

2.4.4 Tests for mass transfer limitations

Mass transfer limitations are routinely tested in fixed bed reactors. These methods are generally applicable to microchannel reactors sometimes with a few modifications (Walter et al. 2005). Two methods that are easily applicable to modelling studies are increasing channel diameter for external effects and increasing catalyst layer thickness for internal effects. These two changes increase the diffusion paths in fluid and solid phases respectively. The presence of the respective transport limitations will be seen if reactor conversion decreases. These tests need to be carried out at constant weight hourly space velocity, or SV as it is referred to in the remainder of the manuscript. This is given by

$$SV = \frac{F_0}{m_{cat}} \tag{2.37}$$

$$= \frac{c_t v_0 X S A_I}{V_{cat}\rho_{cat}} \tag{2.38}$$

This essentially means that the ratio of flow rate to catalyst weight is kept constant. This will negate the effect a change of flow rate or mass of catalyst will have on conversion. The reactor residence time is also kept constant as this affects the residence time distribution of fluid elements in the reactor. This effect is discussed in Section 2.3.4. Thus the effect of varying channel height or catalyst thickness is isolated and the presence of mass transfer limitations can be seen.

2.5 Maxwell-Stefan Approach to Mass Transport

2.5.1 Contrast to Fickian Diffusion

Typically mass transport in chemical processes has been modelled from a macroscopic perspective. This uses Fick's Law of Diffusion and defines a linear relationship between the molar diffusion flux of species i relative to the molar average velocity, J_i and the concentration gradient $\nabla\chi_i$. This is expressed by Fick's Law as

$$\mathbf{J}_i \equiv c_i(\mathbf{v}_i - \mathbf{v}) = -c_t D_{i,m} \nabla\chi_i \tag{2.39}$$

for $i = 1, ..., c$.

where the molar flux with respect to stationary co-ordinates[4], $\mathbf{N}_i$ is given by

$$\mathbf{N}_i \equiv c_i\mathbf{v}_i = c_t\chi_i\mathbf{v}_i = \mathbf{J}_i + \chi_i\mathbf{N}_t \tag{2.40}$$

$$\mathbf{N}_t = \sum_{i=1}^{c} \mathbf{N}_i \tag{2.41}$$

These relationships are only valid under certain circumstances. These are (Krishna & Wesselingh, 1997)

1. binary mixtures
2. diffusion of a dilute species, i in a multicomponent mixture
3. absence of external forces (centrifugal and electrostatic)

The Ficks Law model has two shortcomings. It considers molecular motion due to species-mixture interactions binary species interactions as opposed binary interactions for the

[4]In the case of a stationary reactor

Table 2.3: Initial bulb mole fractions adapted from (Krishna & Wesselingh, 1997)

	χ_{H_2}	χ_{N_2}	χ_{CO_2}
Bulb 1	0.00000	0.50086	0.49914
Bulb 2	0.50121	0.49879	0.00000

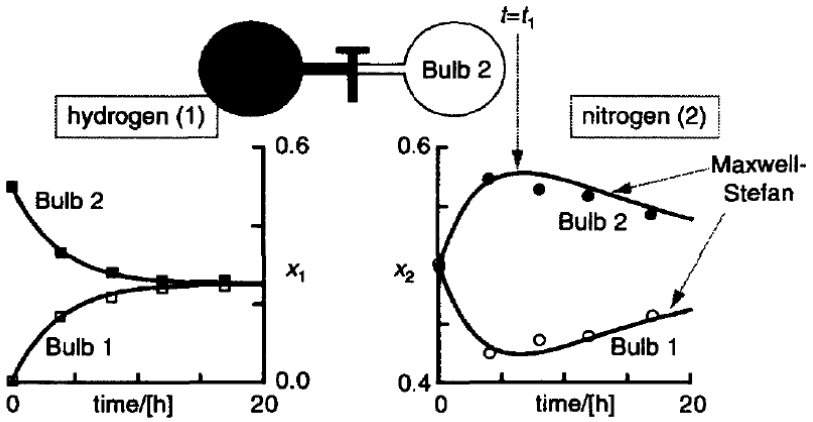

Figure 2.6: The two-bulb diffusion experiment with the system (1) hydrogen, (2) nitrogen and (3) carbon dioxide. Adapted from (Krishna & Wesselingh 1997).

Maxwell-Stefan formulation(Taylor & Krishna, 1993). This means that the often inaccurate mixture diffusivities $D_{i,m}$ are used rather than the more fundamental binary diffusivities $D_{i,j}$.

A further shortcoming is that it does not account for the microscopic interactions between individual sets of molecules as a result of the transfer of momentum by collisions which can lead to some species flowing against their concentration gradients (Taylor & Krishna, 1993). The study of Duncan and Toor illustrates this shortcoming of the Fickian diffusion model in an ideal hydrogen, nitrogen, carbon dioxide mixture and is outlined in (Krishna & Wesselingh, 1997). The study considered two bulbs, 1 and 2 connected by a capillary in Figure 2.6. The initial composition is given in Table 2.3.

The composition profiles in Figure 2.6 show that as expected the diffusion of hydrogen and carbon dioxide follow Fickian behaviour and each diffuse according to their concentration gradients. The interesting behaviour occurs with nitrogen. Initially there is no concentration gradient and hence no driving force for diffusion. The concentration-time profile in Figure 2.6 shows that a concentration gradient does develop between the two bulbs, with a nitrogen flow from bulb 1 to bulb 2. This diffusion of a species against its own concentration gradient is called *reverse diffusion.* It is attributed to the flow of the carbon dioxide in the same direction that carries the nitrogen by momentum transfer due to molecular collisions or drag. The hydrogen, being the lighter species has a more limited ability to carry nitrogen than carbon dioxide and hence a lower ability to carry

the nitrogen molecules.

The Maxwell-Stefan approach to mass transfer takes these microscopic interactions into account and the theory is discussed in the section below.

2.5.2 General Theory

A detailed analysis of the fundamental derivation of the Maxwell-Stefan relationships from the theory of molecular collisions can be found in reviews on the subject (Do, 1998; Taylor & Krishna, 1993; Krishna & Wesselingh, 1997). Some points are reproduced here.

Consider a binary gaseous mixture of molecular species 1 and 2 in a control volume with total pressure P and composition χ_1 and χ_2. The number of collisions between the species will be proportional to each of the compositions

$$\text{Number of collisions per volume per time} \propto \chi_1\chi_2 \tag{2.42}$$

The rate of change of momentum of each species is the momentum transferred between the species multiplied by the number of collisions per volume per time

$$\text{Rate of change of momentum of species 1 molecule} \propto \chi_1\chi_2\,(v_1 - v_2) \tag{2.43}$$

For illustrative purposes a force balance is carried out on the y-direction and yields

$$\text{Net force acting on species 1 per volume in y-direction} = -\frac{dP_1}{dy} \tag{2.44}$$

The expressions in Equations 2.43 and 2.44 are equated by a force balance and are related by a friction factor $f_{12} = \frac{P}{D_{12}}$. This leads to the expression for the binary interaction of species 1 and 2 in all directions

$$\mathbf{d}_1 = -\frac{\chi_1\chi_2\,(\mathbf{v}_1 - \mathbf{v}_2)}{D_{1,2}}$$

where d_1 is the generalised driving force for diffusion. The expression for the interaction between multiple components results from the summation of individual binary interactions

$$\mathbf{d}_i = -\sum_{j=1}^{c} \frac{\chi_i\chi_j\,(\mathbf{v}_i - \mathbf{v}_j)}{D_{i,j}} \tag{2.45}$$

Substitute for $N_i = c_i v_i$ to put it in terms of flux gives a more useful expression in terms of molar fluxes. The derivation is shown in Appendix A.2 and the result is shown in Equation 2.46.

$$\mathbf{d}_i = \sum_{\substack{j=1 \\ j \neq i}}^{c} \frac{\chi_i \mathbf{N}_j - \chi_j \mathbf{N}_i}{c_t D_{i,j}} \tag{2.46}$$

2.5.3 Driving Force

The driving force for mass transport, $\mathbf{d}_i$ is given for various flow and fluid situations. The driving force in its most general form is given by Equation 2.47 (Taylor & Krishna, 1993).

$$c_t RT \mathbf{d}_i \equiv c_i \nabla_{T,P} \mu_i + (\zeta_i - \omega_i) \nabla p - \left(c_i \mathbf{F}_i - \omega_i \sum_{j=1}^{c} c_j \mathbf{F}_j \right) \tag{2.47}$$

The $c_t RT \mathbf{d}_i$ term represents the force acting on species i per unit volume mixture that moves species i relative to the mixture. The $c_i \nabla_{T,P} \mu_i$ term takes into account the the chemical potential gradient as the fundamental driving force for diffusion. The equality of chemical potentials is the condition for equilibrium so a gradient in chemical potential represents a departure from the mixture's equilibrium state and hence a driver of diffusion. The derivative is taken at constant temperature and pressure as the effect of these variables are accounted for by subsequent terms. The $(\zeta_i - \omega_i) \nabla P$ term accounts for the pressure gradients (i.e. absence of mechanical equilibrium). The last term accounts for any external force per unit mass, $\mathbf{F}_i$ applied to the mixture that may influence diffusion. These include gravitational forces, centripetal forces or electromagnetic forces on electrolytes.

For ideal gases there are no volume changes upon mixing, so the volume fraction ζ_i corresponds to the mole fraction χ. The chemical potential now corresponds to the mole fraction gradient, $\nabla \chi_i$ and the driving force becomes

$$\mathbf{d}_i \equiv \nabla \chi_i + (\chi_i - \omega_i) \frac{\nabla P}{P} - \left(c_i \mathbf{F}_i - \omega_i \sum_{j=1}^{c} c_j \mathbf{F}_j \right) \tag{2.48}$$

The absence of external body forces gives

$$\mathbf{d}_i \equiv \nabla \chi_i + (\chi_i - \omega_i) \frac{\nabla P}{P} \tag{2.49}$$

An isobaric system results from neglecting any viscous forces in the direction of diffusion and the driving force finally yields

$$\mathbf{d}_i \equiv \nabla \chi_i \tag{2.50}$$

2.5.4 Auxiliary Relationships

Three auxiliary relationships have to be noted when using the Maxwell-Stefan equations (Bird et al., 2002). These follow from the physical constraints on the system. The first is as a result of the definition of the driving force

$$\sum_{i=1}^{c} \mathbf{d}_i = 0 \tag{2.51}$$

This means that only $c-1$ component driving forces are independent. The second is a result of the Onsager reciprocal relations and states that the diffusivity of species i in j is equal to the diffusivity of j in i.

$$D_{i,j} = D_{j,i} \tag{2.52}$$

The third is a result of the dependent species having to satisfy the physical constraint $\sum_{i=1}^{c} \chi_i = 1$

$$\sum_{i=1}^{c} \frac{\chi_i}{D_{i,j}} = 0 \tag{2.53}$$

2.5.5 Physical Constraint

The multicomponent Maxwell-Stefan equation provides $c-1$ independent equations. A physical constraint is needed for the flux and its form is based on the physical situation. There are three of these that are typically encountered (Do, 1998). These are given for isobaric conditions.

The Open System The fluxes are related by Graham's law of diffusion which relates species fluxes to their molecular masses as $\mathbf{N}_i \propto \frac{1}{\sqrt{M_i}}$ in an isobaric system (Bird et al., 2002). This is used to relate fluxes by

$$\sum_{i=1}^{c} \sqrt{M_i}\mathbf{N}_i = 0 \tag{2.54}$$

or

$$\mathbf{N}_c = -\sum_{i=1}^{c-1} \sqrt{\frac{M_i}{M_c}}\mathbf{N}_i \tag{2.55}$$

The Closed System If the pressure is maintained constant in a direction, y then there is no net velocity v_y. Given that the overall velocity is given by $v_y c_t = N_y$ The sum of fluxes must be zero

$$\sum_{i=1}^{c} \mathbf{N}_i = \mathbf{0} \tag{2.56}$$

or

$$\mathbf{N}_c = -\sum_{i=1}^{c-1} \mathbf{N}_i \tag{2.57}$$

The Stefan Tube The Stefan tube considers the evaporation of $c-1$ components from a liquid surface into a gas space containing the c^{th} component. This is analogous to reaction or adsorption of $c-1$ components with the c^{th} component as the inert. The flux of the inert is given by its diffusional component J_c its convective component $\chi_c \sum_{i=1}^{c} \mathbf{N}_i$ as

$$\mathbf{N}_c = \mathbf{J}_c + \chi_c \sum_{i=1}^{c} \mathbf{N}_i \tag{2.58}$$

The diffusional flux J_c of the gas towards the reaction surface is balanced by the diffusion-induced convective flux $\chi_c \sum_{i=1}^{c} \mathbf{N}_i$ towards the center of the tube (Taylor & Krishna, 1993). The resultant physical constraint is thus

$$\mathbf{N}_c = 0 \tag{2.59}$$

2.5.6 The Inverted Flux Expression

The Maxwell-Stefan expression in Equation 2.46 can be inverted to give the flux in terms of the driving force, analogous to Ficks Law. This is given by (Do 1998)

$$\mathbf{N} = -c_t \left[D^{eff}\right] \mathbf{d} \tag{2.60}$$

where $\mathbf{N}$ and $\mathbf{d}_i$ are size $[c-1]$ and the effective diffusivity D^{eff} is size $[c-1, c-1]$. Here the effective diffusivity is defined as the inversion of B_{eff}. The form of B_{eff} is given in Equation 2.62 and the dependency on physical condition is defined by the parameter υ_i for $i = 1, ..., c-1$. These are given for the different systems in Table 2.4.

Table 2.4: Definitions of υ_i for different systems in Equation 2.62 adapted from (Do, 1998)

	Open system	Closed system	Stefan tube
υ_i $(i = 1...c-1)$	$\sqrt{\frac{M_i}{M_c}}$	1	0

$$D^{eff} = B_{eff}^{-1} \tag{2.61}$$

$$B_{i,j,eff} = \begin{cases} \frac{\chi_i \upsilon_i}{D_{i,c}} + \sum_{\substack{k=1 \\ k \neq i}}^{c} \frac{\chi_k}{D_{i,k}} & \text{for i=j} \\ \chi_i \left(\frac{\upsilon_j}{D_{i,c}} + \frac{1}{D_{i,j}} \right) & \text{for i}\neq\text{j} \end{cases} \tag{2.62}$$

2.5.7 Energy Equation

Having treated the effect of concentration gradients, pressure gradients and external body forces in the previous section, attention is now given to the effect of thermal gradients on mass transport and vice versa. The analysis is treated in some depth in the literature (Taylor & Krishna 1993) and some of the key results are presented here.

The analysis begins with an expression for energy flux, analogous to mass flux in Equation 2.63.

$$\mathbf{e} = \mathbf{q} + \sum_{i=1}^{c} \overline{H}_i \mathbf{N}_i \tag{2.63}$$

To allow for coupling between mass and heat transport, the driving force terms $\mathbf{d}_i$ and $\mathbf{q}$ are constructed. The actual driving forces are given by $(\mathbf{v}_i - \mathbf{v}_j)$ and $\nabla\,(1/T)$ for mass and heat transport respectively. This is included in the expression for conductive heat flux as

$$q = -\lambda \nabla T + \frac{1}{2} c_t RT \sum_{i=1}^{c} \sum_{\substack{j=1 \\ j \neq i}} \frac{\chi_i \chi_j}{D_{i,j}} \left(\frac{D_i^T}{\rho_i} \right) (\mathbf{v}_i - \mathbf{v}_j) \tag{2.64}$$

$$= -\lambda \nabla T + \frac{1}{2} c_t RT \sum_{i=1}^{c} \sum_{\substack{j=1 \\ j \neq i}} \frac{\chi_i \chi_j}{D_{i,j}} \left(\frac{D_i^T}{\rho_i} - \frac{D_j^T}{\rho_j} \right) (\mathbf{v}_i - \mathbf{v}_j) \tag{2.65}$$

where D_i^T is the thermal diffusion coefficient of species i (Taylor & Krishna, 1993). The multicomponent thermal diffusion factors are defined as

$$\alpha_{i,j} = \frac{1}{D_{i,j}} \left(\frac{D_i^T}{\rho_i} - \frac{D_j^T}{\rho_j} \right) \quad i \neq j = 1, 2, \ldots, n \tag{2.66}$$

These have the asymmetric property of

$$\alpha_{i,j} = -\alpha_{j,i} \quad i \neq j = 1, 2, \ldots, n \tag{2.67}$$

Using this definition we have the expression for thermal conduction

$$\mathbf{q} = -\lambda \nabla T + \frac{1}{2} c_t RT \sum_{i=1}^{c} \sum_{\substack{j=1 \\ j \neq i}}^{c} \chi_i \chi_j \alpha_{i,j} \left(\mathbf{v}_i - \mathbf{v}_j \right) \tag{2.68}$$

In terms of mass fluxes, this gives

$$\mathbf{q} = -\lambda \nabla T + \frac{1}{2} c_t RT \sum_{i=1}^{c} \sum_{\substack{j=1 \\ j \neq i}}^{c} \frac{\alpha_{i,j} \left(\chi_j N_i - \chi_i N_j \right)}{c_t} \tag{2.69}$$

The first term gives the conventional heat flux due to transfer of energy due to molecular collisions, or thermal conductivity. The second term accounts for the production of temperature fluxes due to mass fluxes and is known as the *Dufour effect*.

The interaction between mass and heat transport also gives a production of mass flux as a result of heat flux. This is taken into account by augmenting the Maxwell-Stefan equation as

$$\mathbf{d}_i = -\sum_{\substack{j=1 \\ j \neq i}}^{c} \frac{\chi_i \chi_j \left(\mathbf{v}_i - \mathbf{v}_j \right)}{D_{i,j}} - \sum_{\substack{j=1 \\ j \neq i}}^{c} \chi_i \chi_j \alpha_{i,j} \frac{\nabla T}{T} \tag{2.70}$$

$$= \sum_{\substack{j=1 \\ j \neq i}}^{c} \frac{\chi_i N_j - \chi_j N_i}{c_t D_{i,j}} - \sum_{\substack{j=1 \\ j \neq i}}^{c} \chi_i \chi_j \alpha_{i,j} \frac{\nabla T}{T} \tag{2.71}$$

where the generalised driving force is given by Equation 2.47. This is referred to as thermal diffusion or the *Soret effect*.

2.5.7.1 Applicability

The presence of the Dufour and Soret coupling effects have been documented in cases of steep thermal gradients and systems with heavy molecules. In particular these have been studied on space vehicle re-entry, chemical-vapour deposition and non-isothermal

gas absorption. Classic chemical engineering design applications generally neglect these effects as temperature gradients are seldom steep enough or long sustained to make the coupling significant (Taylor & Krishna 1993). No evidence has been found in the literature for the presence of this coupling in microchannel reactors.

2.5.7.2 Non-interacting system

If the Dufour effect is neglected then the expression for thermal conduction in equation 2.69 is reduced to the standard Fourier's Law

$$\mathbf{q} = -\lambda \nabla T \tag{2.72}$$

If the Soret effect is neglected then the expression for mass transport reduces to the standard Maxwell-Stefan equation found in Equation 2.46.

2.6 General Modelling Approaches

The process for reactants to products in microchannel reactors consists of transport of reactant molecules from the bulk gas phase in the channel towards the catalyst coated on the channel wall, simultaneous diffusion and reaction in the porous catalyst wash coat, and transport of product molecules from the channel wall back to the bulk gas phase (Hoebink & Marin 1998).

In this section the different model approaches used to describe these processes in the channels are reviewed to determine the relevant equations and appropriate simplifications that can be made to accurately represent the mass, momentum and heat transfer.

2.6.1 Plug Flow model

The simplest approach is to use the plug flow model. The flow field in this model has the profile of a well mixed plug of fluid. This means there is a uniform velocity across the reaction channel as expected in turbulent flow (Fogler 2006). The model assumes only bulk convective mass and energy transport in the axial direction through the reactor, neglecting any mass and energy transport by diffusion or dispersion. The model also assumes no radial variations in velocity, concentration and temperature resulting in a simplified 1-dimensional model. The general equation for an unsteady state plug flow model with first order reaction is presented below:

$$\frac{\partial c_i}{\partial t} = v_{x,avg} \frac{\partial c_i}{\partial x} - k c_i \tag{2.73}$$

for $i = 1, ..., c$.

The plug flow model is claimed to be appropriate for reactors in which radial diffusion is fast enough to ensure uniform profiles across the reaction channel (Schuurman et al. 2005). This condition is, however is subject to the behaviour of the reaction. If the reaction were reaction rate limited then there would not be a radial gradient and this assumption would be valid. However if the reaction were mass transfer limited, then a radial profile would be expected. This approach therefore depends on the region of operation and is therefore unsuitable for generalised model. A further inherent disadvantage of the plug flow model is that it does not allow for the axial spreading of reacting components as a result of molecular diffusion and the laminar velocity profile. This disadvantage is treated by the Taylor-Aris approach.

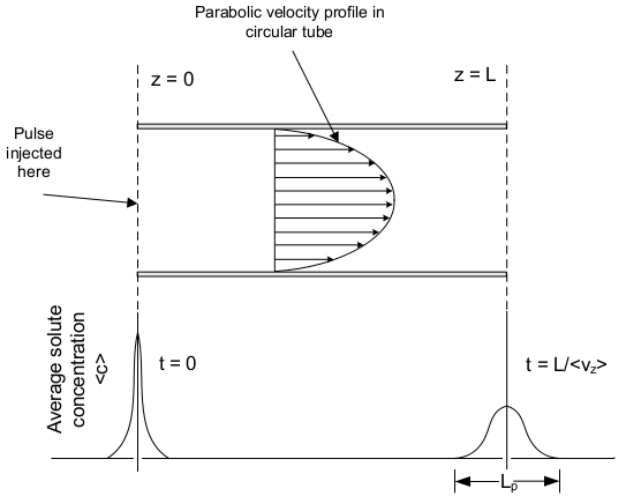

Figure 2.7: Axial broadening of a solute pulse as a result of Taylor dispersion (Bird et al. 2002).

2.6.2 Taylor-Aris Approach

The behaviour of soluble substances in flowing fluids in narrow diameter tubes has been studied with the intention of describing dispersion of salts in blood streams (Taylor (1953, 1954)). A solute pulse that is introduced to a fluid in laminar flow is found to spread out because of both cross-sectional variation of the axial velocity and radial molecular diffusion. This is shown in Figure 2.7.

Once the laminar profile has been fully developed, the solute spread can be described by the following typical convection-diffusion equation.

$$\frac{\partial c_i}{\partial t} = -v_0 \left(1 - \frac{r^2}{R^2}\right) \frac{\partial c_i}{\partial x} + D_{AB} \left(\frac{\partial^2 c_i}{\partial r^2} + \frac{1}{r}\frac{\partial c_i}{\partial r} + \frac{\partial^2 c_i}{\partial x^2}\right) \quad for\, i = 1, c \tag{2.74}$$

The solution of the entire equation was not attempted, however an analytical solution was sought in the case of a simplified operating condition. This was that radial variations in concentration are reduced to a fraction of their initial state by molecular diffusion quicker than changes in axial concentration as a result of convective transport. In other words, a pseudo-steady state is assumed along the x-axis. This means that a radially averaged solution for concentration is obtained. The time for the radial variation of concentration to have reduced to $\frac{1}{e} = 0.36$ of its initial value is given by

$$t' = \frac{a^2}{3.8^2 D_{AB}} \tag{2.75}$$

As the time for a change in concentration due to axial convection over a pulse length L_p has to be greater then t', the following limiting condition is obtained.

$$\frac{L_p}{v_0} \gg \frac{R^2}{3.8^2 D_{AB}} \tag{2.76}$$

The axial spreading is approximated by a theoretical dispersion coefficient, D_{disp} that takes into account axial spreading expected from laminar flow.

$$D_{disp} = \frac{R^2 u_0^2}{48 D_{AB}} = \frac{1}{48} D_{AB} Pe^2 \tag{2.77}$$

This reduces the convection-diffusion equation to get the axial dispersion equation.

$$\frac{\partial c_i}{\partial t} = -v_0 \frac{\partial c_i}{\partial x} + D_{disp} \frac{\partial^2 c_i}{\partial x^2} \tag{2.78}$$

Further work on Taylor flow (Aris 1956) has been conducted for a full range of validity and including molecular diffusion on the z and r directions. A modified dispersion coefficient has been proposed:

$$D_{disp} = D_{AB} \left(1 + \frac{1}{48} Pe^2 \right) \tag{2.79}$$

Limits of Applicability The applicability of the Taylor-Aris solution has limited applicability depending on flow conditions. This has been investigated by finite difference calculations (Ananthakrishnan et al. 1965). The Taylor-Aris solution was extended to reactive systems (Sankarasubramanian & Gill 1973) and shortfalls with this method for reactive systems emerged. The axial dispersion coefficient is not a fluid property, but rather a model coefficient that implicitly includes mass transfer and reaction effects in both axial and radial directions and essentially reduces a 2-dimensional problem to a 1-dimensional one. The coefficient depends on time, transport properties and reaction

kinetics and has to therefore be experimentally determined for each new system and therefore limits the applicability of the model.

This modelling approach shows further weaknesses in fast catalysed reactions that are mass transfer controlled (Wang & Stewart 1989). Figure 2.8 shows that significant deviations occurs in the radially averaged model at short times where the heterogeneous reaction is the fastest. In this region, radial diffusion is controlled by the concentration and temperature gradients generated by reaction, whose rates vary widely along the reactor. This weakens the case for adopting a constant coefficient that describes all mass transfer in the microchannel in both dimensions. As a result, explicit solutions of radial profiles need to be completed for an accurate and generally applicable model.

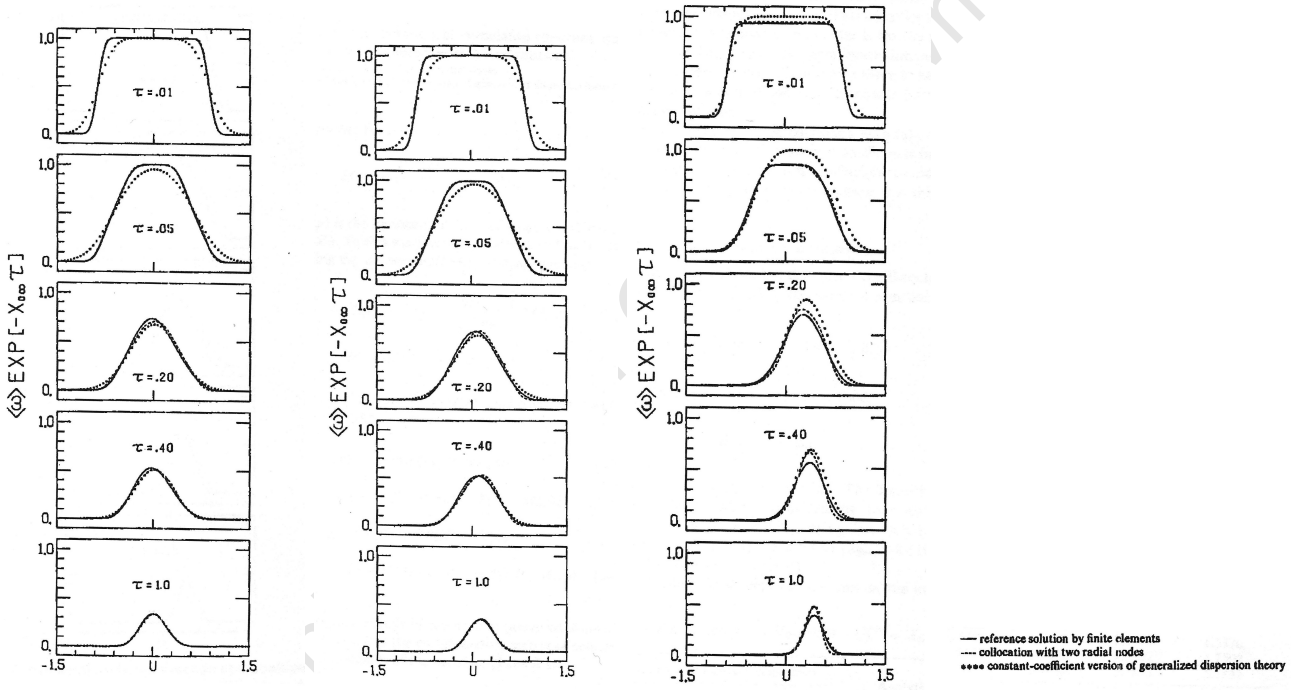

(a) $K'' = 0.1$ (b) $K'' = 1.0$ (c) $K'' = 10.0$

Figure 2.8: Axial concentration profiles along an adjusted length scale, U at different dimensionless times, $\tau = tD_{AB}/R^2$. This is for a binary system with $Pe = 40$, $K''' = 0$ at different heterogeneous reaction rates, K'''. These are all radially averaged to compare to results of dispersion models. Two point collocation method used. (Wang & Stewart 1989)

2.6.3 Multidimensional Approach

The multidimensional approach requires the explicit solution of the convection-diffusion equation in all dimensions considered. These problems have been solved using collocation for non-reactive (Wang & Stewart 1983) and reactive flow (Wang & Stewart 1989) in tubes.

The characteristic equation for homogeneous and heterogeneous reactive flow takes the following form:

$$\frac{\partial c_i}{\partial t} + v(r)\frac{\partial c_i}{\partial x} = D_{AB}\left[\frac{1}{r}\frac{\partial}{\partial r}\left(r\frac{\partial c_i}{\partial r}\right) + \frac{1}{Pe^2}\frac{\partial^2 c_i}{\partial z^2}\right] - K^{'''}c_i \tag{2.80}$$

with BCs

$$\frac{\partial c_i}{\partial r} = 0 \text{ at } r = 0$$

$$D_{AB}\frac{\partial c_i}{\partial r} + K^{''}c_i = 0 \text{ at } r = 1$$

The method of collocation is further described in Section 2.9. In the case of the reactive system the resulting first order ODEs are solved analytically using convolution. This is possible as a first order rate law is used, however a numerical solution would be possible using a stiff integrator if higher order reaction rates are needed. Solutions are represented in Figure 2.8. The results of collocation methods compare well to both finite element and radially averaged calculations. It further supports the use of collocation methods as a fast and accurate solver compared to more rigorous finite elements.

Navier-Stokes Approach The most comprehensive approach to modelling the flow in microchannels is the solution to the complete set of Navier-Stokes (momentum) equations along with the mass and energy conservation equations. The solution to these equations yields the species concentration, temperature, pressure and velocity profiles in both the axial and radial directions for circular channels or axial and both perpendicular directions for rectangular channels. However the equations are intractable and determining the solution to the full set of equations is a computationally expensive and time consuming process (Raja et al. 2000). This approach as applied to microchannel reactor studies is discussed further in Section 2.7.1.

2.7 Microchannel Modelling Approaches

This section contains a review of relevant microchannel modelling studies found in the literature. The studies are divided into two sections. The studies that consider multiple transport in multiple dimensions in a single domain are summarised in Table 2.5 while simplified studies that only consider transport in a single domain are summarised in Table 2.6. Various trends in the approaches are discussed.

Table 2.5: Summary of microchannel modelling studies that are multidimensional in a single domain.

Study	Reaction system	Model considerations[a]	Package (Method)
(Rebrov et al., 2001)	ammonia oxidation : heat exchanger	3-D (M X P T V)	FLUENT (FEM)
(TeGrotenhuis et al., 2002)	WGS	2-D solid, fluid phases (MX T)	FEMLAB (FEM)
(Wan et al., 2003)	1-Pentene Epoxidation	3-D radial, laminar, solid, fluid phases (MX)	FEMLAB (FEM)
(Cao et al., 2005)	Methane steam reforming	3-D Solid, fluid phases (MX T)	FEMLAB (FEM)
(Kim et al., 2005)	WGS : heat exchanger	2-D rectangular Laminar flow (MX T)	FEMLAB (FEM)
(Walter et al., 2005)	Isoprene oxidation	3-D Radial (MX T)	gPROMS (CFDM)
(Chattopadhyay & Veser, 2006)	ignition behavior of H_2/air mixtures	3-D Radial (M X P T V) 1 - 10 min single run on SUN Blade 100	CHEMKIN's CRESLAF (FDM)
Baier & Kolb 2007	WGS: heat exchanger	2-D Solid, fluid phases (M X T V) order hrs single run	Ansys (FEM)
(Tonkovich et al., 2007)	Steam methane reforming	3-D solid, fluid phases (M X P T V)	FLUENT (FEM)
(Yang et al., 2008)	Oxidative dehydrogenation of ethane to ethylene	3-D Multiscale (single/multiple channels) (M X P T V)	unknown
(Arzamendi et al., 2009a)	Methanol reforming : Methanol combustion for heat	3-D reactor-heat exchanger 24 - 72 h single run (M X P T V)	Ansys CFX (FEM)
(Aubin et al., 2009)	-	3-D (M X P T V)	Ansys CFX (FEM)
(Buddoo et al., 2009)	pyrolysis of 2-pinanol	3-D (M X P T V)	COMSOL Multiphysics (FEM)
(Cao et al., 2009)	Fischer-Tropsch	3-D Radial (MX T)	FEMLAB (FEM)
(Karakaya et al., 2009)	Methane steam reforming	3-D Radial, laminar flow (MX T) 10 - 13 h single run on Pentium 4 Xeon 2.8 GHz	MATLAB (FDM)
(Vahabi & Akbari, 2009)	H_2 oxidation, CO oxidation, WGS	3-D (M X P T V)	unknown

[a]Model considerations shorthand: M=Mass balance; X=Species balance; MX=Mass/Species balance; P=Pressure drop; T=Energy balance; V=Momentum balance.

Table 2.6: Summary of microchannel modelling studies that are 1-dimensional in a single domain.

Study	Reaction system	Model considerations[a]	Solution by
(Germani et al., 2005) (Schuurman et al., 2005)	WGS	pseudo-2D heterogeneous, plug flow (MX T)	ODEPACK
(Kim et al., 2005)	WGS : heat exchanger	1-D Plug flow (Packed bed) (MX T)	POLYMATH
(Pfeifer et al., 2005)	Methanol steam reforming	1-D Plug flow, homogeneous (MX)	gPROMS
(Spatenka et al., 2005)	WGS	1-D homogeneous (MX) pseudo-2-D solid, fluid phases, heterogeneous (T)	axial - (BFDM)
(Spatenka et al., 2005)	WGS	pseudo-2-D (MX T) solid, fluid phases transient for convergence	axial - (BFDM) radial - (OCFEM)
(Germani & Schuurman, 2006)	WGS	1-D homogeneous, plug flow (MX)	ODEPACK
Baier & Kolb 2007	WGS: heat exchanger	homogeneous (MX T)	
(Brooks et al., 2007)	Sabatier	1-D Transient (M X P T V)	LIMEX (MOL)
(Goerke et al., 2009)	Ethanol steam reforming	1-D Plug flow homogeneous (MX)	gPROMS

[a]Model considerations shorthand: M=Mass balance; X=Species balance; MX=Mass/Species balance; P=Pressure drop; T=Energy balance; V=Momentum balance. BFDM - backwards finite difference; OCFEM - orthogonal collocation on finite elements; CFDM - central finite difference method

2.7.1 Multidimensional Models

Multidimensional models lead to systems of partial differential equations. The reviewed models in Table 2.5 all use a 1st order finite difference, or finite element method for solution. The advantage of using these low order methods is that the meshing procedures, solvers and equation sets are readily available in commercial packages such as Fluent, Ansys and Femlab. Although this does ensure fast model development, licensing costs mean that for the model to be used, funding has to be continuously maintained. An alternative exists in the form of an open-source CFD package OpenFOAM, however this has not been used in microchannel applications.

A further disadvantage of these solvers is their computational expense that arises from the large mesh sizes required for convergence to a mesh-free solution. The large mesh sizes are a consequence of the low order of the numerical methods used. The computational expense is reported in few studies, three of which are shown in Table 2.5. The two single-channel modelling studies have computational times of 1 - 10 min for the complete (M X P T V) variable set (Chattopadhyay & Veser 2006) and 10 - 13 hr for a reduced (MX T) variable set (Karakaya et al. 2009). Even though the former study has a more complete variable set, its computational time is lower as it uses a SUN supercomputer while the latter uses the more readily available Pentium 4 processor. These single run times are unacceptable for use in optimisation or regression routines and therefore confirm the unsuitability of low order PDE solvers to provide a computationally efficient model. The high computational time of 24 - 72 hrs for the multiscale model (Arzamendi et al. 2009b) is a further indication of the need to develop an efficient single channel model.

The completeness of the available models is only with respect to the variable set that is being solved for and not necessarily the phenomenon that occur within the reactor. All of the reported models consider the presence of molecular diffusion due to the Fickian mechanism rather than the more suitable Maxwell-Stefan formulation for multicomponent mixtures. The advantages of the latter formulation is discussed in Section 2.5.1.

2.7.2 Single dimensional models

Single dimensional models are presented in Table 2.6. These provide computationally efficient models with significant simplifications. The first is the neglection of the laminar flow profile and the assumption of plug flow. This disregards the effect of different particles having different residence times within the reactor and could lead to an overestimation of the reactor conversion as some particles have a lower residence times than the average. This phenomenon is noted in the development of the Damköhler criterion for external mass transport and is discussed in Section 2.4.2.

A further simplification is that external transport limitations are either neglected and justified by film analogy criteria (Goerke et al. 2009) or approximated via film coefficients (Schuurman et al. 2005; Spatenka et al. 2005). It should be noted that, as discussed in Section 2.4.1 the film analogy is invalid under laminar flow conditions and these approached should be avoided.

2.7.3 Model results

Results from WGS modelling studies are represented here for comparison to model results in later sections. A 1-dimensional model is developed (Spatenka et al. 2005) and is used to determine kinetic parameters using experimental data and proposed rate expressions. These kinetic parameters are then used in the 2-dimensional model to simulate the reactor performance for different inlet temperatures. The results indicate adiabatic temperature rises of approximately 80^oC for all inlet temperatures.

The temperature control of the WGS reaction in an integrated micro-channel reactor/heat exchanger has been studied using a plug flow model (Baier & Kolb 2007). The reactor setup consisted of alternate cooling and reaction channels. The model is used to compare the temperature profile that can be achieved in a reactor-heat exchanger to the optimum temperature profile for the reaction. The model initially neglected any mass transfer resistances. The results indicate close agreement between simulated and optimum temperature profiles. The model is then modified to include the effect of external mass transfer limitations. The channel height is varied to determine the effect of mass transfer on reactor performance and the range of heights over which the assumption of negligible mass transfer is valid. The results indicate that for channel height $> 200\mu m$ external mass transfer limitations become significant.

2.8 WGS reaction

This section details thermodynamic and kinetic characteristics of the WGS reaction as well as attempts to model it in microchannel reactors.

2.8.1 Thermodynamics

The WGS reaction is a mildly exothermic reversible reaction that follows the equation (Kolb et al. 2005):

$$CO + H_2O \rightleftharpoons CO_2 + H_2 \tag{2.81}$$

$\Delta H_{rxn}^{25^{\circ}C} = -41.2\,kJ/mol$

The reaction therefore requires low temperatures for high equilibrium conversions. The reaction is limited by thermodynamic equilibrium defined by (Kolb et al. 2005):

$$K_{eq} = exp\left\{\frac{4577.8}{T[K]} - 4.33\right\} \tag{2.82}$$

2.8.2 Kinetic data

Kinetic data is typically given in isothermal conversion-temperature plots. Relevant WGS data is provided in Figures 2.9-2.11. The data in Figure 2.9 is taken for different catalyst samples at different reactor temperatures. This data provides 5-8 data points in the kinetic range and is thus suitable for a the regression of two kinetic coefficients k_0 and E_a. The data in Figure 2.10 only provides 3-4 data points in the kinetic range and is unsuitable as the regression would be very constrained as a result of the few degrees of freedom. The data in Figure 2.11 is also unsuitable as the conversion drops before thermodynamic equilibrium is reached. This is attributed to by-pass flow caused by technical problems (Kolb et al. 2008).

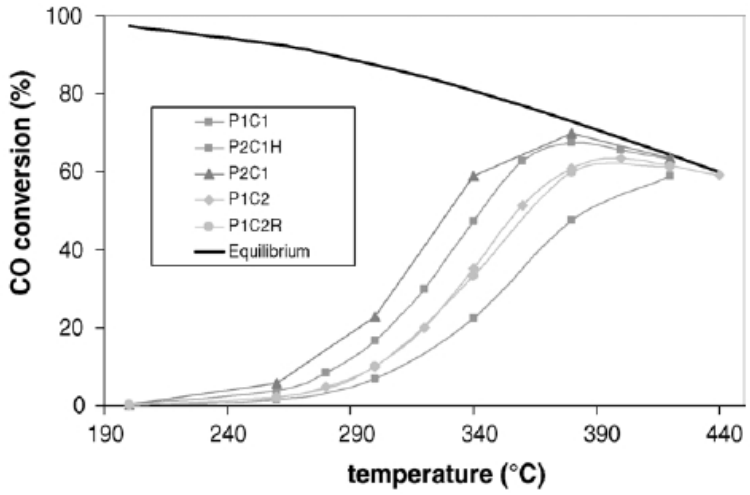

Figure 2.9: CO conversion curves for different Pt/CeO_2 catalyst samples as a function of the temperature. Reactor conditions: χ_i = 9.6 % CO, 23.0 % H_2O, 32.2 % H_2, 8.4 % CO_2, 26.8 % Ar. All 200 $^{Nml}/_{min}$ flow and $SV = 0.59^{mol}/_{s.kg_{cat}}$ for P2C1 sample. (Germani et al. 2005)

2.8.3 Kinetics

Although catalyst choice is not a focus of this investigation, an appropriate catalyst has to be chosen that has been developed for use in microchannel reactors. At low operating

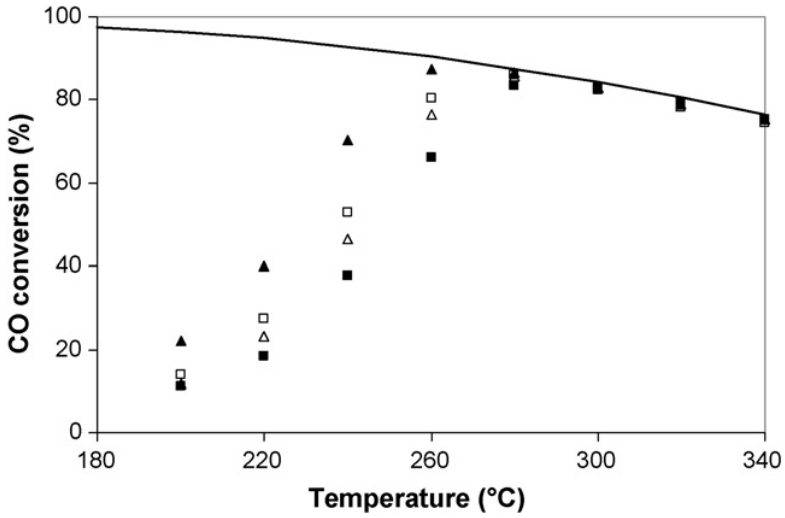

Figure 2.10: HTS CO conversion for $Pt/CeO_2/Al_2O_3$ catalyst as a function of the temperature. Reaction conditions: χ_i = 10.0 % CO, 20.0 % H_2O, 30.0 % H_2, 10.0 % CO_2, 30.0 % Ar. Six platelets each with 106 mg catalyst. (■) 100, (△) 80, (□) 60, (▲) 40 $^{Nml}/_{min}$ or $SV = 0.117^{mol}/_{s.kg_{cat}}$, $0.093^{mol}/_{s.kg_{cat}}$, $0.070^{mol}/_{s.kg_{cat}}$,$0.047^{mol}/_{s.kg_{cat}}$. (Kolb et al. 2008)

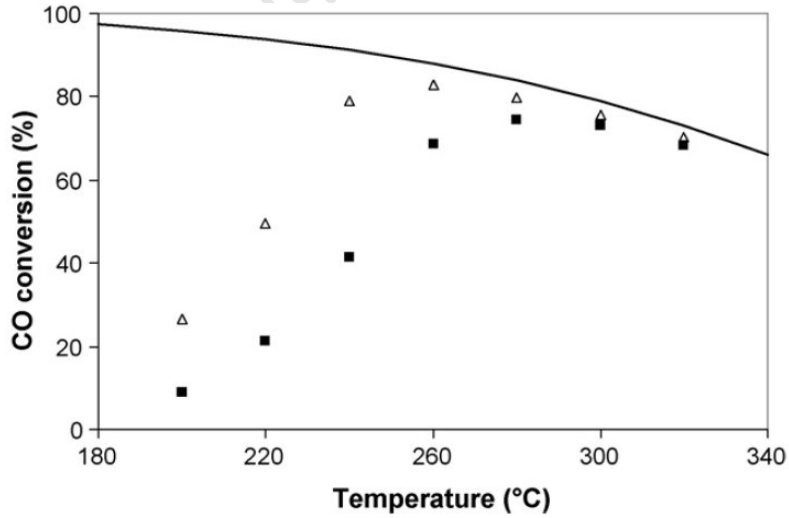

Figure 2.11: LTS CO conversion for $Pt/CeO_2/Al_2O_3$ catalyst as a function of the temperature. Reaction conditions: χ_i =2.6 % CO, 27.5 H_2O, 33.8 H_2, 13.0 % CO_2, 23.1 % Ar. Four platelets each with 106 mg catalyst. (△) 100, (■) 200 Nml/min or $SV = 0.175^{mol}/_{s.kg_{cat}}$ and $0.351^{mol}/_{s.kg_{cat}}$. (Kolb et al. 2008)

temperatures, traditional Fe- and Cu-based WGS catalysts are not very active. New Pt and Ru catalysts have been developed (Goerke et al. 2004; Wheeler et al. 2004; Germani et al. 2005; Kolb et al. 2005) for high CO conversion in microchannel reactors. These are highly active in the 250–600$^{\circ}C$ operating range.

2.8.3.1 Empirical rate expressions

The simplest rate expressions are based on empirical correlations of the following form (Choi & Stenger 2003):

$$r_{CO}[mol/s.kg_{cat}] = kP_{CO}P_{H_2O}\,(1-\beta) \tag{2.83}$$

where

$$\beta = \frac{P_{H_2}P_{CO_2}}{K_{eq}P_{CO}P_{H_2O}} \tag{2.84}$$

This assumes first order dependence on both reactant species, with an activation energy of 5703 J/mol. Further modifications to this law include power dependence (Choi & Stenger 2003):

$$r_{CO} = \rho_{cat}kP_{CO}^{n}P_{H_2O}^{m} \tag{2.85}$$

where n and m have been given as 0.78 and 0.15 respectively (Kieski et al. 1993) and β is as before.

This rate law has been modified for use in simulation studies (Baier & Kolb 2007) and is presented in the following form:

$$r_{CO} = \rho_{cat}k_0 e^{\left\{\frac{-5126}{T[K]}\right\}}c_{CO}^{0.78}c_{H_2O}^{0.15} \tag{2.86}$$

Where concentrations are in $kmol/m^3$, $k0 = 1.32 \times 10^6\, kmol/kg.s(m^3/kmol)^{0.93}$. The k_0 reported has been modified here to correct a reported conversion error.

2.8.3.2 Mechanistic rate expressions

Mechanistic rate expressions for the WGS reaction have been developed and reviewed (Choi & Stenger 2003). These are based on Langmuir-Henshilwood adsorption mechanisms and require considerably more computational effort when combined with a reactor model.

2.8.3.3 Reactor Modelling

Various models have been proposed for the WGS reaction in microchannel reactors (Germani et al. 2005; Schuurman et al. 2005; Spatenka et al. 2005; Quiney et al. 2006). These are all 1-dimensional models and assume plug flow without axial dispersion. A single model (Spatenka et al. 2005) considers both concentration gradients in the axial and radial directions. This is, however not a full 2-dimensional model as it only considers radial variations in the catalyst layer and not in the laminar fluid. This is an inaccurate approach as the mass transfer limitations are expected to be higher in the fluid phase than in the catalyst phase because of lower diffusion distances.

The effect of neglecting the hydrodynamics of the microchannel can be seen in the regressed kinetic expressions. These take the same form as Equation 2.85 and is given for the studies by (Schuurman et al. 2005)

$$r_{CO} = (2.2 \pm 1)\, 10^4 e^{\left\{\frac{-(60.4\pm5)10^3}{RT}\right\}} P_{CO}^{0.28\pm0.1} P_{H_2O}^{0.00} (1-\beta) \tag{2.87}$$

and (Germani et al. 2005)

$$r_{CO} = (1.3 \pm 1)\, 10^6 e^{\left\{\frac{-(86.0\pm15)10^3}{RT}\right\}} P_{CO}^{0.13\pm0.1} P_{H_2O}^{0.49\pm0.1} P_{H_2}^{-0.45\pm0.06} P_{CO_2}^{-0.12\pm0.05} (1-\beta) \tag{2.88}$$

The range of the regressed parameters give the 95% confidence limits. The inaccuracies of the models are reflected in the high variability of the regressed coefficients and the different numbers regressed parameters in each kinetic expression. The presence of fractional powers make the rate laws unstable in reactor models and further lead them finite values very low concentrations. In addition, the presence of negative powers lead the rate to tend to infinity at low concentrations. These observations lead to the conclusion that the proposed plug flow assumption does not hold and a more detailed model needs to be proposed to account for the hydrodynamic effects currently being included in the regressed parameters.

2.9 Numerical Methods

The flow phenomena described in Section 2.3 lead to a set of coupled PDEs that do not always have analytical solutions. This makes it necessary to evaluate possible numerical avenues to solve the model problem. These are reviewed in this section.

2.9.1 Introduction

The convection-diffusion equations with reaction that describe the process in the microchannels require the solution of coupled PDEs, one for each chemical component. This is generally performed numerically using either finite element methods (FEM) or orthogonal collocation (OC) (Rice & Do 1995). Both solve the general problem in time, t and n_{dim} spatial dimensions x_i for solution variables $\mathbf{u}$:

$$\frac{\partial \mathbf{u}}{\partial t} = \mathbf{f}\left(t, \mathbf{u}, \sum_{i=1}^{n_{dim}} \frac{\partial \mathbf{u}}{\partial x_i}, \sum_{i=1}^{n_{dim}} \frac{\partial^2 \mathbf{u}}{\partial x_i^2}\right) \tag{2.89}$$

Each method provides a routine to reduce the spatial derivatives on the right-hand side of Equation 2.89 into either linear or non-linear expressions. This reduces the set of PDEs into a set of ODEs to be solved for, for each variable at each spatial solution point. The ODEs are integrated in time with a separate stiff ODE-solver.

Both FEM and OC are based on the method of weighted residuals. This method uses *trial* and *test functions* to to approximate the solution to the differential equation (DE). The trial function, ϕ is used to construct the solution, while the test function, w_k gives the criterion to minimise the residual, R at each point k on the domain $x\epsilon[a, b]$ of the DE. It should be noted that the residual contains the approximate solution and thus trial function in its calculation. The residual is minimised over the whole domain according to the *inner product* defined as.

$$(R, w) = \int_a^b R(x) w_k(x) dx \tag{2.90}$$

The methods above differ in their choice of test functions and will be explained below.

2.9.2 Finite Element Methods

Finite element methods are based on the Galerkin method of weighted residuals. This uses a trial function, ϕ from the same family as the test function, w_k. This means that the integral in the inner product has to either be analytically or numerically evaluated. The solution of the integral means that this method will close the mass, energy or momentum balances, an important factor in chemical processes. However, the integral leads to difficulties in scaling the problem to higher orders or increasing grid resolution as analytical integration may become intractable and numerical integration computationally expensive and inaccurate.

2.9.3 Collocation

Collocation provides a high order method of solution that is easily scalable to higher number of solution points. This is possible as the trial function, $w_k$is taken as the Dirac delta function.

$$w_k = \delta\left(x - x_k\right) \tag{2.91}$$

This has the property that the integral around the point x of the product of the function and the trial function is just the function evaluated at that point x. This is represented in Equation 2.92. This avoids the solution of the inner product integral in Equation 2.90.

$$\int_{x_k^-}^{x_k^+} f(x)\delta(x - x_k)dx \quad = \quad f(x_k) \tag{2.92}$$

2.9.4 Orthogonal collocation

Orthogonal collocation (OC) differs from collocation in three ways: (1) the trial function is taken as a set of orthogonal polynomials, (2) the solution points are given by the roots of one of those orthogonal polynomials and (3) the solution variables are the required solution values at the mesh points (Finlayson, 1980).

The n solution or collocation points are first defined in each dimension. These are taken as the n roots of Jacobi polynomials. The resultant solution points are a semi-optimised set which yields better results than an arbitrary choice of solution points (Do, 1998). This is a convenient class of orthogonal polynomial as its roots always lie on the domain $[0, 1]$, yielding predictable solution points. This makes it necessary to normalise any domain $(x, y, z) \rightarrow (X, Y, Z)$ along which the integration is being performed shown in Equation 2.93. A further advantage is that the roots bunch up towards the ends of the domain where rapid changes in the dependent variable generally occur and yields a higher resolution at these ends.

$$\begin{aligned} \frac{d}{dx} &= \frac{1}{L}\frac{d}{dX} \\ \frac{d^2}{dx^2} &= \frac{1}{L^2}\frac{d^2}{dX^2} \end{aligned} \tag{2.93}$$

The PDEs will be solved exactly at each of the mesh points and because of the polynomial approximation, interpolation can be used over the same basis set to obtain a approximate

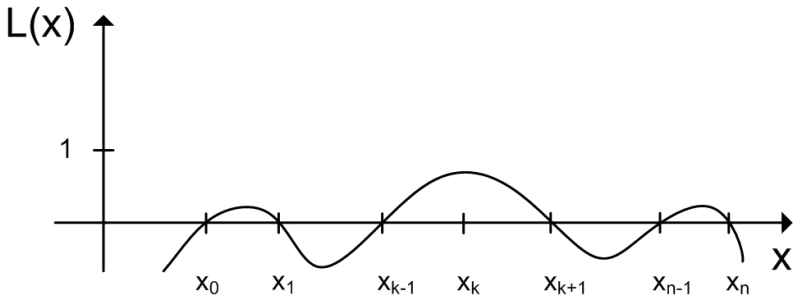

Figure 2.12: General form of the Lagrange interpolation polynomial (Burden & Faires, 2005)

fine solution over each spatial domain. A further advantage of using a collocation method is that it is derived in terms of the number of solution points, N. This means that it can easily be scaled to higher number of solution points for a more accurate solution.

Lagrange interpolation polynomials are used as the basis set to construct a continuous solution approximation (Villadsen & Michelsen, 1978). The form of a typical polynomial is shown in Figure 2.12. This has an oscillatory shape when forced to pass through a single function value, in this case $L(x) = 0$ after an initial steep gradient.

These polynomials yield the $n \times n$ matrices A and B that are used to reduce the first and second differentials respectively of each point u_i to a linear combination of all solution points, u_j. The differentials at each point $\frac{\partial u_i}{\partial X}$ and $\frac{\partial^2 u}{\partial X^2}$ are given by the following equations 2.94 and 2.95.

$$\frac{\partial u_i}{\partial X} = \sum_{j=1}^{n} A_{i,j} u_j \tag{2.94}$$

$$\frac{\partial^2 u_i}{\partial X^2} = \sum_{j=1}^{n} B_{i,j} u_j \tag{2.95}$$

for $i = 1, 2, ..., n$.

2.9.5 Application of Collocation to a Domain

Orthogonal collocation can either be implemented over the whole spatial domain in which case it is referred to as *global collocation* or over individual finite elements in the discretised domain, in which case it is referred to as *collocation on finite elements* (Rice & Do 1995). In the latter case, collocation is applied to each subdomain with boundary conditions between each subdomain of continuity of the solution variable and continuity of its gradient.

The disadvantage of global collocation is that the derivatives at each point in a complete domain depend on the solution values of every other point in that domain. This is acceptable when gradients are shallow. However, steep gradients are present a high order polynomial is required to fit the solution profile. This in turn means that an excessively large number of solution points are required for a mesh-free solution. This leads to computationally inefficient solution pathways as a full dense Jacobian needs to be solved by the ODE integrator to step forward in time.

To solve these problems, collocation is applied on finite elements. This reduces the required order of each polynomial approximation and hence the number of solution points in each subdomain. A further advantage is that the discretised mesh can be made finer over regions of steep gradients. The application on finite elements results in a block-diagonal Jacobian matrix in the ODE integrator and is easier to solve than a full dense matrix with global collocation of similar overall mesh size.

2.9.6 Available software

The FORTRAN software that is available for the solution of PDEs by FEM and FDM are shown in Table 2.7 while the software for solution by collocation is shown in Table 2.8. All solve the class of problem as stated in Equation 2.89. It should be noted that if a steady state solution is desired then the the time dimension can be substituted with one of the spatial dimensions provided that only first order derivatives are present in the chosen spatial dimension. This means that at minimum, a 2-dimensional PDE solver is necessary to solve a full 3-dimensional steady state PDE.

The finite element software in Table 2.7 are based on the method of lines and thus on finite element analysis. This means that an accurate solution of the surface concentration would require a large number of points and lead to long computational times for a continuous, mesh-free solution. This excludes these routines for use in this study on the basis of the requirement of a computationally efficient solution.

Of significant importance in Table 2.8 is that there is no collocation solver that can solve in more than one spatial dimension. This means that if collocation is to be used, the reduction of spatial derivatives will have to be manually implemented.

Table 2.7: Comparison of FORTRAN FEM and FDM PDE solvers

	PDEONE	PDETWO	BDMG	CWRES
TOMS Algorithm	494	565	621	731
Release Date	Sept1975	May1979	Dec1984	June1994
Method	FEM	FEM	FEM	Finite Difference
Description	parabolic, elliptic	parabolic, elliptic	parabolic, non-linear	steep (t,x) gradients
Time	yes	yes	yes	yes
Spatial Dimensions	1-D	2-D	2-D	1-D
Time integrator	user choice	GEARB	BDMG	DASSL or SPRINT
Notes	early solver	early solver	pdetwo with application of BDMG time solver	moving grid interface

Table 2.8: Comparison of FORTRAN Collocation PDE solvers

	PDECOL	PDECHED	BACOL
TOMS Algorithm	540	690	
Release Date	Aug1977	June1991	Dec2004
Method	OC on FE	OC on FE	OC on FE
Basis set	B-spline	Chebyshev	B-spline
Description	non-linear coupled PDEs	C^o method vs C^1 in pdecol	parabolic
Time	yes	yes	yes
Dimensions	1-D	1-D	1-D
Integrator	STIFIB	DASSL	DASSL
Notes		not parabolic gradients convection-diffusion equations	adaptive mesh

Chapter 3

Objectives and Scope

Based on the background and literature review the following objectives, key questions and hypotheses are proposed to develop and analyse the model.

3.1 Current status

Literature microchannel reactor models are either over simplified in that they neglect important subtleties, or too complex and are not usable for optimisation or parameter investigations. The objective of this project is therefore to develop a comprehensive model that obeys the phenomenological laws and can be used for optimisation.

Previous studies use the low order finite element method to solve resultant model PDEs. This can be replaced by the more efficient collocation method which has been effectively used to model 1- and 2-dimensional concentration profiles. A suitable 3-dimensional solver is unavailable.

3.2 Project Objectives

This project has various objectives given the current status of modelling microchannel reactors. These are:

- to develop a generic approach to modelling microchannel reactors that can determine the effects of mass and heat transport limitations
- to simulate steady state behaviour and predict experimental data from literature
- to solve the model PDEs using orthogonal collocation in 3-dimensions
- to implement the solver in a computationally efficient numerical algorithm

3.3 Project scope

The scope of the study is as follows:

- only single phase systems are considered
- this phase is the gas phase
- only external transport is considered as internal transport is assumed negligible from a previous study (Parak et al. 2009)
- the model is applied to a single equimolar reaction, the WGS reaction
- no experimentation is carried out and data is obtained from literature

3.4 Key Questions

Numerical Method Orthogonal collocation has been effectively used to model 1- and 2-dimensional concentration profiles, however it remains to be seen whether it can provide a stable numerical method for 3-dimensional reactor geometry.

Numerical efficiency Orthogonal collocation is a high order method and is expected to require fewer solution points than finite difference methods. However it remains to be seen whether it can be implemented in a algorithm that is more efficient than the more highly developed FEM codes.

Dimensionality This project aims to determine whether radial diffusion can be used to represent external mass transfer limitations to improve on previous radially averaged plug flow models.

Limits of transport limitations As low mass and heat transport limitations are said to be the biggest advantage of microchannel reactors over their conventional counterparts, it is important to predict their significance. The developed model will therefore be used to determine whether mass transport limitations are significant for typical ranges of channel sizes.

3.5 Hypotheses

Based on the literature review, the following hypothesis is proposed to develop and analyse the model:

- A 3-dimensional model more accurately predicts steady state experimental data than 1-dimensional models because it includes the effects of external mass and heat transport limitations.

The following hypotheses are proposed to determine whether mass and heat transfer limitations are significant at typical channel dimensions:

- A decrease in reactor channel height will decrease conversion for a set space velocity and residence time because of reduced mass transport limitations across the reactor channel.
- An increase in catalyst layer thickness decreases conversion for a set space velocity and residence time because of increased internal mass and heat transport limitations.

The following hypothesis is proposed to determine whether orthogonal collocation can be used to model 3-dimensional reactor geometry:

- Orthogonal collocation can be used to model 3-dimensional geometry because scale-up from 2-dimensional only leads to the addition of more variables in the simultaneous ODEs.

Chapter 4

Model Development

This chapter describes the model environment, model assumptions and the development of model equations.

4.1 Preliminary Considerations

4.1.1 Physical environment

A microchannel reactor consists of layers of stainless steel or ceramic plates. These plates are etched to form grooves. When the plates are stacked the channels form in a repeated pattern. A section of the channel is shown in Figure 4.1. The proposed model considers a single microchannel unit of the entire reactor stack. This is sufficient as this unit is repeated across the entire reactor stack in an analogous manner to how unit cells describe crystal lattice structures. This reactor-wide symmetry leads to a repeated solution if the exterior edge effects resulting from contact to the environment are neglected. The rectangular channel is further split by two additional symmetry lines into quadrants. Only one of these quadrants is required to be modelled to capture the behaviour of the entire reactor.

4.1.2 Model assumptions

The model assumptions are listed and justified below.

Negligible edge effects with environment Heat loss to the environment by the sides of the microchannel are neglected as the reactor can be considered well insulated.

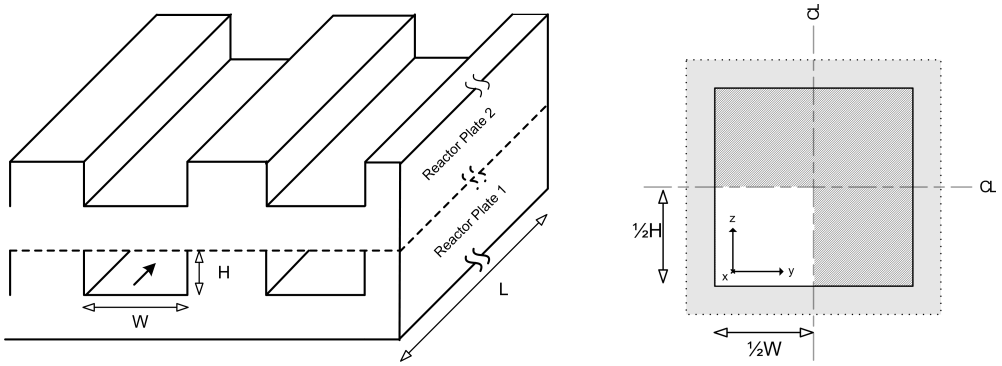

(a) Microchannel configuration (b) Symmetry considerations

Figure 4.1: Schematic diagram of the microchannel and symmetry simplifications

Continuum flow The flow in the channel is considered to be in the continuum flow regime, not molecular flow. This is because the calculated Knudsen number falls below the 0.1 threshold. A detailed analysis of the Knudsen number regime is presented in Appendix B.1.

No-slip boundary condition The no-slip and zero temperature-jump conditions hold as the Knudsen number falls below the 0.001 threshold. A detailed analysis of the Knudsen number regime is presented in Appendix B.1.

Laminar flow The Reynolds number falls below the $Re = 2100$ threshold for turbulent flow.

Unidirectional flow Bulk flow due to viscous effects are neglected in the perpendicular directions. This, however does not exclude the development of a net flux (and hence bulk velocity) due to Maxwell-Stefan effects.

Constant pressure The pressure drop in a microchannel is calculated to be in the order $10\,mbar$ (Kolb et al., 2005), therefore pressure is held constant.

Ideal gas law holds (low pressure) The WGS reaction is conducted in gas phase at pressures of $3 - 5\,bar$, the pressure range of a fuel processor (Schuurman et al., 2005). At these moderate pressures the ideal gas law is applicable.

No homogeneous reactions The high catalyst surface area to volume ratio suppresses the effect of homogeneous reactions (Kolb & Hessel, 2004).

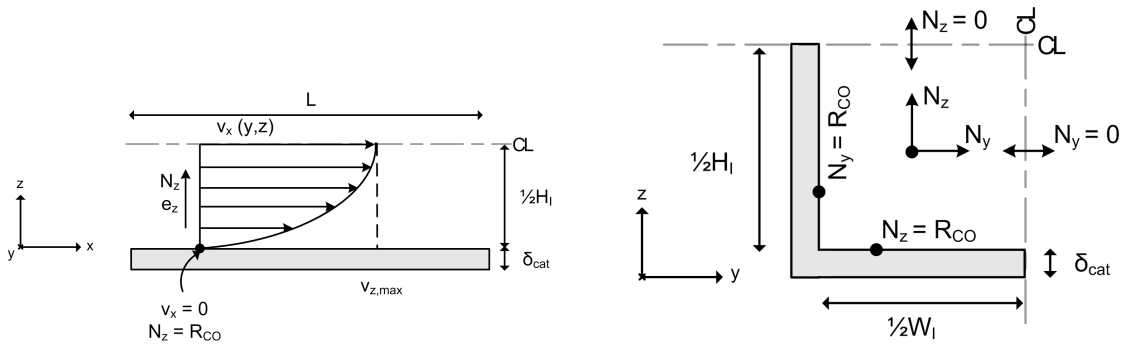

(a) x-z Plane (b) y-z plane

Figure 4.2: Schematic diagram indicating mass and heat transfer phenomena and the axial laminar flow pattern.

Uniform catalyst layer thickness Constant catalyst layer thickness along reactor length

Negligible internal transport limitations Internal mass and heat transport limitations have been found to be negligible in a previous study (Parak et al., 2009). Furthermore, the Weitz-Prater modulus is calculated for different catalyst layer thicknesses and reaction rates and is found to be below the $M_w < 0.15$ threshold for $\eta_{int} \longrightarrow 1$ or negligible internal transport limitations as in Section 2.4.3. The calculations are shown in Appendix B.2.

Negligible Dufour and Soret effects The coupling of mass and heat transport is neglected as the said high rates of mass and heat transport prevent substantial gradients from forming.

4.1.3 Problem statement

A schematic diagram of the phenomena in the system is presented in Figure 4.2. The modelling problem considers flux in three dimensions through a rectangular duct with heterogeneous reaction on catalyst-coated walls. The axial flux is dominated by bulk flow in the laminar flow regime. Mass and heat flux in both perpendicular directions are driven by the WGS reaction. The mass flux is described by the Maxwell-Stefan equations and the heat flux by molar convection and conduction.

Table 4.1: Summary of model variables

Variable, ϕ	Symbol	Nr balances
Axial velocity	v_x	1
Species mole fractions	u_i	5
Concentration	c_t	1
Temperature	T	1
Species molar fluxes, y	$N_{i,y}$	5
Species molar flux, z	$N_{i,z}$	5
		18

4.2 Model variables

The model problem statement leads to the allocation of model variables and so equations to form a fully specified set. The model solution variables, ϕ include 5 individual species mole fractions, y and z-directional molar fluxes, total concentration and temperature. These are presented in Table 4.1. The corresponding balance equations are in the following subsections.

4.3 Axial velocity

The laminar axial profile can be given by the solution of the momentum balance in three equivalent forms (1) the numerical solution over rectangular co-ordinates, (2) the analytical solution by Fourier series over rectangular co-ordinates and (3) the analytical solution over cylindrical co-ordinates. Each will be individually solved and solutions will be compared.

4.3.1 Numerical solution

The bulk axial velocity profile is given by the solution of the x-directional momentum balance. This is given for an incompressible, isothermal fluid with constant pressure gradient by:

$$\rho\frac{\partial v_x}{\partial t} = \mu\frac{\partial^2 v_x}{\partial y^2} + \mu\frac{\partial^2 v_x}{\partial z^2} + \frac{P_0 - P_L}{L} \tag{4.1}$$

with $v_x|_{y=0} = 0$ and $v_x|_{z=0} = 0$ no-slip boundary conditions at all walls and $\frac{\partial v_x}{\partial y}|_{y=1/2W_I} = 0$ and $\frac{\partial v_x}{\partial z}|_{z=1/2H_I} = 0$ at the channel center. This is solved as a reference solution using

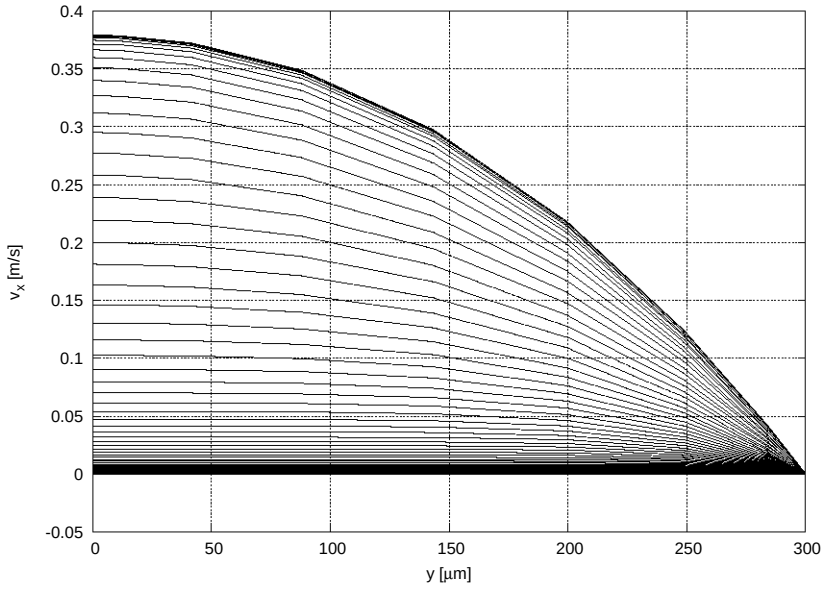

Figure 4.3: Non-steady state development of laminar velocity profile.

orthogonal collocation. The solution is solved in non-steady state via an arbitrary center velocity increase rate defined by the fluid density, ρ. The convergence to steady state is shown in Figure 4.3 and the final solution is shown in Figure 4.4.

4.3.2 Analytical solution - rectangular

The analytical solution given in Equation 2.28 is computed and shown in Figure 4.5b. The same channel conditions are used as in the numerical solution and the mesh size of $[n_y, n_z] = [21, 21]$ is taken as the *interpolated* numerical solution size for purposes of comparison. The infinite sum in Equation 2.28 is allowed to converge to a value of 1.043×10^{-13} within a final summation index of $n, m = 4001$. This is shown in Figure 4.5a.

4.3.3 Analytical solution - cylindrical

The axial velocity is given by the parabolic approximation of laminar flow (Bird et al., 2002). The conventional parabolic profile in Equation 2.22 is augmented for 3 dimensions and rectangular co-ordinates by the substitution of the $\left[1 - \left(\frac{r}{R}\right)^2\right]$ term for the $\left[1 - \left(\frac{y}{W}\right)^2\right]\left[1 - \left(\frac{z}{H}\right)^2\right]$ term. The increase in velocity due to an increase in temperature along the reactor is given by the ideal gas law term $\frac{T}{T_0}$ in the case of equimolar reaction and constant cross-sectional duct (Fogler, 2006). This gives equation 4.2.

$$v_x(y,z) = 2v_{x,avg}\left(\frac{T(y,z)}{T_0}\right)\left[1 - \left(\frac{y}{W}\right)^2\right]\left[1 - \left(\frac{z}{H}\right)^2\right] \tag{4.2}$$

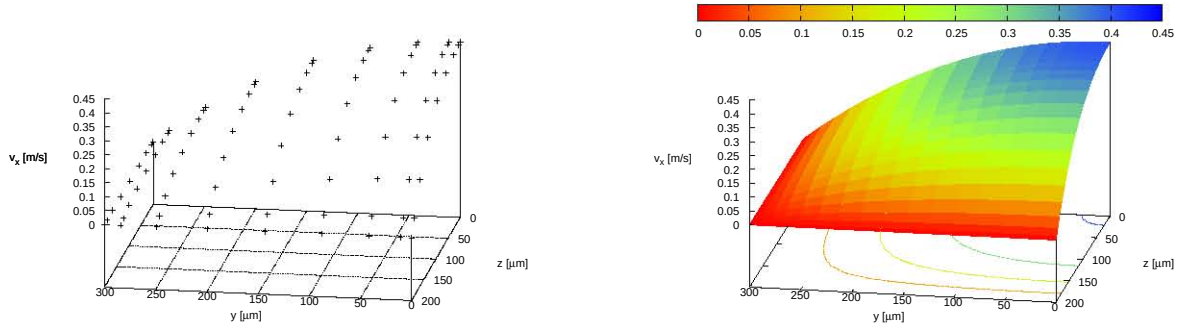

(a) Collocation solution (b) Interpolated solution

Figure 4.4: Steady state solution of velocity profile over rectangular duct. This is carried out over a $[n_y, n_z] = [9, 9]$ mesh interpolated onto a $[n_y, n_z] = [21, 21]$ mesh with $P_0 = 101325\,\text{Pa}$, $P_L = 101300\,\text{Pa}$, $\mu = 1.0 \times 10^{-5}\,\text{kg/m.s}$ and $(L, W, H) = (10cm, 600\,\mu\text{m}, 400\,\mu\text{m})$.

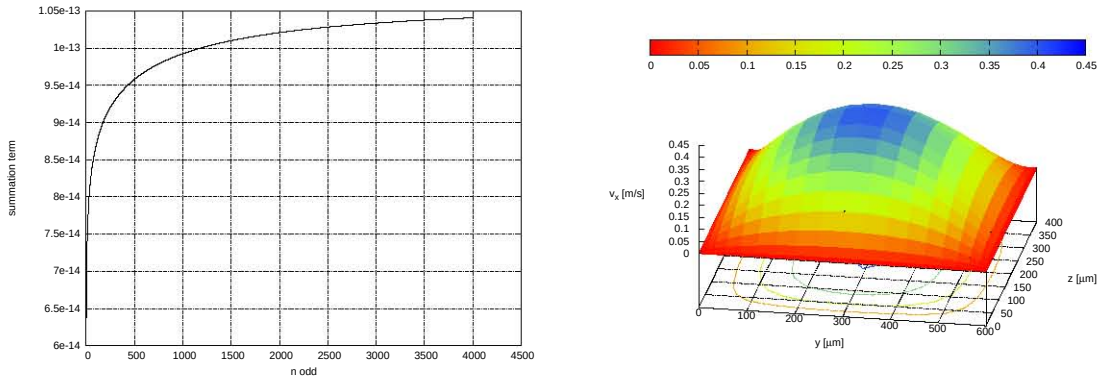

(a) Convergence of summation (b) Full duct solution

Figure 4.5: Analytical solution of velocity profile (Spiga & Morini 1994). This is carried out over a $[n_y, n_z] = [21, 21]$ mesh with $P_0 = 101325\,\text{Pa}$, $P_L = 101300\,\text{Pa}$, $\mu = 1.0 \times 10^{-5}\,\text{kg/m.s}$ and $(L, W, H) = (10\text{cm}, 600\,\mu\text{m}, 400\,\mu\text{m})$.

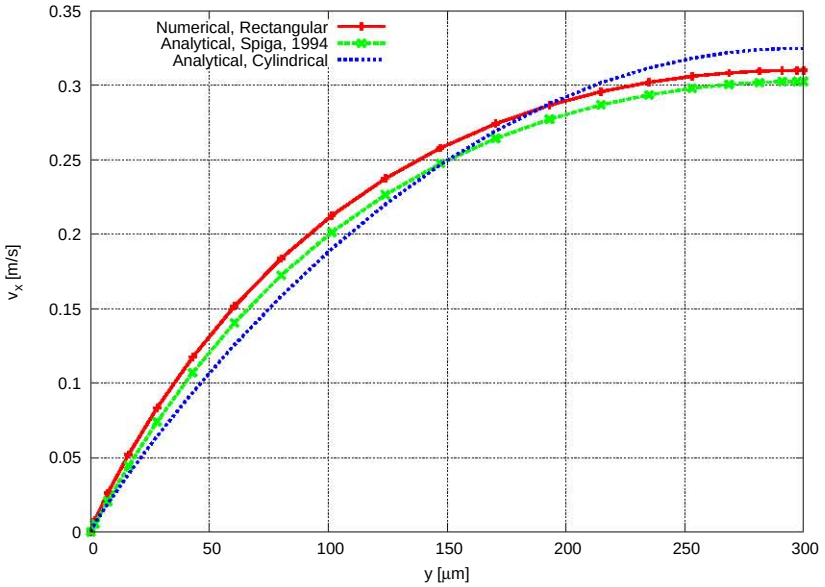

Figure 4.6: Comparison of numerical and analytical velocity profile solutions.

4.3.4 Comparison of solutions

The above three solutions are compared in Figure 4.6. Both solutions in rectangular co-ordinates lie relatively close to each other, however the difference lies in the solution times. The numerical solution solves, for a $[21, 21]$ mesh in $\sim 0.112\,\mathrm{s}$, while the analytical solves in $\sim 280\,\mathrm{s}$. This computational expense eliminates the analytical solution for use in the model equation set.

The solution in cylindrical co-ordinates does deviate slightly from the rectangular ones. In contrast to the numerical solution which requires the solution of a non-steady state PDE it provides a stable function that can be easily evaluated as a function of temperature. The analytical solution in Equation 4.2 is therefore used in the model equation set.

4.4 Species balances

Individual species balances for reactive components in the center domain are given by equation 4.3

$$\frac{\partial\left(\chi_i c_t\right)}{\partial t} = -\frac{\partial\left[\chi_i c_t v_x\right]}{\partial x} - \frac{\partial N_{y,i}}{\partial y} - \frac{\partial N_{z,i}}{\partial z} \tag{4.3}$$

for $i = 1, ..., c-1$.

The dependent species is chosen as the inert N_2 and is given by the physical constraint in Equation 4.4. The reason for this choice is explained in the examination of the Maxwell-Stefan flux expressions below.

$$\sum_{i=1}^{c} \chi_i = 1 \tag{4.4}$$

4.5 Maxwell-Stefan flux expressions

The Maxwell-Stefan equations are used to determine the perpendicular y and z flux densities. As discussed in Section 2.5.1 these are preferred to the Fickian form of the flux equations as they consider molecular motion due to binary species interactions as opposed to the species-mixture interactions in Fick's Law (Taylor & Krishna, 1993). This means that binary diffusivities $D_{i,j}$ can be used rather than the often inaccurate mixture diffusivities $D_{i,m}$. A further advantage is that the Maxwell-Stefan equations account for the momentum transfer from heavier to lighter species allowing species to move against their concentration gradients. This effect may be present in the WGS system because of the high molecular weight difference between H_2 and CO, CO_2. The flux densities in the y-direction, $N_{y,i}$ are treated in full here and those in the z-direction, $N_{z,i}$ are treated briefly thereafter.

4.5.1 The y-directional flux densities

Given the species composition in the channel, the flux densities, $N_{y,i}$ are given by the ideal gas, constant pressure Maxwell-Stefan equation 4.5 (Taylor & Krishna, 1993).

$$N_{y,i} = c_t \sum_{j=1}^{c-1} D_{i,j}^{eff} \frac{d\chi_i}{dy} \tag{4.5}$$

for $i = 1, ..., c-1$.

The multicomponent Maxwell-Stefan equation provides $c-1$ independent equations. A physical constraint is needed and its form is based on the physical situation. There are three of these that are typically encountered, that for open systems, closed systems and the Stefan tube. These are presented in Section 2.5.5. The most applicable to the model situation is that of the closed system.

The closed system The physical system considered is that of flux along a single line in the y-direction with zero net flux at the end points. The zero flux at the reaction wall is due to the equimolar reaction, and at the channel center is due to the channel symmetry condition shown in Equation 4.8. The presence of no flux across the flux domain boundaries thereby allows the analogy of a closed system. The closed system

condition further requires no net flux of species *within* the flux domain such that there is no net velocity. This in turn ensures that there is no change in pressure and is thus consistent with the initial assumption. The form of the effective diffusivities in Equation 2.62 for $\nu_i = 1$ is

$$D^{eff} = B_{eff}^{-1} \tag{4.6}$$

$$B_{i,j,eff} = \begin{cases} \frac{\chi_i}{D_{i,c}} + \sum_{\substack{k=1 \\ k \neq i}}^{c} \frac{\chi_k}{D_{i,k}} & \text{for i=j} \\ \chi_i \left(\frac{1}{D_{i,c}} + \frac{1}{D_{i,j}} \right) & \text{for i}\neq\text{j} \end{cases} \tag{4.7}$$

Boundary conditions

The boundary conditions in Equation 4.8 apply to equation 4.5 in the calculation of all species' flux densities.

$$\begin{array}{cccc} x = 0 & N_{y,i} = 0 & & \\ y = 0 & N_{y,i} = -\nu_i r_{CO} A c & & N_{y,I} = 0 \\ y = {}^1\!/_2 W_I & N_{y,i} = 0 & & \\ z = 0 & N_{y,i} = 0 & & \\ z = {}^1\!/_2 H_I & N_{y,i} = c_t \sum_{j=1}^{c-1} D_{i,j}^{eff} \frac{\partial \chi_j}{\partial y} & & \end{array} \tag{4.8}$$

Note that the flux density of the inert is always kept as $N_{y,I} = 0$ as explained above. The inlet $N_{y,i}$ is taken as zero as the perpendicular composition profiles are kept flat, resulting in a zero potential for diffusion. The flux density gradients across the $y = {}^1\!/_2 W_I$ boundary is kept zero to maintain the flux symmetry in the reactor center, shown in Figure 4.1. The flux at the wall is given by the rate of consumption or generation of reactive species.

4.5.2 The z-directional flux densities

Given the species concentrations in the channel, the flux densities, $N_{z,i}$ are given by the inverted Maxwell-Stefan Equation 4.9.

$$N_{z,i} = c_t \sum_{j=1}^{c-1} D_{i,j}^{eff} \frac{\partial \chi_j}{\partial z} \tag{4.9}$$

for $i = 1, ..., c-1$. The flux density of the inert, I is given by $N_{z,I} = 0$.

Boundary conditions

The boundary conditions for the z-directional fluxes are the y, z transpose of those for the y-directional fluxes. These are shown in equation 4.10. The motivation for these choices are similar to those above.

$$\begin{array}{cccc} x = 0 & N_{z,i} = 0 & & \\ y = 0 & N_{z,i} = 0 & & \\ y = {}^1\!/_2 W_I & N_{z,i} = c_t \sum_{j=1}^{c-1} D_{i,j}^{eff} \frac{\partial \chi_j}{\partial z} & & \\ z = 0 & N_{z,i} = -\nu_i r_{CO} A c & N_{z,I} = 0 & \\ z = {}^1\!/_2 H_I & N_{z,i} = 0 & & \end{array} \tag{4.10}$$

The model could be formulated to take advantage of this y, z symmetry for computational efficiency by equating the *normalised* z-component flux matrix in the y, z plane to the transpose of the *normalised* y-component flux matrix in the same plane. This is not done to ensure that the model is generalised for different catalyst loadings on different surfaces which is sometimes found in the catalyst loading procedure.

4.5.3 Species Balances boundary conditions

The boundary conditions of the species balances are presented in equation 4.14.

$$\begin{array}{cc} x = 0 & \chi_i = \chi_{i,0}(t) \\ y = 0 & \frac{\partial \chi_i}{\partial y} \mid_{y=0} = \sum_{\substack{j=1 \\ j \neq i}}^{c} \frac{\chi_i N_{y,j} - \chi_l N_{y,i}}{c_t D_{i,l}} \\ y = {}^1\!/_2 W_I & \frac{\partial \chi_i}{\partial y} \mid_{y={}^1\!/_2 W_I} = 0 \\ z = 0 & \frac{\partial \chi_i}{\partial z} \mid_{z=0} = \sum_{\substack{j=1 \\ j \neq i}}^{c} \frac{\chi_i N_{z,j} - \chi_l N_{z,i}}{c_t D_{i,l}} \\ z = {}^1\!/_2 H_I & \frac{\partial \chi_i}{\partial z} \mid_{z={}^1\!/_2 H_I} = 0 \end{array} \tag{4.11}$$

At the channel center point$(y, z) = ({}^1\!/_2 W_I, {}^1\!/_2 H_I)$ a single boundary condition is chosen of $\frac{\partial \chi_i}{\partial y}|_{y={}^1\!/_2 W_I} = 0$ or $\frac{\partial \chi_i}{\partial z}|_{z={}^1\!/_2 H_I} = 0$.

Dankwerts' boundary conditions

The boundary condition at $x = 0$ is taken to be independent of dispersion in the reactor as required by the Dankwerts' boundary conditions . This condition for molar transport is given by Equation 4.12.

$$u_{i,0}(t) = u_i - \frac{1}{Pe} \frac{d\chi_i}{dx} \tag{4.12}$$

The Peclet number $Pe = v_x L/D_{AB}$ is the ratio between convective and diffusive mass transport. For microchannel reactor systems operating at high linear velocities Pe is of order 10^4. The third term in Equation 4.12 carries the inverse of Pe which makes any back-mixing negligible. The inlet boundary condition reduces to that of equation 4.14. The time dependence of $\chi_{i,0}$ is discussed in the next section.

The compositions χ_i at the reactive surfaces, $y = 0$ and $z = 0$ are given by the Maxwell-Stefan equation as all the flux density gradients are independently known here. The compositions on the channel center are given by the Maxwell-Stefan equations with the zero flux condition imposed. This leads to the set of continuity of composition expressions shown.

4.6 Overall materials balance

The overall materials balance is used to solve for concentration changes in the channel. This is given by equation 4.13.

$$\frac{\partial c_t}{\partial t} = -\frac{\partial \left(c_t v_x\right)}{\partial x} - \frac{\partial N_{y,t}}{\partial y} - \frac{\partial N_{z,t}}{\partial z} \tag{4.13}$$

where the total fluxes are given by $\mathbf{N}_t = \sum_{i=1}^{c} \mathbf{N}_i$.

The temperature boundary conditions are shown in Equation 4.14. At the reactor inlet, $x = 0$ the concentration is set to the steady state inlet concentration. The boundary conditions on the reaction surfaces is given by the ideal gas equation.

$$\begin{array}{cc} x = 0 & c_t = c_{t,0} \\ y = 0 & c_t = {}^{P}/_{RT} \\ y = {}^{1}/_{2}W_I & \frac{\partial c_t}{\partial y} \mid_{y={}^{1}/_{2}W_I} = 0 \\ z = 0 & c_t = {}^{P}/_{RT} \\ z = {}^{1}/_{2}H_I & \frac{\partial c_t}{\partial z} \mid_{z={}^{1}/_{2}H_I} = 0 \end{array} \tag{4.14}$$

4.7 Energy balance

The energy balance over the main domain and symmetry points is given in vector notation by Equation 4.15.

$$\sum_{i=1}^{c} c_t \chi_i c_{p,i} \frac{\partial T}{\partial t} = -\sum_{i=1}^{c} c_{p,i} \left(\nabla T\right) \cdot \mathbf{N} + \lambda \left(\nabla^2 \cdot T\right) \tag{4.15}$$

This considers energy flux by conduction and convection. For simplicity, the species heat capacity $c_{p,i}$ and thermal conductivity λ are removed from the differential terms. The axial heat conduction term is included for consistency with the perpendicular directions. Even if it may not be significant in this direction, it may be significant compared to the perpendicular terms.

The temperature boundary conditions are shown in Equation 4.16.

$$\begin{array}{cc} x = 0 & T = T_0 \\ y = 0 & \sum_{i=1}^{c} N_{i,y} \overline{H}_i - \lambda \frac{\partial T}{\partial y} = Q_{loss} \\ y = {}^1\!/_2 W_I & \frac{\partial T}{\partial y} \mid_{y={}^1\!/_2 W_I} = 0 \\ z = 0 & \sum_{i=1}^{c} N_{i,z} \overline{H}_i - \lambda \frac{\partial T}{\partial z} = Q_{loss} \\ z = {}^1\!/_2 H_I & \frac{\partial T}{\partial z} \mid_{z={}^1\!/_2 H_I} = 0 \end{array} \tag{4.16}$$

At the reactor inlet, $x = 0$ the temperature is set to the steady state inlet temperature. The heat release due to reaction is taken into account at the catalyst surfaces $y = W$ and $z = H$ by the $\sum_{i=1}^{c} N_i \overline{H}_i$ terms. This simulates the change in enthalpy of the species arriving at the catalyst surface to the species leaving and represents the heat of reaction ΔH_{rxn}. In the case of isothermal operation, the Q_{loss} term is set to remove the heat released by reaction, or more explicitly

$$Q_{loss} = \left(-\Delta \bar{H}_{rxn}\right) r_{CO} A c \tag{4.17}$$

At the channel center point,$(y, z) = ({}^1\!/_2 W_I, {}^1\!/_2 H_I)$ a single boundary condition is chosen of $\frac{\partial T}{\partial y}|_{y={}^1\!/_2 W_I} = 0$ or $\frac{\partial T}{\partial z}|_{z={}^1\!/_2 H_I} = 0$.

4.8 Reaction kinetics

An Arrhenius reaction rate law, equation 4.18 is used (Germani et al., 2005).

$$R_{CO} = \rho_{cat} k_0 e^{\left\{\frac{-E_a}{RT}\right\}} P_{CO}^{0.13} P_{H_2O}^{0.49} P_{H_2}^{-0.45} P_{CO_2}^{-0.12} \left(1 - \beta\right) \tag{4.18}$$

with pressure P_i in [bar], k_0 in ${}^{\text{mol}}\!/_{\text{s.kg}_{\text{cat}}.\text{bar}^{0.05}}$ and E_a in ${}^{\text{J}}\!/_{\text{mol}}$. A reduced order version of this expression may be needed for simpler model interpretation. The first order equation with respect to concentration of CO is given by

$$R_{CO} = \rho_{cat} k_0 e^{\left\{\frac{-E_a}{RT}\right\}} c_t \chi_{CO} (1 - \beta) \tag{4.19}$$

where k_0 the first order rate constant in $^{\mathrm{m}^3}/_{\mathrm{s.kg_{cat}}}$.

Both reactions are limited by thermodynamic equilibrium defined by equation 4.20 (Kolb et al., 2005). The β equilibrium limitation is defined by Equation 4.21.

$$K_{eq} = e^{\left\{\frac{4577.8}{T[K]} - 4.33\right\}} \tag{4.20}$$

$$\beta = \frac{P_{H_2} P_{CO_2}}{K_{eq} P_{CO} P_{H_2O}} \tag{4.21}$$

4.9 Other definitions

4.9.1 Conversion

Reactor conversion is defined with respect to the CO flow rate as

$$X_{CO} = \frac{F_{CO,in} - F_{CO,out}}{F_{CO,in}} \tag{4.22}$$

$$= \frac{v_{x,0} XSA_i c_{t,0} \chi_{CO,0} - v_{x,avg} XSA_I c_{t,avg} \chi_{CO,avg}}{v_{x,0} XSA_i c_{t,0} \chi_{CO,0}} \tag{4.23}$$

4.9.2 Effectiveness factor

For the above modelling approach the external effectiveness factor is a measurement of the effect of radial mass and heat transfer resistances. The overall external effectiveness factor combines the effect of mass and heat transfer limitations via the rate law. This compares the rate of reaction at the reaction wall to the rate at average conditions across the channel width and is shown below.

$$\eta_r = \frac{r_i(\chi_i c_t, T)}{r_i(\chi_{i,avg} c_{t,avg}, T_{avg})} \tag{4.24}$$

These effectiveness factors have been decoupled to examine the effect of mass and heat transfer limitations separately by using concentration and temperature ratios. These are defined as η_c and η_T respectively by

$$\eta_c = \frac{\chi_i c_{t,wall}}{\chi_i c_{t,avg}} \tag{4.25}$$

for $i = 1, ..., c$ and

$$\eta_T = \frac{T|_{wall}}{T|_{avg}} \tag{4.26}$$

Average quantities are calculated by integration across the channel. This is done numerically and the methodology is provided in Section 5.4.5.

4.10 Model limitations

The model assumptions and problem statement lead to a number of implicit model limitations.

- The model assumes two levels of perpendicular symmetry and has two dimensions in that symmetry space. This means that boundary conditions that are asymmetric in more than one plane cannot be accounted for (e.g. a heat source/sink on a *single* channel outer face, or a different catalyst loading on a *single* channel wall).
- The model assumes unidirectional flow. This means that it does not account for radial velocity gradients that may be generated as a result of forced convection by heat flow or differential pressures. The latter case is consistent with the next limitation.
- The model assumes constant pressure. This limits the model's applicability to equimolar reactions where there is no net increase or decrease of pressure either in the perpendicular or axial directions. It can also not predict the effect of an significant increase in the channel length compared to its hydraulic diameter.

Chapter 5

Solution Method

The model equations result in a set of coupled partial differential and algebraic equations. These are solved using the method of global orthogonal collocation which uses a polynomial as an approximation to the differential equation solution. This method is tested against different problems in literature and the results are reported. This chapter then describes the solution algorithm implemented for the solution of the model equations developed in the Chapter 4.

5.1 Test problems

Two problems are solved, the first of which is a 1-dimensional film model. This requires the solution of the Maxwell-Stefan equations and is thus a test of the developed OC solver's ability to handle the non-linearity that this set provides. The second is a 2-dimensional reaction diffusion problem on an autocatalytic reaction. This leads to a oscillating solution profile with steep gradients and is thus a test of the OC solver's stability and robustness in a multidimensional domain.

5.1.1 Film model

The film model of mass transport is described and solved in the literature (Newman 2009; Taylor & Krishna 1993). The problem considered is the evaporation of methanol and acetone into a stagnant layer of air under isobaric, isothermal and steady state conditions. The physical situation is shown in Figure 5.1 and the components are numbered as follows:

(1) acetone; (2) methanol; (3) air

The test conditions are reported in Table 5.1.

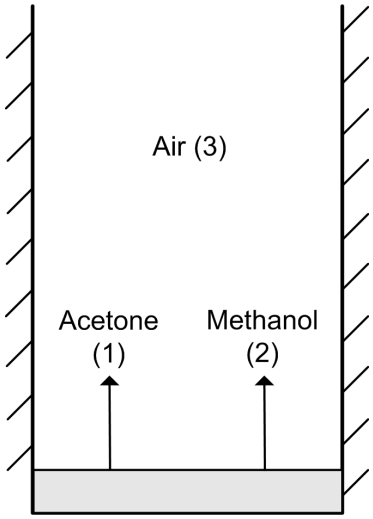

Figure 5.1: Evaporation of methanol and acetone into a stagnant layer of air adapted from (Newman 2009). The infinite medium of air is defined to maintain the $y \to \infty$ boundary condition.

Table 5.1: Conditions and parameters used in the film evaporation problem. Adapted from (Newman 2009)

Parameter	1 Acetone	2 Methanol	3 Air
M_i ($^{\mathrm{g}}/_{\mathrm{mol}}$)	58.08	32.04	29
$\chi_{i,0}$	0.319	0.528	0.153
$\chi_{i,\infty}$	0	0	1
$D_{1,0}, D_{20}, D_{12}(^{\mathrm{m}^2}/_{\mathrm{s}})$	1.372×10^{-5}	1.991×10^{-5}	8.48×10^{-5}
T (K)	328.5		
P (bar)	0.9935		

The materials balance is reduced to the form

$$\frac{\partial N_{i,y}}{\partial y} = 0 \tag{5.1}$$

for components $i = 1, ..., c$. This means that each component flux takes on a constant value across the stagnant film. The Maxwell-Stefan equation is used to solve for the component mole fractions in the film and takes the form

$$\frac{\partial \chi_i}{\partial y} = \sum_{\substack{j=1 \\ j \neq i}}^{c} \frac{\chi_i N_{y,j} - \chi_j N_{y,i}}{c_t D_{i,j}} \tag{5.2}$$

for $i = 1, ..., c-1$. The additional mole fraction is given by the physical constraint $\sum_{i=1}^{c} \chi_i = 1$. The boundary condition at the evaporation surface is given by

$$\chi_{1,0} = 0.319, \quad \chi_{2,0} = 0.528, \quad N_{3,0} = 0 \qquad \text{at y=0} \tag{5.3}$$

while the boundary condition at the film limit is given by

$$\chi_{1,\infty} = 0, \quad \chi_{2,\infty} = 0, \qquad \text{at } y \to \infty \tag{5.4}$$

The mole fractions are fully specified and the remaining two unknowns are the fluxes $N_{y,1}$ and $N_{y,2}$. These are specified by applying the Maxwell-Stefan equation at $y = 0$ for $i = 1, ..., c-1$.

The set of equations is solved numerically using orthogonal collocation. This is done by reducing the $\frac{\partial u_i}{\partial y}$ differential terms into linear combinations using

$$\frac{\partial \chi_i}{\partial Y} = \sum_{j=1}^{n+2} A_{i,j} \chi_j \tag{5.5}$$

where n specifies the number of collocation points and A the $(n+2) \times (n+2)$ matrix of the first derivatives of the Lagrange polynomial basis set.

Using five interior collocation points, n the reported concentration profiles (Newman 2009; Taylor & Krishna 1993) are reproduced. The calculated flux values are

$$\begin{aligned} N_1 &= 1.782 \times 10^{-3} \\ N_2 &= 3.126 \times 10^{-3} \end{aligned}$$

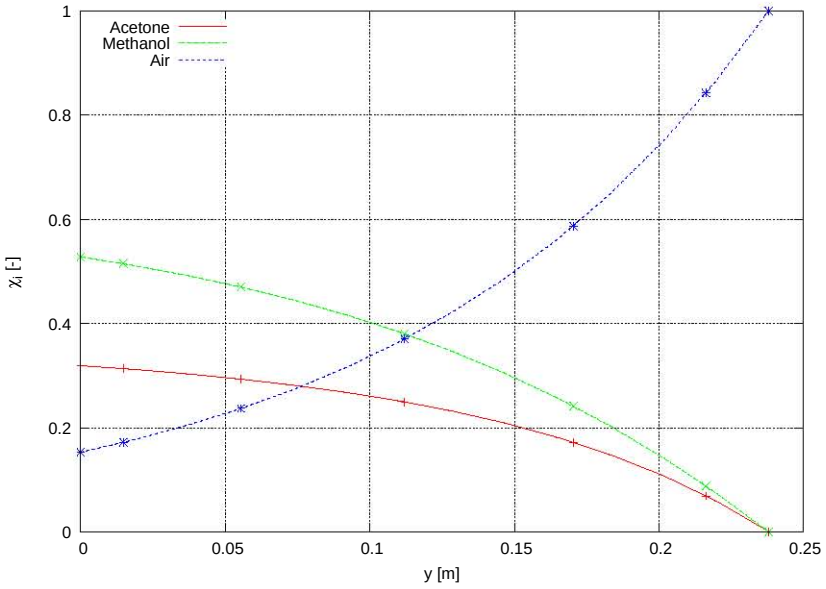

Figure 5.2: Composition profiles of acetone, methanol and air in a stagnant film.

This test validates both the use and coded application of orthogonal collocation to solve equation sets involving the Maxwell-Stefan equations.

5.1.2 Autocatalytic reaction-diffusion model

A series of multidimensional reaction-diffusion problems are solved in the recent literature (Revelli & Ridolfi 2008). One of these problems is a severe test of both the solution method and code as it involves an oscillatory series of auto-catalytic trimolecular reactions. This system's transient behaviour is described by the following species balance

$$\frac{\partial \chi_1}{\partial t} = \kappa\left(a - \chi_1 + \chi_1\chi_2^2\right) + \epsilon\left(\frac{\partial^2 \chi_1}{\partial y^2} + \frac{\partial^2 \chi_1}{\partial z^2}\right) \tag{5.6}$$

$$\frac{\partial \chi_2}{\partial t} = \kappa\left(b - \chi_1^2\chi_2\right) + \left(\frac{\partial^2 \chi_2}{\partial y^2} + \frac{\partial^2 \chi_2}{\partial z^2}\right) \tag{5.7}$$

where χ_1 and χ_2 are the mole fractions of self-activating and self inhibiting chemical species and κ,a,b, and ϵ are dimensionless parameters. This set of parameters allows small perturbations in concentration to be amplified and the initial condition gives the concentration surface a basis from which to interact and spread with time. This feature of the model provides the stiffness in the solution and with that a severe test for the robustness of the collocation solution method. The initial conditions are given by

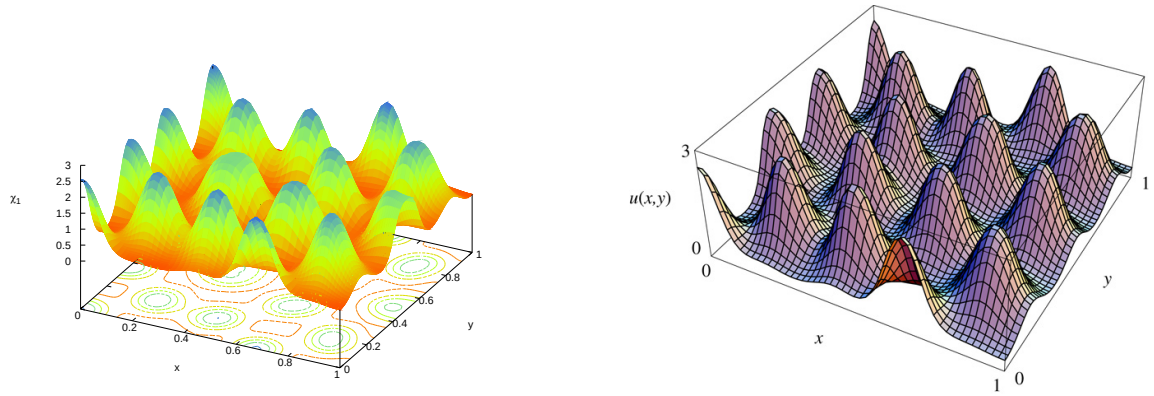

(a) Solution by DDASAC.for

(b) Solution by (Revelli & Ridolfi 2008)

Figure 5.3: Comparison of solution of auto-catalytic reaction - diffusion problem to literature (Revelli & Ridolfi 2008) for species 1 at $t = 1$.

$$\chi_1(0,x,y) = a + b + \frac{1}{1000} e^{-100\left[\left(x-\frac{1}{3}\right)^2+\left(y-\frac{1}{2}\right)^2\right]} \tag{5.8}$$

$$\chi_2(0,x,y) = \frac{b}{(a+b)^2} \tag{5.9}$$

The Neumann boundary conditions are applied at the $x = \{0,1\}$ and $y = \{0,1\}$ for both χ_1 and χ_2. The parameters tale the values $\kappa = 100$, $a = 0.1648$, $b = 0.8352$, and $\epsilon = 0.05$.

The system of equations is solved using 49 interior collocation points and Lagrange polynomials as the collocation basis function. The second derivatives in each of the x and y-directions are approximated by

$$\frac{\partial^2 \chi_i}{\partial Y^2} = \sum_{j=1}^{n+2} B_{i,j}\chi_j \tag{5.10}$$

The resulting mixed set of ODEs and linear equations are solved using the DDASAC.for (Petzold, 1982) DAE software. The solution at $t = 1$ is presented for χ_1 in Figure 5.3 and χ_2 in Figure 5.4. The both solutions compare favourably with the solution obtained by the same method in (Revelli & Ridolfi 2008). This exercise serves as a validation of the robustness of the solution method and the stability of the developed solution code.

5.2 Model solution variables and equations

As the multidimensional collocation solution procedure is suitably tested for convergence and stability, attention needs to be turned to the application of collocation to the mi-

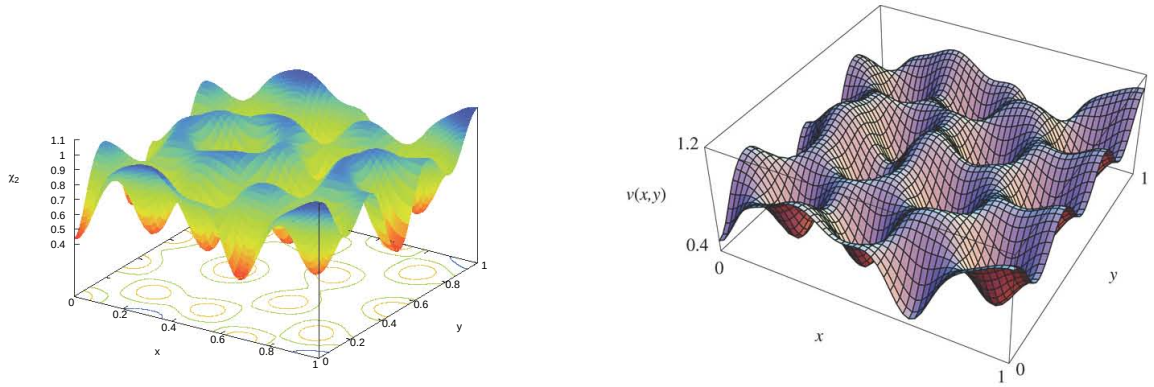

(a) Solution by DDASAC.for

(b) Solution by (Revelli & Ridolfi 2008)

Figure 5.4: Comparison of solution of auto-catalytic reaction - diffusion problem to literature (Revelli & Ridolfi 2008) for species 2 at $t = 1$.

crochannel model equations presented in Chapter 4.

5.2.1 Solution equations

The method is applied to all balance equations and boundary conditions above and is shown for bulk domain balances 4.3,4.5,4.13 and 4.15 in equations 5.11-5.14 as samples.

$$c_t \frac{\partial \chi_i}{\partial t} = -\frac{1}{L}\sum_{j=1}^{n_x} A^x_{i,j}\left(\chi_{i,,j} c_{t,j} v_{x,j}\right) - \frac{1}{W}\sum_{j=1}^{n_y} A^y_{i,j} N_{y,j} - \frac{1}{H}\sum_{j=1}^{n_z} A^z_{i,j} N_{z,j} \quad (5.11)$$

$$0 = \frac{1}{W}\sum_{j=1}^{n_y} A^y_{i,j}\chi_j - \sum_{\substack{j=1 \\ j\neq i}}^{c} \frac{\chi_i N_{y,j} - \chi_j N_{y,i}}{c_t D_{i,j}} \quad (5.12)$$

$$\frac{\partial c_t}{\partial t} = -\frac{1}{L}\sum_{j=1}^{n_x} A^x_{i,j}\left(c_t v_x\right) - \frac{1}{W}\sum_{j=1}^{n_y} A^y_{i,j} N_{y,t,j} - \frac{1}{H}\sum_{j=1}^{n_z} A^z_{i,j} N_{z,t,j} \quad (5.13)$$

$$\sum_{i=1}^{c} c_t \chi_i cp_i \frac{\partial T}{\partial t} = -\sum_{i=1}^{c} cp_i \left[\frac{N_{x,i}}{L}\sum_{j=1}^{n_x} A^x_{i,j} T_j + \frac{N_{y,i}}{W}\sum_{j=1}^{n_y} A^y_{i,j} T_j + \frac{N_{z,i}}{H}\sum_{j=1}^{n_z} A^z_{i,j} T_j\right] \quad (5.14)$$
$$+\lambda\left[\frac{1}{L^2}\sum_{j=1}^{n_x} B^x_{i,j} T_j + \frac{1}{W^2}\sum_{j=1}^{n_y} B^y_{i,j} T_j + \frac{1}{H^2}\sum_{j=1}^{n_z} B^z_{i,j} T_j\right]$$

This reduces the set of PDEs coupled with non-linear equations into a set of DAEs. The steady state equations are those in Equations 5.11-5.14 with the time derivatives on the left hand side set to zero. This leads to a set of simultaneous non-linear equations (NLEs). Both transient and steady state sets will be used in the solution algorithm.

Each variable in Table 4.1 is solved for at each solution point and is coupled to each other

solution point via the collocation expressions. This can lead to large systems of equations that expand rapidly with each change in mesh size. So a relatively fine mesh with size $(11, 5, 5)$ will require the solution of 4950 equations. The non-linearity provided by the reaction rate law and Maxwell-Stefan equations are sources of instability which require a numerical algorithm for a convergent solution. This is presented in Section 5.5.

5.2.2 Dependent variables

The number of simultaneous equations entered into DDASAC.for and HYBRD.for is reduced by designating certain variables as dependent. These are velocity v_x and molar fluxes $N_{y,i}$ and $N_{z,i}$. This reduces the number of simultaneous solution variables, ϕ from 18 to 7 in Table 4.1 for a 5 species system. The dependent variables are calculated using the input values of the remaining solution variables before determining the solution residuals.

As the calculated fluxes are not solved simultaneously with the remaining solution variables, ϕ the entire solution set is not solved simultaneously at each time step. This is rectified by allowing the reactor to run at steady state compositions for a time. This allows iterative simultaneous solution of the entire set of 18 equations in an updating procedure not unlike the Rachford-Rice updating procedure in VLE flash calculations.

Binary diffusivities, $D_{i,j}$ are calculated by the Fuller equation (Fuller et al., 1969) while the thermal diffusivity, λ is calculated by the Euken equation (Reid et al., 1987) and are updated in each function call. The diffusivities are further calculated for each solution point because of its composition and temperature dependency. The formulation of these equations are shown in Appendices C.2 and C.3 respectively.

5.3 User interaction

The model input and output structure is shown in Figure 5.5. Both input and output use modules to store their data. This ensures that the data is available to the user outside of the main call to the microchannel model. Each of the three stages in implementing the model is briefly discussed.

5.3.1 User input

The input structure is divided into three sections:

1. Reactor setup The reactor setup is specified in the module `reactordata.f90`. This module requires inputs for the reactor dimensions, initial conditions at $t = 0$, the equivalent inlet conditions at steady state, $t = t_e$ and the reaction stoichiometry and power rate law parameters. Where more sophisticated kinetic laws are required, the user can manually adapt the `rate` function in the `module_physical.f90` file. Two toggles are available for use. The mode of operation can either be specified as adiabatic or isothermal. Where intermediate heat removal schemes are needed (example a temperature profile) the user can manually edit the `Qloss` function in the `module_physical.f90` file. The physical constraint on fluxes described in Section 2.5.5 can also be chosen.

2. Problem size The problem size and numerical convergence parameters are specified in the `problemsize.f90` module. The number of inlet species is specified. The transient ramp-up time parameters are available including the α and γ parameters in Equation 5.16. The number of collocation points are specified for the transient and steady state problems, the latter as a vector of length number of remeshes. The size of the evenly spaced mesh for the final interpolated solution is also specified. A single toggle is available. This controls the level of plotted output required. When calling the model multiple times, it is necessary to turn this toggle off as the temporary data files overwrite each other. All solution information is available upon model exit and the user can plot as necessary.

3. Species data The species data is specified in the `speciesdata.f90` module and includes physical and thermodynamic properties. The form of the c_p coefficients should be consistent with the Fomate formula shown in Equation D.1.

5.3.2 Model call

The model is called with the command

```
CALL MICROCHANNEL(ExitConversion,ExitTemperature)
```

Two outputs are specified through the subroutine interface, the exit conversion and the exit temperature. These are outputted for convenience sake as they are necessary outputs when calling the model in a regression routine.

5.3.3 Model output

The model output is divided into two sections

Table 5.2: Summary of available solution variables and their corresponding mesh points. Array sizes are indicated in brackets below the variable names.

Data description	Variable symbol	Array name	Mesh name
Unsteady state data	$\phi(x, y, z, nbal, t)$	*utgrid* *(ndx,ndy,ndz,nbal,ntime+1)*	rootx, rooty, rootz (ndx),(ndy),(ndz)
Steady state data	$\phi(x, y, z, nbal)$	umesh (nintrpx,nintrpy,nintrpz,nbal)	meshx, meshy, meshz (nintrpx),(nintrpy),(nintrpz)
	$N_y(x, y, z, sp + 1)$ $N_z(x, y, z, sp + 1)$	nymesh, nzmesh (nintrpx,nintrpy,nintrpz,nsp+1)	
	$v_x(x, y, z, 1)$ $P(x, y, z, 1)$	vxmesh, pmesh (nintrpx,nintrpy,nintrpz,1)	
Interpolated data	$\phi(x, y, z, nbal)$	udata (ndatax,ndatay,ndataz,nbal)	datax, datay, dataz (ndatax),(ndatay),(ndataz)
	$N_y(x, y, z, sp + 1)^a$ $N_z(x, y, z, sp + 1)$	nydata, nzdata (ndatax,ndatay,ndataz,nsp+1)	
	$v_x(x, y, z, 1)$	vdata, pdata (ndatax,ndatay,ndataz,1)	
Average data	$\overline{\phi}(x, 1, 1, nbal)$ $\overline{v}_x(x, 1, 1, 1)$	uaverage, vxaverage (nintrpx,1,1,nbal),(nintrpx,1,1,1)	meshx(nintrpx)

[a] flux values availabe for each species + total flux

1. Solution structure Solution structure variables are available in the `collocationdata.f90` module. These include the collocation matricies A and B and the mesh point vectors individually in the x, y and z-directions.

2. Solution data Solution data is specified in the `solutiondata.f90` module. This includes the unsteady state data grid at all time steps. Steady state data is available for all solution variables ϕ as well as N_y, N_z, v_x and P on both the collocation mesh and the interpolation data mesh. All these solutions are over the single quadrant of the reactor described in Section 4.1.1. Average profiles are available for variables ϕ and v_x. The sizes of each of the solution variables is shown in Table 5.2.

5.4 Numerical algorithm

To ensure computational efficiency a custom FORTRAN collocation code is used. Convergence and stability are provided by a solution algorithm in the same language. The algorithm is shown in Figure 5.6 and described briefly below. All calculations are performed on a quad core Intel 2.66 GHz Core2 Processor with 8GB RAM available.

The transient problem is solved using DDASAC.for (Caracotsios & Stewart, 1996) as the

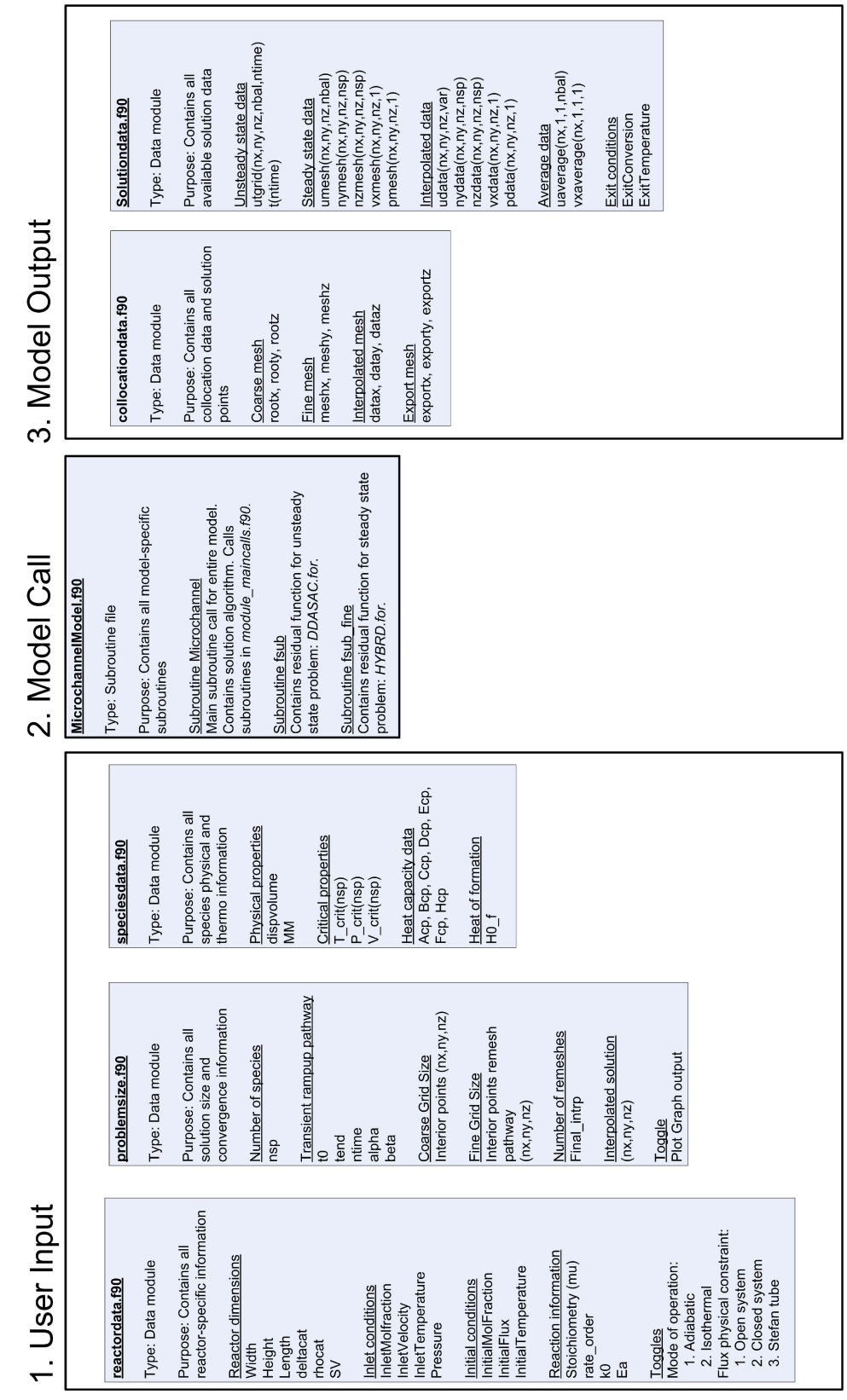

Figure 5.5: Schematic of user input parameters and storage structure

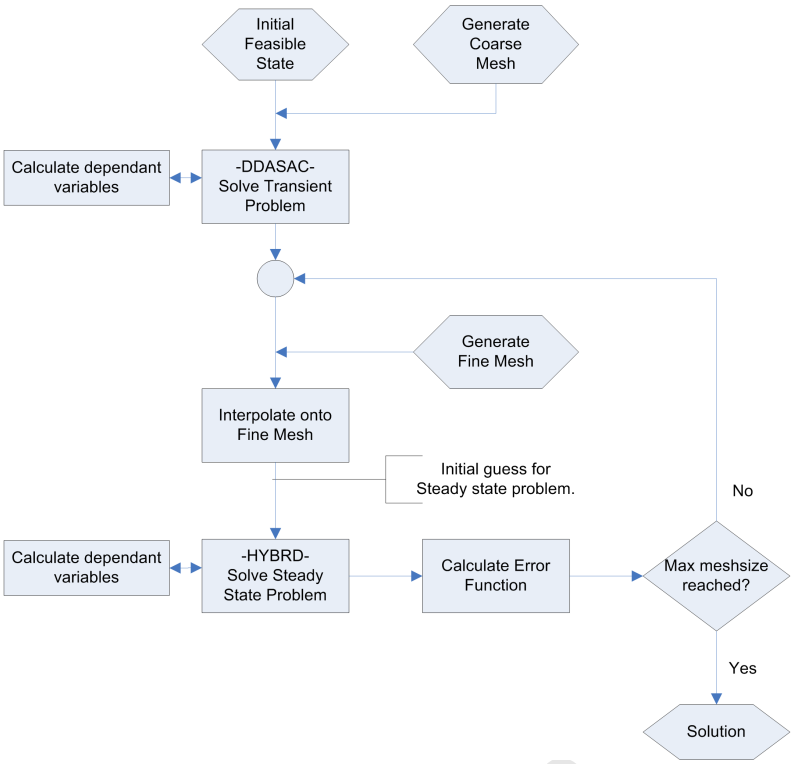

Figure 5.6: Numerical algorithm

DAE solver. `DDASAC.for` is based on the DASSL DAE solver package (Petzold, 1982). The initial condition provides a feasible but physically irrelevant solution. The transient solution is then solved on a coarse $(7, 3, 3)$ grid to provide a fast solution. This solution is then interpolated onto a finer mesh and is used as the initial condition to the steady state problem. This steady state problem is solved using the hybrid NLE solver `HYBRD.for` (Garbow et al., 1980). The steady state solution is then interpolated onto a finer grid to provide the initial guess for a new problem and a new solution is obtained. This iteration can be done until a mesh-free solution is obtained.

5.4.1 Grid generation

The solution grid is chosen as the roots of the Jacobi polynomials whose positions provide a partially optimised set for collocation (Rice & Do 1995). These are computed for $N+2$ points in each dimension meaning that both boundary conditions are considered. This gives a polynomial of the form $J^{(\alpha+1,\beta+1)}$ where $\alpha = 0$ and $\beta = \frac{ia+1}{2}$ with $ia = 0$ for planar geometry. A sample mesh is shown in Figure 5.7 for illustrative purposes. The subroutine `POINTS` performs this operation and is in the module_collocation.for module. This calls the Jacobi subroutine available in the `abwlib.for` file (Villadsen & Michelsen 1978).

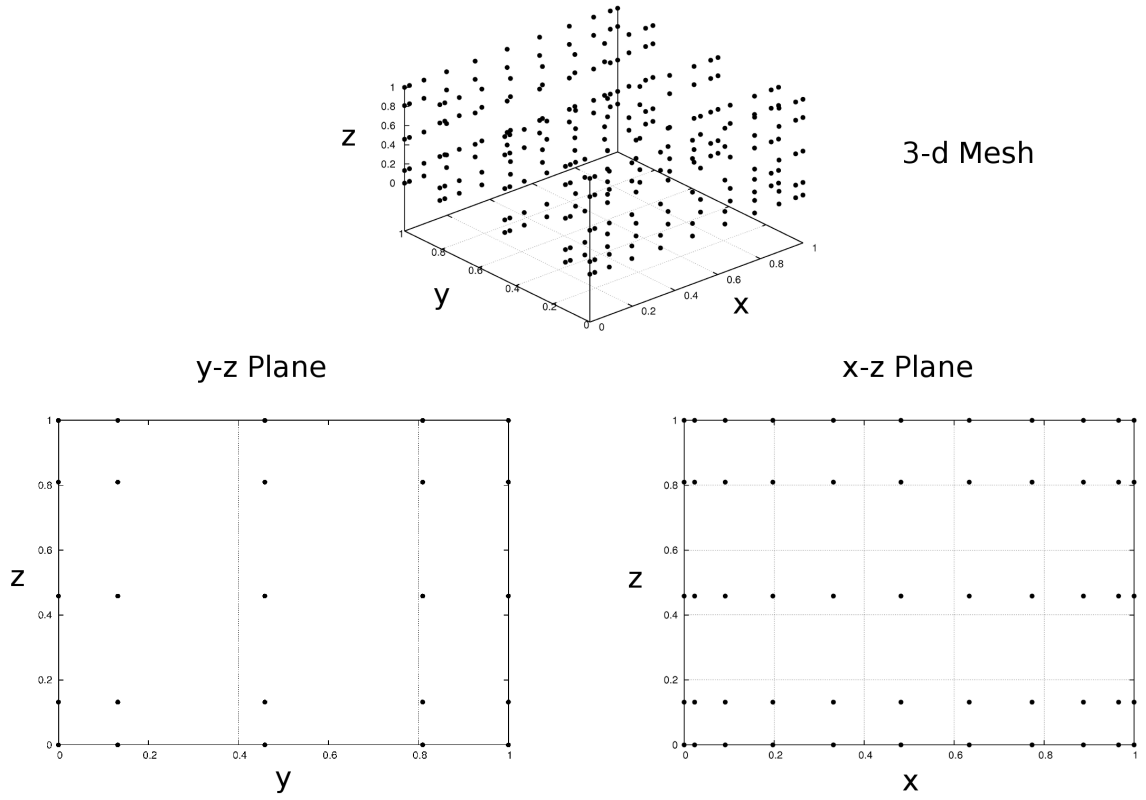

Figure 5.7: Orthographic projection of $[n_x, n_y, n_z] = [11, 5, 5]$ solution mesh generated from the set of $J^{(\alpha+1,\beta+1)}$ Jacobi polynomials.

5.4.2 Setup of collocation matrices

Collocation matrices A and B are generated for each dimensions using Lagrange polynomials as the basis function. These are $n \times n$ sized according to the mesh size $[n_x, n_y, n_z]$ and are recalculated at each remeshing stage. The subroutine `COLSETUP` performs this operation and is in the `module_collocation.for` module. This calls the `DFOPR` subroutine available in the `abwlib.for` file (Villadsen & Michelsen 1978).

5.4.3 Solver usage and Variable storage

The task of incorporating the solvers used in the numerical algorithm is discussed here. The function of a DAE integrator and an NLE solver is to integrate in 1-dimension given a *vector* function, $\mathbf{f}$ or minimise the residual of the same function given a general solution *vector* ψ. Both are of length n_{de}. Furthermore, the problem definition requires the solution of variables ϕ over each solution point $[n_x, n_y, n_z]$. Two problems arise and are treated:

1. **Mesh dimensionality:** each solver requires a vector in $\mathbb{R}^1$ as an input and the problem specifies a 3-dimensional solution mesh with solution values at each point in $\mathbb{R}^{3+1} = \mathbb{R}^4$

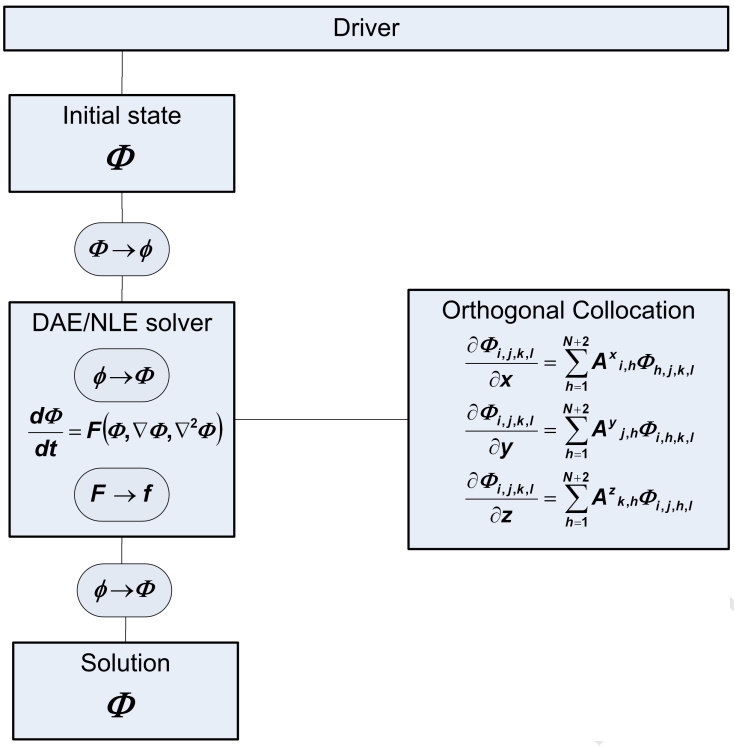

Figure 5.8: Reduction of differential terms, $\nabla\phi$ within the solver.

Table 5.3: Mappings of solution matrix, $\mathbf{\Psi}$ to vector Φ

	Stage	Instance	Mapping
1	Initial condition/guess	$\Psi \rightarrow \psi$	$\mathbb{R}^4 \longrightarrow \mathbb{R}^1$
2	Entry to residual subroutine	$\psi \rightarrow \Psi$	$\mathbb{R}^1 \longrightarrow \mathbb{R}^4$
3	Exit from residual subroutine	$\mathbf{F} \rightarrow \mathbf{f}$	$\mathbb{R}^4 \longrightarrow \mathbb{R}^1$
4	Exit from solver	$\psi \rightarrow \Psi$	$\mathbb{R}^1 \longrightarrow \mathbb{R}^4$

2. **Differential dimensionality:** differential terms, $\nabla\phi$ are present in all directions and an integrator in 1-dimension, time t

Treatment of mesh dimensionality The storage matrix of all solution variables, $\mathbf{\Psi}$ is in $\mathbb{R}^4$ and has size $[n_x, n_y, n_z, n_\phi]$. A consistent indexing nomenclature used to reduce the possibility of error and is $\Psi_{i,j,k,l}$. The discrepancy between the dimensionality of ψ_h and $\Psi_{i,j,k,l}$ occurs at various places, shown in Figure 5.8. These are treated by the mappings shown in Table 5.3.

These mappings are implemented in a nested do-loop. The order in which the loops are placed takes into account the column-major nature of Fortran's array storage system. The matrix $\Psi_{i,j,k,l}$ will be stored as a single column starting with the primary index $i = 1...n_x$ for $[j, k, l] = [1, 1, 1]$. The indicies are updated to $[j, k, l] = [2, 1, 1]$ and the primary index

is once more stored in the order $i = 1...n_x$. Each subsequent index is updated (secondary to quaternary) until the index $[j, k, l] = [n_y, n_z, n_\phi]$ is reached.

It should therefore follow that the most computationally efficient method of accessing this data is to nest the do-loop in the ascending order i, j, k, l as:

```
h = 1
do l = 1,nbal
  do k = 1,nz
    do j = 1,ny
      do i = 1,nx
        PSI(i,j,k,l) = psi(h)
        h = h + 1
```

for the $\mathbb{R}^1 \longrightarrow \mathbb{R}^4$ mapping. This will ensure that data is accessed in the order that it is stored.

The physical meaning of this storage scheme is the that the basic storage of data occurs for a single solution variable along a line down the main axis of the microchannel. The next level is that of a slab in the x, y plane. These slabs are then built up to form a 3-dimensional mesh for a single variable. This scheme is repeated for each other variable.

Treatment of differential dimensionality Each of the spatial derivatives are reduced via collocation to linear combinations of the values of the same variable in the direction of the derivative. This is shown for the transient case in Figure 5.8. This procedure is carried out manually within the subroutine `FSUB` and the derivatives are stored in 4-dimensional matrices with the same structure as the solution matrix, ϕ. This now allows for the calculation of the model equations in Chapter 4 to give the matrix residual, $\mathbf{f}$.

5.4.4 Initial conditions and ramp-up to steady state

The initial conditions are shown in Equation 5.15.

$$\begin{aligned} \chi_i &= 1.0 \times 10^{-6} \qquad i = 1, ..., c-1 \\ \chi_I &= 1.0 - 10^{-6} n_{sp} \\ N_{i,y} &= 1.0 \times 10^{-5} \qquad i = 1, ..., c \\ N_{i,z} &= 1.0 \times 10^{-5} \qquad i = 1, ..., c \\ c_t &= c_{t,0} \\ T &= T_0 \end{aligned} \tag{5.15}$$

These are set so that the reactor is initially completely filled with inert which removes any reaction from the microchannel. This eliminates the non-linearity of the rate law and ensures that no concentration gradients develop. As the flux densities are dependent on the concentration gradients, these will then be set to zero which in turn eliminates the Maxwell-Stefan non-linearity. The temperature and bulk concentration are set to steady state inlet conditions.

The reactive components are ramped up according to a modified sigmoid function

$$\chi_i(t) = \frac{\chi_{i,ss}}{1+\exp\{-\alpha_i(t-\gamma)\}} \tag{5.16}$$

for $i = 1, ...c - 1$where the parameter γ sets the time for the maximum rise rate and the parameter α_i sets the rise rate required for convergence to the steady state inlet composition, $\chi_{i,ss}$. The value α_i takes is problem dependent given that the time for convergence and initial and final points all need to be specified. Substitution of the initial boundary condition $t = 0$, $\chi_i = \chi_{i,0}$ into Equation 5.16 gives

$$\alpha_i = \frac{1}{\gamma} \ln\left(\frac{\chi_{i,ss} - \chi_{i,0}}{\chi_{i,0}}\right) \tag{5.17}$$

The ramp-up function is shown in Figure 5.9.

As the reactive components are increased, the significance of the reaction rate term in Figure 5.10a and flux gradients increases in Figure 5.10b. This progressively adds to the non-linearity of the system. However each time-step presents a feasible solution for the initial condition of the next, allowing for the directed and hence smooth convergence to the steady state solution.

The choice of this curve is arbitrary in as much as the physical situation is concerned as only the steady state solution is desired. However, it provides numerical stability as the smallest ramps are present at the start where convergence is necessary from the initial state and at the end where reaction rate is highest and non-linearity is a concern.

5.4.5 Numerical Integration

The average composition, concentration and temperature in the channel are evaluated using the quadrature weighting functions w_i (Rice & Do 1995). These are obtained using Radau quadrature weights obtained at the Jacobi polynomial roots with the inclusion

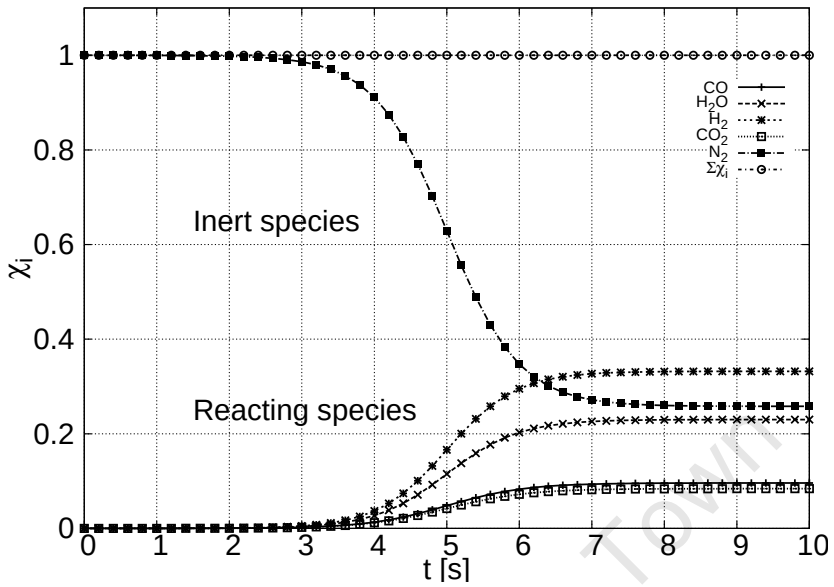

Figure 5.9: Sigmoid function ramp-up to final composition of $\left[\ \chi_{CO}\ \ \chi_{H_2O}\ \ \chi_{H_2}\ \ \chi_{CO_2}\ \ \chi_{N_2}\ \right] = \left[\ 9.6\ \ 23.0\ \ 32.2\ \ 8.4\ \ 26.8\ \right]$ from (Germani et al. 2005).

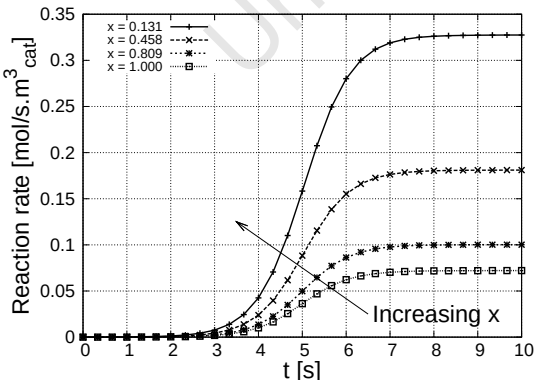

(a) Reaction rate at different x-positions

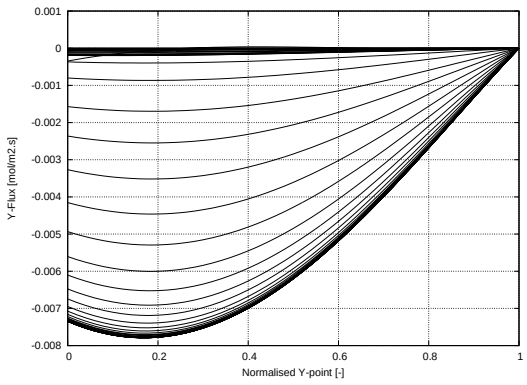

(b) Flux profiles at $x = 0.5$ for different time steps

Figure 5.10: Transient reaction rate and radial flux profiles

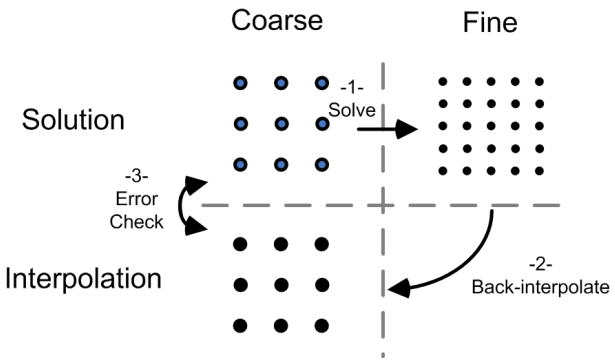

Figure 5.11: Schematic of error checking procedure

of the two boundary conditions as quadrature points i.e. for $J^{(\alpha+1,\beta+1)}$. The subroutine `COLSETUP` performs this operation and is in the module_collocation.for module. This calls the `Radau` subroutine available in the `abwlib.for` file (Villadsen & Michelsen 1978).

The average solution variable ψ in general form is merely the linear combination of the weighting function w to the corresponding solution value ψ at each point.

$$\begin{aligned} \overline{\psi} &= \frac{1}{b-a}\int_a^b \psi(x)dx \\ &= \frac{1}{1-0}\sum_{i=1}^{N+2} w_i\psi_i \\ &= \sum_{i=1}^{N+2} w_i\psi_i \end{aligned} \tag{5.18}$$

Only the y and z dimensions are integrated to give an average profile along the length of the microchannel. Firstly, quadrature is applied in the z-direction at each x, y combination point. This gives a 2-dimensional solution. Quadrature is then applied in the y-direction to each of the x points to give the average 1-dimensional profile. The subroutine `INTEGRATE` performs this operation and is in the `module_collocation.for` module.

5.4.6 Mesh-free convergence condition

The procedure for the evaluation of the convergence to a mesh-free solution of each iteration is shown in Figure 5.11. A global error function is used to evaluate whether the deviations between successive grid sizes have converged to a steady state. It is not an absolute error measurement as the computed solution is not compared to an exact solution.

The new fine mesh solution is back-interpolated as $\mathbf{u}_{2,i}$ to the collocation points of the

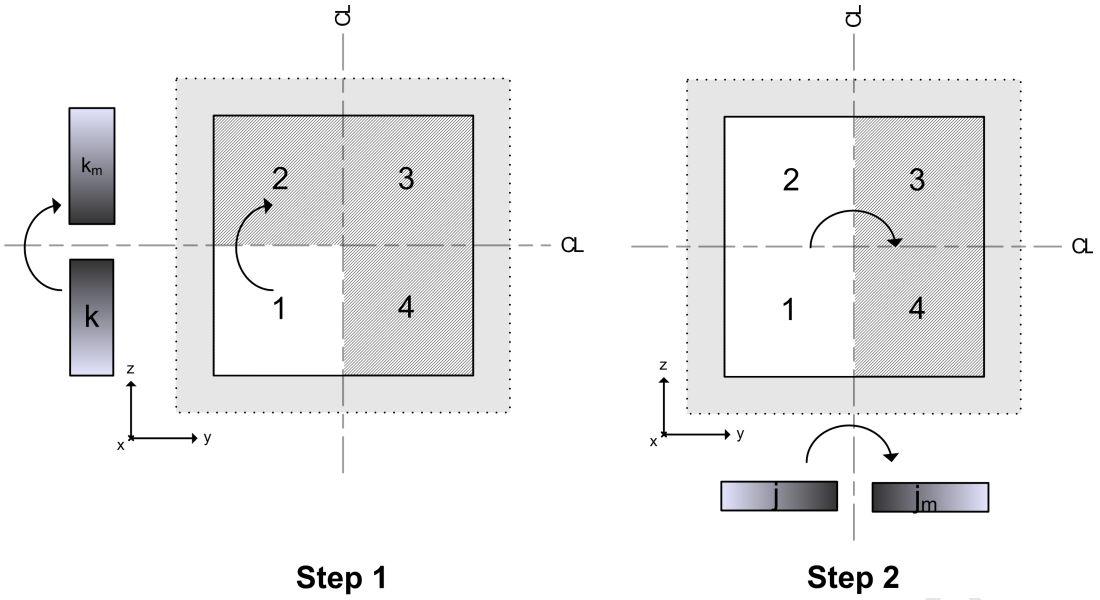

Figure 5.12: Order of reflection

previous coarse mesh solution, $\mathbf{u}_{1,i}$. This is defined in Equation 5.19 as the root mean square error (RMSE) of each solution variable across all points. For purposes of comparison, the normalised RMSE (NRMSE) is divided by the average balance variable over both solution sets in a manner similar to the calculation of the coefficient of variation.

$$\begin{aligned} RMSE_i &= \sqrt{\frac{\sum_{i=1}^{n_{pts}} (\mathbf{u}_{1,i} - \mathbf{u}_{2,i})^2}{n_{pts}}} \\ NRMSE_i &= \frac{RMSE_i}{\mu_i} \end{aligned} \tag{5.19}$$

for $i = 1, ..., n_{bal}$

5.5 Reflection for symmetry

5.5.1 The problem

The solution space shown in Figure 5.13 has to be reflected for symmetry to the other quadrants. In effect the problem is that of reflecting each of the local index values, k about a symmetry plane and equating them to the new global channel index system, k_m. This mapping is shown in in Figure 5.13.

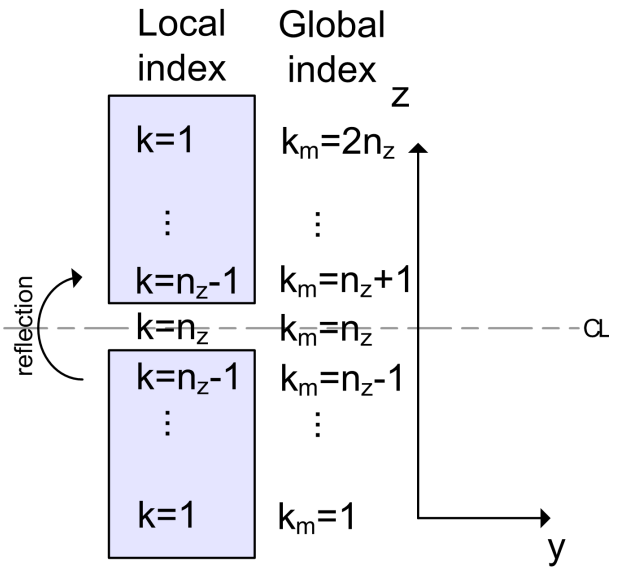

Figure 5.13: Schematic representation of reflection of indicies about symmetry line onto global index system.

5.5.2 The approach

The above problem is treated in general as the reflection of a point P_1 across an arbitrary plane to the point P_m, shown in Figure 5.14. The equation for a plane is given by (Stewart, 2001)

$$Ax + By + Cz = D \tag{5.20}$$

This has normal $n = [A, B, C, D]$. An origin on the plane is designated as point P_0 and the vector connecting P_0 and P_1 is $\mathbf{v} = \begin{bmatrix} x_1 - x_0 & y_1 - y_0 & z_1 - z_0 & 0 \end{bmatrix}$. Now the distance between the point P_1 to the plane is the scalar component of the projection of P_1 onto the normal vector and is given by

$$d = comp_{\mathbf{n}}\mathbf{v} = \frac{\mathbf{n} \cdot \mathbf{v}}{|\mathbf{n}|} \tag{5.21}$$

In the case that the plane is non-zero at the origin, this is best written as

$$d = \frac{\mathbf{n} \cdot P_1 - D}{|\mathbf{n}|} \tag{5.22}$$

Now the distance between P_1 and P_m is twice the distance between P_1 and the plane in the direction of the *unit* normal vector, $\hat{\mathbf{n}}$. This means that the point P_m is given by

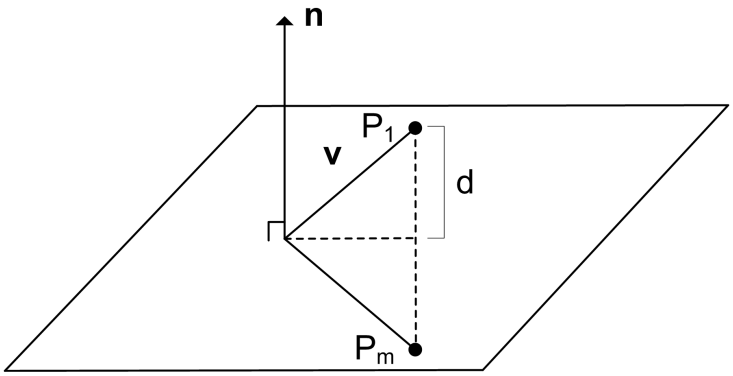

Figure 5.14: Reflection of a point about an arbitrary plane.

$$\begin{aligned} P_m &= P_1 - 2D\hat{\mathbf{n}} \\ &= P_1 - 2\frac{\mathbf{n}\cdot P_1 - D}{|\mathbf{n}|}\frac{\mathbf{n}}{|\mathbf{n}|} \\ &= P_1 - \frac{2\mathbf{n}\left(\mathbf{n}\cdot P_1 - D\right)}{|\mathbf{n}|^2} \end{aligned} \tag{5.23}$$

5.5.3 Application to reflection problem

The approach above is applied to the problem shown in Figure 5.13 and the order of implementation is shown in Figure 5.12. The mapping of quadrant 1 to quadrant 2 is first considered and shown schematically in Figure 5.13. This involves the mapping of the z-index, k of the co-ordinate $P_1 = [x, y, k_1]$ to an equivalent point $P_m = [x, y, k_m]$ in the global domain about the plane defined by $\mathbf{n} = \begin{bmatrix} 0 & 0 & 1 & n_z \end{bmatrix}$. Application of Equation 5.23 gives

$$\begin{aligned} P_m &= [x, y, k_1] - \frac{2\,[0,0,1]\left([0,0,1]\cdot[x,y,k_1] - n_z\right)}{\sqrt{0^2+0^2+1^2}^2} \\ &= [x, y, k_1] - [0, 0, 2]\,(k_1 - n_z) \end{aligned}$$

or more conveniently, just the mapping of the index $k_1 \rightarrow k_m$ as the x and y indicies remain the same

$$k_m = k_1 - 2\,(k_1 - n_z) \tag{5.24}$$

The mapping of quadrants 1 and 2 to 4 and 3 respectively are done in a similar manner. In this case the y-index, j is mapped as $j_1 \rightarrow j_m$ in an analogous manner to the z index.

$$j_m = j_1 - 2\,(j_1 - n_y) \tag{5.25}$$

All this is implemented in the Fortran subroutine `REFLECT` in the module `module_evaluate.f90`.

5.6 Compiler Considerations

5.6.1 Gfortran vs Ifort

The first choice that has to be made is the choice of Fortran compiler to be used. The performance of two available compilers, GNU Fortran (Gfortran) 4.3.3 and the Intel Fortran Professional Edition 11.0.081 are compared. The comparison is done on a test code that replicates the calculation of the derivative of seven variables by a linear combination for each point in 3-dimensional mesh. This calculation applies Equation 2.94 and represents the model code as it is expected to be repeated multiple times in the solution procedure. Furthermore it tests the memory handling ability of the compilers as it calls up elements of multidimensional arrays much like the model code. The formulation is represented by the following pseudo-code

```
do l = 1,7
  do k = 1,n
    do j = 1,n
      do i = 1,n
        dudy(i,j,k,l) = 0.d0
        do h = 1,n
          dudy(i,j,k,l) = dudy(i,j,k,l) + Amat(k,h)*umat(i,j,h,l)
        end do
```

The number of elements in each dimension is represented by the constant n. This is varied and the computational time for each value of n is plotted against CPU time on a single processor. This is shown in Figure 5.15. The Intel compiler outperforms the GNU compiler at all computational mesh sizes. This is because ifort applies an optimisation procedure to multiple loops that vectorises them to make use of a single set of instructions at the processor for multiple data commands. All further model calculations are done on the ifort compiler to ensure computational efficiency.

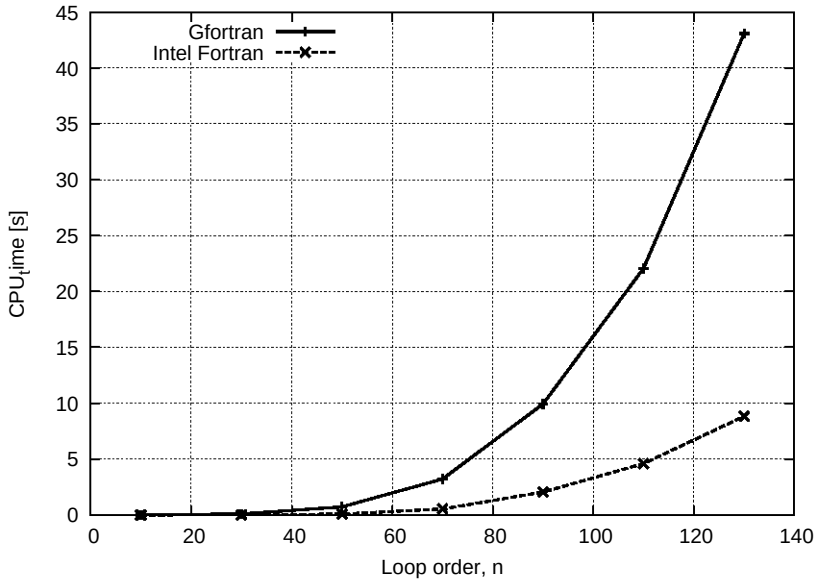

Figure 5.15: Comparison of CPU times for different values of mesh size, n.

5.6.2 Ifort Compiler options

Intel Fortran compiler options are adjusted depending on the run time situation. If the model is in the code generation phase, certain compiler flags are used for error-checking while if the model is executed to obtain results, compiler flags are chosen for speed. The flags used are reported below.

On testing The following flags are used: -autodouble -vec-report0 -traceback -check bounds -fpe0

-autodouble Automatically makes all real numbers double precision

-check bounds Checks if the array indicies accessed during run time are within the initial memory allocation

-traceback Traces source of run time error to the line, procedure and file name.

-vec-report0 Controls the diagnostic information reported by the loop vectoriser: (0) tells the vectoriser to report no diagnostic information, (1) tells the vectoriser to report on vectorized loops.

-fpe0 Allows control over floating-point exception information at run time including: (1) calculations result in a divide by zero, overflow, or invalid operation, (2) calculations

that result in an underflow and (3) when an exceptional number ($\pm\infty$, NaN) is present in a calculation. The location of the error is reported if the -traceback option is enabled.

On running The following flags are used: -autodouble -vec-report0 -xP

-xP Compiler generates specialised code to maximise performance on the processor that executes the it. Here P stands for Intel Core Duo processors.

All others are as before.

5.7 Parallelisation

A further method used to speed up the code execution is to parallelise the algorithm by processing it on multiple cores. This is carried out using the OpenMP specification and implemented using two methods: (1) linking of parallelised libraries and (2) manual parallelisation of routines within the algorithm.

A general piece of code is executed as follows. A compiler generates a set of instructions for the computer to execute in sequential order that is wrapped up in the executable program. This set of instructions is referred to as a *thread* and unless told otherwise a single thread is used throughout execution, known as a *master thread*. When a single thread is generated the program is said to run in the serial mode (Chapman et al., 2008).

A parallelised program has specific break points in the code which instruct the compiler to split the master thread into multiple threads. Each thread will be allocated to and executed by an individual processor. At the end of the parallelised region, the threads recombine to the master thread. The choice of break point is extremely important as the memory of each of the variables generated in each thread are unique and cannot be shared by processors. These can only shared at the end of the parallel region. This means that the allocation of work must be done in such a way that a calculation in one thread is independent of any other calculation in any other thread.

The performance of the parallelisation is measured by the *speedup* and the *efficiency* (Chapman et al. 2008). The *speedup ratio, S* is the ratio of the elapsed time of the serial version, T_1 and the elapsed time on p processors, T_p

$$S = \frac{T_1}{T_p} \tag{5.26}$$

while the *efficiency, e* is obtained by dividing the speedup by the number of processors.

Table 5.4: Parallel performance and speedup of DDASAC.for for an (11,5,5) mesh using the MKL library.

Version	Number of Processors	CPU time	Elapsed time	Speedup	Efficiency
		[s]	[s]		[%]
Serial	1	129.66	129.73	1.0000	100.00
Parallel	1	130.53	129.74	1.0000	100.00
	2	131.9	122.63	1.0579	52.895
	3	134.59	120.18	1.0794	35.980
	4	139.17	119.39	1.0866	27.165

$$e = \frac{S}{p} \tag{5.27}$$

A high speedup ratio is an indication of low overheads incurred by the compiler in allocating threads. This is normally achieved by single parallelised regions encompassing large portions of the code and is referred to as coarse-grain parallelisation. A low efficiency is an indication of a low usage of parallel regions and the presence of large serial regions. The maximum speedup can be calculated by *Amdahl's Law* (Chapman et al. 2008)

$$S = \frac{1}{\frac{f_{par}}{p} + (1 - f_{par})} \tag{5.28}$$

where f_{par} is the parallel fraction of the code.

5.7.1 MKL Libraries

The Intel Fortran Math Kernel Libraries (MKL) are statically linked to the model. These provide the linear algebra routines in BLAS and LAPACK required by `DDASAC.for` to solve the non-steady state problem. The solution times for `DDASAC.for` at different mesh sizes are given in Table 5.4. The speedup for 4 processors is only 1.0866 with a low processor efficiency of 27.2%. This means that there is a very low level of parallelisation. The reason for this may be that DDASAC does not make substantial use of the BLAS and LAPACK libraries and that the parallelised sections of these libraries are not substantial. Either way this is an example of the implementation and evaluation of a parallelisation scheme and a motivation to test the theoretical extent of possible parallelisation before developing parallelised code.

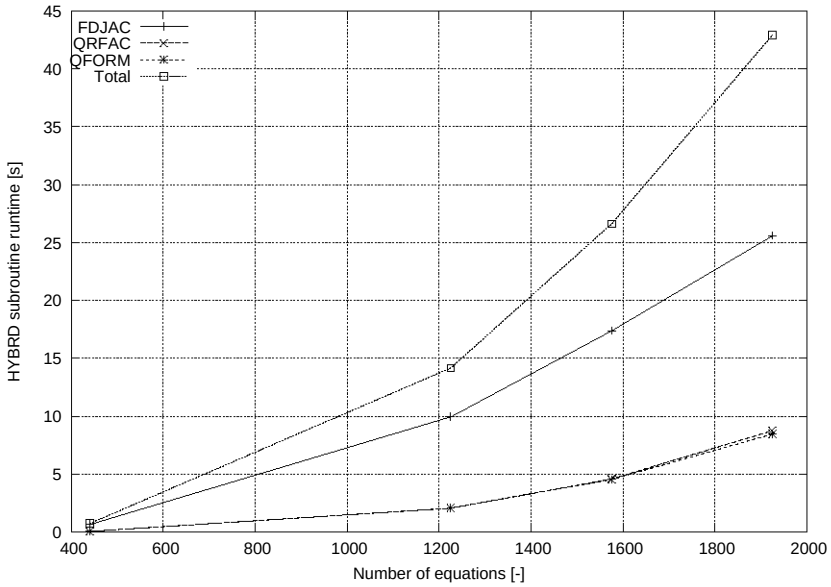

Figure 5.16: Computational times for different HYBRD.for subroutines as a function of number of equations.

5.7.2 HYBRD.for Parallelisation

The HYBRD.for solver does not make use of either the BLAS or LAPACK libraries and has to be manually parallelised. The HYBRD-called subroutines that have the highest computational times are shown in Figure 5.16. These are chosen as the main targets of parallelisation as they represent >99% of the computational time of a single call to the solver. The subroutine with the highest computational expense is `FDJAC` which calculates the Jacobian of the problem system by forward difference approximation. This is followed by the `QRFAC` and `QRCALC` routines which respectively compute the QR factorisation of the Jacobian matrix and recompose Q from its factorised form. The latter routines are difficult to parallelise as they require the reconfiguration of the calculation scheme. This have been attempted by previous studies (Wright 1991; Matstoms 1995; Rotella & Zambettakis 1999) with varied success. All attempts require substantial changes to the calculation algorithm and the implementation of such reconfigurations is out of the scope of this study. These considerations of potential speedup and coding effort justifies the targeting of only `FDJAC` for parallelisation.

Figure 5.16 shows that the fraction of parallelised code through FDJAC is $f_{par} = 0.6$. Substituting this value into Amdhal's law in Equation 5.28 shows that the maximum speedup on a 4 processor system is $S = 1.81$. This speedup can be a substantial time saver if the model is called multiple times in a regression or optimisation routine and justifies its application.

The forward difference Jacobian calculation works as follows. The $n \times n$ Jacobian, $[\mathbf{J}]$ of the minimisation function, $\mathbf{f}$ of size n in terms of the approximate solution variable $\mathbf{u}$ of

size n is made up of the following elements:

$$[\mathbf{J}] = \begin{bmatrix} \frac{\partial f_1}{\partial u_1} & \cdots & \frac{\partial f_1}{\partial u_n} \\ \cdots & \ddots & \vdots \\ \frac{\partial f_n}{\partial u_1} & \cdots & \frac{\partial f_n}{\partial u_n} \end{bmatrix} \tag{5.29}$$

Each element u_i is perturbed by some increment h and the entire minimisation function calculated at this perturbed value. This is referred to as at $\mathbf{f}_p$. A column of the Jacobian can now be calculated as

$$\frac{\partial \mathbf{f}}{\partial u_i} = \frac{\mathbf{f}_p - \mathbf{f}}{h} \tag{5.30}$$

This scheme means that a column of the Jacobian is calculated at each function evaluation so that the function needs to be called n times. Furthermore the calculation of each of these columns is independent of the others so the work in calling the function by the do-loop may be divided up across multiple processors. This is done by the following OpenMP parallel construct.

```
!$OMP PARALLEL IF (N>30) DEFAULT(NONE) SHARED(N,EPS,FVECP,FJACP)
PRIVATE(I,J,TEMP,H,WA1) FIRSTPRIVATE(X,IFLAG,LRPARP,RPARP)
!$OMP DO SCHEDULE(STATIC,100)
...
!$OMP END DO
!$OMP END PARALLEL
```

The following clauses are explained

if — Region only executed in parallel if requires greater than 30 function evaluations. Else will have substantial parallel overheads.

default — No default data access permissions across threads

shared — These variables are shared across the threads and are not to be changed within any thread. For example the size of the Jacobian, $n \equiv N$ is required in each thread and is thus shared.

private — These variables can take on values unique to each thread but have unassigned values upon entry and exit of the parallel region. For example the do loop indicies i, j have to take on values unique to each thread and are thus private.

firstprivate These variables are private to each thread but take on their entry value in the parallel region. For example the approximate solution variable $\mathbf{u} \equiv X$ is required in each call to the minimisation function but needs to take on unique perturbed values in each call.

schedule(static,100) This clause allocates each thread a chunk of 100 calls to the do-loop in a static, or sequential fashion. For example thread0 gets $i = 1, 100$, thread1 gets $i = 101, 200$ etc. As soon as a processor has completed its thread, a new chunk of 100 calls is allocated to it. This static allocation is the simplest allocation method and thus has the least parallel overheads.

This method of parallelisation requires the model subroutine to have multiple instances of its variables and internal subroutines active at the same time. This places some strict requirements on the programming structure. The first requirement is that the model subroutine and *every* procedure (function or subroutine) called by it to be *recursive*. This argument placed before the procedure definition allows each instance of it to have its own memory. This is typically used to call procedures from within themselves[1], but the same rationale holds here. Procedures are made recursive automatically when the source file containing the procedure is compiled with the -openmp flag, however not all procedures are allowed to be recursive. Specifically, procedures containing the `deallocate` statement are excluded as you cannot have multiple instances of a deallocation running when the memory has not been allocated yet.

The second requirement is that no calculated values are to be written to a common memory, for example in a data module. This would create two problems. The first is that if all active instances of the model subroutine wrote their own calculated values to the same location, the values read from the same location would end up being garbled combinations of multiple instances of these variables. The second problem is that multiple threads would try to write to the same memory location concurrently. This would cause the execution to crash. The Fortran model is modified to accommodate these requirements.

A single instance of code is tested for parallelisation and the results are shown in Table 5.5. The speedup for 4 processors is only $S = 1.17$ with a processor efficiency of 29.35%. This low level of parallelisation compares to that of the MKL speedup in Table 5.4 notwithstanding the high potential for parallelisation shown in Figure 5.16 and the speedup of $S = 1.81$ predicted by Amdhal's Law. This cannot be attributed to the parallelisation overheads as a statically-scheduled directive is known to have a low overhead (Hermanns, 2002). A possible reason is that the overheads incurred in accessing the variables $\mathbf{u}_i$ in Equation 5.29 from the main RAM is the limiting step in the calculation of the Jacobian.

[1]Such as call one instance of an NLE solver from within the minimisation function of another instance of it.

Table 5.5: Parallel performance and speedup of HYBRD.for for an (11,5,5) mesh using OpenMP specification. The meshing sequence is (7,3,3); (9,3,3),(11,5,5)

Version	Number of Processors	CPU time	Elapsed time	Speedup	Efficiency
		[s]	[s]		[%]
Serial	1	29.59	29.87	1.000	100.0
Parallel	1	29.79	29.88	1.000	100.0
	2	31.92	26.76	1.116	55.80
	3	34.72	26.15	1.142	38.07
	4	36.75	25.44	1.174	29.35

It may therefore be possible to improve performance by using distributed memory processors, where each processor has its own internal memory is more easily accessed than the current setup.

Chapter 6

Model Test Results

The model performance is examined against severe conditions that may not be physically realistic, but provides a test of the solution algorithm's robustness and computational efficiency. The simulation conditions are first shown followed by tests of computational performance. The criterion for a mesh-free solution is examined and solution trends discussed. The model is then validated against experimental data from literature.

6.1 Reactor Conditions

WGS reactor dimensions and experimental conditions are provided to give model inputs and are shown in Table 6.1. The channel dimensions chosen are common for lab scale reactors (Germani et al. 2005; Kolb et al. 2008) to provide a realistic physical basis for operation. The reported inlet space velocity gives an inlet velocity $v_0 = 11.0\,\mathrm{m/s}$ to yield a Reynolds number of $Re = 295$. This is low enough to satisfy the laminar flow condition of $Re < 2100$. The reason for operating at such a high linear velocity is to enhance transport effects by increasing the axial transport time to a similar order as the radial diffusive transport time. An equimolar feed composition is given to be able to compare the radial profiles of each species given their different diffusivities.

The kinetic rate expression is given in Equation 4.19. The values taken for the kinetic constants k_0 and E_a define the overall conversion of the system. The k_0 is chosen such that the reactor initially runs at high reaction rates to equilibrium conversion where the rate is forced to slow down. This will enable the evaluation of radial profiles at both steep and shallow gradients respectively. The activation energy for reaction is taken as that reported for the same catalyst system (Germani et al. 2005). These are shown in Table 6.2.

The chosen parameters lead to a solution with steep gradients in each of the solved parameters. This is a stiff system which is difficult to solve and provides an extreme test

Table 6.1: Model inputs for reactor model run for induced mass and heat transfer effects

Property	Value
Channel dimensions $W \times H$	$400.0 \times 600.0\,\mu$m
Channel length L	5.0cm
Catalyst layer thickness δ_{cat}	$10.0\,\mu$m
Space Velocity SV	$120.0\,{}^{\text{mol}}/_{\text{s.kg}_{\text{cat}}}$
Inlet Composition (%)	
$(\ CO \quad H_2O \quad H_2 \quad CO_2 \quad N_2\ )$	$(\ 20.0 \quad 20.0 \quad 20.0 \quad 20.0 \quad 20.0\ )$
Inlet Temperature	300 °C
Total Pressure	3 bar

Table 6.2: Rate constants for the extreme model evaluation runs compared to that of the *approximate* first order equivalents of the (Germani et al. 2005) study.

	k_0 ${}^{\text{m}^3}/_{\text{s.kg}_{\text{cat}}}$	E_a ${}^{\text{J}}/_{\text{mol}}$	SV ${}^{\text{mol}}/_{\text{s.kg}_{\text{cat}}}$
Germani et al. 2005	1.7×10^5	86.0×10^3	0.59
Extreme	4.4×10^7	86.0×10^3	120.

of the model's robustness and solution efficiency.

6.2 Model Performance

The performance of the model presented is evaluated against the extreme test conditions shown in Tables 6.1 and 6.2. The purpose of this evaluation is to determine the mesh-size required for a reasonably accurate solution versus solution time.

6.2.1 Run-time

The mesh is incrementally increased according to the update scheme shown in Table 6.3. The transient problem is solved on a $(7, 3, 3)$ mesh, the most stable coarse mesh found. This requires a computational time of $\sim$4.12s. Each successive re-mesh is shown in the same table.

The run-time of the proposed hybrid algorithm is compared to that of solving the unsteady state problem over the same final mesh size in Figure 6.1. These are plotted against the number of mesh points n_{pts} and not the individual dimensional points n_x,n_y or n_z as the entire domain is treated as one simultaneous system of equations and the solvers only "see" the total number of mesh points.

Table 6.3: Mesh update scheme for hybrid solution procedure.

#	n_x	n_y	n_z	n_{pts}
1	5	3	3	45
2	9	3	3	81
3	9	5	5	225
4	11	7	7	539
5	11	9	9	891
6	21	9	9	1701

The transient model becomes unstable and does not solve for meshes 5 and 6 in Table 6.3 hence these mesh sizes are not reported in Figure 6.1. It is clear that the solution time for the transient solution increases more rapidly than that of the combined steady/non-steady state 3-step method. This means that the 3-step algorithm is preferred to the transient with regard to run-time. The actual run times are in the order of minutes/seconds and hence provide a computationally efficient model for further regression and parameter estimation work.

A possible reason for this difference in run times between the transient and 3-step algorithm lies with the solution of the Jacobian matrix. Each solver is required to evaluate this square matrix that contains $(n_{pts} \times n_{bal})^2$ elements. This is done by perturbing each of $n_{pts} \times n_{bal}$ variable values to evaluate the response of the residual function. Thus each movement to a new solution requires the evaluation of the residual functions at least $n_{pts} \times n_{bal}$ times. The transient DAE solver is required to re-evaluate for the Jacobian repeatedly in the approach to steady state.

In contrast the steady state NLE solver is required to evaluate the Jacobian once as a result of the good initial guess. This is because the solution equations are to a great extent linear. The collocation equations are linear when properties are constant over the temperature change, the Maxwell-Stefan equations are almost linear and it is only the kinetic rate law that can vastly deviate from linearity[1]. As the HYBRD solver has between quadratic and 1.6 convergence, it can give a solution in a single Jacobian evaluation. It is therefore more efficient to solve for the transient system on a coarse mesh as it requires multiple evaluations of a small Jacobian, rather than on a fine mesh that requires multiple evaluations of a sizable Jacobian.

[1]Except in the case of an isothermal first order reaction the rate law reduces to a linear expression.

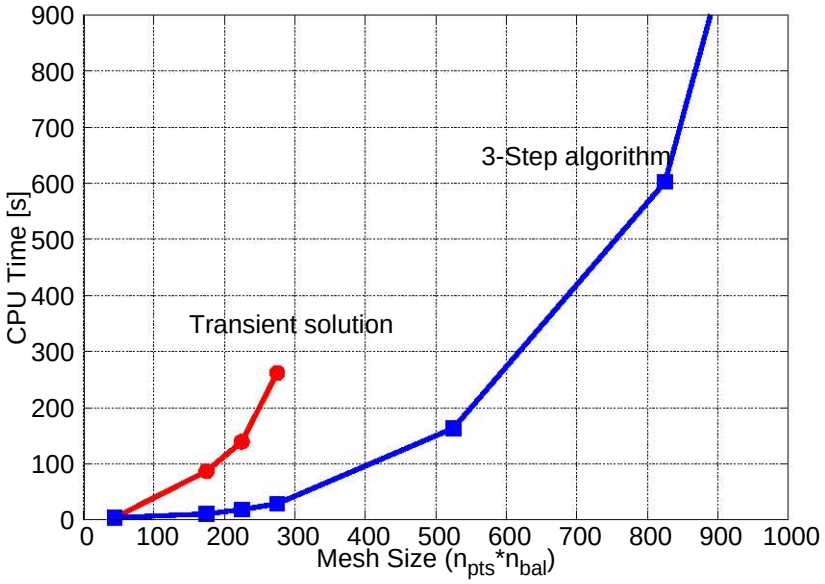

Figure 6.1: Comparison of CPU run-times for non-steady state only and proposed 3-step algorithm. Point not shown: $n_{pts} = 1701$ for CPU time of 4647 s. $W \times H \times L = 400.0 \times 600.0\mu m \times 5.0cm$, $\delta_{cat} = 10.0\mu m$, $SV = 120.0\, mol/s.kg_{cat}$ $P = 3\, bar$ $T = 573.15\, K$, $k_0 = 4.4 \times 10^7\, m^3/s.kg_{cat}$, $E_a = 86.0 \times 10^3\, J/mol$ and inlet composition $\begin{pmatrix} CO & H_2O & H_2 & CO_2 & N_2 \end{pmatrix} = 20.0$. Full 3-dimensional model used.

6.2.2 Mesh-free solution

The $NRMSE$ for each successive remesh is calculated as described in 5.4.6. The $NRMSE$ for each balance is plotted against number of mesh points in Figure 6.2a. This shows a convergence to a steady state error of ∼1% for each variable. The minimum error is found at a mesh size of 891 points or the $(11, 9, 9)$ mesh. It should be noted that this case has steep gradients that are unlikely to be encountered in further simulations. As the steepness of gradients increases, the order of the polynomial approximation, and hence the number of required solution points increases for a mesh-free solution. Therefore the mesh size obtained here can be regarded as an empirical maximum size for convergence to the mesh-free solution. The solution time is ∼686 s which compares well against the hour magnitude solution times of FEM simulators.

The dependency of the convergence to mesh free solution on the number of axial points, n_x and the number of perpendicular points n_y and n_z is shown in Figures 6.2b and 6.2c respectively. An increase in $n_x > 11$ does not make any significant difference while the number of axial points controls the convergence to $NRMSE < 1\%$ from $n_{y/z} = 5$ to $n_{y/z} = 9$.

The convergence profiles of CO mole fraction and temperature in the axial and perpendicular directions are shown in Figures 6.3 and 6.4. These variables are chosen as CO conversion is the primary function of this reactor and the energy balance is dependent

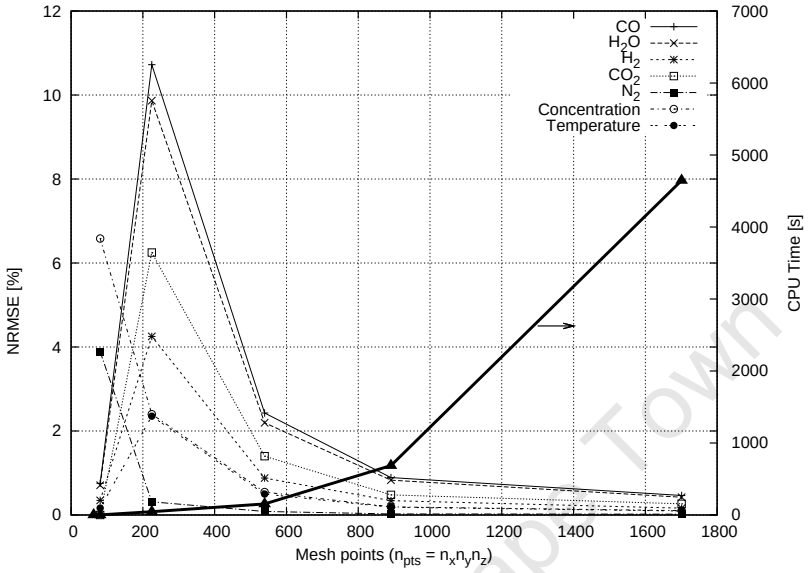

(a) NRMSE convergence to steady error as a function of overall number of mesh points.

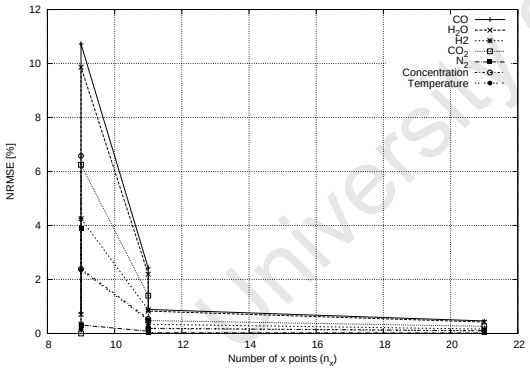

(b) NRMSE convergence to steady error as a function of number of x-points.

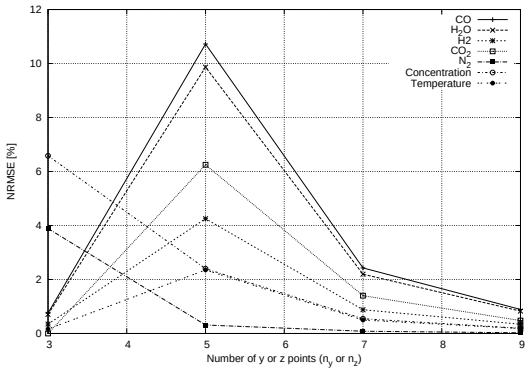

(c) NRMSE convergence to steady error as a function of number of y or z-points.

Figure 6.2: Convergence of NRMSE. An NRMSE of below 1% threshold is achieved for an (11,9,9) mesh with a CPU time of 686 s. $W \times H \times L = 400.0 \times 600.0\mu m \times 5.0cm$, $\delta_{cat} = 10.0\mu m$, $SV = 120.0\, mol/s.kg_{cat}$ $P = 3\, bar$ $T = 573.15\, K$, $k_0 = 4.4{\times}10^7\, m^3/s.kg_{cat}$, $E_a = 86.0 \times 10^3\, J/mol$ and inlet composition $\begin{pmatrix} CO & H_2O & H_2 & CO_2 & N_2 \end{pmatrix} = 20.0$. Full 3-dimensional model used.

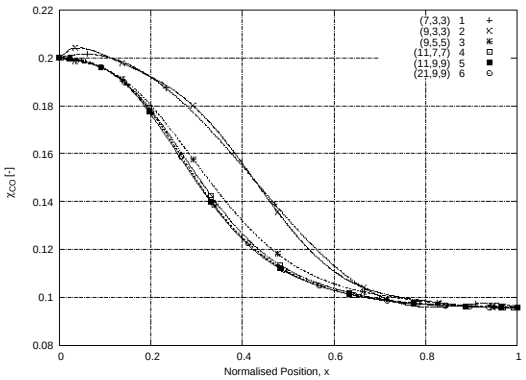

(a) Profile along x-axis along channel center (x, n_y, n_z)

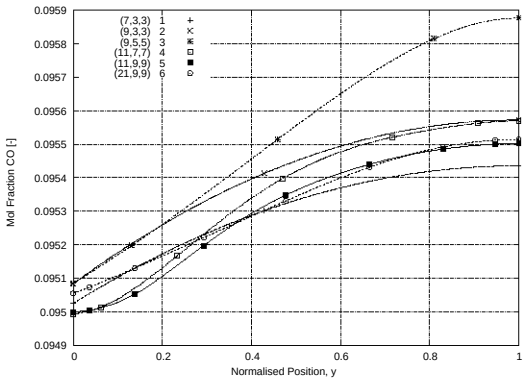

(b) Profile along y-axis across reactor center $(\frac{1}{2}n_x, y, n_z)$

Figure 6.3: Convergence of CO mole fraction to mesh-free solution. $W \times H \times L = 400.0 \times 600.0\mu m \times 5.0cm$, $\delta_{cat} = 10.0\mu m$, $SV = 120.0\, mol/s.kg_{cat}$ $P = 3\, bar$ $T = 573.15\, K$, $k_0 = 4.4 \times 10^7\, m^3/s.kg_{cat}$, $E_a = 86.0 \times 10^3\, J/mol$ and inlet composition $\begin{pmatrix} CO & H_2O & H_2 & CO_2 & N_2 \end{pmatrix} = 20.0$. Full 3-dimensional model used.

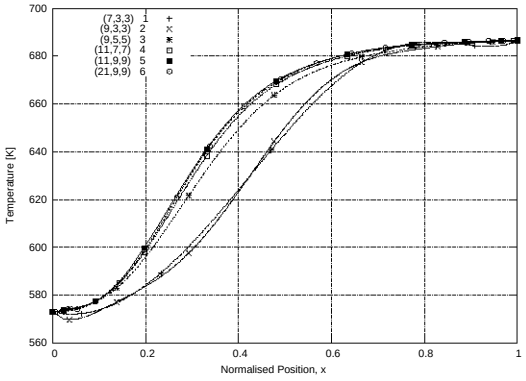

(a) Profile along x-axis along channel center (x, n_y, n_z)

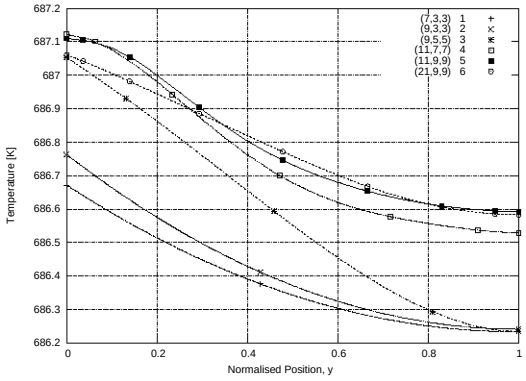

(b) Profile along y-axis across reactor center $(\frac{1}{2}n_x, y, n_z)$

Figure 6.4: Convergence of temperature profiles to mesh-free solution. $W \times H \times L = 400.0 \times 600.0\mu m \times 5.0cm$, $\delta_{cat} = 10.0\mu m$, $SV = 120.0\, mol/s.kg_{cat}$ $P = 3\, bar$ $T = 573.15\, K$, $k_0 = 4.4 \times 10^7\, m^3/s.kg_{cat}$, $E_a = 86.0 \times 10^3\, J/mol$ and inlet composition $\begin{pmatrix} CO & H_2O & H_2 & CO_2 & N_2 \end{pmatrix} = 20.0$. Full 3-dimensional model used.

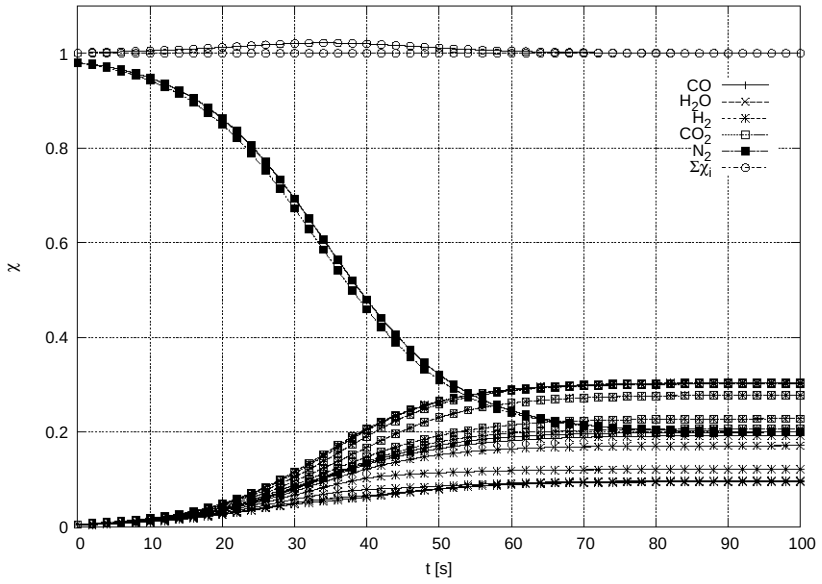

Figure 6.5: Composition ramp-up in time over all x points for all species. $W \times H \times L = 400.0 \times 600.0\mu m \times 5.0cm$, $\delta_{cat} = 10.0\mu m$, $SV = 120.0\, mol/s.kg_{cat}$ $P = 3\, bar$ $T = 573.15\, K$, $k_0 = 4.4 \times 10^7\, m^3/s.kg_{cat}$, $E_a = 86.0 \times 10^3\, J/mol$ and inlet composition $\begin{pmatrix} CO & H_2O & H_2 & CO_2 & N_2 \end{pmatrix} = 20.0$. Full 3-dimensional model used.

on the solution of all other balances and therefore shows the cumulative behaviour of the entire solution set. The CO mole fraction shows good convergence in both the x- and y-directions. Remeshs 3 - 6 show almost exact agreement on the axial profile in Figure 6.3a and close agreement between the y-perpendicular profiles 5 - 6 in Figure 6.3b. Similar trends are seen in the convergence of the temperature profiles. If only the axial behavior is required, for example to predict exit temperature and conversion then to run the simulation to re-mesh 3 for a $(9, 5, 5)$ mesh is sufficient as a close approximation to mesh free behavior.

6.3 Physical Tests

Various checks are performed to verify that the model holds the physical constraints imposed on the model equation set and predicts expected trends with respect to behaviour in all spatial dimensions. These tests are described in this section.

6.3.1 Physical constraints

The first test of the model integrity is to evaluate whether the physical constraints imposed on the system are met. Figure 6.5 gives the transient change in species compositions for different points along the reactor. Of interest here is that the physical constraint $\sum_{i=1}^{c} \chi_i = 1$ is held at steady state. The time profile of $\sum_{i=1}^{c} \chi_i$ shows a deviation from

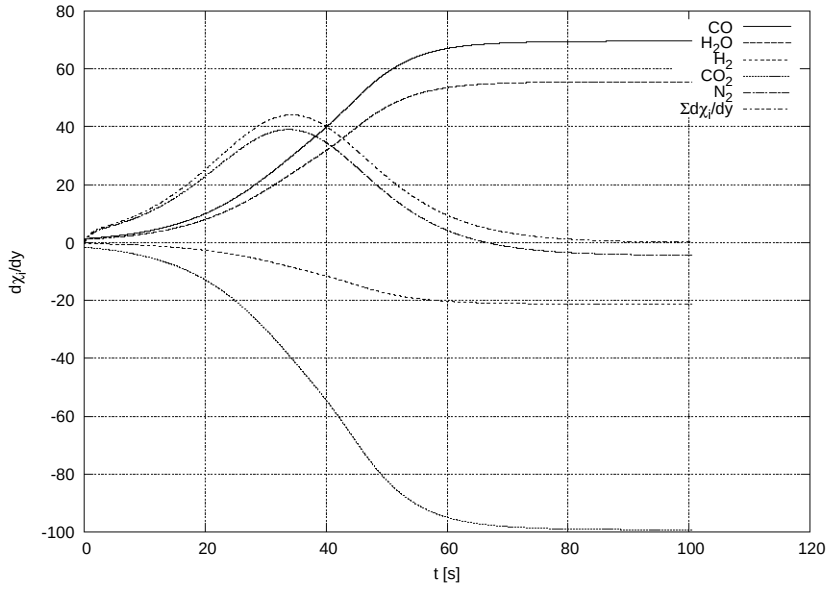

Figure 6.6: Effect of composition ramp-up on physical constraint $\sum_{i=1}^{c} \frac{\partial \chi_i}{\partial y} = 0$ plotted for the interior collocation point $[x, y, z] = \left[\frac{n_x}{2}, \frac{n_y}{2}, \frac{n_z}{2}\right]$. $W \times H \times L = 400.0 \times 600.0 \mu m \times 5.0 cm$, $\delta_{cat} = 10.0 \mu m$, $SV = 120.0\, mol/s.kg_{cat}$ $P = 3\, bar$ $T = 573.15\, K$, $k_0 = 4.4 \times 10^7\, m^3/s.kg_{cat}$, $E_a = 86.0 \times 10^3\, J/mol$ and inlet composition $\begin{pmatrix} CO & H_2O & H_2 & CO_2 & N_2 \end{pmatrix} = 20.0$. Full 3-dimensional model used.

unity as the compositions are changing with maximum deviation at the point of maximum composition change which is set to $t = \frac{t_e}{3}$. As the change in compositions levels off, the deviation reduces and $\sum_{i=1}^{c} \chi_i$ tends back to unity.

It is not within the scope of this study to investigate non-steady state behavior and the transient balances are merely used as a means to obtain a steady-state solution. It is therefore necessary to adjust the time of maximum ramp-up, γ in Equation 5.16 to ensure that sufficient time is allowed for the mole fractions to converge to unity.

A possible reason is proposed for this deviation. This involves a second physical constraint, this one dependent on the first; that the driving forces for molecular diffusion equal zero or $\sum_{i=1}^{c} \mathbf{d}_i = 0$. In this case the driving forces are the composition gradients in the y- and z-directions, $\frac{\partial \chi_i}{\partial y}$ and $\frac{\partial \chi_i}{\partial z}$ respectively. These are plotted against time for all species in Figure 6.6. This shows that the reactants CO and H_2O, and the products H_2 and CO_2 have opposite gradients because of WGS reaction stoichiometry and that the heaviest species, CO_2 has the steepest gradient at each point in time. These trends are further discussed in Section 6.3.3. Of interest here, similarly to the sum of mole fractions is the deviation of $\sum_{i=1}^{c} \mathbf{d}_i$ from zero in the region of maximum composition ramp-up. In particular, this deviation follows the trend of the inert N_2 species. Now these driving forces in terms of mole fractions are obtained from the species balances which are derived for the transient state. These are to be solved simultaneously with the flux expressions hence this is an area to search for the likely cause of the deviation.

Two possible causes are discussed.

Cause 1 The most likely reason for the deviation is that the fluxes are not solved for simultaneously with the species balances, but rather in a Rachford-Rice type updating procedure for computational efficiency. This is described in Section 5.2.2. There is thus a lag between the updated mole fractions and the fluxes which results in the deviation in the driving force at the times of maximum change in mole fractions. As the changes in mole fractions level off, the updating procedure allows the simultaneous solution of the fluxes and mole fractions.

Cause 2 A second possible cause lies with the steady state approximation of the flux physical constraint. The flux of the designated dependent species, N_2 is governed by the choice of the physical constraint on the fluxes. This is chosen as $\sum_{i=1}^{c} N_i = 0$ for a constant pressure closed system described in Section 4.5.2. This holds for the steady state only, however in the non-steady state there will be an accumulation of species fluxes[2] in the channel.

6.3.2 Overall Materials and Energy Balances

Overall materials and energy balances are carried out over the reactor shown schematically in Figure 6.7. The overall mass balance is calculated at steady state by

$$\sum_{i=1}^{c} \dot{m}_{i,in} = \sum_{i=1}^{c} \dot{m}_{i,out} \tag{6.1}$$

$$\sum_{i=1}^{c} c_{t,0}\chi_{i,0}M_i v_{x,0} XSA = \sum_{i=1}^{c} c_t \chi_i M_i v_x XSA \tag{6.2}$$

and the overall energy balance is carried out by

$$\sum_{i=1}^{c} \dot{H}_{i,in} = \sum_{i=1}^{c} \dot{H}_{i,out} \tag{6.3}$$

$$\sum_{i=1}^{c} \overline{H}_{i,in} c_{t,0}\chi_{i,0} v_{x,0} XSA = \sum_{i=1}^{c} \overline{H}_{i,out} c_t \chi_i M_i v_x XSA \tag{6.4}$$

The reported values are given in Table 6.4. The overall mass balance is held to within a 10^{-8} decimal places which is within the tolerance of the solver set to 10^{-7}. This yields a

[2] Opposite to the flux dissipation described in Section 6.3.3.

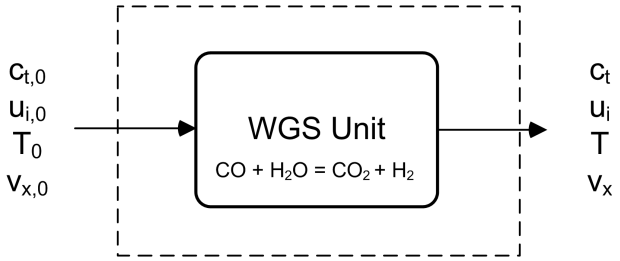

Figure 6.7: Schematic of control volume for overall materials and energy balances.

Table 6.4: Overall mass and energy balances

	Mass Balance $^{kg}/_{s}$	Energy Balance $^{J}/_{s}$
IN	3.67119×10^{-6}	2.14150×10^{1}
OUT	3.67012×10^{-6}	2.14113×10^{1}
% Difference	-2.93091×10^{-2}	-1.69291×10^{-2}

mass loss of $\sim 10^{-2}\%$ which is acceptable for the accuracy of the final conversion that is desired. The energy balance shows a loss of $\sim 10^{-2}\%$, similar to that of the mass balance. This deviation can be attributed to the mass loss which lowers the energy leaving the system.

6.3.3 Molar fluxes

The main trends in the molar flux fields are investigated to verify the solution of the Maxwell-Stefan equations. The y-component flux fields are shown in Figure 6.8 for all components and a sample z-component field for CO is shown in Figure 6.9. A few simple verifications are carried out for these fields.

The first is that each of the fluxes are maximum in absolute value at the channel entrance. This is in the region of kinetic control where the reaction rate is the highest resulting in the highest fluxes. As expected the direction of the fluxes of the reactants CO and H_2O are negative which indicates diffusion towards the catalyst surface. This is opposite to that of the products H_2 and CO_2 which have positive fluxes for diffusion away from the catalyst surface.

The fluxes are not a maximum at the inlet, but rather at some point on the catalyst surface further down the channel. This is because the reaction is adiabatic which leads to a higher temperature on the catalyst surface. This causes an increase in reaction rate and so species flux. This flux then decreases down the length of the reactor as reactants are consumed and equilibrium is reached.

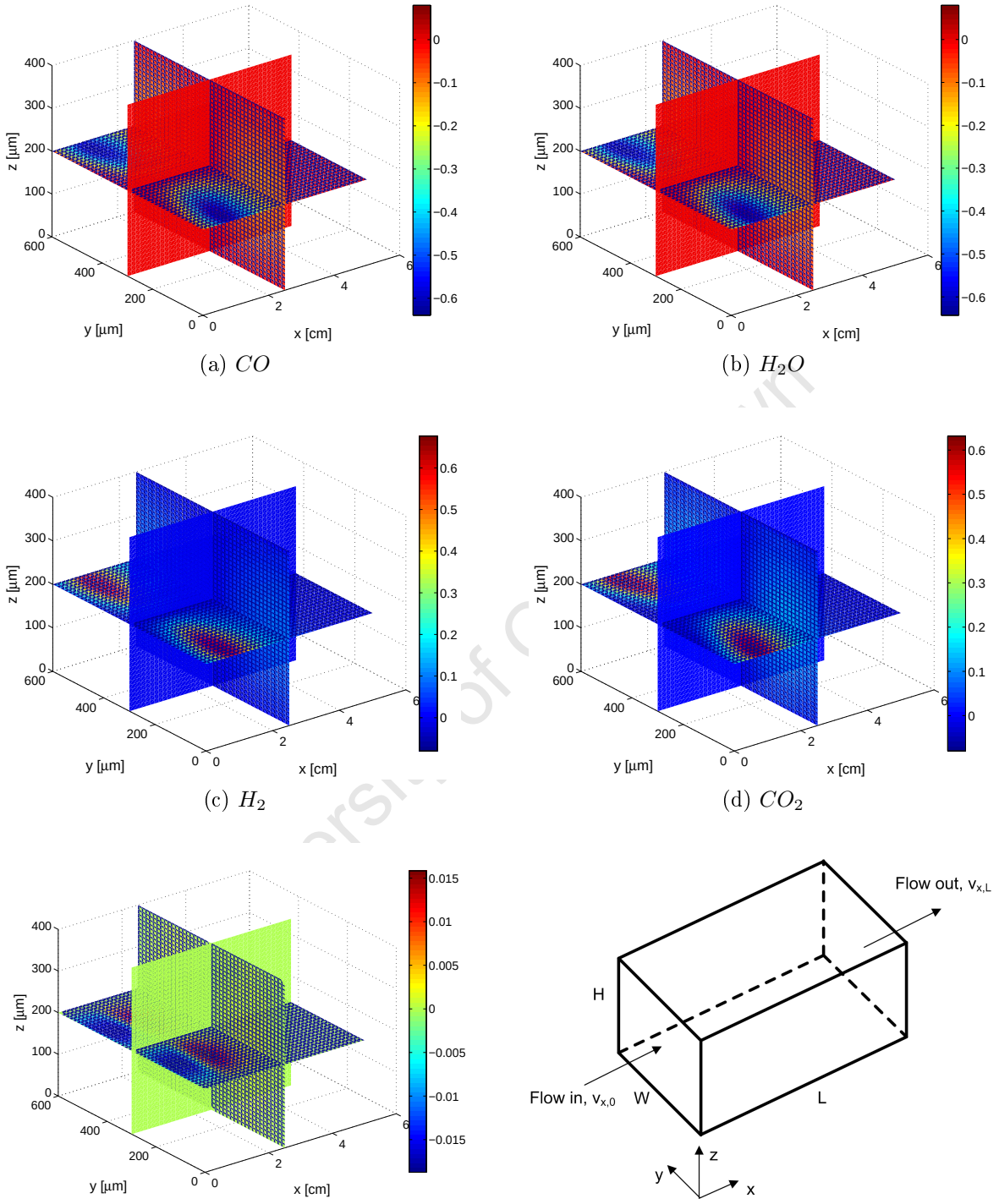

(a) CO (b) H_2O

(c) H_2 (d) CO_2

(e) N_2 (f) Schematic microchannel

Figure 6.8: y-Component flux fields, $N_y\,[mol/m^2.s]$. $W \times H \times L = 400.0 \times 600.0\mu m \times 5.0cm$, $\delta_{cat} = 10.0\mu m$, $SV = 120.0\,mol/s.kg_{cat}$ $P = 3\,bar$ $T = 573.15\,K$, $k_0 = 4.4 \times 10^7\,m^3/s.kg_{cat}$, $E_a = 86.0 \times 10^3\,J/mol$ and inlet composition $\begin{pmatrix} CO & H_2O & H_2 & CO_2 & N_2 \end{pmatrix} = 20.0$. Full 3-dimensional model used.

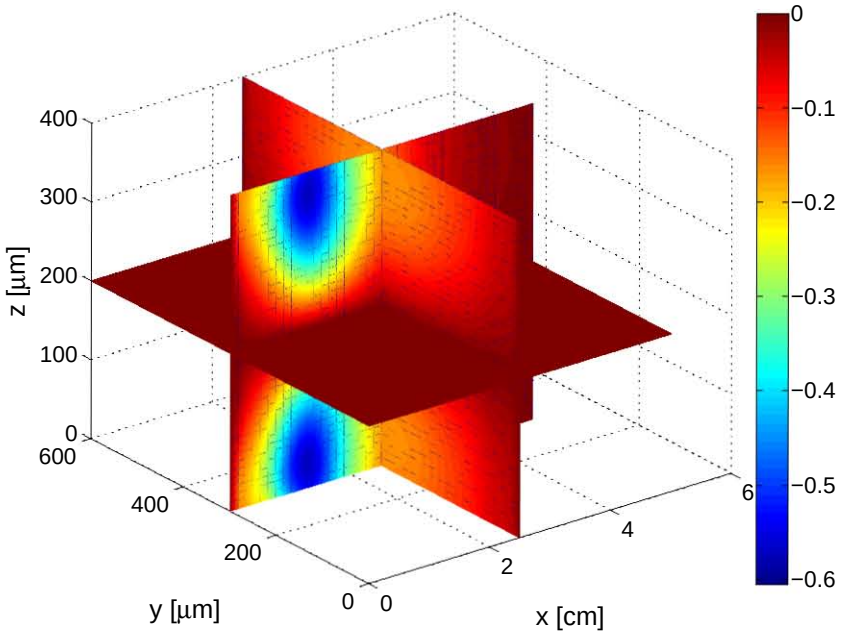

Figure 6.9: z-Component flux field of CO $[mol/m^2.s]$

The fluxes of the reacting components are maximum at the wall and decrease to zero at the channel center. There are two points of discussion here. The first is that the flux is not held constant across the channel as in a stagnant film balance. This requires $\frac{dN_{y,i}}{dy} = 0$ through the mass balance across the film domain which essentially states that $N_{y,i}$ is constant across it. This is not the case in the microchannel domain as a species can take multiple directions of movement simultaneously. This is shown in the steady state species balance which takes the form

$$\frac{\partial N_{y,i}}{\partial y} = -\frac{\partial \left(\chi_i c_t v_{x,i}\right)}{\partial x} - \frac{\partial N_{z,i}}{\partial z} \tag{6.5}$$

So, a molecule that starts off with a y-directional flux at the wall and has that flux dissipated in the x and z directions as it moves to the channel center. If the channel were to have y, z symmetry, then the flux loss from the y- to the z-direction would be balanced by the gain from the z- to the y-direction. This would mean that the flux dissipation would occur in the x-direction only and the rate of dissipation would be a function of the bulk gradient $\frac{\partial(\chi_i c_t v_{x,i})}{\partial x}$ only. This bulk gradient would now give the flux value at the end of the y-domain which is at the channel center. However this flux would have to be set to zero for two conceptually similar scenarios.

1. Center symmetry requires that the flux from the reaction wall considered in the model be balanced with the y-component flux in the opposite direction from the opposite wall. This means that the center flux should be zero, and is shown as such in the solution.

2. Had there been a non-reactive wall at the center point, the y-component flux would also have to be zero.

A comparison of Figures 6.8a and 6.9 shows that the z-component flux fields exhibit the same behaviour as y-components. This is expected as the microchannel has diagonal symmetry in its flux behaviour and the normalised z-component flux matrix is just the transpose (or rotation around the diagonal) of the normalised y-component flux matrix. Although this simplification is not built into the model the for purposes of generalisation (see Section 4.5.2), the observed symmetry shows that the reaction at the different catalyst surfaces generate similar flux profiles.

6.3.4 Composition profile

The main trends in the composition (mole fraction) fields are investigated to validate the solution of the species balances. The composition field across all quadrants is shown for all species in Figure 6.10 for illustrative purposes. The 2-dimensional x-directional profiles taken at different y positions for a chosen z position at $z = 1/2 H_I$ is shown for all species in Figure 6.11.

The first consideration is that the species are consumed and formed as expected, so that the reacting species CO and H_2O reach the same final composition of 0.095 and the product species H_2 and CO_2 that of 0.305. The final composition of the inert N_2 is the same as its inlet composition.

The second consideration is the form of the profiles in the kinetic range. These are flatter for H_2 compared to other species e.g. CO_2 as H_2 has a lower molar mass and hence a faster diffusivity. The heaviest species, CO_2 exhibits interesting behaviour as it overshoots its final composition at the wall. This is attributed to the high rate of reaction that leads to accumulation at the wall. This is not seen for the other product, H_2 as it has a higher diffusivity than CO_2. The composition of the inert N_2 also shows some deviation from its inlet composition as it partially compensates for the increase in the CO_2 composition. The other species compositions also adjust to compensate for the increased CO_2 composition but the effect is not observable above the effect of the reaction on these species.

The third consideration is that the perpendicular y and z profiles flatten out as equilibrium is reached and can be seen as such in Figure 6.10. It is also seen in Figure 6.11 as a convergence of all perpendicular axial profiles. This verifies that the flux is correctly driven by the rate of reaction and the solution is stable under zero reaction.

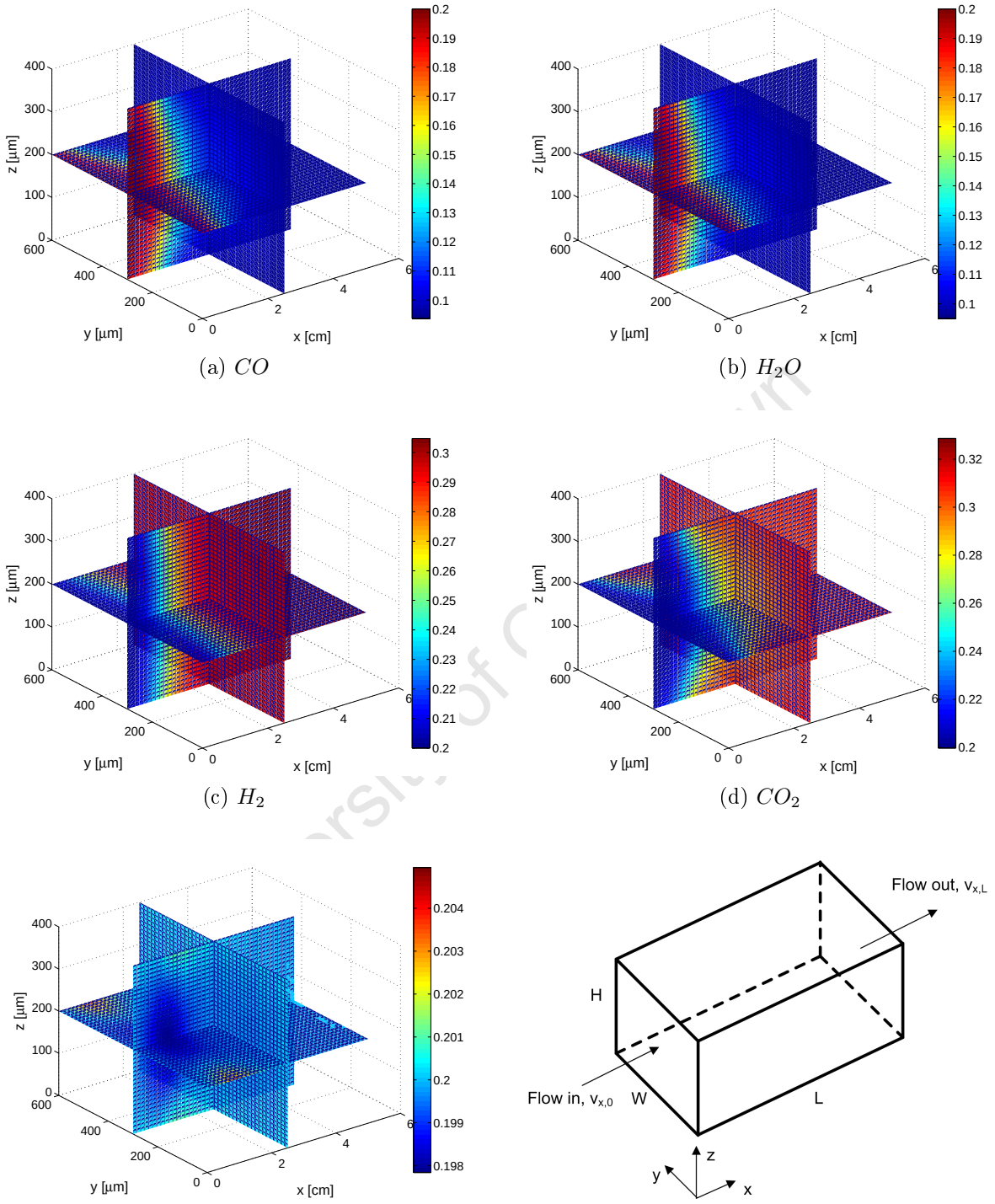

(a) CO (b) H_2O

(c) H_2 (d) CO_2

(e) N_2 (f) Schematic microchannel

Figure 6.10: Composition fields. $W \times H \times L = 400.0 \times 600.0 \mu m \times 5.0 cm$, $\delta_{cat} = 10.0 \mu m$, $SV = 120.0\, mol/s.kg_{cat}$ $P = 3\, bar$ $T = 573.15\, K$, $k_0 = 4.4 \times 10^7\, m^3/s.kg_{cat}$, $E_a = 86.0 \times 10^3\, J/mol$ and inlet composition $\begin{pmatrix} CO & H_2O & H_2 & CO_2 & N_2 \end{pmatrix} = 20.0$. Full 3-dimensional model used.

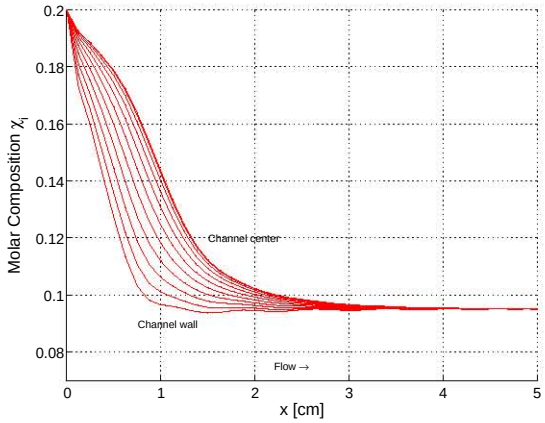

(a) CO

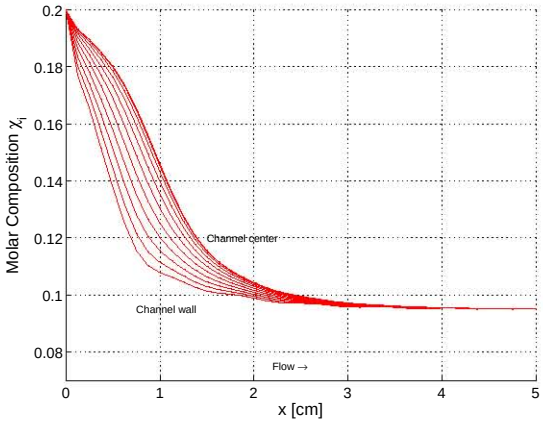

(b) H_2O

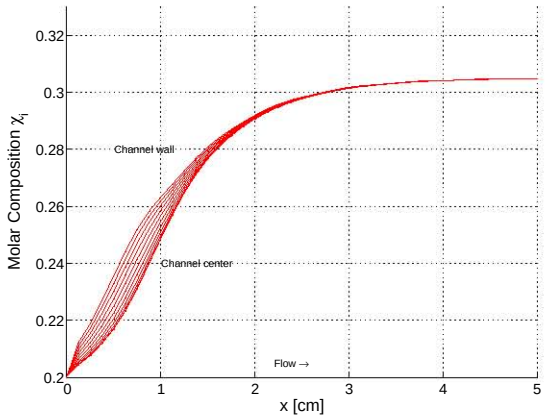

(c) H_2

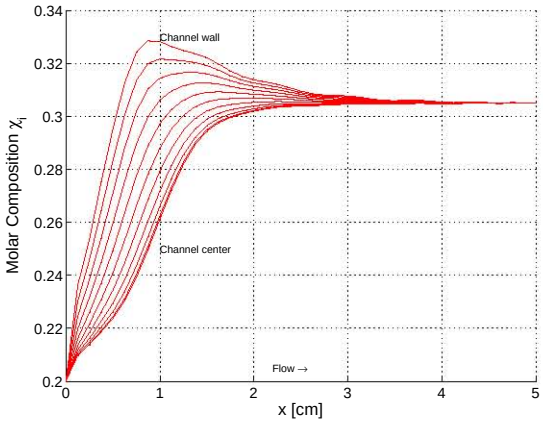

(d) CO_2

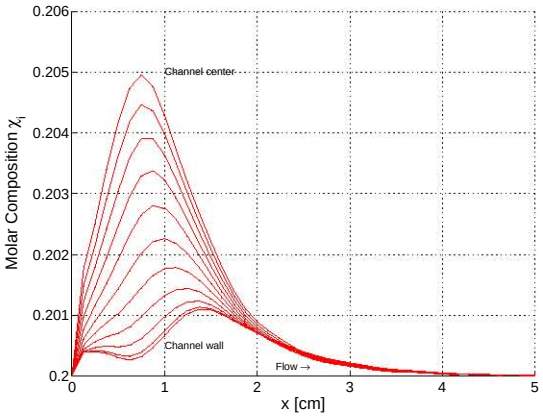

(e) N_2

Figure 6.11: Axial composition profiles at different y perpendicular positions for $z = 200\,\mu m$, center of channel height. $W \times H \times L = 400.0 \times 600.0\mu m \times 5.0cm$, $\delta_{cat} = 10.0\mu m$, $SV = 120.0\,mol/s.kg_{cat}$ $P = 3\,bar$ $T = 573.15\,K$, $k_0 = 4.4 \times 10^7\,m^3/s.kg_{cat}$, $E_a = 86.0 \times 10^3\,J/mol$ and inlet composition $\begin{pmatrix} CO & H_2O & H_2 & CO_2 & N_2 \end{pmatrix} = 20.0$. Full 3-dimensional model used.

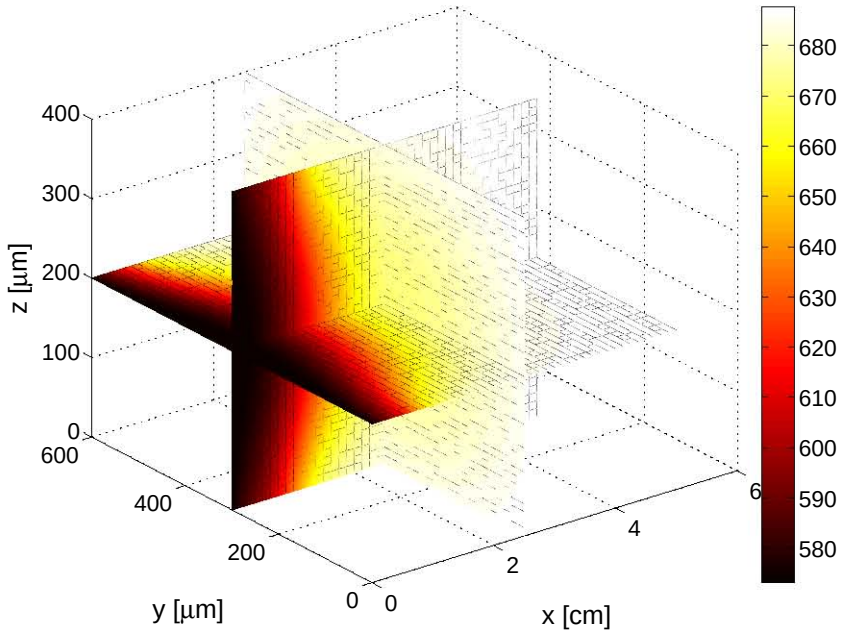

(a) Temperature field, T [K].

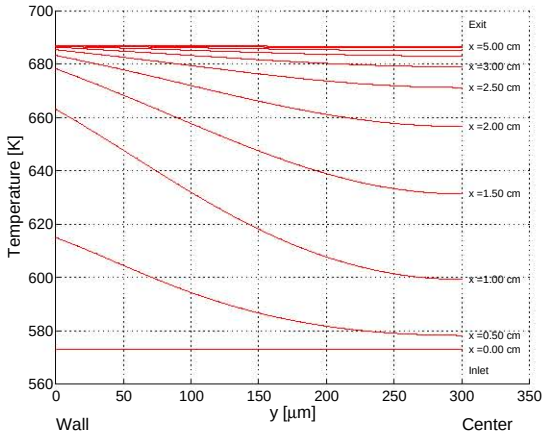

(b) Perpendicular temperature profiles.

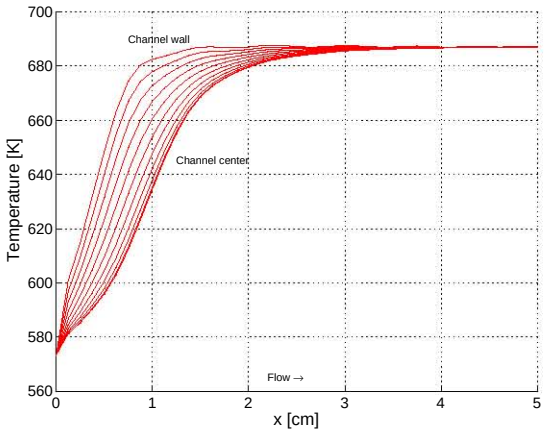

(c) Axial temperature profiles

Figure 6.12: Temperature profiles at $z = 200\,\mu m$, center of channel height. $W \times H \times L = 400.0 \times 600.0 \mu m \times 5.0 cm$, $\delta_{cat} = 10.0 \mu m$, $SV = 120.0\,mol/s.kg_{cat}$ $P = 3\,bar$ $T = 573.15\,K$, $k_0 = 4.4 \times 10^7\,m^3/s.kg_{cat}$, $E_a = 86.0 \times 10^3\,J/mol$ and inlet composition $\begin{pmatrix} CO & H_2O & H_2 & CO_2 & N_2 \end{pmatrix} = 20.0$. Full 3-dimensional model used.

6.3.5 Temperature profile

The main trends in the temperature field are investigated to verify the solution of the energy balance. The temperature field across all quadrants is shown in Figure 6.12a for illustrative purposes. The 2-dimensional axial profiles taken at different y positions for a chosen z position at $z = 200\,\mu m$ is shown in Figure 6.12b while the y-directional profiles taken at different x positions for a chosen z position at $z = 200\,\mu m$ is shown in Figure 6.12c.

Temperature field The temperature field is shown in Figure 6.12a. This shows that the temperature in the bulk does not exceed the wall temperature. This means that the energy balance formulation and solution is sound and no unaccounted energy is being numerically added or lost via the center or wall boundary conditions respectively.

The temperature rise of $\sim 113^oC$ is roughly comparable to that of a previously simulated $\sim 80^oC$ rise (Spatenka et al., 2005), with the difference attributable to the higher assumed reaction rate. This rough agreement confirms that the model does not lose heat to a numerical sink or gain heat as a result of a double addition of heat through differential heat fluxes *and* a separate heat of reaction term.

Temperature gradient Figure 6.12c shows that the temperature gradient increases sharply at the beginning when the reaction rate is highest and as reaction slows down due to equilibrium limitations the gradient in the profiles level off. This indicates the action of heat transport due to species diffusion and thermal conduction. The temperature gradients at the center point, $y = 300\,\mu m$ in Figure 6.12b are zero ensuring that continuity across the symmetry line is held.

6.3.6 Axial velocity profile

The axial velocity field is shown in Figure 6.13. This analysis is done to verify expected trends. The laminar form of the field, given by Equation 4.2 is maintained across the whole solution space while the overall axial velocity at each point is increased proportional to temperature increase. The reason for this is that as the temperature increases the gas expands and, as the channel is an open system, the velocity is allowed to increase to ensure that there is no buildup of pressure at any point within the reactor. The effect of this increased velocity and temperature on the concentration profile is discussed in the next section.

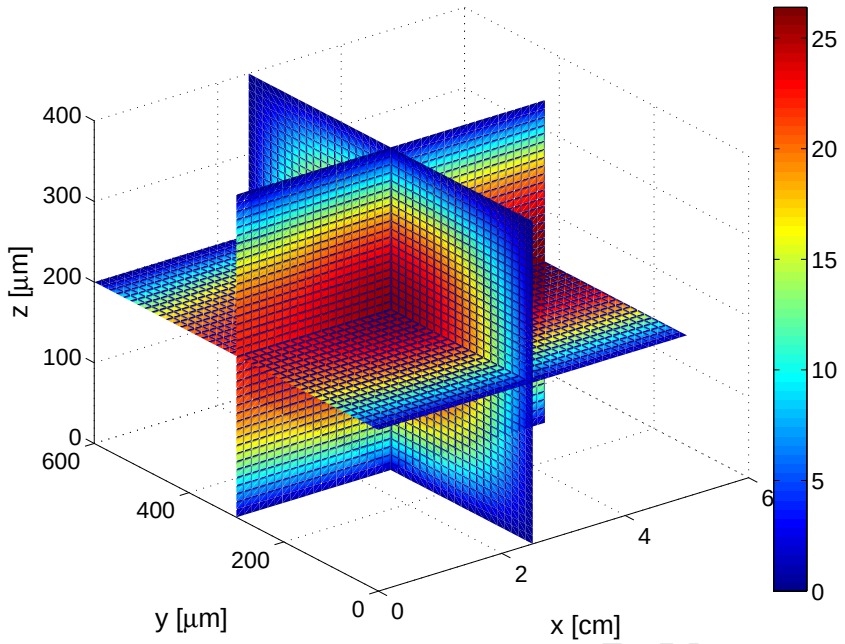

Figure 6.13: Axial velocity field, v_x $[^m/_s]$. $W \times H \times L = 400.0 \times 600.0\mu m \times 5.0cm$, $\delta_{cat} = 10.0\mu m$, $SV = 120.0\, mol/s.kg_{cat}$ $P = 3\, bar$ $T = 573.15\, K$, $k_0 = 4.4{\times}10^7\, m^3/s.kg_{cat}$, $E_a = 86.0 \times 10^3\, J/mol$ and inlet composition $\begin{pmatrix} CO & H_2O & H_2 & CO_2 & N_2 \end{pmatrix} = 20.0$. Full 3-dimensional model used.

6.3.7 Total concentration profile

The main trends in the total concentration field are investigated to verify the solution of the continuum equation. The concentration field across all quadrants is shown in Figure 6.14a for illustrative purposes. The 2-dimensional axial profiles taken at different y positions for a chosen z position at $z = 200\,\mu m$ is shown in Figure 6.14b while the y-directional profiles taken at different x positions for a chosen z position at $z = 200\,\mu m$ is shown in Figure 6.14c.

The concentration profiles in Figure 6.14c shows that it has exactly the opposite trends as the temperature profiles in Figure 6.12c. These two solution variables are linked via the ideal gas law $c_t = \frac{p}{R}\frac{1}{T}$ therefore in a constant pressure environment, the inverse relationship is expected. This relationship is not found explicitly in the equation set however the link is provided by the axial velocity calculation in Equation 4.2. The axial velocity is present in the continuity equation in Equation 4.13. As velocity increases with temperature we have a positive $\frac{\partial v_x}{\partial x}$ which has to be balanced out with a negative $\frac{\partial c_t}{\partial x}$. For the overall mass balance to hold the total concentration has to decrease proportionately with any increase in velocity, and in turn temperature which is expected from the ideal gas law.

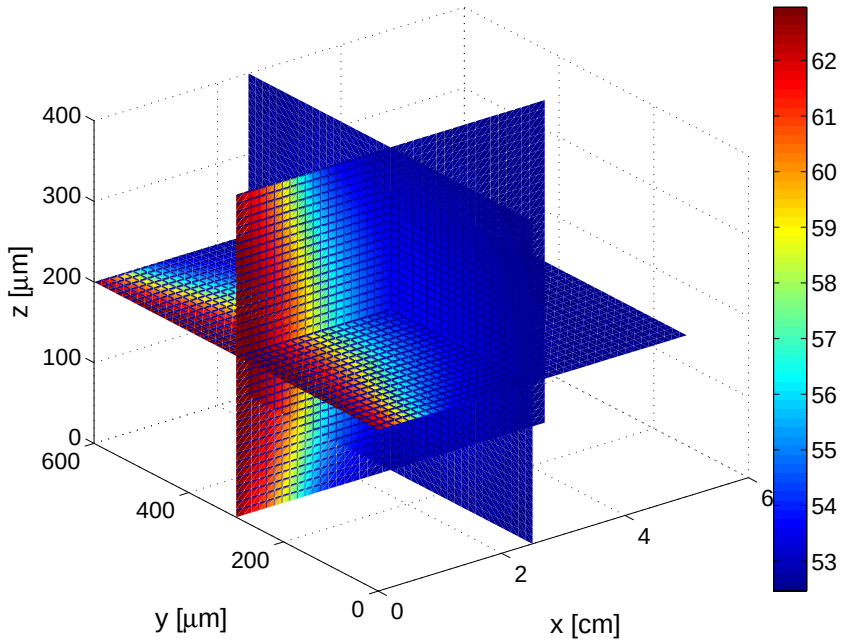

(a) Total concentration field, $c_t\ ^{mol}/_{m^3}$.

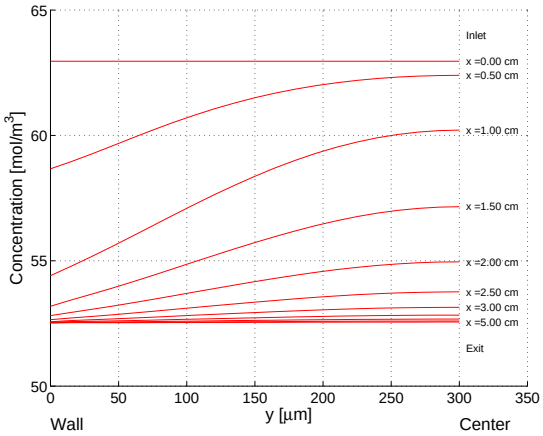

(b) Perpendicular profiles.

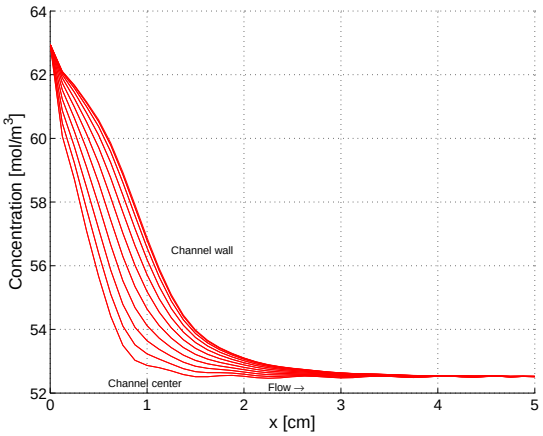

(c) y axis profiles

Figure 6.14: Total concentration profiles at $z = 200\,\mu m$: center of channel height. $W \times H \times L = 400.0 \times 600.0 \mu m \times 5.0 cm$, $\delta_{cat} = 10.0 \mu m$, $SV = 120.0\,mol/s.kg_{cat}$ $P = 3\,bar$ $T = 573.15\,K$, $k_0 = 4.4 \times 10^7\,m^3/s.kg_{cat}$, $E_a = 86.0 \times 10^3\,J/mol$ and inlet composition $\begin{pmatrix} CO & H_2O & H_2 & CO_2 & N_2 \end{pmatrix} = 20.0$. Full 3-dimensional model used.

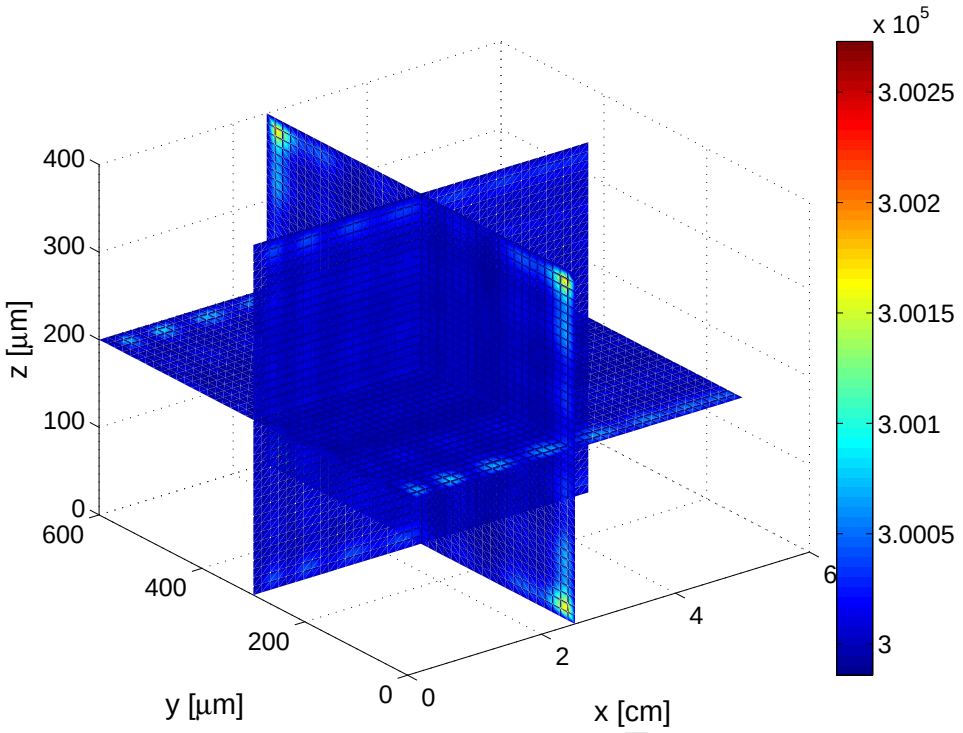

Figure 6.15: Pressure field, $P\ [bar]$. $W \times H \times L = 400.0 \times 600.0\mu m \times 5.0cm$, $\delta_{cat} = 10.0\mu m$, $SV = 120.0\, mol/s.kg_{cat}$ $P = 3\, bar$ $T = 573.15\, K$, $k_0 = 4.4 \times 10^7\, m^3/s.kg_{cat}$, $E_a = 86.0 \times 10^3\, J/mol$ and inlet composition $\begin{pmatrix} CO & H_2O & H_2 & CO_2 & N_2 \end{pmatrix} = 20.0$. Full 3-dimensional model used.

6.3.8 Pressure

The pressure field is calculated by the ideal gas law using the solution variables from the continuum equation and the energy balance. The reason for this is to confirm that the initial assumption of constant pressure holds through the numerical solution. The field is shown in Figure 6.15. The pressure at the solution points remains at 3 bar while the interpolated solution between these points shows some oscillation. This means that the Lagrange polynomials provide the solution at the collocation points, but deviate in its total form. The oscillatory nature of the solution is consistent with the form that the Lagrange polynomials take when they are expected to take a constant value over a large domain. This is shown in Section 2.9.4. The variations in the field are, however in the order of *mbar* and pressure can be reasonably thought of as constant.

6.4 Regression studies

The purpose of this investigation is both to test the reactor model's ability to predict experimental data generated at isothermal conditions and evaluate the model's computational efficiency and numerical stability when called in a regression routine.

Table 6.5: Conditions for regression from Germani et al. (2005)

Parameter						Value					
Reactor dimensions			L	W	H	0.05	600×10^{-6}	400×10^{-6}	m		
Catalyst layer thickness			δ_{cat}			$10 \times 10^{-6}\, m$					
Inlet composition	χ_{CO}	χ_{H_2O}	χ_{H_2}	χ_{CO_2}	χ_{N_2}	9.6	23.0	32.2	8.4	26.8	$mol\%$
Pressure			p			3 bar					
Space velocity			SV			$0.59\,{}^{\text{mol}}/_{\text{s.kg}_{\text{cat}}}$					
Operation						Isothermal					

Regression is performed against data from literature (Germani et al. 2005) also shown in Figure 2.9 with corresponding reactor conditions given in Table 6.5. The data provides CO conversions for different operating temperatures at a single space velocity. The data points used are in the kinetic range. This allows the estimation of two kinetic coefficients k_0 and E_a. This is an overspecified problem and requires the solution of a non-linear least squares problem. The regression uses a Levenberg-Marquard routine LMDIF.for.

All runs are carried out using a $[7, 3, 3]$ mesh as steep gradients are not expected. The model is called in isothermal model by heat loss term to the heat of reaction as in Equation 4.17.

6.4.1 Regression study 1

Regression is carried out on the P2C1 sample of the study in (Germani et al., 2005). This data has been regressed against in the study for k_0 and E_a in the rate law in Equation 2.88. The developed model is run at the same conditions as the literature data and the conversion profiles are plotted in Figure 6.16. The space velocity is taken as $SV = 0.59{}^{\text{mol}}/_{\text{s.kg}_{\text{cat}}}$. The calculation is based on information presented in the reference and is shown in Appendix B.3.

The parameters obtained upon regression are reported in Table 6.6 and compared to the reported parameters. Figure 6.16 compares the experimental data to the model predictions and indicates the close fit of model conversions to experimental data.

It is of interest to note that the P2C1 sample coefficients are similar to that reported (Germani et al., 2005). The model used in the literature study assumed plug flow to generate its model coefficients. As the full 3-dimensional model predicts very similar coefficients, the assumption of zero mass transport at these reaction conditions holds well. However upon scale-up of capacity, the channel width and height can be increased (Kolb et al., 2008) which makes it valuable from a design point of view to determine

Table 6.6: Comparison of parameters used. The regressed P2C1 sample is compared to that of (Germani et al., 2005). The P2C1R and P2C1H are independently obtained by trial and error.

	k_0 $\text{s.kg}_{\text{cat}}/\text{mol.bar}^{0.05}$	E_a J/mol
(Germani et al., 2005)	1.3×10^6	86.0×10^3
Model: P2C1	1.3×10^6	86.1×10^3
Model: P2C1R	6.0×10^5	86.0×10^3
Model: P2C1H	3.8×10^5	86.0×10^3

the regions and extent of mass transport limitations. This test does, however validate the model's ability to predict exit conversion against existing experimental data and rate expressions.

This test also serves as a validation of the models ability to reduce to plug-flow as the reactor conditions demand. The measure of the plug flow nature of the reactor profiles is given by the external effectiveness factor defined in Equation 4.24. The external effectiveness factor is calculated to be $\eta_r > 0.99$ for the conditions of regression and is shown in Figure 7.14a. This shows that radial composition and temperature profiles are negligible. The reduction of a laminar flow model to a plug flow model under certain situations is further investigated in Section 7.4.

Germani et al. 2005 further indicated that the conversions of the P2C1R and P2C1H catalyst samples can also be predicted by maintaining a constant activation energy $E_a = 86.0 \times 10^3 \text{J}/\text{mol}$ and merely varying the activity k_0. This was not reported but is done by trial and error using the developed model. The obtained parameters are shown in Table 6.6 while the approximated data is shown in Figure 6.16. The close fit to the data is a further indication of the models ability to predict data in both the kinetic and thermodynamically controlled regimes.

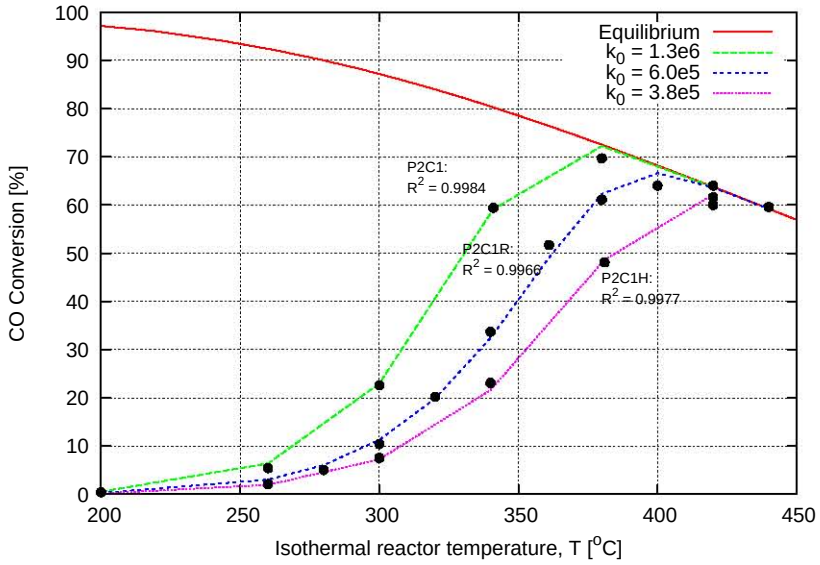

Figure 6.16: Isothermal conversion of carbon dioxide over $Pt/CeO_2/Al_2O_3$ as a function of inlet temperature. Results are shown for different k_0 values at a constant $E_a = 86.0 \times 10^3$ J/mol. The solid line indicates the thermodynamic equilibrium of the WGS reaction at inlet conditions: 9.6 mol % CO, 23.0 mol % H_2O, 33.2 mol % H_2, 8.40 mol % CO_2, 26.8 mol % N_2. Channel dimensions are: $L = 5$cm, $W = 600\mu$m, $H = 400\mu$m$\delta_{cat} = 10\mu$m $SV = 0.59^{\text{mol}}/_{\text{s.kg}_{\text{cat}}}$ $p = 3$ bar.

6.4.2 Regression study 2

A reduced order WGS rate law is required for a simplified analysis of mass transfer effects. The rate law can feasibly be modified to first order in concentration of CO. The first order approximation has a basis in the kinetic study of (Kieski et al., 1993). At low concentrations of CO there is a risk of the reaction proceeding even if no H_2O is present. This is not an issue in the reactor setup presented in Figure 1.2 as H_2O is normally in large excess as a result of its production in the upstream reformer unit.

The modified rate law takes the form

$$r_{CO} = \rho_{cat} k_0 e^{\frac{-Ea}{RT}} c_t \chi_{CO} (1 - \beta) \tag{6.6}$$

An approximate k_0 with units $\frac{m^3}{s.kg_{cat}}$ is now required. This constant needs to yield a reaction rate that is similar to that of experimental data for a feasible catalyst system. Regression is carried out and the fit is reported in Figure 6.17. The regressed coefficients are $k_0 = 9.92 \times 10^4$ and $E_a = 83.4 \times 10^3$J/mol. The estimated activation energy is similar to that obtained for the full order kinetic model in Table 6.6. This indicates that only the catalyst activity, k_0 adjusts its change in units.

The fit obtained deviates from the experimental data on observation and has an $R^2 =$

0.9915 compared to an $R^2 = 0.9984$ for the full order model. The first order model is therefore less adequate than the full order model in describing the catalyst system but it nevertheless provides a good approximation of the system's behaviour.

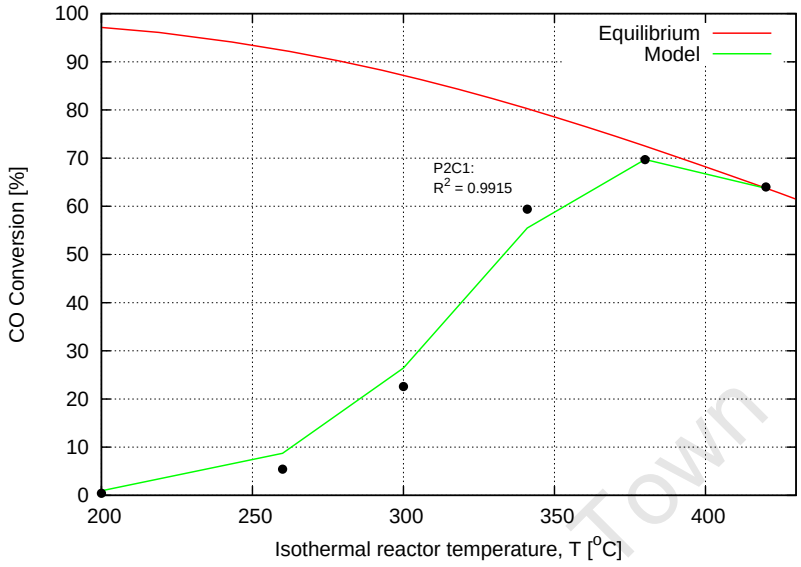

Figure 6.17: Isothermal conversion of carbon dioxide over $Pt/CeO_2/Al_2O_3$ as a function of inlet temperature. The solid line indicates the thermodynamic equilibrium of the WGS reaction at inlet conditions: 9.6 mol % CO, 23.0 mol % H_2O, 33.2 mol % H_2, 8.40 mol % CO_2, 26.8 mol % N_2. Channel dimensions are: $L = 5$cm, $W = 600\mu$m, $H = 400\mu\text{m}\delta_{cat} = 10\mu$m $SV = 0.59^{\text{mol}}/_{\text{s.kg}_{\text{cat}}}$ $p = 3$ bar.

6.4.3 Regression study 3

A third regression is carried out at a contrived space velocity of $SV = 6.2^{\text{mol}}/_{\text{s.kg}_{\text{cat}}}$ that induces transport limitations. This is done merely to test the stability of the model under regression conditions and is not performed to compare the regressed parameters to previous studies. A modified rate law of order 1.5 is used to obtain a closer fit to the data than the first order rate law. The fit of the model is shown in Figure 6.18. The regressed coefficients give the rate law the form

$$r_{CO} = 867.2 \times 10^6 e^{\frac{97.9\times10^3}{RT}} p_{CO}^{1.0} p_{H_2O}^{0.5} (1-\beta) \tag{6.7}$$

The regression is completed in 58 objective function evaluations in 773 s ($12m53s$) at approximately $13s$ per model evaluation. This is a verification of the model's robustness within a regression environment.

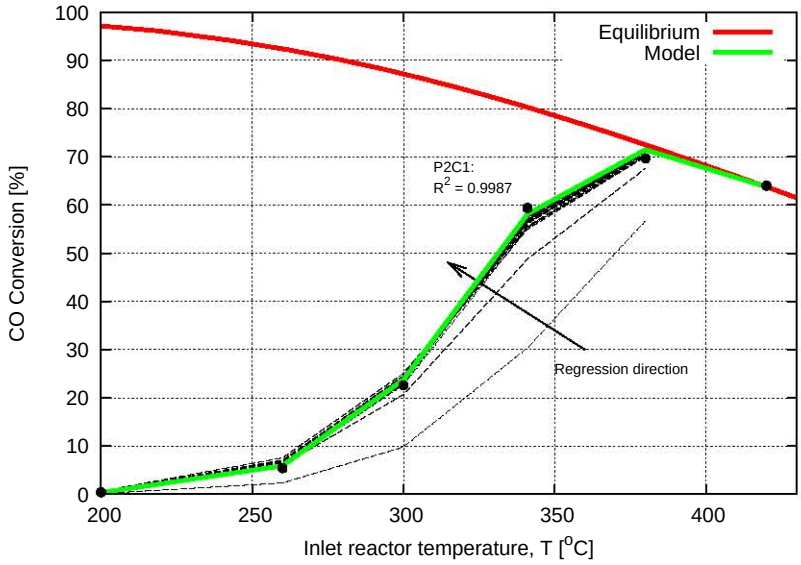

Figure 6.18: Isothermal conversion of carbon dioxide over $Pt/CeO_2/Al_2O_3$ as a function of inlet temperature. The solid line indicates the thermodynamic equilibrium of the WGS reaction at inlet conditions: 9.6 mol % CO, 23.0 mol % H_2O, 33.2 mol % H_2, 8.40 mol % CO_2, 26.8 mol % N_2. Channel dimensions are: $L = 5\text{cm}$, $W = 600\mu\text{m}$, $H = 400\mu\text{m}$, $\delta_{cat} = 10\mu\text{m}$, $SV = 6.2^{\text{mol}}/_{\text{s.kg}_{\text{cat}}}$, $p = 3\text{bar}$.

Chapter 7

Mass Transport Effects

7.1 Analysis of dimensional effects

Before any investigations are carried out on mass transfer effects, the physical situation is analysed to determine an appropriate methodology. The most common methods of evaluating external and internal mass transport limitations are variation of channel height and catalyst layer thickness respectively (Walter et al. 2005). These methods are analysed for the microchannel system with reaction at all walls shown in Figure 4.2.

7.1.1 Variation of Channel Width and Height

Channel height is varied to increase the diffusional distance between channel center and reaction surface. As this distance is increased, the conversion is expected to change given the presence of external transport limitations. The severity of this change is an indication of the extent of external transport limitations. To isolate the effect of diffusional distance on conversion both the space velocity, SV and the average reactor residence time $\tau = \frac{L}{v_0}$ need to be kept constant (Walter et al., 2005). It is sufficient to maintain the SV constant in an ideal reactor to keep conversion constant, however in a non-ideal LFR a change in velocity will also change reactor RTD and so conversion. This is discussed in Section 2.3.4. To isolate the effect of any edge effects, the aspect ratio, $AR = \frac{W_I}{H_I}$ is also kept constant.

Constant aspect ratio Consider a doubling of the internal width and height W_I and H_I at constant aspect ratio, AR. This increases the internal cross-sectional area, $XSA_I = W_I H_I$ by a factor 4 and volume of catalyst $V_{cat} = L\,(WH - XSA_I)$ by a factor $\sim$<2 at

constant catalyst layer thickness δ_{cat}.[1] This means that the space velocity will increase by a factor $\sim<2$ as in 7.1.

$$SV = \frac{v_0 XSA_I c_t}{V_{cat}\rho_{cat}} \tag{7.1}$$

$$= \frac{v_0 XSA_I c_t}{L\left(WH - XSA_I\right)\rho_{cat}}$$

$$= \frac{XSA_I c_t}{\tau\left(WH - XSA_I\right)\rho_{cat}} \tag{7.2}$$

For the space velocity to remain constant, the only parameter that can be varied in Equation 7.2 is the total channel cross-sectional area $WH = (W_I + 2\delta_{cat})(H_I + 2\delta_{cat})$ through a change in catalyst thickness, δ_{cat}. This is consistent with literature evaluations (Walter et al., 2005). Substituting this expression into Equation 7.2 and rearranging gives a quadratic expression for the adjusted catalyst thickness

$$4\delta_{cat}^2 + 2\left(W_I + H_I\right)\delta_{cat} - \frac{v_0 XSA_I c_t}{SV\, L\rho_{cat}} = 0 \tag{7.3}$$

The catalyst thickness is now added to the inner width and height to give the total channel dimensions.

Constant height The same analysis can be applied for a doubling of just one of the channel dimensions, W_I or H_I while maintaining the other constant. As an increase in catalyst volume is not directly proportional to internal cross-sectional area a similar adjustment as in Equation 7.3 will have to be made to catalyst layer thickness to maintain constant space velocity.

These results means that channel dimensions cannot be varied independently of catalyst layer thickness for constant space velocity and residence time in a channel with catalyst coated on the walls. For purposes of investigation this means that the effects of a change in external dimensions on external transport limitations cannot be evaluated for constant internal dimensions and their effects.

7.1.2 Variation of Catalyst Layer Thickness

As similar analysis is carried out for a change in catalyst layer thickness. Catalyst layer thickness is changed to evaluate the effect of a change in diffusional distance within the

[1] The volume of catalyst will increase by a factor less than 2 as the catalyst volume behind the exposed surface area doubles, but the volume in the four corners remains constant ($4 \times \delta_{cat}^2$). This lag between the factor increase in V_{cat} to XSA_I therefore becomes more significant at higher catalyst thicknesses.

catalyst on the reactor conversion. A change in conversion upon a change in thickness is an indication of the presence of internal transport limitations. The effect of catalyst layer thickness on external transport limitations has been noted in a previous study (Parak et al. 2009). This is that the conversion increased with catalyst thickness in the region of transport control as the surface area for mass and heat transport decreases per volume catalyst with an increase in layer thickness. This allows less heat to dissipate from the catalyst layer given the presence of external transport limitations and therefore enhances the rate of reaction within the catalyst.

To isolate the effect of a change in catalyst layer thickness on conversion, the space velocity and residence time have to be kept constant. Space velocity is given by Equation 7.2. With a change in catalyst layer thickness δ_{cat} the value of WH changes. For a constant residence time, the only parameter left to change is the internal channel dimensions W_I and H_i. For a constant aspect ratio, we have $W_I = AR\,H_I$ and the adjusted H_I can be solved for by substituting this into Equation 7.2 and rearranging to give

$$\frac{v_0 ARc_t}{L\,SV\rho_{cat}} H_I^2 - (2AR\rho_{cat} + 2\delta_{cat})\,H_i - 4\delta_{cat}^2 = 0 \tag{7.4}$$

This result is the corollary to that when changing channel dimensions. That is, the catalyst layer thickness cannot be varied independently of the channel dimensions for constant space velocity and residence time in a channel with catalyst coated on the walls. For purposes of investigation this means that the effects of a change in internal dimensions on external transport limitations cannot be evaluated for constant external dimensions and their effects.

The question that needs to be asked is whether conversion will be kept constant if the above formulations were to be applied to reactor conditions that lead to no mass transport limitations. The answer can be obtained in the evaluation of the non-dimensional effects that occur in the microchannel system.

7.2 Analysis of non-dimensional effects

The reactor as described in Chapter 4 is separated into its two constituent components, that of a laminar flow reactor with no diffusion effects (homogeneous effects) and that of a wall reaction with diffusion limitations and no flow (heterogeneous effects). The overall reactor behaviour will be the combination of the effects of the reaction rate and convection (homogeneous effect) and the reaction rate and diffusion (heterogeneous effect). These are coupled in a manner that is given by the complete 3-dimensional model. The homogeneous effects are captured by the laminar flow RTD patterns discussed in Section 2.3.4 and is not treated here. It is necessary to conduct an analysis of heterogeneous effects.

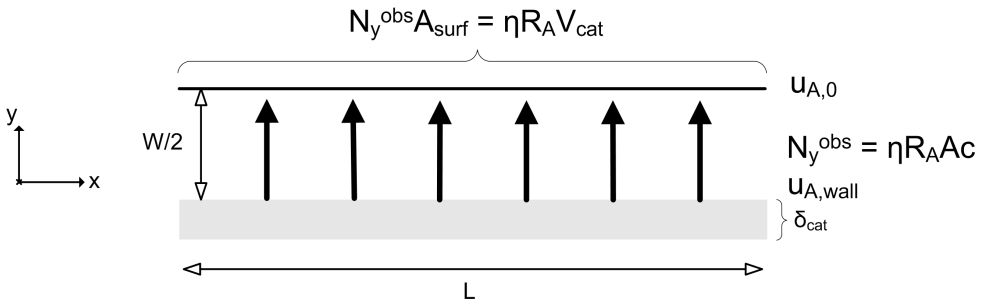

Figure 7.1: Schematic of system described by the second Damköhler number, Da_{II}

7.2.1 Heterogeneous effects

The interaction between the channel dimensions and catalyst layer is now analysed. This analysis is conducted over a hypothetical reactor shown in Figure 7.1. This reactor, now geometry dependent consists of a rectangular duct with reaction surface on the inner walls. The reactant is supplied by an instantaneous source in the center that is uniform for all lengths. No flow is considered as this is a homogeneous effect therefore no integration is possible along the reactor length. This limitation has two consequences. Firstly, the flux generated will not be limited by complete conversion of reactants which will lead to an overestimation of mass transport effects. This also means that the development of a concentration gradient along the reactor length is not accounted for and transport limitations will be underestimated in this regard[2]. However, what is important is not the magnitude of the limitations, but the general behaviour that the reactor configuration described in Section 7.1 leads to.

The channel boundary effects are studied by the manipulation of the wall boundary condition which relates product flux to reaction rate

$$N_y A_{surf} = -r_A V_{cat} \tag{7.5}$$

Assuming Fickian diffusion for flux $N_y = -c_t D_{AB} \frac{\partial u_A}{\partial y}$ and first order reaction $-r_A = \rho_{cat} k c_t \chi_{A,wall}$ gives

$$c_t D_{AB} \frac{\partial \chi_A}{\partial y} A_{surf} = \rho_{cat} k c_t \chi_{A,wall} V_{cat} \tag{7.6}$$

$$\frac{1}{\chi_{A,wall}} \frac{\partial \chi_A}{\partial y} = \frac{\rho_{cat} k \frac{V_{cat}}{A_{surf}}}{D_{AB}} \tag{7.7}$$

[2]At least for a LFR. A PFR will have no development of concentration gradients as the gradient is equalised across the channel width after each axial point.

Given in terms of a non-dimensional perpendicular dimension, $y = YW_I$

$$\frac{1}{\chi_{A,wall}}\frac{\partial \chi_A}{\partial Y} = \frac{\rho_{cat} k \frac{V_{cat}}{A_{surf}} W_I}{D_{AB}} \tag{7.8}$$

$$= Da_{II} \tag{7.9}$$

Assuming plug flow in the center of the channel, the concentration gradient can be linearised as $\frac{\partial \chi_A}{\partial Y} = \frac{\chi_{A,center} - \chi_{A,wall}}{1-0}$. Substituting this expression into Equation 7.8 and given the definition of the concentration effectiveness factor for a first order reaction,$\eta_c = \frac{\chi_{A,wall}}{\chi_{A,center}}$

$$\eta_c = \frac{1}{\frac{\rho_{cat} k \frac{V_{cat}}{A_{surf}} W_I}{D_{AB}} + 1} = \frac{1}{Da_{II} + 1} \tag{7.10}$$

Thus, the conditions for a low effectiveness factor are high channel width, W_I, catalyst activity k (fast reaction) and high $\frac{V_{cat}}{A_{surf}} = Ac$. The last parameter essentially requires a low surface area available for mass flux per volume catalyst to enhance transport limitations. The analytical trends in the expression above are therefore consistent with the physical understanding of reaction systems.

Application of Equation 7.10 converts the conditions given by Damköhler in Equation 2.30 for the regions of mass transport, transition and kinetic control into the effectiveness factor. These are given by

$$\begin{array}{cc} \eta_c > 0.91 & \text{kinetic regime} \\ 0.01 \leq \eta_c \leq 0.91 & \text{transient regime} \\ \eta_c < 0.01 & \text{mass transfer controlled regime} \end{array} \tag{7.11}$$

A further quantity of interest is the observed flux, $N_y^{obs} = \eta_c r_A(\chi_{A,0}) Ac$ which is given for a specific area, $\Delta y \Delta z$ in the reactor. As reactor conversion cannot be integrated for, the behaviour of the entire reactor is given by the observed mass flux across the total catalyst surface area and can be seen as a proxy for conversion. Thus the higher the flux generated across the whole reactor, the higher the conversion. This overall flux is given by

Table 7.1: Range of variation of heterogeneous parameters

Parameter	Symbol	Range
Hydraulic Diameter	D_h	$50 - 1000\,\mu m$
Space velocity	SV	$0.02 - 6.0^{\text{mol}}/_{\text{s.kg}_{\text{cat}}}$
Catalyst activity	k_0	$1 \times 10^4 - 1 \times 10^{12}{}^{\text{m}^3}/_{\text{s.m}^3_{\text{cat}}}$
Activation energy	E_a	$83.4 \times 10^3{}^{\text{J}}/_{\text{mol}}$
Inlet temperature	T	573.15 K
Total pressure	P	3 bar
Inlet velocity	v_0	$0.14^{\text{m}}/_{\text{s}}$
Diffusivity	D_{AB}	$5.0 \times 10^{-5}{}^{\text{m}^2}/_{\text{s}}$

$$N_y^{obs} A_{surf} = \eta_c r_A(\chi_{A,0}) V_{cat} \tag{7.12}$$

$$= \frac{r_A(\chi_{A,0}) V_{cat}}{\frac{\rho_{cat} k_0 e^{\left\{\frac{E_a}{RT}\right\}} \frac{V_{cat}}{A_{surf}} W_I}{D_{AB}} + 1} \tag{7.13}$$

$$= \frac{r_A(\chi_{A,0})}{\frac{\rho_{cat} k_0 e^{\left\{\frac{E_a}{RT}\right\}} \frac{W_I}{A_{surf}}}{D_{AB}} + \frac{1}{V_{cat}}} \tag{7.14}$$

7.3 Evaluation of Heterogeneous Effects

The heterogeneous effects that are analysed in Section 7.2.1 are now evaluated for expected reaction conditions. The ranges of these conditions is shown in Table 7.1. The range of hydraulic diameters is chosen to keep the dimensions within the μm range while the space velocity is chosen an order of magnitude above and below the experimental value of (Germani et al. 2005). The catalyst rate constant is varied between an order of magnitude below and a few orders of magnitude above 10^5, the first order rate constant regressed for in Section 6.4.2. The reason for choosing these values is to constrain the investigation to the microchannel region (D_h and SV) but allow for the evaluation of all possible effects (k_0).

7.3.1 1-Dimensional model: variation of height and width

Channel width and height are varied according to the hydraulic diameters in Table 7.1 with a constant aspect ratio of 1.5.

The changes in the important spatial parameters in Equation 7.12, A_{surf} and V_{cat} are shown in Figure 7.2. Catalyst inner surface area remains constant $O(0)$ (or zero order) with space velocity as it is independent of catalyst thickness but varies linearly in $O(1)$ with changes in hydraulic diameter. The catalyst volume increases quadratically, $O(2)$ with both a decrease in space velocity and an increase in hydraulic diameter. This is seen as a quadratic change with respect to space velocity as it has an $O(2)$ relationship with catalyst layer thickness as shown in Equation 7.3 and an $O(2)$ relationship with a *simultaneous* change in the two $O(1)$ parameters, width and height.

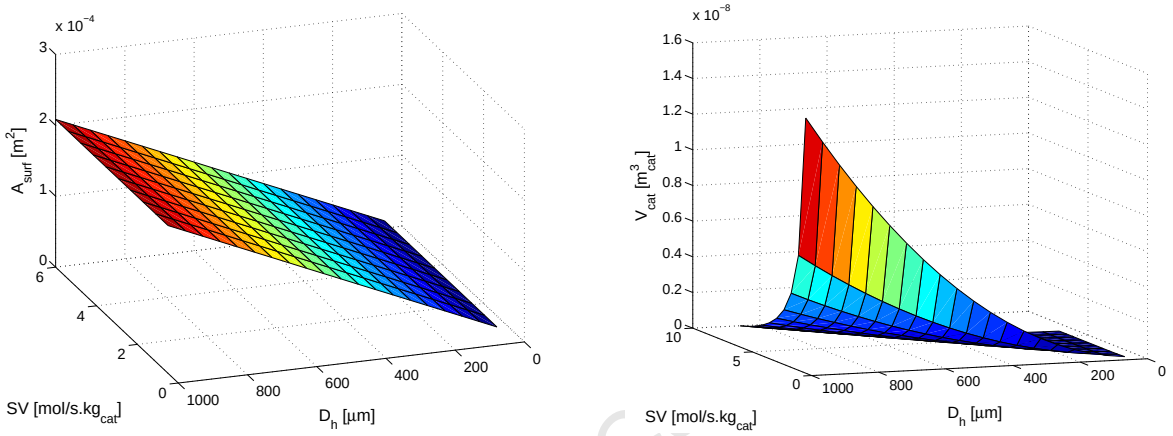

(a) A_{surf} (b) V_{cat}

Figure 7.2: Changes in spatial parameters with D_h and SV. $H_i = 500\,\mu m$ and all other parameters as in Table 7.1.

It should be noted that channel radius has a first order effect on surface area $A_{surf} = 2\pi R_I$ and a second order effect on volume of catalyst $V_{cat} = \pi\left(R^2 - R_I^2\right)$. These effects are the same as that of varying both channel width and height simultaneously. This means that the results obtained from this analysis is equally applicable to a cylindrical channel.

The parameters $Ac = \frac{V_{cat}}{A_{surf}}$ and η_c that form the observed flux are plotted in Figure 7.3 for changes in space velocity and hydraulic diameter. The volume of catalyst per unit surface area increases quadratically with space velocity as it is the quotient of $O(2)$ and $O(0)$ functions while the change with hydraulic diameter is linear as it is the quotient of $O(2)$ and $O(1)$ functions. The concentration effectiveness factor is plotted for changes in the same variables as Ac but for different values of k_0. The effectiveness factor decreases both with a decrease in space velocity and with an increase in k_0 and D_h. The decrease with respect to SV is attributed to the higher volume of catalyst per unit surface area. This decreases the surface area available for mass flux to flatten out the concentration profiles. An increased D_h causes a longer diffusion path while an increased k_0 causes faster reaction which increases the consumption of reactant close to the wall. Both variables thereby enhance the formation of concentration gradients.

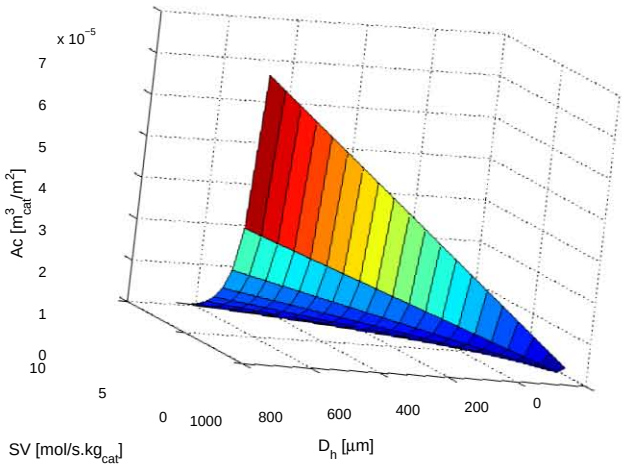

(a) Ac for different SV and D_h

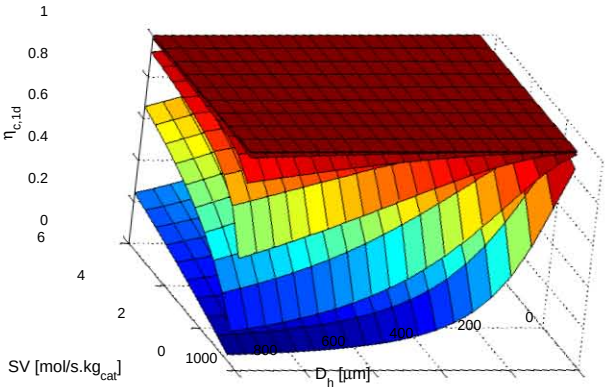

(b) Change in concentration effectiveness factor $\eta_{c,1d}$ with SV and D_h at different k_0.

Figure 7.3: Variation of the parameters on which the observed flux N_y^{obs} depends. $H_i = 500\,\mu m$ and all other parameters as in Table 7.1. Using 1-dimensional model.

As Ac and η_c are acting in opposite directions with respect to SV and D_h, an optimum in N_y^{obs} is expected. This is shown in Figure 7.4. This is however a localised flux and does not take into account the change of catalyst surface area with hydraulic diameter. The more interesting total flux generated over the whole catalyst surface area, $N_y^{obs} A_{surf}$ is plotted against reaction rate and in Figure 7.5 for different values of SV.

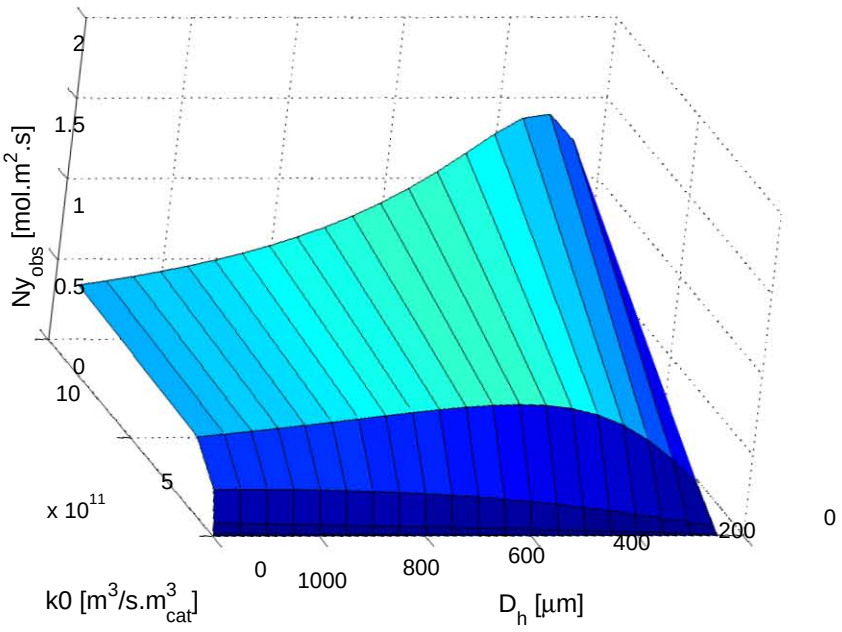

Figure 7.4: Change in observed flux $N_y^{obs} = \eta_c R_A Ac$ with k_0 and D_h. $SV = 0.02\,{}^{\mathrm{mol}}/_{\mathrm{s.kg_{cat}}}$. $H_i = 500\,\mu m$ and all other parameters as in Table 7.1. Using 1-dimensional model.

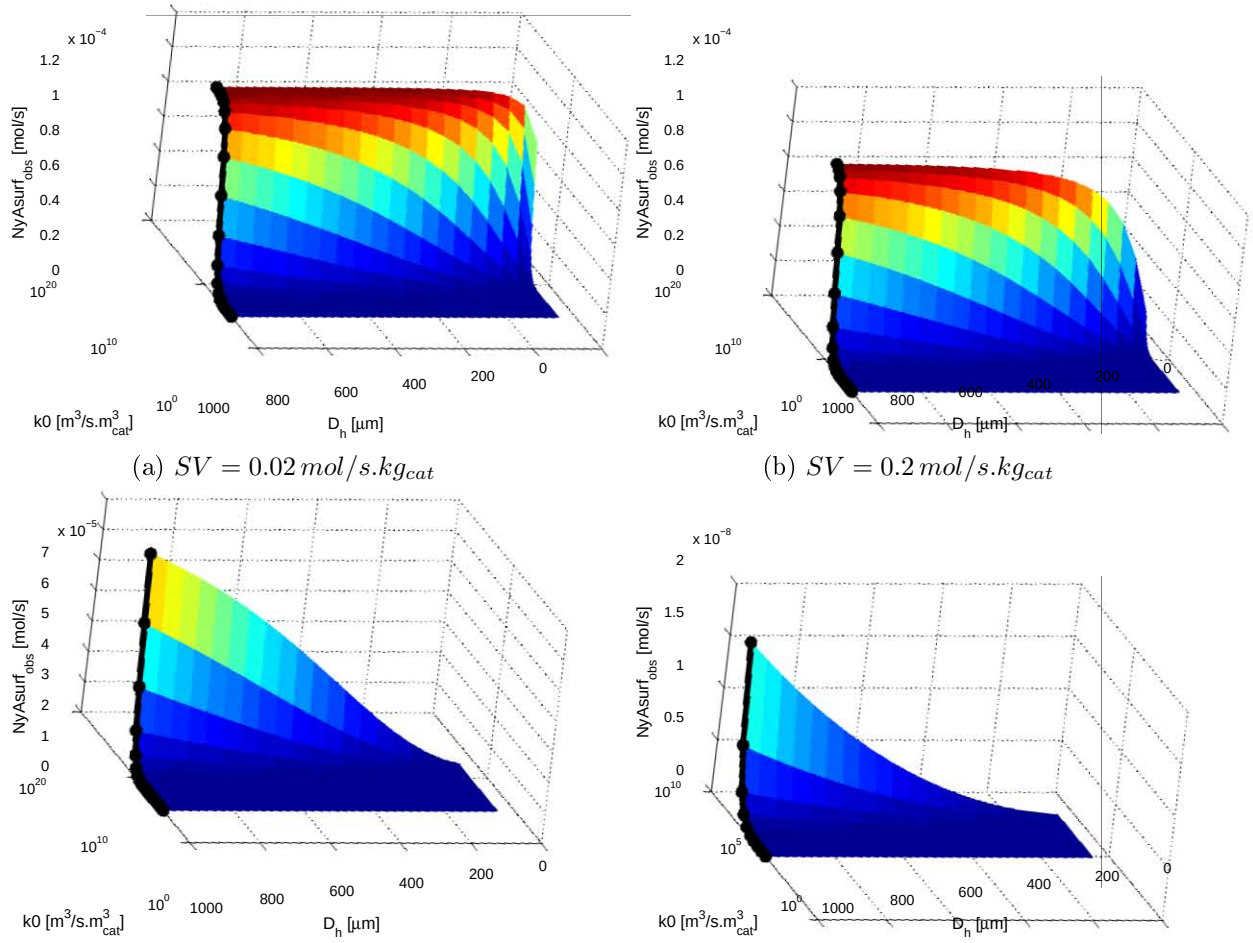

(a) $SV = 0.02\,mol/s.kg_{cat}$ (b) $SV = 0.2\,mol/s.kg_{cat}$

(c) $SV = 10\,mol/s.kg_{cat}$ (d) $SV = 25\,mol/s.kg_{cat}$

Figure 7.5: Change in $N_y A_{surf}$ with $D_h = 50 - 1000\,\mu m$ $k_0 = 1 \times 10^4 - 1 \times 10^{12}\,{}^{\mathrm{m}^3}/_{\mathrm{s.kg_{cat}}}$ for different space velocities. $H_i = 500\,\mu m$ and all other parameters as in Table 7.1. The black lines indicate the points of maximum total flux. Using 1-dimensional model.

The notable trends are as follows:

1. The highest total flux $N_y^{obs} A_{surf}$ occurs at low SV and high k_0 (high reaction rate) as expected

2. The total flux increases with D_h even at constant SV and τ. The quadratic shape of the curve is given by the $\frac{1}{V_{cat}}$ term in Equation 7.14 which increases in $O(2)$ with D_h as discussed earlier. This dominates over the $O(1)$ increase in the $\frac{1}{A_{surf}}$ term as has higher values by a few orders of magnitude.

3. The total flux plateaus off at high k_0 and hydraulic diameter as effectiveness factor limits reaction

4. No maximum is reached for either variable as with N_y^{obs} as surface area available per surface area partially cancels the effect of the decrease in effectiveness factor that gave the optimum in Figure 7.4.

5. The shape of the total flux change with hydraulic diameter is the same for all SV and k_0, within the range of values studied.

6. The ability to reach the maximum total flux depends on SV and k_0. An increase in SV requires higher catalyst activity to reach the maximum level of total flux.

7. All the regions of trends shown in Figure 7.5 may not be accessible in a flow reactor as at high k_0 and low SV, full conversion may limit the influence of the effectiveness factor decrease and thus the plateau will not be reached. The most likely trend in the flux curve (and so conversion trend) with changes in D_h are those of Figure 7.5 (c) and (d).

This simulation indicates that an increase in channel hydraulic diameter does not independently increase diffusional distance without increasing overall conversion. The proposed test for external transport limitations (Walter et al., 2005) presented in Section 2.4.4 can therefore not be applied experimentally in microchannel reactors.

7.3.2 1-Dimensional model: variation of width only

A similar analysis is conducted for the case of a change in channel width in the range of the hydraulic diameters in Table 7.1 with a constant height of 500 μm.

The changes in the important spatial parameters in Equation 7.12, A_{surf} and V_{cat} are shown in Figure 7.6 while the parameters $Ac = \frac{V_{cat}}{A_{surf}}$ and η_c that form the observed flux are plotted in Figure 7.7 for changes in space velocity and channel width. All trends are the same as the case of a 2-dimensional variation except for the change in V_{cat} with channel width. This now increases in $O(1)$ with an $O(1)$ increase in channel width.

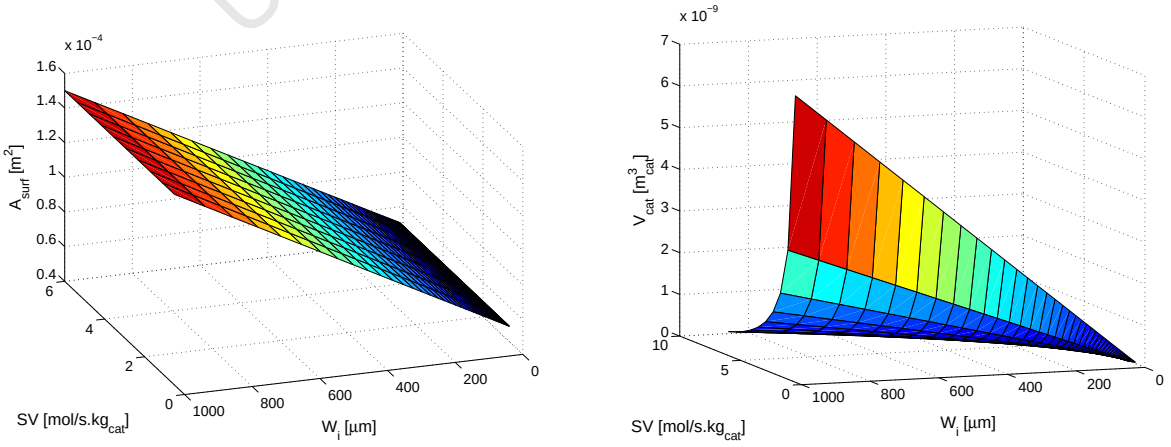

(a) A_{surf} (b) V_{cat}

Figure 7.6: Changes in spatial parameters with W_I and SV. $AR = 1.5$ and all other parameters as in Table 7.1.

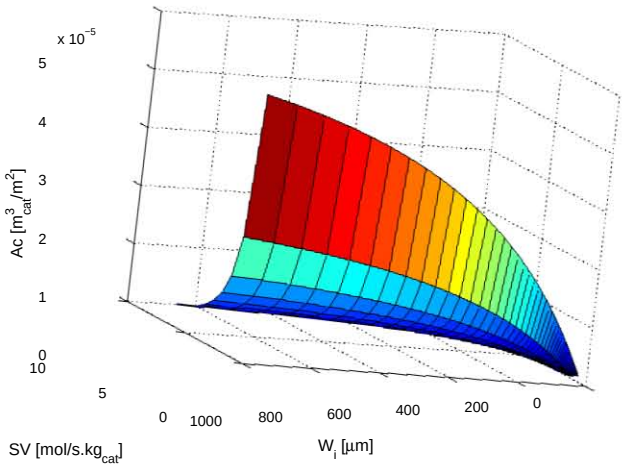

(a) Ac for different SV and W_I

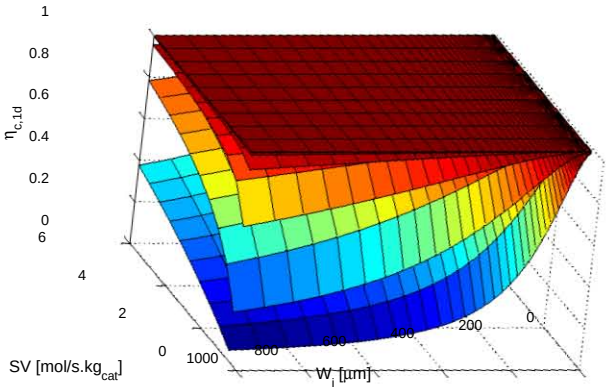

(b) Change in concentration effectiveness factor $\eta_{c,1d}$ with SV and W_I at different k_0

Figure 7.7: Variation of the parameters on which the observed flux N_y^{obs} depends. $AR = 1.5$ and all other parameters as in Table 7.1. Using 1-dimensional model.

Catalyst inner surface area remains constant with space velocity as it is independent of catalyst thickness but varies linearly in $O(1)$ with changes in channel width. The change in catalyst volume with SV is the same as in increases in $O(1)$ with an $O(1)$ increase in channel width.

The same trend in observed flux is seen as above and is shown in Figure 7.8. However a significant change occurs in the behaviour of the overall flux $N_y^{obs} A_{surf}$ which is plotted against reaction rate and channel width in Figure 7.9 for different values of SV.

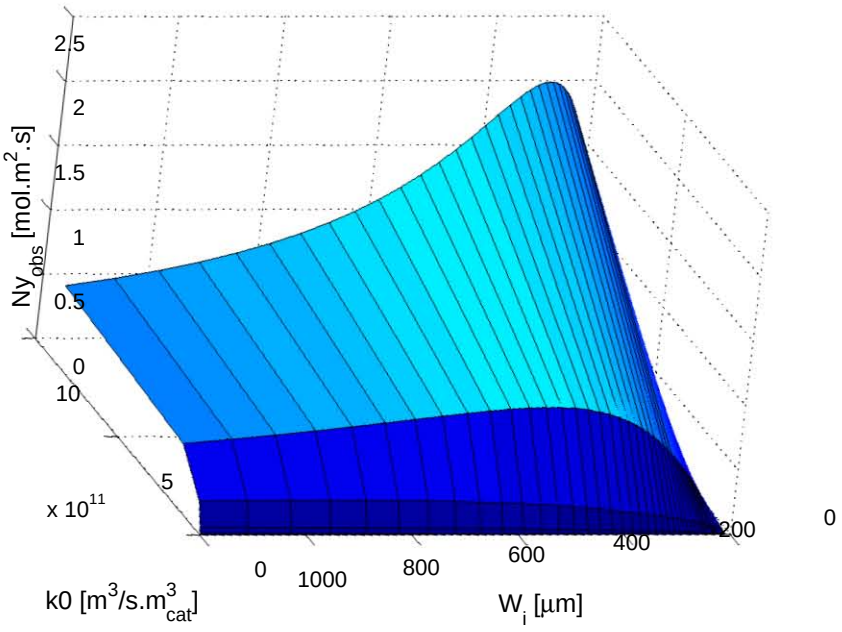

Figure 7.8: Change in observed flux $N_y^{obs} = \eta_c R_A Ac$ with k_0 and W_I. $SV = 0.02\,^{\mathrm{mol}}/_{\mathrm{s.kg_{cat}}}$. $AR = 1.5$ and all other parameters as in Table 7.1. Using 1-dimensional model.

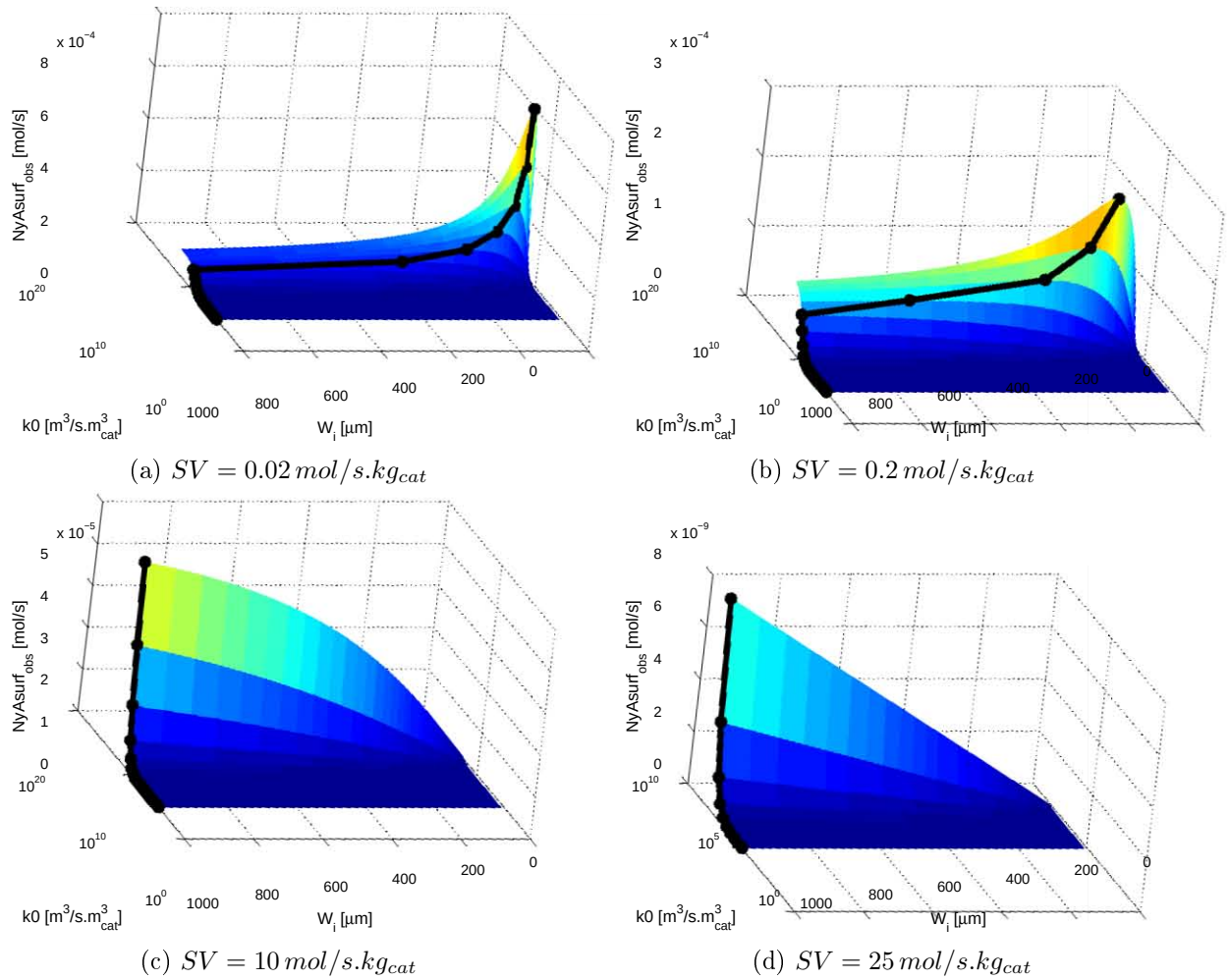

Figure 7.9: Change in $N_y A_{surf}$ with $W_I = 50 - 1000\,\mu m$ $k_0 = 1 \times 10^4 - 1 \times 10^{12}\,\mathrm{m^3/s.kg_{cat}}$ for different space velocities. $AR = 1.5$ and all other parameters as in Table 7.1. The black lines indicate the points of maximum total flux. Use 1-dimensional model.

The notable trends are as follows:

1. Unlike the previous case, a maximum total flux occurs at intermediate SV and k_0.
2. The total flux initially increases with W_I even at constant SV and τ. The initial linear shape of the curve best seen in (d) is given by the $\frac{1}{V_{cat}}$ term in Equation 7.14 which increases in $O(1)$ with W_I as discussed above.
3. The increase in total flux slows to reach a maximum, after which the low effectiveness factor limits reaction.
4. The shape of the total flux change with channel width is the same for all SV and k_0, however the window of view is constrained by the choice of μm domain.
5. The ability to reach a maximum changes with SV and k_0. An increase in SV requires higher catalyst activity or higher channel width to reach the maximum total flux.

6. All the regions of trends shown in Figure 7.9 may not be accessible in a flow reactor as full conversion may limit the influence of the effectiveness factor drop and hence maximum. The most likely conversion shapes with changes in W_I are those of (c) and (d).

7.3.3 3-Dimensional model: variation of channel height and width

The configuration discussed in the analysis in Section 7.1.1 and applied to the 1-dimensional model in Section 7.2.1 is now simulated using the full 3-dimensional model using conditions shown in Table 7.1. The model is run in its isothermal mode so that all concentration gradients seen will be due to mass transport limitations and not heat transport effects. The results for different space velocities is shown in Figure 7.10 while a magnified range of rate constants for $SV = 2\,mol/s.kg_{cat}$ is shown in Figure 7.11.

The general trend across all SV is that a low SV leads to a high conversion which leads to equilibrium limitations. As the SV is lowered the reaction moves into the kinetic or transport limited range.

The dependence of conversion on k_0 shows similar behaviour to the convex shape of the dependence of total flux, $N_y^{obs} A_{surf}$ on k_0 in Figures 7.5 (a-b). This validates the previous statement in Section 7.2.1 where the total flux is introduced as a proxy for conversion. This leads to the statement

$$X_{CO} \propto N_y^{obs} Ac \tag{7.15}$$

In the case of total flux, the reaction is mass transport controlled as the effectiveness factor is allowed to reach zero in the absence of any conversion restriction to give the leveling off of the profiles. In this case the reaction is either equilibrium limited or restricted by complete conversion, but the effect is the same. With lower conversions, the dependence on k_0 becomes less convex and linearises as in Figures 7.10 (c-d) at low channel widths.

The change with channel hydraulic diameter similar to that of the 1-dimensional case in Figure 7.5 (c) where conversion increases with hydraulic diameter even at constant SV and τ. The increase is seen the most clearly in Figure 7.10 (d). This confirms the applicability of the previous analysis. However where the 1-dimensional simulation predicts the conversion to level off to a constant value plateau, at high channel diameters, the simulations here level off and then decrease. This decrease is best shown at low values of space velocity as in Figure 7.10 (a) and more clearly in Figure 7.11. The reason for the decrease is that the laminar flow increases mass transport limitations due to different velocities at each perpendicular position. Thus a molecule entering the reactor at the center has a higher velocity than that at the channel wall, it has a lower chance of being

converted. If velocity is sufficiently higher than the perpendicular diffusion speeds then this profile will increase concentration gradients, decrease the effectiveness factor and hence lead to decrease in conversion.

The drop in conversion with increased channel width is most pronounced at low SV. Here the mass flux from the channel walls is the highest across the whole reactor as shown for the 1-dimensional analysis in Figure 7.12. This high flux corresponds to the region of highest conversion but also lowest effectiveness factor as a result of the higher catalyst thickness compared to lower higher SV. This leads to a low surface area available for reactant diffusion into the catalyst on a per volume catalyst basis for the same channel width. This is expressed as the dominance of the $\frac{V_{cat}}{A_{surf}}$ term over the $\frac{k}{D_{AB}}$ term in Equation 7.10 which decreases the effectiveness factor and increases mass transport limitations.

The conversion profile depends on both mass transport limitations and catalyst volume per surface area, or total flux generated off the catalyst surface. An increase in channel width increases the $\frac{1}{V_{cat}}$ term in Equation 7.14 leads to an independent increase in the total flux generated, $N_y^{obs} A_{surf}$ and hence an increase in conversion. Thus the mass transport limitations have to compete with the increase in catalyst volume per surface area for dominance in the conversion profile with increased channel width.

This means that the effects of mass transport cannot be independently tested by comparing conversions. An alternate method is required to compare the actual reactor effectiveness factors at different conditions. This can be done using effectiveness factors and is further explored in Section 7.3.4.

7.3.4 Comparison of effectiveness factors

The trends in the behaviour of the concentration effectiveness factor averaged along the reactor length are evaluated. The independent variables are v_0, SV, k_0 and D_h. As this is a more specific study than the previous analysis of mass transfer effects so the ranges of variables are constrained to those found in literature studies. The space velocity chosen in the 0.02 - 2.5 range as this falls around the experimental value of $SV = 0.59\,{}^{\text{mol}}/_{\text{s.kg}_{\text{cat}}}$ used in literature (Germani et al. 2005) while inlet velocity was chosen in the $v_0 = 0.01 - 3.0\,{}^{\text{m}}/_{\text{s}}$ range as this around the experimental value of $v_0 = 0.05\,{}^{\text{m}}/_{\text{s}}$ used in the same study. The maximum Reynolds number is expected at $v_0 = 3.0\,{}^{\text{m}}/_{\text{s}}$ and $D_h = 2000\,\mu m$ and is calculated to be $Re = 350$ which is safely in the laminar flow regime. The first order rate constant is varied in the range $k_0 = 1 \times 10^4 - 1 \times 10^7\,{}^{\text{m}^3}/_{\text{s.m}^3_{\text{cat}}}$ as this is about the value determined in the regression study for first order kinetics in Section 6.4.2.

The equilibrium limitation is neglected for three reasons. Firstly, this generalises the results obtained to any first order reaction. Secondly, it removes the instability that the $(1 - \beta)$ rate law term brings to the concentration profile when operating close to

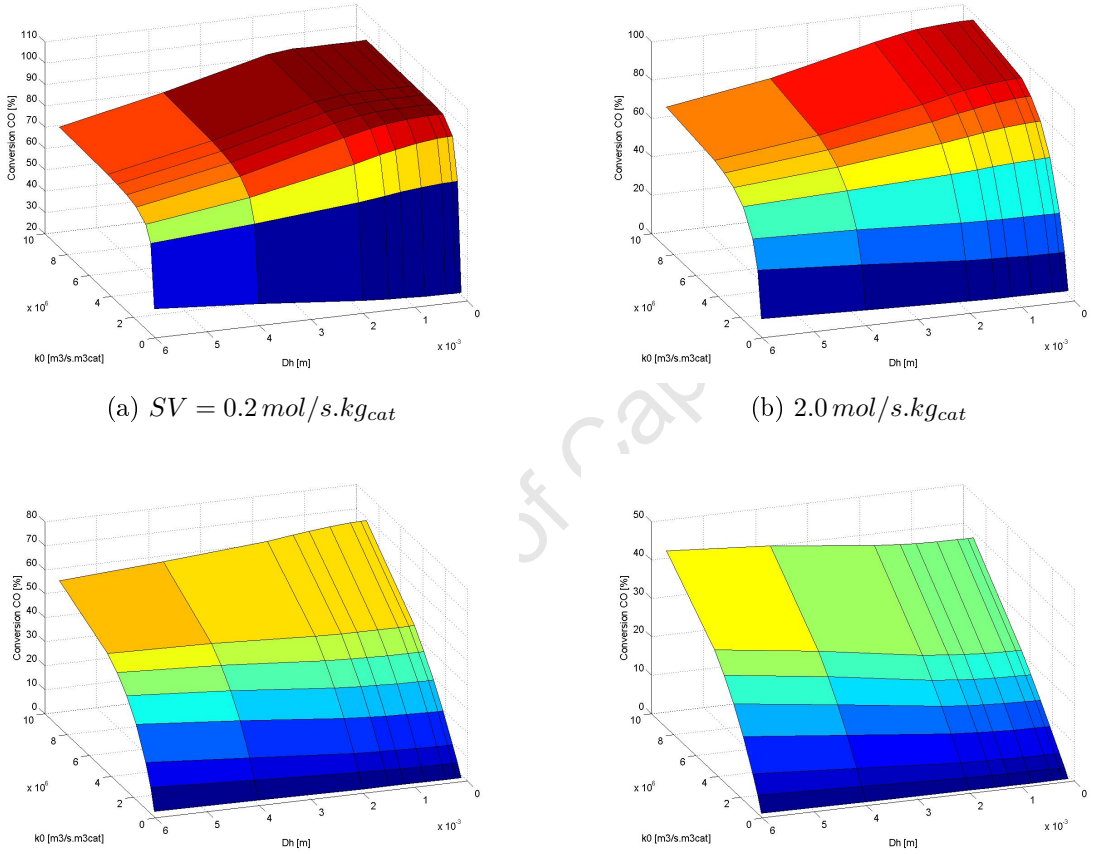

(a) $SV = 0.2\,mol/s.kg_{cat}$ (b) $2.0\,mol/s.kg_{cat}$

(c) $SV = 10\,mol/s.kg_{cat}$ (d) $SV = 25\,mol/s.kg_{cat}$

Figure 7.10: Change in reactor conversion with $D_h = 100 - 6000\,\mu m$ and $k_0 = 1 \times 10^4 - 1 \times 10^6\,{}^{\mathrm{m}^3}/_{\mathrm{s.m}^3_{\mathrm{cat}}}$ for different space velocities. $v_0 = 1.0\,{}^{\mathrm{m}}/_{\mathrm{s}}$ $P = 3\,bar$ $T = 573.15\,K$ $AR = 1.5$ $L = 0.05\,m$. Using the full 3-dimensional model in isothermal mode.

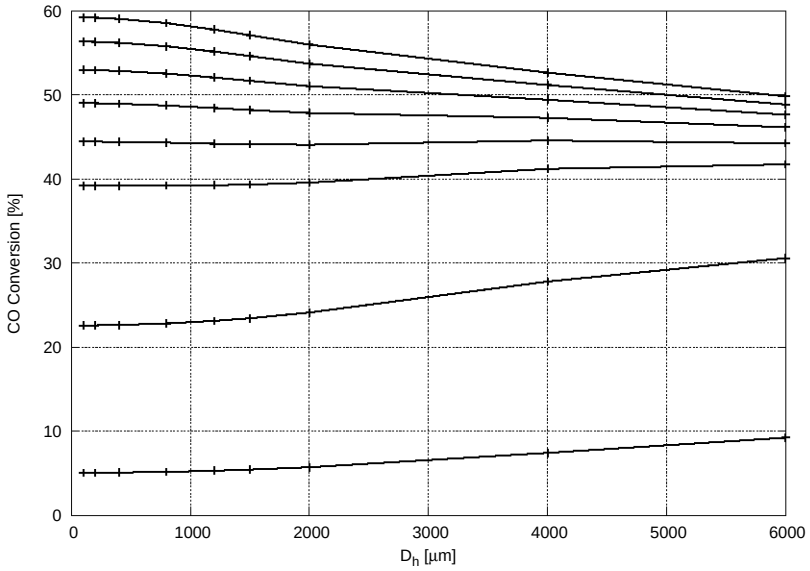

Figure 7.11: Change in reactor conversion with $D_h = 100 - 6000\,\mu m$ and $k_0 = 1 \times 10^5 - 2 \times 10^5\,{}^{\mathrm{m}^3}/_{\mathrm{s.m}^3_{\mathrm{cat}}}$ for $SV = 2\,mol/s.kg_{cat}$ $v_0 = 1.0\,{}^{\mathrm{m}}/_{\mathrm{s}}$ $P = 3\,bar$ $T = 573.15\,K$. Using the full 3-dimensional model in isothermal mode.

equilibrium. Thirdly, it also matches the simple 1-dimensional model and allows for some degree of comparison between the models.

The concentration effectiveness factor for $v_0 = 3.0\,{}^{\mathrm{m}}/_{\mathrm{s}}$ is shown in Figure 7.12 for different SV as a function of k_0 and D_h. These same runs are compared to the concentration effectiveness factor as predicted by the analysis of the Damköhler number in resulting in Equation 7.10 in Figure 7.13. Notable trends are discussed.

Figures 7.12 (a-d) shows that the effectiveness factor is the lowest at the lowest SV and corresponds to the region of highest mass transport limitations. As in the 1-dimensional case it is attributed to the higher volume of catalyst per unit surface area which decreases the surface area available per mass of converted reactant for mass flux to flatten the concentration profiles . The trends with respect to the k_0 and D_h are also the same as in the 1-dimensional analysis. The effectiveness factor is inversely proportional to these variables and therefore decreases hyperbolically with them.

Of more interest here is the effect of the laminar velocity profile on mass transport limitations. Figure 7.13 shows the same data from the 3-dimensional model as in Figure 7.12 with the addition of the effectiveness factors from the 1-dimensional analysis as an overlay. At all space velocities, the 1-dimensional model significantly over-predicts the effectiveness factor with a resulting under-prediction of the effect of mass transport limitations. This under-prediction is expected from the Damköhler analysis as stated in Section 2.4.2. As the Mears criterion is based on the Damköhler number, a similar underprediction of mass transfer limitations is expected from the Mears criterion. The steeper concentration

gradients for laminar flow compared to plug flow is attributed to the velocity profile which carries species faster in the channel center compared to the average plug flow velocity. This results in a lower residence time in the reactor and so a lower conversion. There is thus a high concentration of unreacted species in the center compared to the wall which increases perpendicular concentration gradients. The laminar velocity profile effect is therefore independent of the effects of SV, k_0 and D_h and is therefore studied further.

Figure 7.14 shows the effectiveness factors for different velocities at $SV = 0.5\,{}^{\mathrm{mol}}/_{\mathrm{s.kg_{cat}}}$. The difference between the predicted effectiveness factor by the Damköhler number and the model effectiveness factor grows with increased velocity. This is because the steepness of the velocity gradient grows with increased velocity at constant channel diameter which takes the flow further away from the plug flow behaviour assumed by the analysis of the Damköhler number. Care should therefore be taken when applying the Damköhler number to predict mass transport limitations in laminar flow problems. Given the plug flow assumption of the Damköhler analysis, this caution can be extended to the application of the 1-dimensional models as well.

The conditions of operation shown in Figure 7.14 are in the range of that of Germani et al., 2005. The presented space velocity is approximately that of the experimental $SV = 0.59\,{}^{\mathrm{mol}}/_{\mathrm{s.kg_{cat}}}$ and inlet velocities in (a) and (b) are representative of the experimental $v_0 = 0.05\,{}^{\mathrm{m}}/_{\mathrm{s}}$. All other conditions are held the same as that in Table 6.5. Figure 7.14 (a) and (b) shows that this experimental operation is safely in the region of kinetic control. Only a substantial increase in inlet velocity, or catalyst activity will shift operation to a mass transport controlled region.

7.4 Significance of the time factor

It is of interest to characterise the limits of applicability of a plug flow model compared to the application of a laminar flow model. Following the previous discussion, as the velocity is decreased, the velocity gradient shallows. If the velocity is decreased *sufficiently*, then diffusion will be able to transport species across the channel width in the same timescale as the velocity transports down the channel length. This will essentially lead to plug flow.

This study evaluates the required velocity decrease that enables analysis using a plug flow assumption[3]. It should also be noted that the velocity could be increased for turbulent flow which would also enable the use of a plug flow model. It is not, however within the scope of this work to go into turbulent flow, so the upper limit of the laminar flow model is not evaluated.

[3] i.e. by the Damköhler number analysis

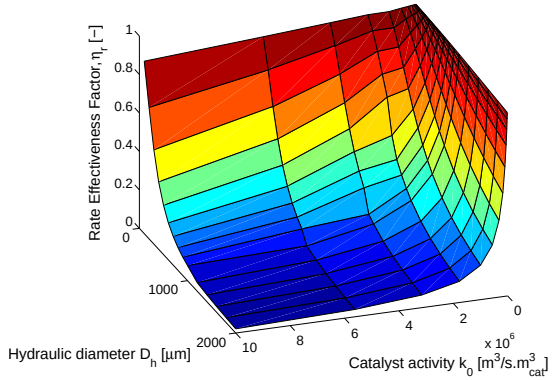

(a) $SV = 0.02\,mol/s.kg_{cat}$

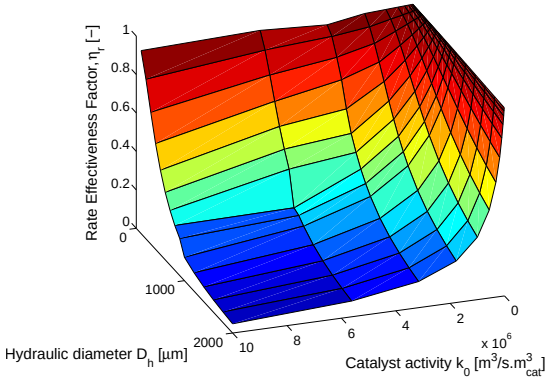

(b) $0.1\,mol/s.kg_{cat}$

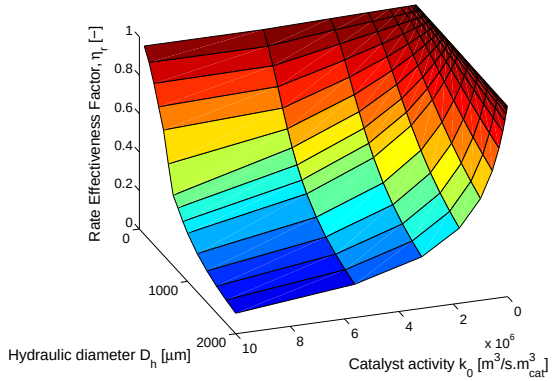

(c) $SV = 0.5\,mol/s.kg_{cat}$

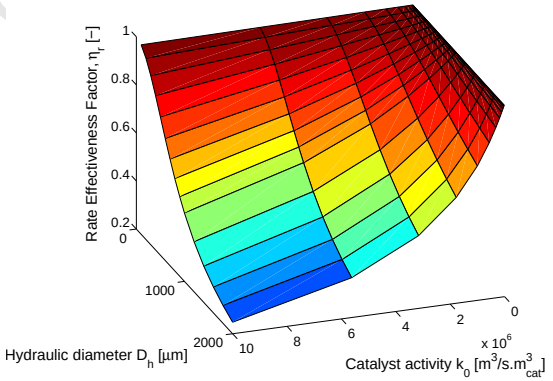

(d) $SV = 2.5\,mol/s.kg_{cat}$

Figure 7.12: Change in average effectiveness factor with $D_h = 100 - 2000\,\mu m$ and $k_0 = 1 \times 10^4 - 1 \times 10^7\,{}^{\mathrm{m}^3}/_{\mathrm{s.m}^3_{\mathrm{cat}}}$ for different space velocities. $v_0 = 3.0\,{}^{\mathrm{m}}/_{\mathrm{s}}$ $P = 3\,bar$ $T = 573.15\,K$ $AR = 1.5$ $L = 0.05\,m$. Full 3-dimensional model used in isothermal mode.

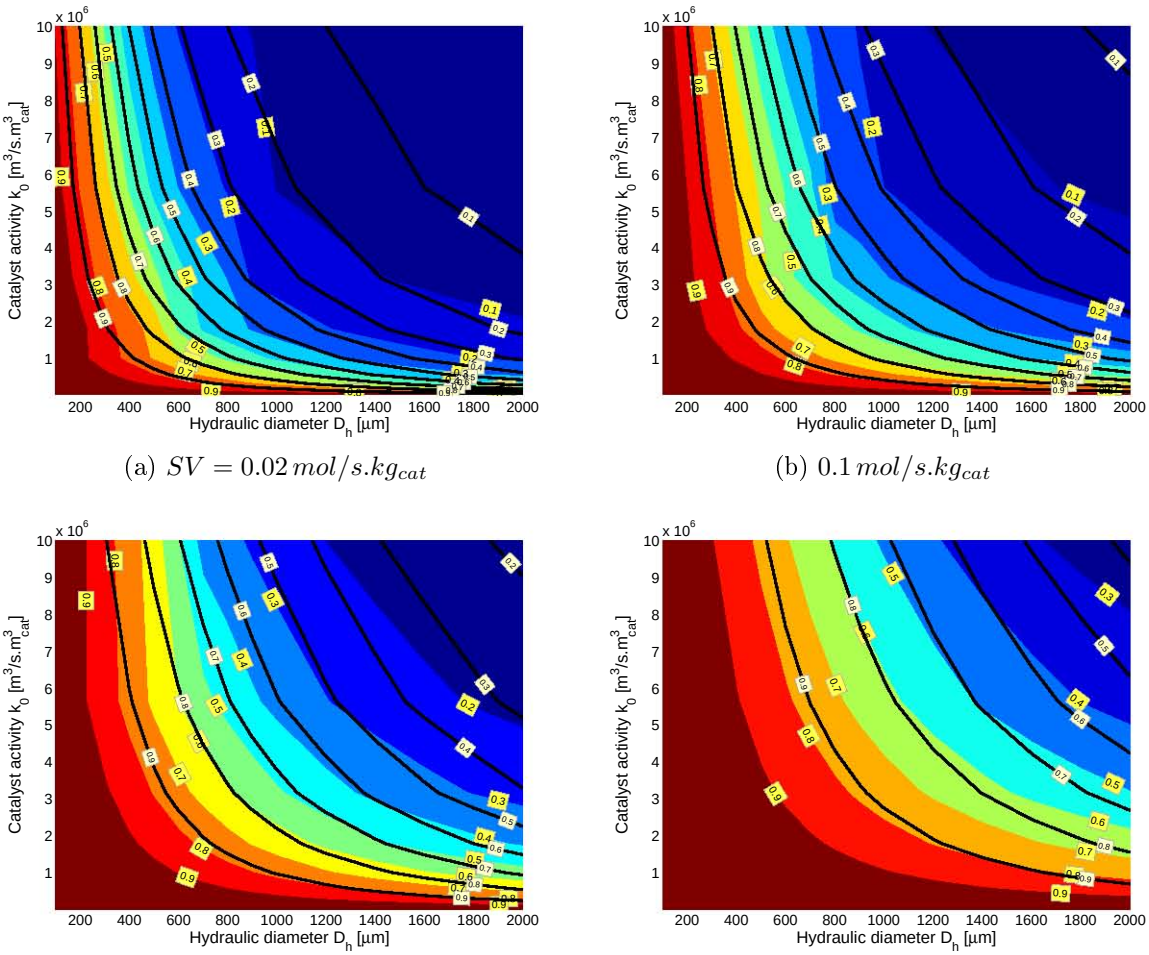

(a) $SV = 0.02\,mol/s.kg_{cat}$ (b) $0.1\,mol/s.kg_{cat}$

(c) $SV = 0.5\,mol/s.kg_{cat}$ (d) $SV = 2.5\,mol/s.kg_{cat}$

Figure 7.13: Comparison of average effectiveness factors, η_r from the isothermal 3-dimensional (yellow labels) and 1-dimensional model (white labels) for different space velocities. $D_h = 100 - 2000\,\mu m$ and $k_0 = 1 \times 10^4 - 1 \times 10^7\,{}^{\mathrm{m}^3}/_{\mathrm{s.m}^3_{\mathrm{cat}}}$ for different space velocities. $v_0 = 3.0\,{}^{\mathrm{m}}/_{\mathrm{s}}$ $P = 3\,bar$ $T = 573.15\,K$ $AR = 1.5$ $L = 0.05\,m$.

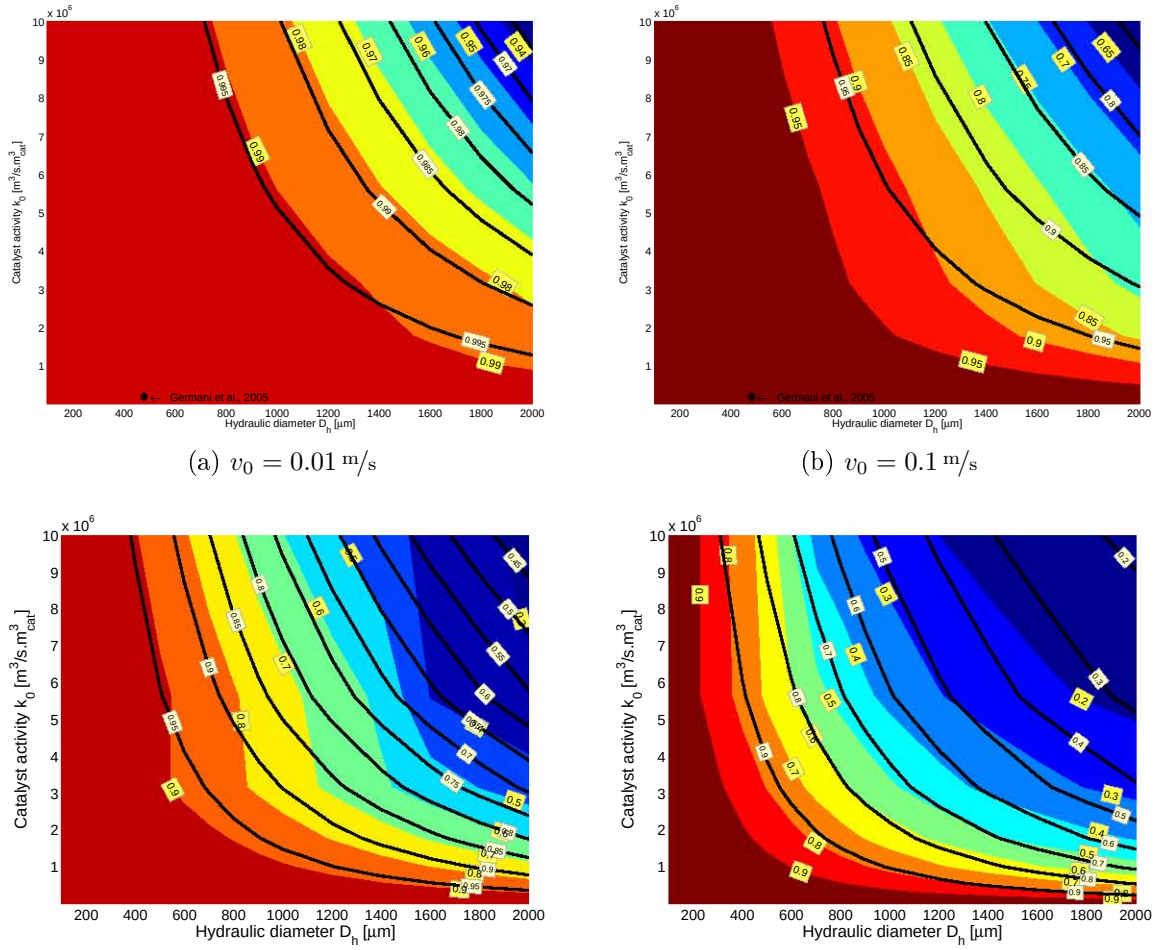

(a) $v_0 = 0.01\,\mathrm{m/s}$

(b) $v_0 = 0.1\,\mathrm{m/s}$

(c) $v_0 = 0.5\,\mathrm{m/s}$

(d) $v_0 = 3.0\,\mathrm{m/s}$

Figure 7.14: Comparison of average effectiveness factors from the sothermal 3-dimensional (yellow labels) and 1-dimensional model (white labels) for different velocities. $SV = 0.5\,\mathrm{mol/s.kg_{cat}}$ $D_h = 100 - 2000\,\mu m$ $k_0 = 1 \times 10^4 - 1 \times 10^7\,\mathrm{m^3/s.m^3_{cat}}$ $P = 3\,bar$ $T = 573.15\,K$ $AR = 1.5$ $L = 0.05\,m$. Study by Germani et al., 2005 indicated.

7.4.1 Problem setup

The ratio appropriate to this analysis is the time-scale of diffusion to the time-scale of flow, or residence time τ in the relation $\frac{\tau}{\tau_D}$. This has been discussed in Section 2.4.2.

The ratio $\frac{\tau}{\tau_D}$ is evaluated as follows

$$\frac{\tau}{\tau_D} = \frac{\frac{L}{v_0}}{\frac{D_h^2}{4D_{AB}}} \tag{7.16}$$

This ratio is varied by changing the value of the inlet velocity, v_0 while keeping SV, D_h and L constant. A change in v_0 will change residence time and so the reactor conversion. However it is the perpendicular concentration gradients which are of interest and not the actual conversion so this reactor output is neglected.

The concentration gradients for both the plug flow and laminar flow models are evaluated using the concentration effectiveness factor, η_c. The plug flow factor, $\eta_{c,1d}$ only accounts for diffusional effects while the laminar flow factor, $\eta_{c,3d,isothermal}$ accounts for both diffusional effects and the laminar flow effect. Therefore the extent of mass transport limitations by laminar flow is given by $|\eta_{c,3d,isothermal} - \eta_{c,1d}|$. The fraction of mass transport due to laminar flow is now given by dividing this difference by the total transport limitations and is given by the ratio

$$R_{1,3} = \frac{|\eta_{c,3d,isothermal} - \eta_{c,1d}|}{\eta_{c,3d,isothermal}} \tag{7.17}$$

This ratio evaluates the fraction of the total mass transport limitations that is accounted for by the plug flow model. As this fraction tends to zero, the laminar flow effect becomes negligible and the mass transport is mostly due to diffusional effects. At this point, the Damköhler number model can be used to evaluate for mass transport effects.

7.4.2 Results

The effectiveness factors are evaluated for both the 1-dimensional and 3-dimensional models at the same conditions as in the evaluation of the effectiveness factor in Section 7.3.4. These are plotted as separate curves for different velocities at different hydraulic diameters and catalyst activity within each plot with different subplots for each space velocity. These curves are shown in Figure 7.15.

At high k_0 the effectiveness factor data becomes scattered and is particularly evident at low $SV = 0.02$, 0.1 and $0.5\,{}^{\text{mol}}/_{\text{s.kg}_{\text{cat}}}$ values. This scatter is because $\sim$100% conversion is reached at these conditions which causes the 3-dimensional model to become unstable.

The scattered effectiveness factor data is shown for corresponding conversion plots in Figures E.10 and E.7 in Appendix E.2. These curves with scatter are neglected in the subsequent discussions.

The reason for this instability is that the species compositions at the reactor entrance close to the wall drop sharply from the inlet composition to ∼zero along the channel wall. This is expected in a mass transport controlled regime. The Lagrange polynomial now takes the oscillatory form along the axial direction (shown in Figure 2.12) and hence the effectiveness factors oscillate significantly.

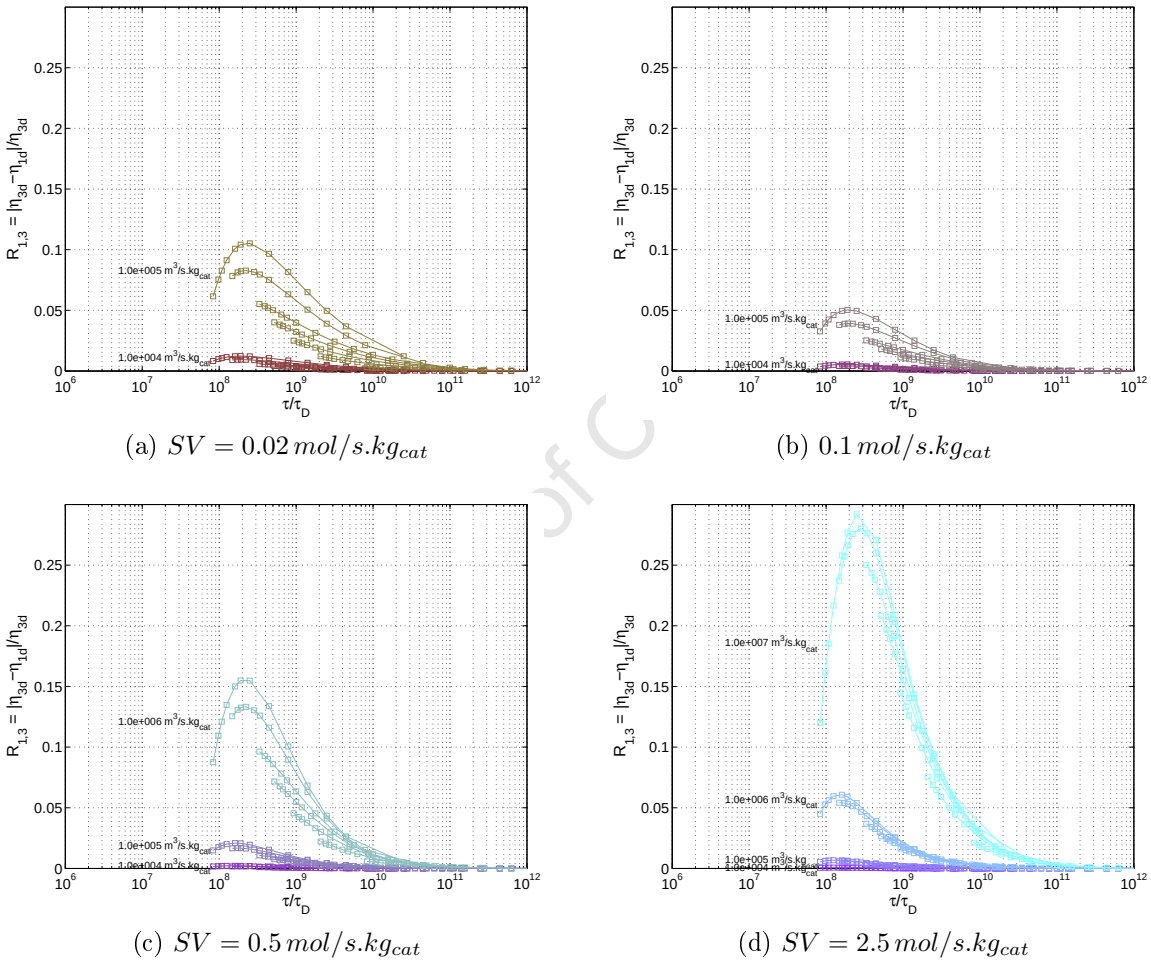

(a) $SV = 0.02\,mol/s.kg_{cat}$ (b) $0.1\,mol/s.kg_{cat}$

(c) $SV = 0.5\,mol/s.kg_{cat}$ (d) $SV = 2.5\,mol/s.kg_{cat}$

Figure 7.15: Plot of ratio of fraction of mass transport by laminar flow against ratio of convective to diffusive time for different space velocities. $D_h = 100 - 2000\,\mu m$ $v_0 = 0.01 - 3.0\,\mathrm{m/s}$ $k_0 = 1\times10^4 - 1\times10^7\,\mathrm{m^3/s.m^3_{cat}}$ $P = 3\,bar$ $T = 573.15\,K$ $AR = 1.5$ $L = 0.05\,m$.

7.4.3 Discussion

It is evident from Figure 7.15 that all curves for individual D_h and v_0 values roughly overlap at constant SV and k_0 and represent each curve on the plot. This is because each of the curves are normalised by $D_h^2 = XSA_I$ and v_0 and a change in these variables have

the same effect on δ_{cat} by Equation 7.3. A change in δ_{cat} changes the overall flux and so the η_c at constant k_0 and SV.

Velocity effect All $R_{1,3}$ curves approach zero asymptotically with high $\frac{\tau}{\tau_D}$. This corresponds to either a low velocity or low D_h. As expected, at low average velocity and constant D_h the velocity gradient decreases and flow approaches that of a plug. However, $R_{1,3}$ only approaches zero and does not reach it as there is a numerically imposed laminar flow profile and so always a laminar flow contribution to mass transport limitations.

Hydraulic diameter effect A change in D_h results two opposing effects. Firstly a decrease in D_h gives a steeper velocity gradient and so a stronger influence of the laminar flow. This increase in the fraction of mass transport limitations by the laminar flow influence with a decrease in $\frac{\tau}{\tau_D}$ is seen for all values of SV and k_0. The second effect is that a decrease in D_h results in a smaller diffusive time which means lower overall mass transport limitations and so a lower overall $R_{1,3}$ compared to that of a similar velocity. This effect will be most significant where the effectiveness factors are the lowest, i.e. at low SV and high k_0. Therefore the deviations between curves of different D_h values are most pronounced for these conditions. This is seen for a change in SV in the comparison the curves for $k_0 = 1 \times 10^5 \mathrm{m^3/s.kg_{cat}}$ in Figures 7.15 (a-b) and for a change in k_0 in Figure 7.15 (a).

Conversion effect A further feature common to all curves is the maximum with respect to each constant D_h curve. The plots of both $\eta_{c,1d}$ and $\eta_{c,3d,isothermal}$ both decrease monotonically with $\frac{\tau}{\tau_D}$ as seen in Figures E.8 and E.9 respectively in Appendix E.2. The maximum in $R_{1,3}$ is caused by the faster approach to constant of $\eta_{c,3d,isothermal}$ compared to $\eta_{c,1d}$. This difference in relative rates of decrease with velocity causes the $R_{1,3}$ maximum. The difference in relative rates is explained by the effect of conversion along the reactor length. An increase in velocity decreases conversion which leads to a higher effectiveness factor, $\eta_{c,3d,isothermal}$ and so a decrease in $R_{1,3}$. This analysis only applies to the 3-dimensional model where conversion is accounted for and it will be the $\eta_{c,3d,isothermal}$ that will decrease quicker than the $\eta_{c,1d}$.

Flux effect The approach of $R_{1,3}$ to zero is also enhanced by a low flux from the catalyst reaction surface as a result of a low k_0 or high SV. These conditions result in increased effectiveness factors as is seen in previous discussions in Sections 7.3.1 and 7.1.1. This means that both $\eta_{c,1d}$ and $\eta_{c,3d}$ approach unity and so their difference will approach zero. There are thus two effects here, both of which lead to the same result.

Significance It should therefore be noted that an $R_{1,3}$ approach to zero does not necessarily mean the absence of mass transport limitations, but rather that whatever limitations exist are accounted for by diffusional limitations. This means that in the regions of low $R_{1,3}$ the Damköhler number analysis can be applied to determine the extent of mass transport limitations. The results presented should therefore be used as an initial screen of the applicability of a chosen model rather than to provide an estimate of the extent of transport limitations.

Chapter 8

Conclusions

Based on the results and discussion the following conclusions can be drawn

8.1 Model development

A 3-dimensional single phase model has been developed for microchannel reactors and applied to a single channel. This accounts for laminar flow in the channel bulk with reaction at the walls and perpendicular diffusion.

The laminar flow profile is given by an analytical expression for circular geometry that is modified for rectangular co-ordinates. The resultant profile closely matches that of the numerical solution of the momentum balance and an analytical solution over rectangular co-ordinates by Fourier series. It is chosen as it is the most computationally efficient routine. Pressure is assumed constant and velocity is increased with an increase in temperature as a result of a decrease in concentration.

The species balances account for convective flow in the axial direction and perpendicular diffusion given by the Maxwell-Stefan approach to mass transfer. The driving force for diffusion is the heterogeneous reaction at the channel walls. Internal mass transport is assumed to be negligible and the reaction is treated as a surface reaction on a equivalent volume of catalyst.

The continuity equation gives the change in total concentration with temperature and velocity. This accounts for convective flow in the axial direction and perpendicular diffusion given by the sum of species fluxes.

The energy balance accounts for heat movement by convection in the axial direction and both convection and conduction in each of the perpendicular directions. The heat of reaction is generated implicitly at the wall as a result of the differential heat fluxes to and from the wall of the reactant and product species. A heat loss term is included in the wall

boundary condition that allows the user to generate any temperature profile necessary. Options are given for adiabatic and isothermal operation.

8.2 Numerical solution and computational efficiency

The model results in a system of DAEs. This is solved over just one quadrant of the channel to decrease the required mesh size and ensure computational efficiency. The set is converted to a set of ODEs and NLEs in time by the reduction of the spatial derivatives with orthogonal collocation. The chosen polynomial basis set is the Lagrange polynomials.

The reduced NLE set cannot be solved in the steady state as a result of convergence problems. It can be solved in the transient state following a concentration ramp up of reactive species and a ramp down of inert species from the initial state of a reactor filled with inert.

Numerical efficiency is ensured by the implementation of a three step algorithm where the equation set is solved in the transient state with a coarse mesh. This solution mesh is interpolated onto a fine mesh which is then used as the initial guess for the steady state solution. The algorithm provides stability as the transient solver does not solve above 275 solution points whereas the steady state solver is tested to 1701 points. The algorithm is also significantly more numerically efficient than the purely transient solver.

Computational efficiency is provided by the use of the ifort compiler over the gfortran compiler. The NLE solver's Jacobian calculation is parallelised with a speedup of 1.18 over 4 processors compared to a theoretical speedup of 1.81. The difference is due to the large data blocks that are read from the main RAM which acts as the rate limiting step.

8.3 Model tests

The model is tested for a case with induced mass and heat transport limitations. A mesh-free solution is obtained for an $[11, 9, 9]$ mesh with 891 points with a convergence of the NRMSE of within 1% for a solution time of ∼686 s. The overall mass and energy balances are met to within 10^{-2}%. Solution times are dependent on the reactor conditions and range from $\sim 13\,s$ for an isothermal approximate plug flow case to $\sim 40\,s$ for an isothermal transport limited regime for similar NRMSE and overall mass balance convergences. These tests confirm the model's computational efficiency compared to low order FEM-based models which take in the order of hours to solve.

The model is able to predict expected outcomes for mass and energy transport in the steady state. This includes correct mass flux directions and species profiles, thermal

expansion of the gas and speedup of fluid flow and equalisation of perpendicular composition and temperature profiles after reaction equilibrium is reached. The constant pressure assumption is also held.

In the unsteady state the physical condition of $\sum_{i=1}^{c} \chi_i = 1$ is violated either because of an imposed steady state physical criterion for flux or a lag in the flux calculations as they are updated a step behind the main balance variables.

The model is validated against experimental data from literature. It predicts isothermal conversions over a range of inlet temperatures with a goodness of fit of 0.9984. Similar accuracy is obtained for the prediction of the conversion of different catalyst samples by merely adjusting catalyst activity as recommended in the literature. The model can also be called under a regression routine with good stability and computational efficiency.

8.4 Mass transport effects

The test of mass transport limitations by increasing channel hydraulic diameter is examined. This increase in channel hydraulic diameter at constant space velocity and residence time requires that the catalyst layer thickness be increased. As a result, the total flux off the reaction surface increases which leads to a higher conversion. This is true for a channel of any cross section. The increase in conversion is demonstrated in a 1-dimensional radial model, based on the second Damköhler number and simulated in the 3-dimensional model. This result means that an increase in channel hydraulic diameter does not independently increase diffusional distance without increasing overall conversion. This test can therefore not be applied to microchannel reactor systems with catalyst coated walls.

The difference between the conversion dependence on channel diameter between the radial 1-dimensional and 3-dimensional models is that the conversion increases and then plateaus off in the former and increases and then decreases in the latter. This decrease is attributed to the laminar flow profile which carries its own intrinsic mass transport limitations.

The extent of mass transport limitations is captured in the concentration effectiveness factor. This is found to be lower in the case of the 3-dimensional model compared to that predicted by the 1-dimensional model. This is attributed to laminar flow and the result is as predicted by the original Damköhler studies. Even though this study does not arrive at a unified criterion for the limits of applicability of the Damköhler and Mears critera, the extent to which laminar flow dominates mass transport is documented for different space velocities, catalyst activities as a function of inlet velocity and channel diameter. This information can be applied to further studies on microchannel reactors with first order reactions. This study indicates the limitations of the application of both an axial 1-dimensional model and both the Damköhler number and Mears criteria for evaluation

of reactor conversion and mass transport effects respectively.

Chapter 9

Recommendations

Based on the model development and discussion of results some recommendations can be made for further work in modelling microchannel reactors.

Model setup

- Extension to non-equimolar reactions. A non-equimolar reaction will lead to a change in reactor pressure both axially and radially. This will require the addition of a momentum balance account for radial velocities that arise.
- Extension to non-symmetric boundary conditions. The existing model solves for a single quadrant in the channel. This restricts the solution to symmetric boundary conditions in at least degree of symmetry. Solution of the entire domain would allow the user to specify different wall boundary conditions for
  - different catalyst loadings
  - different heat-loss terms (i.e. if there is a cooling channel at one end and not on the other
  - and would allow the single channel model to be incorporated into a multi-scale model of the entire microchannel reactor

Model speed In order to further speed up the model solution time the following can be implemented

- Speedup of existing Jacobian parallelisation on HYBRD.for NLE solver. This can be done by the use of distributed memory processors, where each processor has its own memory. This can reduce computational time by decreasing the limitation of data transfer from the main RAM to the processor-level memory.

- Further parallelisation. This will have to be done by implementing a new QR factorisation algorithm into the existing solver package.

Further investigations

- Non-steady state behaviour. This aspect has not been investigated and there remains scope to study the reactor behaviour in startup and shutdown or in the case of different hydrogen requirements. The flux physical condition will have to be corrected possibly with the implementation of bootstrap for physical constraint $\sum_{i=1}^{c} N_i = k\,(T)$.
- Evaluation of heat transport effects. These have still to be evaluated particularly with respect to a constant wall temperature, an imposed temperature profile and integrated reactor-heat-exchanger operation. This will allow the determination of the conditions necessary to follow the optimal rate line.
- Implementation in a process flowsheet. This can be done in either the COCO or Aspen platforms. This will allow the modelling of the entire fuel processing unit with a heat integration study where reactor-heat exchanger boundary conditions are implemented.

Bibliography

V. Ananthakrishnan, et al. (1965). 'Laminar Dispersion in Capillaries: Part I. Mathematical analysis'. *AIChE Journal* **31**:236–244.

R. Aris (1956). 'On the Dispersion of a Solute in a Fluid Flowing through a Tube'. *Proceedings of the Royal Society of London. Series A, Mathematical and Physical Sciences* **235A**:67–77.

G. Arzamendi, et al. (2009a). 'Integration of methanol steam reforming and combustion in a microchannel reactor for H2 production: A CFD simulation study'. *Catalysis Today* **143**(1-2):25 – 31. International Symposium on Catalysis for Clean Energy and Sustainable Chemistry, on occasion of the 60th birthday of Prof. Jose L.G. Fierro.

G. Arzamendi, et al. (2009b). 'Methane steam reforming in a microchannel reactor for GTL intensification: A computational fluid dynamics simulation study'. *Chemical Engineering Journal* **154**(1-3):168 – 173.

J. Aubin, et al. (2009). 'Effect of microchannel aspect ratio on residence time distributions and the axial dispersion coefficient'. *Chemical Engineering and Processing: Process Intensification* **48**(1):554 – 559.

T. Baier & G. Kolb (2007). 'Temperature control of the water gas shift reaction in microstructured reactors'. *Chemical Engineering Science* **62**(17):4602 – 4611.

R. Bird, et al. (2002). *Transport Phenomena*. John Wiley & Sons, New York.

O. Brand, et al. (2006). *Micro Process Engineering Fundamentas, Devices, Fabrication and Applications*, vol. 5 of *Advanced Micro and Nanosystems*. Wiley-VCH.

J. Brandner, et al. (2006). *Microprocess Engineering: Fundamentals, Devices, Fabrication and Applications*, vol. 5 of *Advanced Micro and Nanosystems*, chap. Microfabrication in Metals and Polymers, pp. 267 – 319. Wiley-VCH Verlag, Weinheim.

K. P. Brooks, et al. (2007). 'Methanation of carbon dioxide by hydrogen reduction using the Sabatier process in microchannel reactors'. *Chemical Engineering Science* **62**(4):1161 – 1170.

S. Buddoo, et al. (2009). 'Study of the pyrolysis of 2-pinanol in tubular and microreactor systems with reaction kinetics and modelling.'. *Chemical Engineering and Processing* .

R. Burden & J. Faires (2005). *Numerical Analysis*. Thomson, 8th edition edn.

K. Campbell (2009). 'SA programme seeks to extract hydrogen's clean power potential'. http://www.engineeringnews.co.za/article/r67-million-first-stage-of-20-year-sa-hydrogen-programme-now-under-way-2009-05-15. Accessed 20 May 2009.

C. Cao, et al. (2009). 'Intensified Fischer-Tropsch synthesis process with microchannel catalytic reactors'. *Catalysis Today* **140**(3-4):149 – 156. Catalysis and Chemistry for the Synthesis of Fuels, Chemicals and Petrochemicals.

C. Cao, et al. (2005). 'Heterogeneous reactor model for steam reforming of methane in a microchannel reactor with microstructured catalysts'. *Catalysis Today* **110**(1-2):92 – 97. Catalytic Microstructured Reactors - Catalytic Microstructured Reactors.

M. Caracotsios & W. E. Stewart (1996). *DDASAC*, version 1996.2 edn.

B. Chapman, et al. (2008). *Using OpenMP: Portable shared memory parallel processing*. The MIT Press, Cambridge, Massachusetts.

J. Chase, M.W. (1998). 'NIST-JANAF Themochemical Tables'. *J. Phys. Chem. Ref. Data* **Monograph 9**:1–1951. Retrieved: http://webbook.nist.gov/.

S. Chattopadhyay & G. Veser (2006). 'Heterogeneous-homogeneous interactions in catalytic microchannel reactors'. *AIChE Journal* **52**(6):2217–2229.

Y. Choi & H. G. Stenger (2003). 'Water gas shift reaction kinetics and reactor modeling for fuel cell grade hydrogen'. *Journal of Power Sources* **124**(2):432 – 439.

D. D. Do (1998). *Adsorption analysis: equilibria and kinetics*. Imperial College Press.

W. Ehrfeld, et al. (2000). *Microreactors: New technology for Modern Chemistry*. Wiley-VCH, Weinheim.

M. G. el Hak (1999). 'The Fluid Dynamics of Microdevices - The Freeman Scholar Lecture'. *Journal of Fluids Engineering* **121**(5):5 – 33.

B. Finlayson (1980). *Non-linear analysis in chemical engineering*. McGraw-Hill, New York.

S. Fitzgerald, et al. (2008). 'Reduced Complexity in representation of Fischer-Tropsch Chemistry'. In *Proceedings of AIChE Spring National Meeting*.

H. Fogler (2006). *Elements of Chemical Reaction Engineering*. Pearson Education, Massachusetts, 4 edn.

E. Fuller, et al. (1969). 'Diffusion of Halogenated Hydrocarbons in Helium. The Effect of Structure on Collision Cross Sections'. *Journal of Physical Chemistry A* **75**:3679.

B. S. Garbow, et al. (1980). *Minpack subroutine HYBRD*. Argonne National Laboratory.

G. Germani, et al. (2005). 'Platinum/ceria/alumina catalysts on microstructures for carbon monoxide conversion'. *Catalysis Today* **110**(1-2):114 – 120. Catalytic Microstructured Reactors - Catalytic Microstructured Reactors.

G. Germani & Y. Schuurman (2006). 'Water-gas shift reaction kinetics over mu-structured Pt/CeO'. *AIChE Journal* **52**(5):1806–1813.

O. Goerke, et al. (2004). 'Water gas shift reaction and selective oxidation of CO in microreactors'. *Applied Catalysis A: General* **263**(1):11 – 18.

O. Goerke, et al. (2009). 'Kinetic study of ethanol reforming in a microreactor'. *Applied Catalysis A: General* **360**(2):232 – 241.

S. V. Gokhale, et al. (2005). 'Microchannel Reactors: Applications and Use in Process Development'. *International Journal of Chemical Reactor Engineering* **3**(R2):R2.

M. Hermanns (2002). *Parallel Programming in Fortran 95 using OpenMP*. School of Aeronautical Engineering, Departamento de Motopropulsi'on y Termofluidodin'amica; Universidad Polit'ecnica de Madrid.

V. Hessel, et al. (2004). *Chemical Microprocess Engineering: Fundamentals, Modelling and Reactions*. Wiley-VCH, Weinheim.

H. M. Hettiarachchi, et al. (2008). 'Three-dimensional laminar slip-flow and heat transfer in a rectangular microchannel with constant wall temperature'. *International Journal of Heat and Mass Transfer* **51**(21-22):5088 – 5096.

J. Hoebink & G. Marin (1998). *Structured Catalysts and Reactors*, chap. Modelling of Monolithic Reactors for Automotive Exhaust Gas Treatment, pp. 209 – 212. Marcel Dekker, New York, 2nd edn.

M. Karakaya, et al. (2009). 'Steady-state and dynamic modeling of indirect partial oxidation of methane in a wall-coated microchannel'. *Catalysis Today* **139**(4):312 – 321. Hydrogen Production - Selected papers from the Hydrogen Production Symposium at the American Chemical Society 234th National Meeting & Exposition, August 19-23, 2007, Boston, MA, USA.

R. Kieski, et al. (1993). 'Kinetics of the water gas shift reaction over several alkane activation and water gas shift catalyst'. *Applied Catalysis A: General* **101**:317–338.

G.-Y. Kim, et al. (2005). 'Parametric study of microreactor design for water gas shift reactor using an integrated reaction and heat exchange model'. *Chemical Engineering Journal* **110**(1-3):1 – 10.

G. Kolb, et al. (2008). 'A micro-structured 5ÂăkW complete fuel processor for iso-octane as hydrogen supply system for mobile auxiliary power units: Part II–Development of water-gas shift and preferential oxidation catalysts reactors and assembly of the fuel processor'. *Chemical Engineering Journal* **138**(1-3):474 – 489.

G. Kolb & V. Hessel (2004). 'Micro-structured reactors for gas phase reactions'. *Chemical Engineering Journal* **98**(1-2):1 – 38.

G. Kolb, et al. (2005). 'Water-gas shift reaction in micro-channels–Results from catalyst screening and optimisation'. *Catalysis Today* **110**(1-2):121 – 131. Catalytic Microstructured Reactors - Catalytic Microstructured Reactors.

R. Krishna & J. A. Wesselingh (1997). 'The Maxwell-Stefan approach to mass transfer'. *Chemical Engineering Science* **52**(6):861 – 911.

O. Levenspiel (1999). *Chemical Rection Engineering*. Wiley, New York, 3rd edition edn.

P. Matstoms (1995). 'Parallel sparse QR factorization on shared memory architectures'. *Parallel Computing* **21**(3):473 – 486.

D. Mears (1971). 'Tests for Transport limitations in Experimental Catalytic Reactors'. *Industrial & engineering chemistry process design and development* **10**(4):541 – 547.

J. Newman (2009). 'Stefan-Maxwell mass transport'. *Chemical Engineering Science* **64**(22):4796 – 4803. Morton Denn Festschrift.

M. Parak, et al. (2009). 'Development of a Microchannel Reactor Model for the Water-Gas Shift Reaction'. In *Conference Proceedings Conference of the South African Institution of Chemical Engineers*.

R. Perry (ed.) (1997). *Perry's Chemical Engineers' Handbook*. McGraw-Hill, 7th edition edn.

L. Petzold (1982). *A description of DASSL: A differential/agebraic system solver*. Sandia National Laboratories, sand82-8637 edn.

P. Pfeifer, et al. (2005). 'Kinetic investigations on methanol steam reforming on PdZn catalysts in microchannel reactors and model transfer into the pressure gap region'.

Catalysis Today **110**(1-2):76 – 85. Catalytic Microstructured Reactors - Catalytic Microstructured Reactors.

A. Quiney, et al. (2006). 'Optimization of a water-gas shift reactor over a Pt/ceria/alumina monolith'. *Journal of Power Sources* **160**(2):1163 – 1169. Special issue including selected papers presented at the International Workshop on Molten Carbonate Fuel Cells and Related Science and Technology 2005 together with regular papers.

L. L. Raja, et al. (2000). 'A critical evaluation of Navier-Stokes, boundary-layer, and plug-flow models of the flow and chemistry in a catalytic-combustion monolith'. *Catalysis Today* **59**(1-2):47 – 60.

E. V. Rebrov, et al. (2001). 'Design of a microstructured reactor with integrated heat-exchanger for optimum performance of a highly exothermic reaction'. *Catalysis Today* **69**(1-4):183 – 192.

R. Reid, et al. (1987). *The Properties of Gases and Liquids*. McGraw Hill Inc., 4th edition edn.

R. Revelli & L. Ridolfi (2008). 'Generalized collocation method for two-dimensional reaction-diffusion problems with homogeneous Neumann boundary conditions'. *Computers & Mathematics with Applications* **56**(9):2360 – 2370.

R. Rice & D. Do (1995). *Applied Mathematics and Modelling for Engineers*. John Wiley & Sons, New York.

D. H. Richardson, et al. (2000). 'Low Reynolds number flow inside straight micro channels with irregular cross sections'. *Heat and Mass Transfer* **36**(3):187 – 193.

F. Rotella & I. Zambettakis (1999). 'Block Householder transformation for parallel QR factorization'. *Applied Mathematics Letters* **12**(4):29 – 34.

R. Sankarasubramanian & W. N. Gill (1973). 'Unsteady Convective Diffusion with Interphase Mass Transfer'. *Proceedings of the Royal Society of London. Series A, Mathematical and Physical Sciences* **333**(1592):115–132.

Y. Schuurman, et al. (2005). 'Comparison of fixed bed and monolith reactors for the water gas shift reaction'. In *Proceedings of the Seventh World Congress of Chemical Engineering*, Glasgow.

D. P. Sekulic, et al. (1997). 'Irreversibility phenomena associated with heat transfer and fluid friction in laminar flows through singly connected ducts'. *International Journal of Heat and Mass Transfer* **40**(4):905 – 914.

S. Spatenka, et al. (2005). 'Modelling and simulation of micro-channel catalytic WGS reactor for an automotive fuel processor'. *Chemical Industry & Chemical Engineering Quarterly* **3**:143–151.

M. Spiga & G. Morini (1994). 'A symmetric solution for velocity profile in laminar flow through rectangular ducts'. *International Communications in Heat and Mass Transfer* **21**(4):469–475.

J. Spurk (1997). *Fluid Mechanics*. Springer.

A. Stankiewicz & J. Moulijn (2000). 'Process Intensification: transforming chemical engineering'. *Chemical Engineering Progress* **1**:22–34.

J. Stewart (2001). *Calculus Concepts and Contexts*. Brooks/Cole, Australia, 2nd edition edn.

G. Taylor (1953). 'Dispersion of Soluble Matter in Solvent Flowing Slowly through a Tube'. *Proceedings of the Royal Society of London. Series A, Mathematical and Physical Sciences* **219**(1137):186–203.

G. Taylor (1954). 'Conditions under Which Dispersion of a Solute in a Stream of Solvent can be Used to Measure Molecular Diffusion'. *Proceedings of the Royal Society of London. Series A, Mathematical and Physical Sciences* **225**(1163):473–477.

R. Taylor & R. Krishna (1993). *Multicomponent Mass Transfer*. John Wiley and Sons.

W. TeGrotenhuis, et al. (2002). 'Optimizing Microchannel Reactors by Trading-Off Equilibrium and reaction Kinetics through Temperature Management'. In *IMRET 6 - 6th International Conference on Microreaction Technology*, New Orleans.

A. Tonkovich, et al. (2005). 'Microchannel Technology Scale-up to Commercial Capacity'. *Chemical Engineering Research and Design* **83**(6):634 – 639. 7th World Congress of Chemical Engineering.

A. L. Y. Tonkovich, et al. (2007). 'From seconds to milliseconds to microseconds through tailored microchannel reactor design of a steam methane reformer'. *Catalysis Today* **120**(1):21 – 29. The Novel Compact Catalytic Reactor.

A. Y. Tonkovich, et al. (1999). 'Microchannel reactors for fuel processing applications. I. Water gas shift reactor'. *Chemical Engineering Science* **54**(13-14):2947 – 2951.

A. Tonkovitch (2008). 'Micro-channel Heat Exchanger'. http://www.velocys.com/news/conferences.php. Retrieved 22 Feb 2009.

M. Vahabi & M. Akbari (2009). 'Three-dimensional simulation and optimization of an isothermal PROX microreactor for fuel cell applications'. *International Journal of Hydrogen Energy* **34**(3):1531 – 1541.

J. Villadsen & M. Michelsen (1978). *Solution of Differential Equation Models by Polynomial Approximation*. Prentice Hall, New Jersey.

S. Walter, et al. (2005). 'Mass transfer limitations in microchannel reactors'. *Catalysis Today* **110**(1-2):15 – 25. Catalytic Microstructured Reactors - Catalytic Microstructured Reactors.

Y. Wan, et al. (2003). '1-Pentene Epoxidation in Titanium Silicalite-1 Microchannel Reactor: Experiments and Modelling'. *Chemical Engineering Research and Design* **81**(7):753 – 759. Reaction Engineering: Microstructured Reactors.

J. Wang & W. Stewart (1983). 'New descriptions of Dispersion in Flow through Tubes: Convolution and Collocation'. *AIChE Journal* **29**(3):493–498.

J. Wang & W. Stewart (1989). 'Multicomponent Reactive Dispersion in Tubes: Collocation vs. Radial Averaging'. *AIChE Journal* **35**(3):490–499.

J. Welty, et al. (2001). *Fundmentals of Momentum, Heat and Mass Transfer*. John Wiler & Sons, New Jersey, 4 edn.

C. Wheeler, et al. (2004). 'The water-gas-shift reaction at short contact times'. *Journal of Catalysis* **223**(1):191 – 199.

K. Wright (1991). 'Parallel algorithms for QR decomposition on a shared memory multiprocessor'. *Parallel Computing* **17**(6-7):779 – 790.

B. Yang, et al. (2008). 'Multi-scale modeling of microstructured reactors for the oxidative dehydrogenation of ethane to ethylene'. *Chemical Engineering Journal* **135**(Supplement 1):S147 – S152. Microreaction Technology IMRET 9: Proceedings of the Ninth International Conference on Microreaction Technology - IMRET9 Special Issue.

Appendix A

Derivations

A.1 Derivations of Continuum Equations

This Appendix outlines the formulation of the continuum equations for mass, momentum and energy in their most basic forms. The assumptions that lead to the derived equations are:

- laws of non-relativistic mechanics hold
- continuum model applies

The conversion between the Maxwell-Stefan equation for velocity and species flux is also shown.

A.1.1 Conservation of Mass

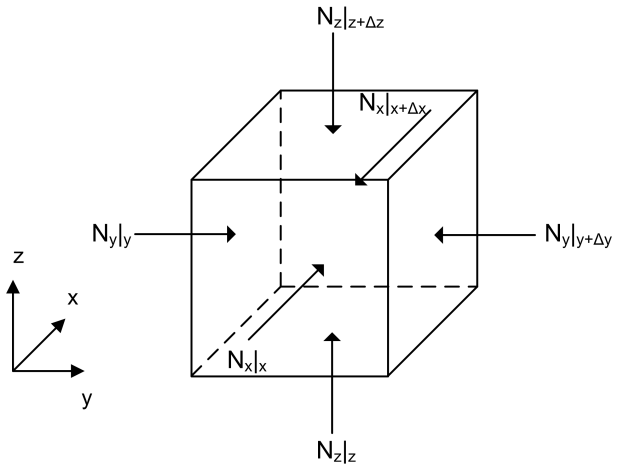

Figure A.1: Control volume over which mass balance is carried out and mass fluxes

An overall mass balance is carried out over a cube of fluid with dimensions $[\Delta x, \Delta y, \Delta z]$ containing mass m_{sys}. This is shown in Figure A.1. The mass flux vector $\mathbf{n} = [n_x, n_y, n_z]$, represents inflow and outflow of mass. The shell balance is as follows

$$\begin{aligned} ACC &= IN - OUT \\ \frac{\partial m_{sys}}{\partial t} &= \Delta y \Delta z \left(n_x \mid_x - n_x \mid_{x+\Delta x}\right) + \Delta x \Delta z \left(n_y \mid_y - n_y \mid_{y+\Delta y}\right) + \Delta x \Delta y \left(n_z \mid_z - n_z \mid_{z+\Delta z}\right) \end{aligned}$$

$\div \Delta x \Delta y \Delta z$ and rearranging

$$\frac{\partial \rho}{\partial t} = -\frac{\left(n_x \mid_{x+\Delta x} - n_x \mid_x\right)}{\Delta x} - \frac{\left(n_y \mid_{y+\Delta y} - n_y \mid_y\right)}{\Delta y} - \frac{\left(n_z \mid_{z+\Delta z} - n_z \mid_z\right)}{\Delta z}$$

take $\lim_{[\Delta x, \Delta y, \Delta z] \to 0}$

$$\frac{\partial \rho}{\partial t} = -\frac{\partial n_x}{\partial x} - \frac{\partial n_y}{\partial y} - \frac{\partial n_z}{\partial z}$$

substitute for $\mathbf{n} = \rho \mathbf{v}$

$$\frac{\partial \rho}{\partial t} + \frac{\partial}{\partial x}\left(\rho v_x\right) + \frac{\partial}{\partial y}\left(\rho v_y\right) + \frac{\partial}{\partial z}\left(\rho v_z\right) = 0 \quad \text{(A.1)}$$

$$\frac{\partial \rho}{\partial t} + \left(\nabla \cdot \rho \mathbf{v}\right) = 0 \quad \text{(A.2)}$$

A.1.2 Conservation of Momentum

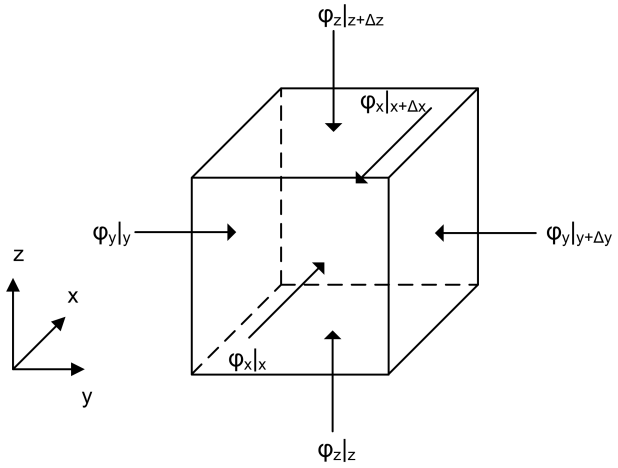

Figure A.2: Control volume over which momentum balance is carried out and momentum fluxes.

Table A.1: Summary of the form of momentum flux tensors adapted from (Bird et al., 2002)

Symbol	Meaning
$\rho\mathbf{vv}$	convective momentum flux tensor
τ	viscous momentum flux tensor
$\pi = p\delta + \tau$	molecular momentum flux tensor
$\phi = \pi + \rho\mathbf{vv}$	combined momentum flux tensor

A balance on the x-momentum is carried out over a cube of fluid with dimensions $[\Delta x, \Delta y, \Delta z]$ containing momentum $m_{sys}v_x$. This is shown in Figure A.2. The first column of the (second order) combined momentum flux tensor $\phi = [\phi_{xx}, \phi_{yx}, \phi_{zx}]$ represents the transfer of x-momentum to the $[x, y, z]$ directions[1].

The form of the combined momentum flux tensor is summarised in Table A.1. A brief explanation of the various tensors is given here but a more detailed and informative analysis can be found in the publication (Bird et al., 2002). The combined momentum flux tensor is made up of the *convective momentum flux tensor*, $\rho\mathbf{vv}$ which accounts for momentum transfer by bulk flow and the *molecular momentum flux tensor*, π. This accounts for momentum transfer by molecular motion and consists of a molecular force, τ proportional to the viscosity of the medium, μ and the force of molecular collisions normal to the exposed surface represented by the pressure force $p\delta$. Here, the tensor δ_{ij} is referred to as the *Kronecker delta* which is 1 when $i = j$ and 0 when $i \neq j$ to ensure that pressure is retained as a normal force.

An external body force, $m_{sys}g_x$ is also accounted for. The shell balance is as follows

$$\begin{aligned} ACC &= IN - OUT + EXT \\ \frac{\partial}{\partial t}(m_{sys}v_x) &= \Delta y\Delta z\left(\phi_{xx}\mid_x - \phi_{xx}\mid_{x+\Delta x}\right) + \Delta x\Delta z\left(\phi_{yx}\mid_y - \phi_{yx}\mid_{y+\Delta y}\right) + \Delta x\Delta y\left(\phi_{zx}\mid_z - \phi_{zx}\mid_{z+\Delta z}\right) + \end{aligned}$$

$\div \Delta x\Delta y\Delta z$ and rearranging

$$\frac{\partial}{\partial t}(\rho v_x) = -\frac{\left(\phi_{xx}\mid_{x+\Delta x} - \phi_{xx}\mid_x\right)}{\Delta x} - \frac{\left(\phi_{yx}\mid_{y+\Delta y} - \phi_{yx}\mid_y\right)}{\Delta y} - \frac{\left(\phi_{zx}\mid_{z+\Delta z} - \phi_{zx}\mid_z\right)}{\Delta z} + \rho g_x$$

take $\lim_{[\Delta x,\Delta y,\Delta z]\to 0}$

[1]The notation ϕ_{ij} represents the force in the j-direction acting on a unit area in the i-direction. This is a *normal force* if $j = i$ and a *shear force* if $j \neq i$.

$$\frac{\partial}{\partial t}(\rho v_x) = -\frac{\partial \phi_{xx}}{\partial x} - \frac{\partial \phi_{yx}}{\partial y} - \frac{\partial \phi_{zx}}{\partial z} + \rho g_x$$

Substitute the expression for the combined momentum flux tensor$\phi_{ij} = \pi_{ij} + \rho v_i v_j$

$$\frac{\partial}{\partial t}(\rho v_x) = -\frac{\partial \pi_{xx}}{\partial x} - \frac{\partial}{\partial x}(\rho v_x v_x) - \frac{\partial \pi_{yx}}{\partial y} - \frac{\partial}{\partial y}(\rho v_y v_x) - \frac{\partial \pi_{zx}}{\partial z} - \frac{\partial}{\partial z}(\rho v_z v_x) + \rho g_x$$

Substitute the mass balance in Equation A.1 for $\frac{\partial \rho}{\partial t}$

$$\begin{aligned}
\rho\frac{\partial v_x}{\partial t} + v_x\left[-\frac{\partial}{\partial x}(\rho v_x) - \frac{\partial}{\partial y}(\rho v_y) - \frac{\partial}{\partial z}(\rho v_z)\right] &= -\frac{\partial \pi_{xx}}{\partial x} - \frac{\partial \pi_{yx}}{\partial y} - \frac{\partial \pi_{zx}}{\partial z} - \\
&\quad \frac{\partial}{\partial x}(\rho v_x v_x) - \frac{\partial}{\partial y}(\rho v_y v_x) - \frac{\partial}{\partial z}(\rho v_z v_x) + \rho g_x \\
\therefore \rho\frac{\partial v_x}{\partial t} &= -\frac{\partial \pi_{xx}}{\partial x} - \frac{\partial \pi_{yx}}{\partial y} - \frac{\partial \pi_{zx}}{\partial z} - \\
&\quad \rho v_x\frac{\partial v_x}{\partial x} - \rho v_y\frac{\partial v_x}{\partial y} - \rho v_z\frac{\partial v_x}{\partial z} + \rho g_x \\
\therefore \rho\left(\frac{\partial v_x}{\partial t} + v_x\frac{\partial v_x}{\partial x} + v_y\frac{\partial v_x}{\partial y} + v_z\frac{\partial v_x}{\partial z}\right) &= -\frac{\partial \pi_{xx}}{\partial x} - \frac{\partial \pi_{yx}}{\partial y} - \frac{\partial \pi_{zx}}{\partial z} + \rho g_x
\end{aligned}$$

Or in vector notation

$$\therefore \rho\left[\frac{\partial v_x}{\partial t} + (\mathbf{v}\cdot\nabla v_x)\right] = -(\nabla\cdot\pi_x) + \rho g_x \tag{A.3}$$

The equations for conservation of y- and z-momentum are similarly derived and are as follows

$$\rho\left[\frac{\partial v_y}{\partial t} + (\mathbf{v}\cdot\nabla v_y)\right] = -(\nabla\cdot\pi_y) + \rho g_y \tag{A.4}$$

$$\rho\left[\frac{\partial v_z}{\partial t} + (\mathbf{v}\cdot\nabla v_z)\right] = -(\nabla\cdot\pi_z) + \rho g_z \tag{A.5}$$

A.1.3 Conservation of Energy

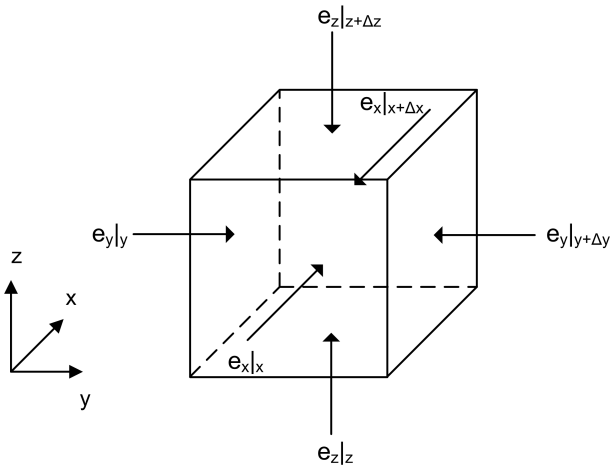

Figure A.3: Control volume over which energy balance is carried out and energy fluxes

An overall energy balance is carried out over a cube of fluid with dimensions $[\Delta x, \Delta y, \Delta z]$ containing total energy E_{sys}. This is shown in Figure A.3. The energy flux vector $\mathbf{e} = [e_x, e_y, e_z]$, represents inflow and outflow of energy. The rate at which work is done on the system volume by external body forces is is $\rho \Delta x \Delta y \Delta z \left(v_x g_x + v_y g_y + v_z g_z\right)$. No internal source of heat is accounted for, i.e. homogeneous chemical reaction. The shell balance is as follows

$$\begin{aligned} ACC &= IN - OUT \\ \frac{\partial}{\partial t}\left(m_{sys}\hat{E}_{sys}\right) &= \Delta y \Delta z \left(e_x\,|_x - e_x\,|_{x+\Delta x}\right) + \Delta x \Delta z \left(e_y\,|_y - e_y\,|_{y+\Delta y}\right) + \\ &\quad \Delta x \Delta y \left(e_z\,|_z - e_z\,|_{z+\Delta z}\right) + \rho \Delta x \Delta y \Delta z \left(v_x g_x + v_y g_y + v_z g_z\right) \end{aligned}$$

$\div \Delta x \Delta y \Delta z$ and rearranging

$$\frac{\partial}{\partial t}\left(\rho \hat{E}_{sys}\right) = -\frac{\left(e_x\,|_{x+\Delta x} - e_x\,|_x\right)}{\Delta x} - \frac{\left(e_y\,|_{y+\Delta y} - e_y\,|_y\right)}{\Delta y} - \frac{\left(e_z\,|_{z+\Delta z} - e_z\,|_z\right)}{\Delta z} + \rho\left(v_x g_x + v_y g_y + v_z g_z\right)$$

take $\lim_{[\Delta x, \Delta y, \Delta z] \to 0}$

$$\begin{aligned} \frac{\partial}{\partial t}\left(\rho \hat{E}_{sys}\right) &= -\frac{\partial e_x}{\partial x} - \frac{\partial e_y}{\partial y} - \frac{\partial e_z}{\partial z} + \rho\left(v_x g_x + v_y g_y + v_z g_z\right) \\ &= -\nabla \mathbf{e} + \rho\left(\mathbf{v} \cdot \mathbf{g}\right) \end{aligned}$$

Now the system energy is given by the contribution of internal energy per unit volume $\rho\hat{U}$, the kinetic energy per unit volume $E_k = \frac{1}{2}\rho v^2 = \frac{1}{2}\rho\left(v_x^2 + v_y^2 + v_z^2\right)$ or

$$\begin{aligned} E_{sys} &= U + E_k \\ &= \rho\hat{U} + \frac{1}{2}\rho v^2 \end{aligned}$$

The energy flux is composed of the contributions of the system energy transfer due to mass transfer, the contribution due to internal friction in a viscous fluid and thermal conduction which depends on the presence of a temperature gradient. This gives respectively

$$\mathbf{e} = \mathbf{v}\left(U + E_k\right) + (\mathbf{v}\cdot\pi) + \mathbf{q}$$

The general law of conservation of energy is thus given by

$$\frac{\partial}{\partial t}\left[\rho\left(\hat{U} + \frac{1}{2}v^2\right)\right] = -\nabla\left[\mathbf{v}\left(\rho\hat{U} + \frac{1}{2}\rho v^2\right) + (\mathbf{v}\cdot\pi) + \mathbf{q}\right] + \rho\left(\mathbf{v}\cdot\mathbf{g}\right) \tag{A.6}$$

If kinetic energy is considered negligible and external body forces do not exist then upon substitution of the continuity and momentum equations we have (el Hak 1999)

$$\rho\left[\frac{\partial\hat{U}}{\partial t} + \mathbf{v}\cdot\left(\nabla\cdot\hat{U}\right)\right] = -\nabla\cdot\mathbf{q} + \pi\left(\nabla\cdot\mathbf{v}\right) \tag{A.7}$$

A.2 Maxwell-Stefan Equation

The Maxwell-Stefan equation is presented in terms of individual species velocity in Equation 2.45. This can be represented in terms of fluxes as in Equation 2.46. The conversion is shown here, starting from Equation 2.45.

Given the relationship between the driving force for diffusion and species composition and velocity

$$d_i = -\sum_{j=1}^{c}\frac{\chi_i\chi_j\left(v_i - v_j\right)}{D_{i,j}} \tag{A.8}$$

Substitution of $N_i = c_i v_i$ gives

$$\begin{aligned} d_i &= -\sum_{j=1}^{c} \frac{\chi_i \chi_j \left(\frac{N_i}{c_i} - \frac{N_j}{c_j}\right)}{D_{i,j}} \\ &= -\sum_{j=1}^{c} \chi_i \chi_j \frac{N_i}{c_i D_{i,j}} + \sum_{j=1}^{c} \chi_i \chi_j \frac{N_j}{c_j D_{i,j}} \\ &= -\chi_i \frac{N_i}{c_i} \sum_{j=1}^{c} \frac{\chi_j}{D_{i,j}} + \chi_i \sum_{j=1}^{c} \chi_j \frac{N_j}{c_j D_{i,j}} \end{aligned}$$

Given that $c_i = c_t \chi_i$

$$\begin{aligned} d_i &= -\frac{N_i}{c_t} \sum_{j=1}^{c} \frac{\chi_j}{D_{i,j}} + u_i \sum_{j=1}^{c} \frac{N_j}{c_t D_{i,j}} \\ &= \sum_{\substack{j=1 \\ j \neq i}}^{c} \frac{\chi_i N_j - \chi_j N_i}{c_t D_{i,j}} \end{aligned} \tag{A.9}$$

Appendix B

Miscellaneous calculations

B.1 Knudsen number

The Knudsen number is given by the substitution of Equation 2.1 into Equation 2.2 to give

$$Kn = \frac{k_B T}{\sqrt{2}\pi P \sigma^2 D_h} \tag{B.1}$$

For the worst case scenario (i.e. maximum Kn) we have low pressure and particle diameter, σ. The parameters are thus set to $P = 1bar$ and the gas is assumed to be pure hydrogen.

The conditions and constants used in the analysis are summarised in Table B.1. The calculated Knudsen numbers are shown for different hydraulic diameters and temperatures in Table B.2. The condition for continuum flow, $Kn < 0.1$ is held everywhere while the condition for slip boundary conditions is held at $D_h < 40\,\mu m$ and $T > 500\,K$. As the D_h is to be kept above $100\,\mu m$ the flow at the surface can be considered to have no-slip and zero temperature jump.

Table B.1: Summary of variables and constants used in the Knudsen Number analysis

Parameter	Value
k_B	$1.38 \times 10^{-23}\,\mathrm{J/K}$
P	$101325\,\mathrm{Pa}$
σ	$3.82 \times 10^{-10}\,\mathrm{m}$
D_h	$10 - 200\,\mu\mathrm{m}$
T	$300 - 1000\,\mathrm{K}$

Table B.2: Calculated Knudsen Numbers for the parameters shown in Table B.1. The Knudsen numbers below the no-slip condition threshold of 0.001 are shown in bold.

	300 K	350 K	400 K	450 K	500 K	600 K	700 K	800 K	1000 K
10 μm	6.30E-003	7.35E-003	8.40E-003	9.45E-003	**1.05E-002**	**1.26E-002**	**1.47E-002**	**1.68E-002**	**2.10E-002**
20 μm	3.15E-003	3.68E-003	4.20E-003	4.73E-003	5.25E-003	6.30E-003	7.35E-003	8.40E-003	**1.05E-002**
40 μm	1.58E-003	1.84E-003	2.10E-003	2.36E-003	2.63E-003	3.15E-003	3.68E-003	4.20E-003	5.25E-003
100 μm	6.30E-004	7.35E-004	8.40E-004	9.45E-004	1.05E-003	1.26E-003	1.47E-003	1.68E-003	2.10E-003
200 μm	3.15E-004	3.68E-004	4.20E-004	4.73E-004	5.25E-004	6.30E-004	7.35E-004	8.40E-004	1.05E-003

Table B.3: Summary of variables and constants used in the Weitz-Prater criterion analysis.

Parameter	Value
k_0	1.3×10^6 mol/s.bar$^{0.05}$
E_a	86.0×10^3 J/mol
P	$3\,bar$
D_{eff}	5.0×10^{-5} m^2/s
T	$573 - 773\,K$
δ_{cat}	$5 - 45\,\mu m$

B.2 Weitz-Prater Criterion

The Weitz-Prater criterion, M_w is calculated according to the expression in Equation 2.36, using the kinetic expression in Equation 2.88. The values of the constants and variables used are shown in Table B.3. The calculated values are shown in Table B.4. At expected conditions, none of the calculated values fall below the $M_w < 0.15$ criterion for internal mass transport.

B.3 Space velocity

The space velocity at the conditions of the study conducted in (Germani et al. 2005) is calculated here. The given molar flow rate of $100^{\text{Nml}}/_{\text{min}}$ through 49 channels is converted into SI units

$$q = 100\frac{Nml}{min}.\frac{1m^3}{1 \times 10^6 ml}.\frac{1min}{60s} = 3.33 \times 10^{-6\text{m}^3}/_{\text{s}}$$

At normal conditions we have $T_N = 273.15K$ and $P_N = 101325Pa$ the flow rate q becomes the molar flow rate

$$\begin{aligned} \bar{n} &= \frac{qP_N}{RT_N} \\ &= 1.49 \times 10^{-4\text{mol}}/_{\text{s}} \end{aligned}$$

The catalyst mass is reported to be $m_{cat}252mg = 2.52 \times 10^{-4}$kg. The space velocity can now be calculated

Table B.4: Calculated values of the Weitz-Prater criterion for the parameters shown in Table B.3.

	$5\,\mu m$	$10\,\mu m$	$15\,\mu m$	$20\,\mu m$	$25\,\mu m$	$30\,\mu m$	$35\,\mu m$	$40\,\mu m$	$45\,\mu m$
$573\,K$	9.38E-007	3.75E-006	8.44E-006	1.50E-005	2.34E-005	3.38E-005	4.59E-005	6.00E-005	7.59E-005
$623\,K$	4.34E-006	1.73E-005	3.90E-005	6.94E-005	1.08E-004	1.56E-004	2.13E-004	2.78E-004	3.51E-004
$673\,K$	1.61E-005	6.43E-005	1.45E-004	2.57E-004	4.02E-004	5.79E-004	7.88E-004	1.03E-003	1.30E-003
$723\,K$	5.00E-005	2.00E-004	4.50E-004	8.00E-004	1.25E-003	1.80E-003	2.45E-003	3.20E-003	4.05E-003
$773\,K$	1.35E-004	5.39E-004	1.21E-003	2.16E-003	3.37E-003	4.85E-003	6.60E-003	8.62E-003	1.09E-002

$$\begin{aligned} SV &= \frac{\bar{n}}{m_{cat}} \\ &= 0.59^{\mathrm{mol}/\mathrm{s.kg_{cat}}} \end{aligned}$$

B.4 Velocity

The inlet velocity can be calculated given the reactor dimensions, catalyst thickness and space velocity. From the definition of space velocity in Equation 2.38

$$SV = \frac{c_t v_0 X S A_I}{V_{cat} \rho_{cat}}$$

which gives the velocity after rearrangement

$$\begin{aligned} v_0 &= \frac{V_{cat} \rho_{cat} SV}{X S A_I c_t} \\ &= \frac{L\left[WH - (W - 2\delta_{cat})(H - 2\delta_{cat})\right] \rho_{cat} SV}{(W - 2\delta_{cat})(H - 2\delta_{cat}) \frac{p}{RT}} \end{aligned}$$

The inlet velocity is calculated for the conditions reported by (Germani et al. 2005) and shown in Table 6.5.

$$\begin{aligned} v_0 &= \frac{(0.05)\left[\left(600 \times 10^{-6}\right)\left(400 \times 10^{-6}\right) - \left(400 \times 10^{-6} - 2\left(10 \times 10^{-6}\right)\right)\left(400 \times 10^{-6} - 2\left(10 \times 10^{-6}\right)\right)\right](1300)(0.59)}{\left(400 \times 10^{-6} - 2\left(10 \times 10^{-6}\right)\right)\left(400 \times 10^{-6} - 2\left(10 \times 10^{-6}\right)\right)\frac{3.03 \times 10^5}{(8.314)(573.15)}} \\ &= 0.0535\,^{\mathrm{m}/\mathrm{s}} \end{aligned}$$

Appendix C

Physical Property Data

In contrast to liquids, the prediction of physical properties of gasses is quite well advanced mainly due to the application of the kinetic theory of gasses. This theory uses the elementary gas model which assumes all molecules are rigid non-interacting spheres in random motion at a particular mean velocity v. The gas has density n molecules per unit volume. The collisions of the gas lead to the transfer of momentum or heat in the presence of velocity and thermal gradients respectively. The movement of mass also leads to a transfer of species in the presence of concentration gradients. Each of the mass, momentum and heat fluxes are proportional to the density, momentum and energy gradients, ρ'

$$Flux \propto -\frac{d\rho'}{dy} \tag{C.1}$$

The generic property is substituted by ρ_i for mass density, nmv_x for momentum density and $c_v nT$ for energy density. Kinetic theory gives the constant of proportionality for each of these fluxes as $\frac{vL}{3}$ where v is the average molecular velocity and L is the mean free path. This expression is used to derive generic expressions for the transport coefficient of diffusion D, viscosity, μ and thermal conductivity, λ. This gives

$$Mass\,flux = -D\frac{dc_i}{dy} = -\frac{vL}{3}\frac{d\rho_i}{dy} \tag{C.2}$$

$$Momentum\,flux = -\mu\frac{dv_x}{dy} = -\frac{vL}{3}mn\frac{dv_x}{dy} \tag{C.3}$$

$$Energy\,flux = -\lambda\frac{dT}{dy} = -\frac{vL}{3}c_v n\frac{dT}{dy} \tag{C.4}$$

Each transport coefficient is now given by analogy in the expressions above. Kinetic theory gives

$$v \propto \sqrt{\frac{RT}{M}} \tag{C.5}$$

$$L \propto \frac{1}{n\sigma^2} \tag{C.6}$$

while the ideal gas law gives

$$n \propto \frac{p}{RT} \tag{C.7}$$

and by definition $M = nN_A$

Each transport coefficient is now given by

$$D = \frac{vL}{3} = k_1 \frac{T^{3/2}}{M^{1/2} p\sigma^2} \tag{C.8}$$

$$\mu = \frac{mnvL}{3} = k_2 \frac{T^{1/2} M^{1/2}}{\sigma^2} \tag{C.9}$$

$$\lambda = \frac{vLc_v n}{3} = k_3 \frac{T^{1/2}}{M^{1/2}\sigma^2} \tag{C.10}$$

These expressions are for idealised gasses but nevertheless are useful in that they form the basis for other empirical correlations. These correlations are discussed in further sections.

C.1 Viscosity

If a shear stress is applied to a closed fluid, then the fluid will accelerate and a velocity gradient will be established. The velocity of the fluid will be maximum at the point at which the force is applied. A Newtonian fluid is defined as a fluid in which the shear stress per unit area is proportional to the negative of the velocity gradient

$$\tau_{yx} \propto -\frac{dv_x}{dy} \tag{C.11}$$

The constant of proportionality is called the viscosity and it leads to the familiar Newton's law of viscosity

$$\tau_{yx} = -\mu \frac{dv_x}{dy} \tag{C.12}$$

Viscosity is a state property of the fluid and is a measure of the friction between layers of fluid which opposes the motion in the direction of the shear force. So if a constant shear

stress is applied to a range of fluids with increasing viscosity each layer exerts a larger frictional force between layers so the velocity gradient will decrease (Bird et al., 2002).

C.1.1 Theory predictions for viscosity

The viscosity of an elementary gas (non-interacting rigid spheres) is given by

$$\mu = 26.69 \frac{(MT)^{1/2}}{\sigma^2} \tag{C.13}$$

where μ = viscosity μP

M = molar mass, $\frac{\text{g}}{\text{mol}}$

T = temperature, K

σ = hard shell diameter, Å

C.1.2 Estimation of Viscosity

This is however only strictly valid at high temperature and low pressures or for monatomic gasses that satisfy the condition of non-interaction. To account for attraction and repulsion of molecules by intermolecular forces the Chapman-Enskog theory is applied. This requires the inclusion of a collision integral, Ω_v

$$\mu = 26.69 \frac{(MT)^{1/2}}{\sigma^2 \Omega_v} \tag{C.14}$$

The collision integral is given as a function of the dimensionless temperature

$$T^* = \frac{k_B T}{\epsilon} \tag{C.15}$$

where ϵ is the characteristic energy. This energy is the minimum potential energy of interaction between molecules. The intermolecular potential energy function $\Phi(r)$ where r is the distance between molecules is given by an appropriate intermolecular force law (e.g. Lennard-Jones potential function). Using this law the collision integral is given as

$$\Omega_v = A (T^*)^{-B} + C \exp(-DT^*) + E \exp(-FT^*) \tag{C.16}$$

and the constants are given in the table below.

The values of σ and $\frac{\epsilon}{k_b}$ cannot be obtained from experimentation and have to be estimated. The method of Chung gives

Table C.1: Constants in the collision integral function

Constant	Value
A	1.16145
B	0.14874
C	0.52487
D	0.77320
E	2.16178
F	2.43787

$$\frac{\epsilon}{k_B} = \frac{T_c}{1.2593} \tag{C.17}$$

$$\sigma = 0.809 V_c^{1/3} \tag{C.18}$$

with V_c = critical volume in cm^3/mol

T_c= critical temperature in K

Neglecting polarities and different molecular shapes, the final viscosity equation is given by

$$\mu = 40.78 \frac{(MT)^{1/2}}{V_c^{2/3} \Omega_v} \tag{C.19}$$

Over a wide range of species this gives an average error of about 1.5 percent.

C.1.3 Mixture properties

The simplest method from kinetic theory is Wilke's Method which gives the mixture viscosity as

$$\mu_m = \sum_{i=1}^{c} \frac{u_i \mu_i}{\sum_{j=1}^{c} u_j \phi_{ij}} \tag{C.20}$$

where

$$\phi_{ij} = \frac{\left[1 + \left(\frac{\mu_i}{\mu_j}\right)^{1/2} \left(\frac{M_j}{M_i}\right)^{1/4}\right]^2}{\left[8\left(1 + \frac{M_i}{M_j}\right)\right]^{1/2}} \tag{C.21}$$

This gives an average error of less than 1 % compared to binary species data.

C.2 Diffusion Coefficients

Diffusion describes the motion of materials in a single phase and the absence of mechanical or convective mixing. Diffusion depends on the presence of a gradient. Different types of gradients predicted by theory and experimentation lead to diffusion including pressure, temperature, external force fields and concentration Reid et al. (1987). This section only considers diffusion due to concentration gradients.

The diffusion gradient provides the relationship between the diffusive mass flux relative to a plane of no net molar flow, J_i and the driving force, ∇x_i. In a binary mixture this leads to the Fickian definition of diffusion flux

$$J_A = -cD_{AB}\frac{du_A}{dx} \tag{C.22}$$

$$J_B = -cD_{BA}\frac{du_B}{dx} \tag{C.23}$$

As J_i is defined relative to a plane of no net molar flow, we have

$$J_A + J_B = 0 \tag{C.24}$$

and since $\sum_{i=1}^{c} u_i = 1$ we have

$$\frac{du_A}{dx} + \frac{du_B}{dx} = 0 \tag{C.25}$$

Combining the above two expressions, we have $D_{AB} = D_{BA}$. This coefficient is sometimes called the mutual diffusion coefficient.

C.2.1 Chemical potential driving force

The mutual diffusion coefficient takes the diffusive flux to be proportional to the concentration gradient. However it could also be affected by other factors such as the force fields around molecules. These are themselves complex functions of temperature and pressure around these molecules and it is simplistic to assume that J_i is linear with concentration gradient. An alternate driving force proposed is the chemical potential gradient, $\frac{d\mu_i}{dx}$. This states that of the equilibrium composition in a binary system is disturbed, then

the diffusive flow necessary to return to equilibrium is proportional to $\frac{d\mu_i}{dx}$. A thermodynamic correction term, α can be used with D_{AB} to correct diffusive flux in terms of a concentration gradient. This is given by

$$\alpha = \left[\frac{\partial \ln a_A}{\partial \ln u_A}\right] \tag{C.26}$$

For gaseous systems, α is close to unity except at high pressures. The correction is however routinely used in the case of liquid systems.

C.2.2 Theory predictions for diffusion coefficients

The theory for predicting binary diffusion coefficients at low and moderate pressures is well developed Reid et al. (1987). The theory comes from the solution of the Boltzmann equation and leads to the equation

$$D_{AB} = \frac{3}{16}\frac{(4\pi kT/M_{AB})^{1/2}}{n\pi\sigma_{AB}^2\Omega_D} f_D \tag{C.27}$$

where $M_{AB} = 2\left[(1/M_A) + (1/M_B)\right]^{-1}$

n is the number density of the molecules in the mixture

k is the Boltzmann constant

Ω_D is the collision integral. It is given by choice of the intermolecular forces law chosen (e.g. Lennard-Jones)

σ_{AB} is the characteristic length and also depends on choice of the intermolecular force law

f_D is a correction factor of order 1. If M_A is the same order as M_B, f_D lies between 1.00 and 1.02. In other cases f_D lies between 1.0 and 1.1.

If the ideal gas law is applied to n then D_{AB} is given by

$$D_{AB} = \frac{0.00266T^{3/2}}{pM_{AB}^{1/2}\sigma_{AB}^2\Omega_D} \tag{C.28}$$

where D_{AB} = diffusion coefficient$[^{cm^2}/_{\mathrm{s}}]$

T = temperature, [K]

P = pressure, [bar]

σ_{AB} = characteristic length,$[\text{Å}]$

Ω_D = diffusion collision integral, $[-]$

Table C.2: Atomic diffusion volumes (adapted from Reid et al. (1987)originally in Fuller et al. (1969))

Atomic and Structural Diffusion Volume Increments			
C	15.9	F	14.7
H	2.31	Cl	21.0
O	6.11	Br	21.9
N	4.54	I	29.8
Aromatic Ring	-18.3	S	22.9
Heterocyclic ring	-18.3		

Diffusion Volumes of Simple Molecules			
He	2.67	CO	18.0
Ne	5.98	CO_2	26.9
Ar	16.2	N_2O	35.9
Kr	24.5	NH_3	20.7
Xe	32.7	H_2O	13.1
H_2	6.12	SF_6	71.3
D_2	6.84	Cl_2	38.4
N_2	18.5	Br_2	69.0
O_2	16.3	SO_2	41.8
Air	19.7		

C.2.3 Experimental predictions for diffusion coefficients

The equation above is used in its form to include empirical parameters based on regression of experimental data. These include the Wilke-Lee equation and that of Fuller. Whereas the Wilke-Lee equation requires the use of an intermolecular force law to obtain values of σ_{AB} and Ω_D, the Fuller equation substitutes these for atomic diffusion volumes. These volumes are obtained by regression of experimental data. The equation below gives a reported error of about 4 percent.

$$D_{AB} = \frac{0.00143T^{1.75}}{pM_{AB}^{1/2}\left[(\Sigma_v)_A^{1/3} + (\Sigma_v)_B^{1/3}\right]^2} \tag{C.29}$$

C.3 Thermal Conductivity

C.3.1 Theory predictions for thermal conductivity

The thermal conductivity of an elementary gas (non-interacting rigid spheres) is given by

$$\lambda = 2.63 \times 10^{-23} \frac{T^{1/2}}{M^{1/2}\sigma^2\Omega_v} \tag{C.30}$$

where λ = thermal conductivity W/ (m.K)

M = molar mass, $\frac{\text{kg}}{\text{mol}}$

T = temperature, K

σ = hard shell diameter, m

Ω_v = collision integral−

This is however only valid for monatomic gasses which have translational motion only (Reid et al., 1987). Polyatomic gasses have both translational and internal energy contributions to the overall thermal conductivity. These have been included in the familiar Eucken equation as

$$\lambda = \frac{\mu c_v}{M_i}\left[1.15 + \frac{2.03}{\left(\frac{c_p}{R}\right) - 1}\right] \tag{C.31}$$

where for an ideal gas $c_v = c_p - R$.

This predicts the thermal conductivity of CO_2 with an error of between 2-4 percent depending on temperature.

C.3.2 Mixture properties

The mixture thermal conductivity is calculated in an analogous manner as that of viscosity

$$\mu_m = \sum_{i=1}^{c} \frac{u_i \lambda_i}{\sum_{j=1}^{c} u_j A_{ij}} \tag{C.32}$$

It has been shown that $A_{ij} = \phi_{ij}$ (Reid et al., 1987) which allows the use of equation C.21 for the calculation of A_{ij}.

Appendix D

Data

D.1 Thermodynamic data

The heat capacity, enthalpy and entropy of each species is calculated by Equations D.1,D.2 and D.3 respectively. The coefficients $A - H$ are given in the sections that follow.

$$c_p(T) = A + BT' + CT'^2 + DT'^3 + \frac{E}{T'^2} \tag{D.1}$$

$$H^\circ - H^\circ_{298.15} = AT' + \frac{1}{2}BT'^2 + \frac{1}{3}CT'^3 + \frac{1}{4}DT'^4 - \frac{E}{T'} + F - H \tag{D.2}$$

$$S^\circ = Aln(T') + BT' + \frac{1}{2}CT'^2 + \frac{1}{3}DT'^3 - \frac{E}{2T'^2} + G \tag{D.3}$$

with

c_p= heat capacity ($^{J}/_{mol.K}$)

H^o = standard enthalpy ($^{kJ}/_{mol}$)

S^o= standard entropy ($^{J}/_{mol.K}$)

T'= temperature $^{K}/_{1000}$

D.1.1 Carbon Monoxide

Table D.1: Coefficients $A - H$ in Equations D.1,D.2 and D.3 for carbon monoxide.

Temperature (K)	298. - 1300.	1300. - 6000.
A	25.56759	35.15070
B	6.096130	1.300095
C	4.054656	-0.205921
D	-2.671301	0.013550
E	0.131021	-3.282780
F	-118.0089	-127.8375
G	227.3665	231.7120
H	-110.5271	-110.5271
Reference	Chase 1998	Chase 1998

D.1.2 Water

Table D.2: Coefficients $A - H$ in Equations D.1,D.2 and D.3 for water.

Temperature (K)	500. - 1700.	1700. - 6000.
A	30.09200	41.96426
B	6.832514	8.622053
C	6.793435	-1.499780
D	-2.534480	0.098119
E	0.082139	-11.15764
F	-250.8810	-272.1797
G	223.3967	219.7809
H	-241.8264	-241.8264
Reference	Chase 1998	Chase 1998
Comment	Data last reviewed in March, 1979	Data last reviewed in March, 1979

D.1.3 Hydrogen

Table D.3: Coefficients $A - H$ in Equations D.1,D.2 and D.3 for hydrogen.

Temperature (K)	298. - 1000.	1000. - 2500.	2500. - 6000.
A	33.066178	18.563083	43.413560
B	-11.363417	12.257357	-4.293079
C	11.432816	-2.859786	1.272428
D	-2.772874	0.268238	-0.096876
E	-0.158558	1.977990	-20.533862
F	-9.980797	-1.147438	-38.515158
G	172.707974	156.288133	162.081354
H	0.0	0.0	0.0
Reference	Chase 1998	Chase 1998	Chase 1998
Comment	Data last reviewed in March, 1977 New parameter fit in October 2001		

D.1.4 Carbon Dioxide

Table D.4: Coefficients $A - H$ in Equations D.1,D.2 and D.3 for carbon dioxide.

Temperature (K)	298. - 1200.	1200. - 6000.
A	24.99735	58.16639
B	55.18696	2.720074
C	-33.69137	-0.492289
D	7.948387	0.038844
E	-0.136638	-6.447293
F	-403.6075	-425.9186
G	228.2431	263.6125
H	-393.5224	-393.5224
Reference	Chase 1998	Chase 1998
Comment	Data last reviewed in September, 1965	

D.1.5 Nitrogen

Table D.5: Coefficients $A - H$ in Equations D.1,D.2 and D.3 for nitrogen.

Temperature (K)	100. - 500.	500. - 2000.	2000. - 6000.
A	28.98641	19.50583	35.51872
B	1.853978	19.88705	1.128728
C	-9.647459	-8.598535	-0.196103
D	16.63537	1.369784	0.014662
E	0.000117	0.527601	-4.553760
F	-8.671914	-4.935202	-18.97091
G	226.4168	212.3900	224.9810
H	0.0	0.0	0.0
Reference	Chase 1998	Chase 1998	Chase 1998
Comment	Data last reviewed in March, 1977 New parameter fit in January 2009		

D.1.6 Argon

Table D.6: Coefficients $A - H$ in Equations D.1,D.2 and D.3 for nitrogen.

Temperature (K)	298. - 6000.
A	20.78600
B	2.825911×10-7
C	-1.464191×10-7
D	1.092131×10-8
E	-3.661371×10-8
F	-6.197350
G	179.9990
H	0.0000
Reference	Chase 1998
Comment	Data last reviewed in March, 1982

D.2 Heat of Formation

Figure D.1: Heats of formation at the standard state of an ideal gas at 298.15 K and 1 bar (?)

Species	Heat of formation
	$^{kJ}/_{mol}$
carbon monoxide	-110.5
water	-241.8
hydrogen	0.
carbon dioxide	-393.5
nitrogen	0.
argon	0.

D.3 Critical Properties

Figure D.2: Critical properties. (Perry 1997 2-164)

Species	T_c	P_c	V_c
	K	$Pa \times 10^{-6}$	$^{m^3}/_{mol} \times 10^3$
carbon monoxide	132.92	3.49	0.095
water	647.13	21.94	0.056
hydrogen	33.19	1.32	0.064
carbon dioxide	304.21	7.39	0.095
nitrogen	126.2	3.39	0.089
argon	150.86	4.9	0.0075

D.4 Physical properties

Figure D.3: Physical properties.

Species	Dispersion volume	Molar mass
	cm^3	$^{g}/_{mol}$
carbon monoxide	18.0	28.011
water	13.1	18.016
hydrogen	6.12	2.0158
carbon dioxide	26.9	44.011
nitrogen	18.5	28.014
argon	16.2	39.95
Source		(Perry, 1997)

Appendix E

Miscellanous Plots

E.1 Dankwerts' plots for different conditions

E.1.1 v_0= 0.5 m/s

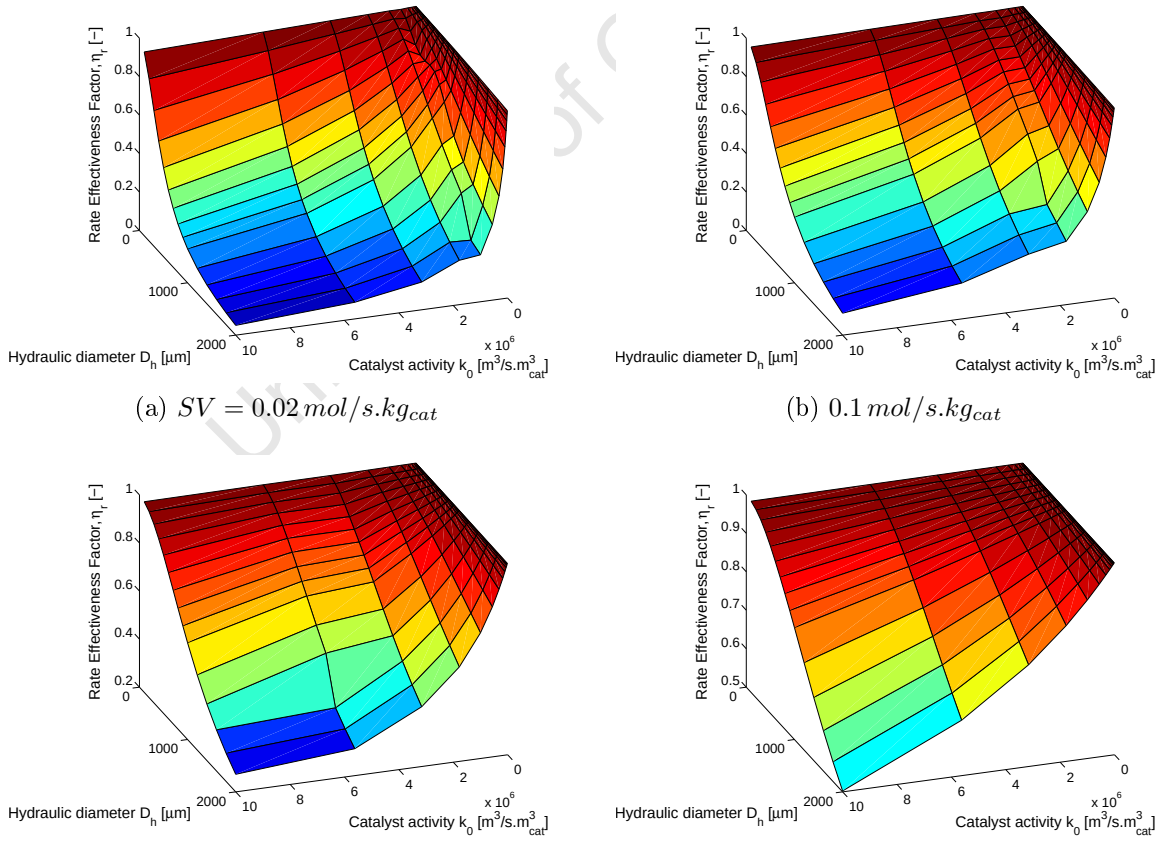

(a) $SV = 0.02\,mol/s.kg_{cat}$ (b) $0.1\,mol/s.kg_{cat}$

(c) $SV = 0.5\,mol/s.kg_{cat}$ (d) $SV = 2.5\,mol/s.kg_{cat}$

Figure E.1: Change in average effectiveness factor with $D_h = 100 - 2000\,\mu m$ and $k_0 = 1 \times 10^4 - 1 \times 10^7\ {}^{\mathrm{m}^3}/_{\mathrm{s.m}^3_{\mathrm{cat}}}$ for different space velocities. $v_0 = 0.5\ {}^{\mathrm{m}}/_{\mathrm{s}}$ $P = 3\,bar$ $T = 573.15\,K$ $AR = 1.5$ $L = 0.05\,m$. Full 3-dimensional model used.

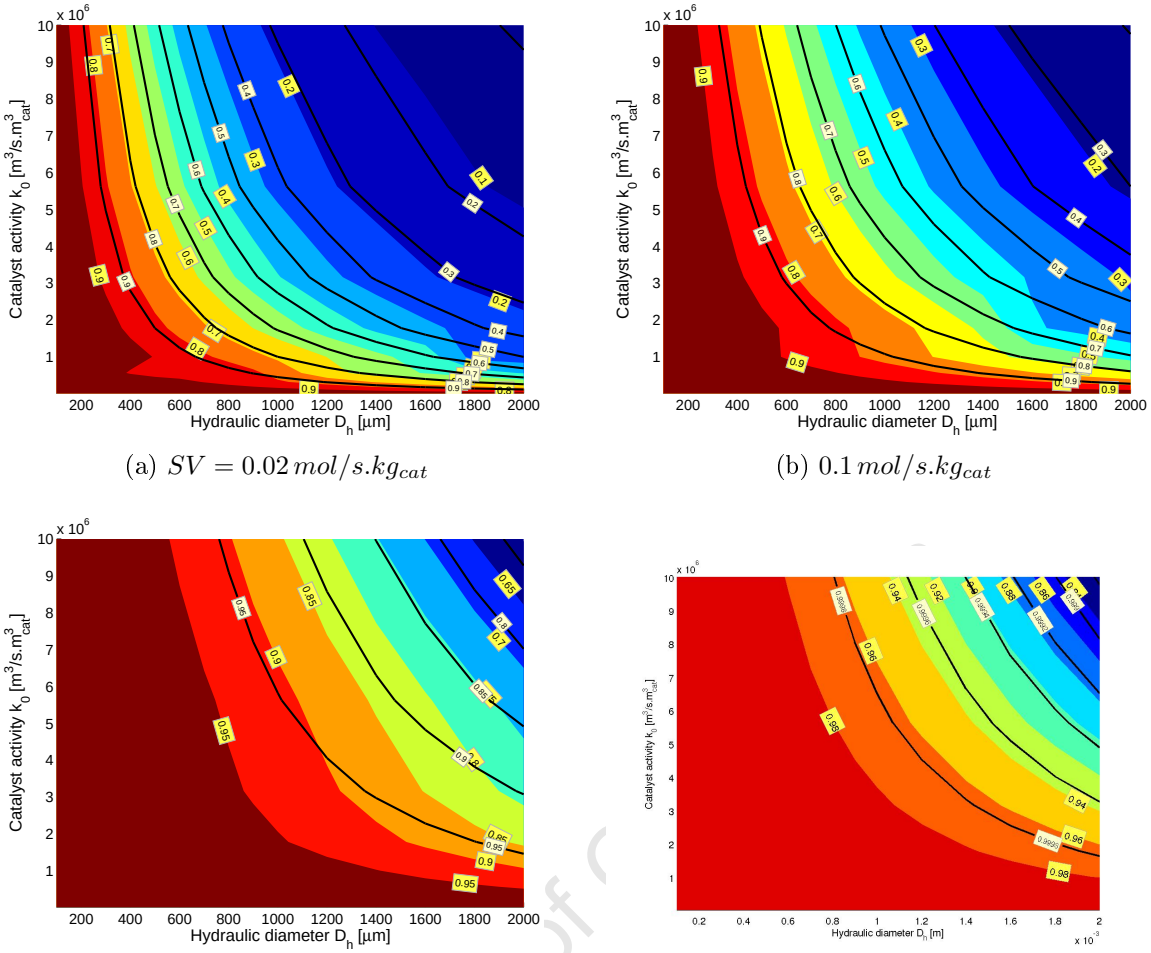

(a) $SV = 0.02\,mol/s.kg_{cat}$

(b) $0.1\,mol/s.kg_{cat}$

(c) $SV = 0.5\,mol/s.kg_{cat}$

(d) $SV = 2.5\,mol/s.kg_{cat}$

Figure E.2: Comparison of average effectiveness factors from the 3-dimensional (yellow labels) and 1-dimensional model (white label) for different space velocities. $D_h = 100 - 2000\,\mu m$ and $k_0 = 1 \times 10^4 - 1 \times 10^7\,{}^{\mathrm{m}^3}/_{\mathrm{s.m}^3_{\mathrm{cat}}}$ $v_0 = 0.5\,{}^{\mathrm{m}}/_{\mathrm{s}}$ $P = 3\,bar$ $T = 573.15\,K$ $AR = 1.5$ $L = 0.05\,m$.

E.1.2 v_0= 0.1 m/s

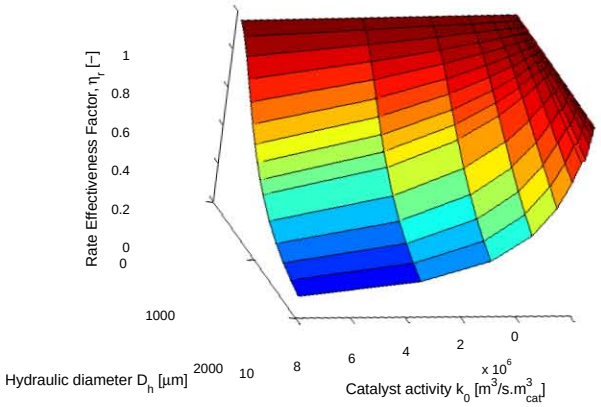

(a) $SV = 0.02\,mol/s.kg_{cat}$

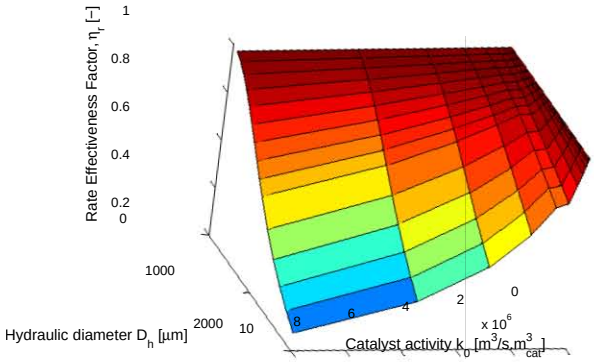

(b) $0.1\,mol/s.kg_{cat}$

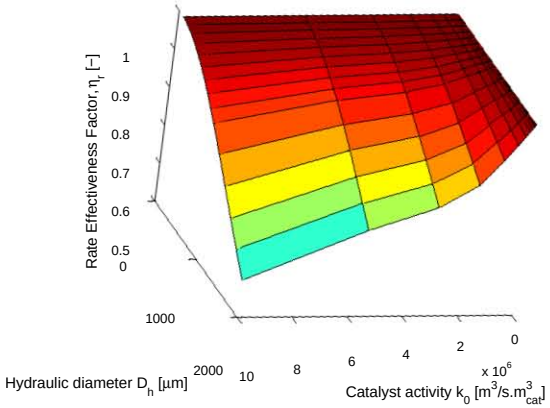

(c) $SV = 0.5\,mol/s.kg_{cat}$

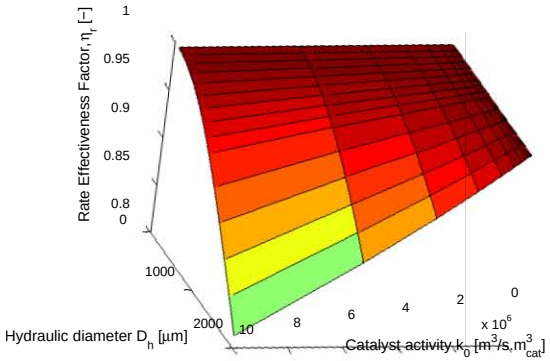

(d) $SV = 2.5\,mol/s.kg_{cat}$

Figure E.3: Change in average effectiveness factor with $D_h = 100 - 2000\,\mu m$ and $k_0 = 1\times10^4 - 1\times10^7\ {}^{\mathrm{m}^3}/_{\mathrm{s.m}^3_{\mathrm{cat}}}$ for different space velocities. $v_0 = 0.1\ {}^{\mathrm{m}}/_{\mathrm{s}}$ $P = 3\,bar$ $T = 573.15\,K$ $AR = 1.5$ $L = 0.05\,m$. Full 3-dimensional model used.

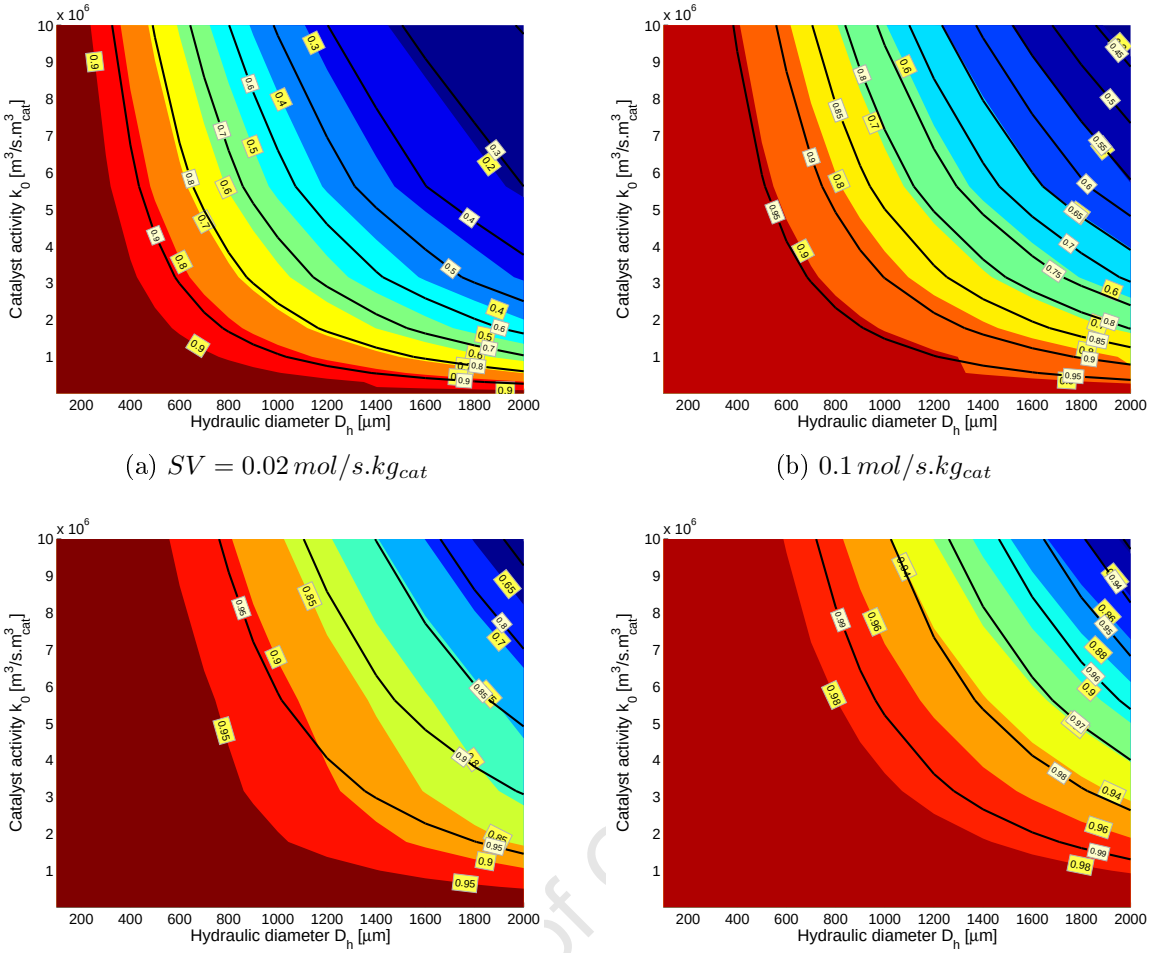

(a) $SV = 0.02\,mol/s.kg_{cat}$ (b) $0.1\,mol/s.kg_{cat}$

(c) $SV = 0.5\,mol/s.kg_{cat}$ (d) $SV = 2.5\,mol/s.kg_{cat}$

Figure E.4: Comparison of average effectiveness factors from the 3-dimensional (yellow labels) and 1-dimensional model (white label) for different space velocities. $D_h = 100 - 2000\,\mu m$ and $k_0 = 1 \times 10^4 - 1 \times 10^7\,\mathrm{m^3/s.m^3_{cat}}$ for different space velocities. $v_0 = 0.1\,\mathrm{m/s}$ $P = 3\,bar$ $T = 573.15\,K$ $AR = 1.5$ $L = 0.05\,m$.

E.1.3 $v_0 = 0.01$ m/s

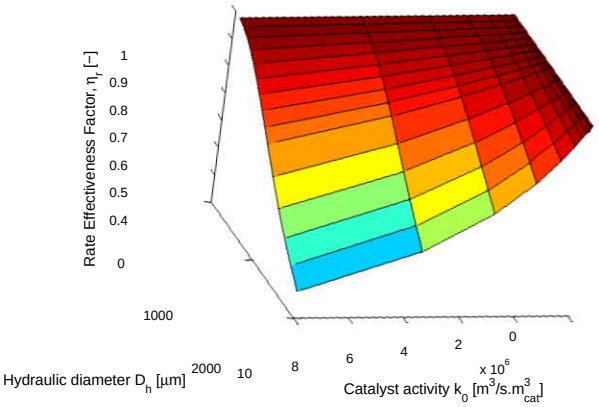

(a) $SV = 0.02\,mol/s.kg_{cat}$

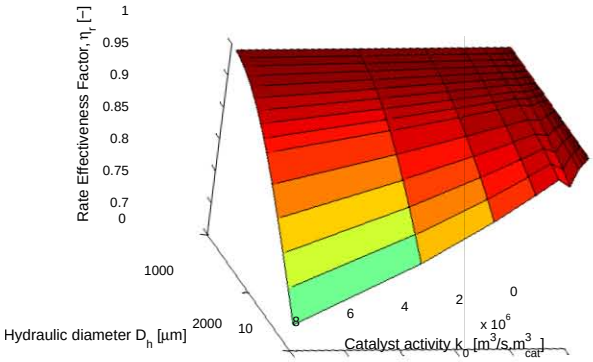

(b) $0.1\,mol/s.kg_{cat}$

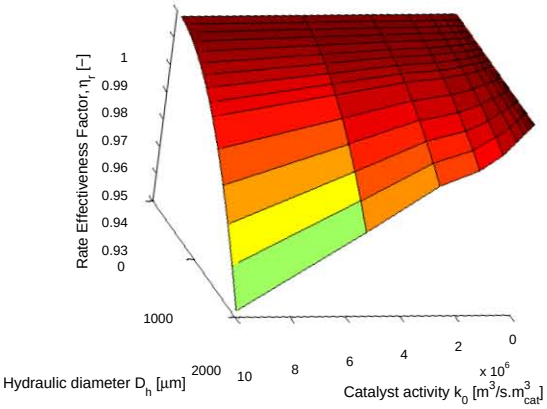

(c) $SV = 0.5\,mol/s.kg_{cat}$

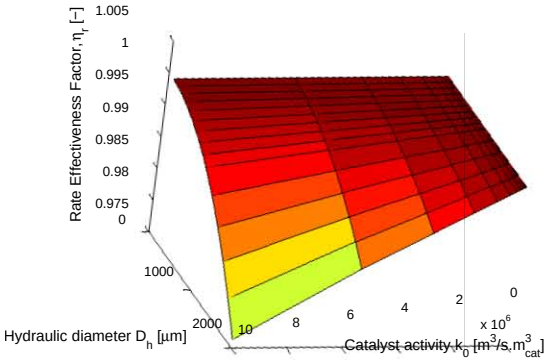

(d) $SV = 2.5\,mol/s.kg_{cat}$

Figure E.5: Change in average effectiveness factor with $D_h = 100 - 2000\,\mu m$ and $k_0 = 1\times10^4 - 1\times10^7\ {}^{\mathrm{m}^3}/_{\mathrm{s.m}^3_{\mathrm{cat}}}$ for different space velocities. $v_0 = 0.01\ {}^{\mathrm{m}}/_{\mathrm{s}}$ $P = 3\,bar$ $T = 573.15\,K$ $AR = 1.5$ $L = 0.05\,m$. Full 3-dimensional model used.

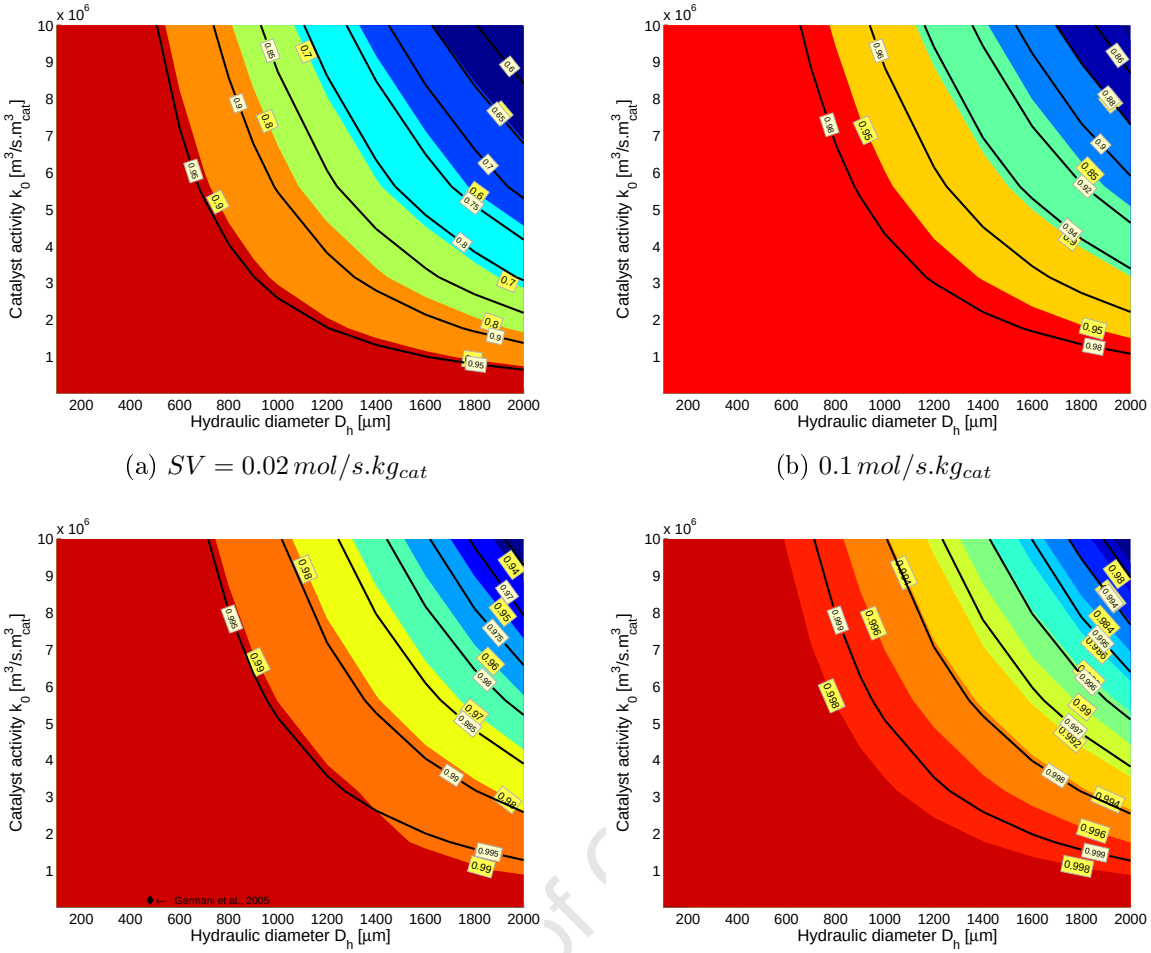

(a) $SV = 0.02\,mol/s.kg_{cat}$ (b) $0.1\,mol/s.kg_{cat}$

(c) $SV = 0.5\,mol/s.kg_{cat}$ (d) $SV = 2.5\,mol/s.kg_{cat}$

Figure E.6: Comparison of average effectiveness factors from the 3-dimensional (yellow labels) and 1-dimensional model (white label) for different space velocities. $D_h = 100 - 2000\,\mu m$ and $k_0 = 1 \times 10^4 - 1 \times 10^7\,\mathrm{m^3/s.m^3_{cat}}$ for different space velocities. $v_0 = 0.01\,\mathrm{m/s}$ $P = 3\,bar$ $T = 573.15\,K$ $AR = 1.5$ $L = 0.05\,m$.

E.2 Plots for time factor simulation

E.2.1 Conversion plots

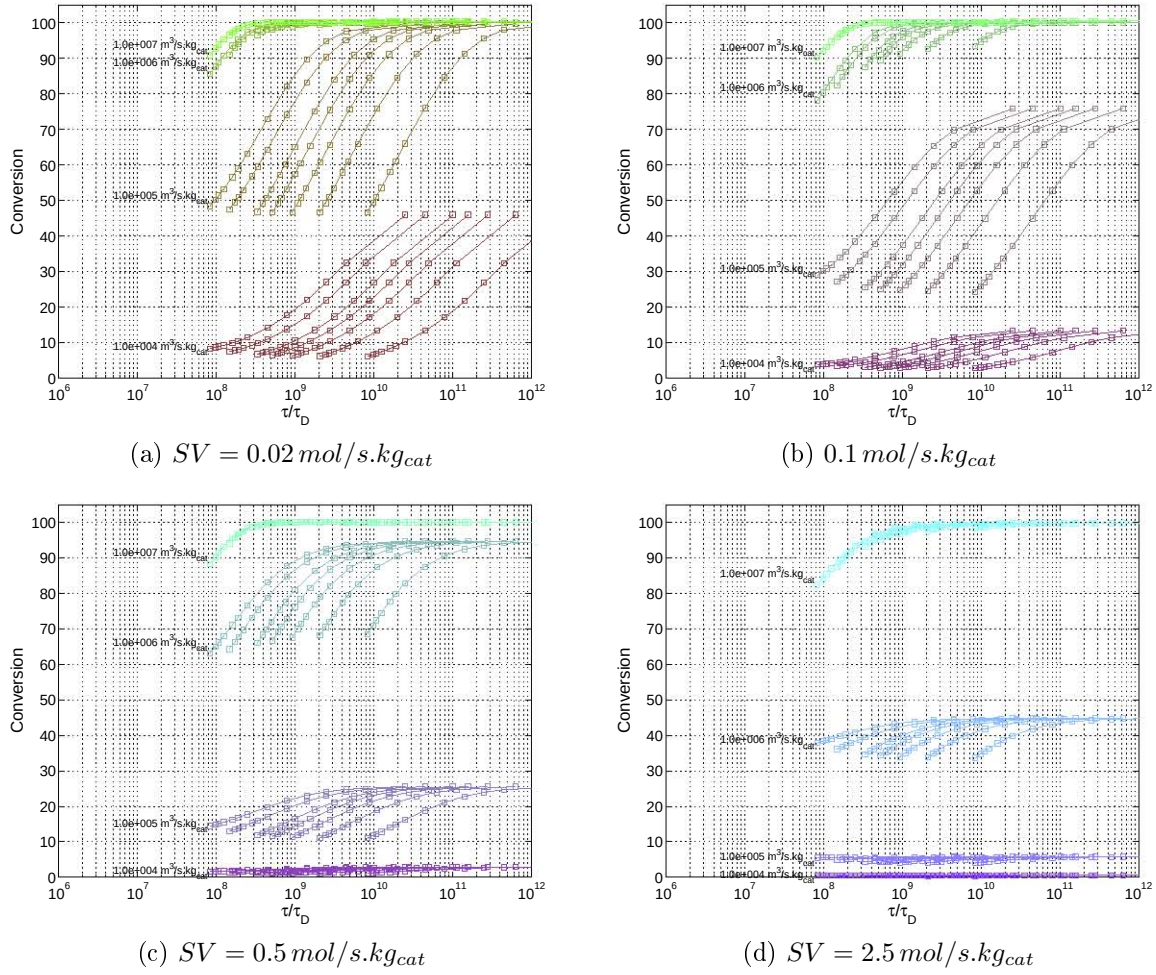

(a) $SV = 0.02\,mol/s.kg_{cat}$ (b) $0.1\,mol/s.kg_{cat}$

(c) $SV = 0.5\,mol/s.kg_{cat}$ (d) $SV = 2.5\,mol/s.kg_{cat}$

Figure E.7: Average effectiveness factor, $\eta_{c,1d}$ with $D_h = 100 - 2000\,\mu m$ and $k_0 = 1 \times 10^4 - 1 \times 10^7\,{}^{\mathrm{m}^3}/_{\mathrm{s.m}^3_{\mathrm{cat}}}$ for different space velocities. $v_0 = 0.5\,{}^{\mathrm{m}}/_{\mathrm{s}}$ $P = 3\,bar$ $T = 573.15\,K$ $AR = 1.5$ $L = 0.05\,m$. Dankwerts' 1-dimensional model used.

E.2.2 Effectiveness factor plots

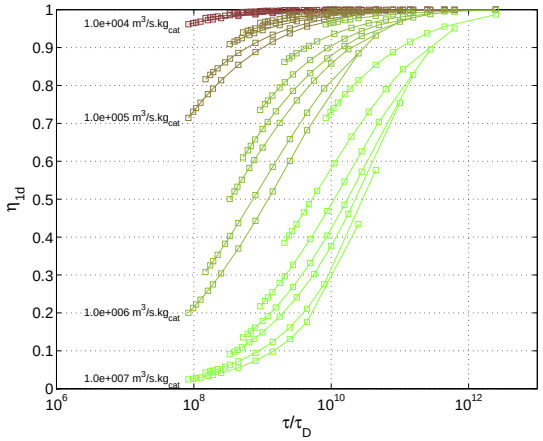

(a) $SV = 0.02\,mol/s.kg_{cat}$

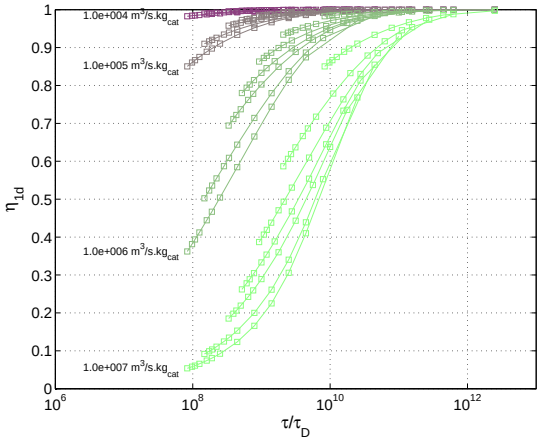

(b) $0.1\,mol/s.kg_{cat}$

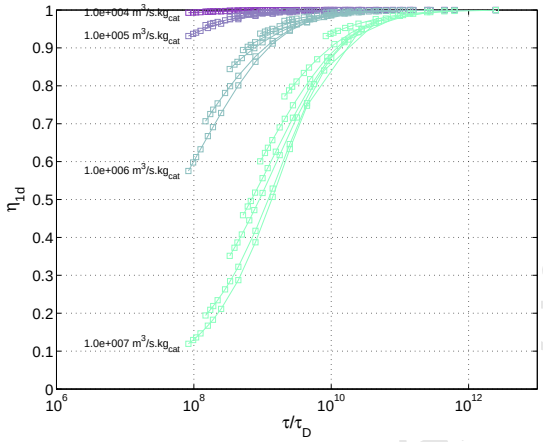

(c) $SV = 0.5\,mol/s.kg_{cat}$

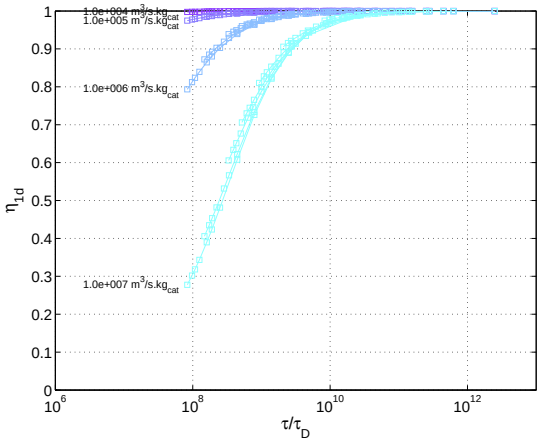

(d) $SV = 2.5\,mol/s.kg_{cat}$

Figure E.8: Average effectiveness factor, $\eta_{c,1d}$ with $D_h = 100 - 2000\,\mu m$ and $k_0 = 1 \times 10^4 - 1 \times 10^7\,{}^{\mathrm{m}^3}/_{\mathrm{s.m}^3_{\mathrm{cat}}}$ for different space velocities. $v_0 = 0.5\,{}^{\mathrm{m}}/_{\mathrm{s}}$ $P = 3\,bar$ $T = 573.15\,K$ $AR = 1.5$ $L = 0.05\,m$. Dankwerts' 1-dimensional model used.

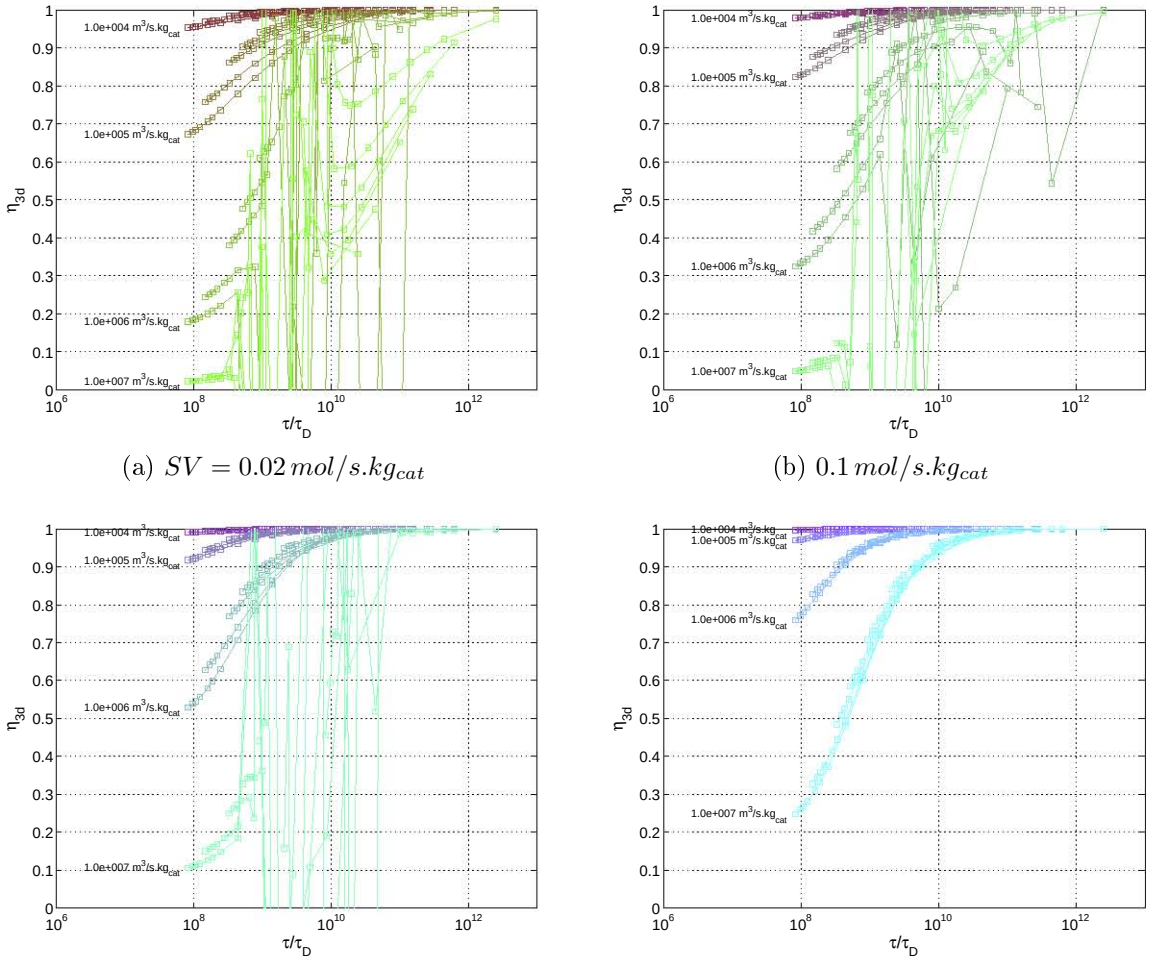

(a) $SV = 0.02\,mol/s.kg_{cat}$ (b) $0.1\,mol/s.kg_{cat}$

(c) $SV = 0.5\,mol/s.kg_{cat}$ (d) $SV = 2.5\,mol/s.kg_{cat}$

Figure E.9: Average effectiveness factor, $\eta_{c,3d}$ with $D_h = 100 - 2000\,\mu m$ and $k_0 = 1 \times 10^4 - 1 \times 10^7\,{}^{\mathrm{m}^3}/_{\mathrm{s.m}^3_{\mathrm{cat}}}$ for different space velocities. $v_0 = 0.5\,{}^{\mathrm{m}}/_{\mathrm{s}}$ $P = 3\,bar$ $T = 573.15\,K$ $AR = 1.5$ $L = 0.05\,m$. Full 3-dimensional model used.

E.2.3 Raw $R_{1,3}$ plots

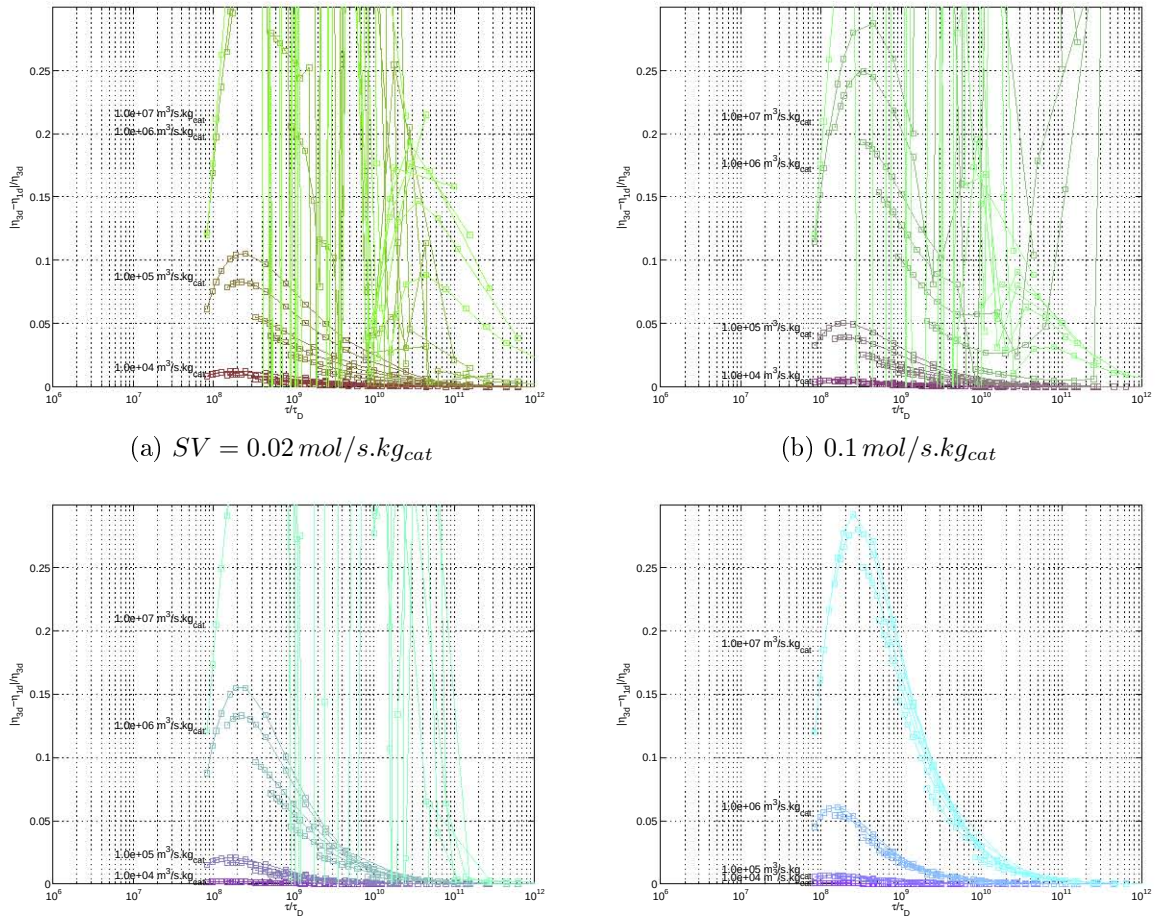

(a) $SV = 0.02\,mol/s.kg_{cat}$ (b) $0.1\,mol/s.kg_{cat}$

(c) $SV = 0.5\,mol/s.kg_{cat}$ (d) $SV = 2.5\,mol/s.kg_{cat}$

Figure E.10: Raw plot of ratio of fraction of mass transport by laminar flow against ratio of convective to diffusive time for different space velocities. $D_h = 100 - 2000\,\mu m$ $v_0 = 0.01 - 3.0\,\mathrm{m/s}$ $k_0 = 1 \times 10^4 - 1 \times 10^7\,\mathrm{m^3/s.m^3_{cat}}$ $P = 3\,bar$ $T = 573.15\,K$ $AR = 1.5$ $L = 0.05\,m$.